Dissertation zur Erlangung des Doktorgrades
der Fakultät für Chemie und Pharmazie
der Ludwig-Maximilians-Universität München

Computational Methods for the Quantitative Analysis of Membranes in Cryo-Electron Tomography

Maria Salfer geb. Kalemanov

aus

Kiew, Ukraine

2020

Erklärung

Diese Dissertation wurde im Sinne von §7 der Promotionsordnung vom 28. November 2011 von Prof. Dr. Wolfgang Baumeister betreut und von Prof. Dr. Karl-Peter Hopfner von der Fakultät für Chemie und Pharmazie vertreten.

Eidesstattliche Versicherung

Diese Dissertation wurde eigenständig und ohne unerlaubte Hilfe erarbeitet.

München, 18.12.2020

Maria Salfer

Dissertation eingereicht am:	11.11.2020
1. Gutachterin/Gutachter:	Prof. Dr. Karl-Peter Hopfner
2. Gutachterin/Gutachter:	Prof. Dr. Wolfgang Baumeister
Mündliche Prüfung am:	10.12.2020

This thesis was prepared from May 2015 to November 2020 in the laboratory of Professor Dr. Wolfgang Baumeister under representation by Professor Dr. Karl-Peter Hopfner from the Gene Center of the Ludwig-Maximilians-Universität (LMU) München.

This is a cumulative thesis based on the following three publications:

1. Felix J.B. Bäuerlein, Itika Saha*, Archana Mishra*, Maria Kalemanov, Antonio Martínez-Sánchez, Rüdiger Klein, Irina Dudanova, Mark S. Hipp, F. Ulrich Hartl, Wolfgang Baumeister & Rubén Fernández-Busnadiego (2017).
   In Situ Architecture and Cellular Interactions of PolyQ Inclusions.
   Cell 171: 179-187, September 21, 2017

2. Javier Collado, Maria Kalemanov*, Felix Campelo*, Clélia Bourgoint*, Ffion Thomas, Robbie Loewith, Antonio Martínez-Sánchez, Wolfgang Baumeister, Christopher J. Stefan & Rubén Fernández-Busnadiego (2019).
   Tricalbin-Mediated Contact Sites Control ER Curvature to Maintain Plasma Membrane Integrity.
   Developmental Cell 51: 476-487, November 18, 2019

3. Maria Salfer, Javier Collado, Wolfgang Baumeister, Rubén Fernández-Busnadiego & Antonio Martínez-Sánchez (2020).
   Reliable Estimation of Membrane Curvature for Cryo-Electron Tomography.
   PLoS Computational Biology, August 10, 2020: 1-29

* These authors contributed equally

Parts of this thesis have been presented at international conferences:

1. Maria Kalemanov, Javier Collado, Wolfgang Baumeister, Rubén Fernández-Busnadiego & Antonio Martínez-Sánchez.
   Membrane Curvature Estimation Method for Cryo-Electron Tomography.
   Talk at 2019 Quantitative BioImaging (QBI) Conference: 8-11.01.2019 in Rennes, France.
   QBI Conference (2019), Abstract 118: 137

2. Maria Salfer, Javier Collado, Wolfgang Baumeister, Rubén Fernández-Busnadiego & Antonio Martínez-Sánchez.
   Reliable Estimation of Membrane and Surface Curvature for Cryo-Electron Tomography and Beyond.
   Poster presentation at the 17th international PhD student symposium Horizons in Molecular Biology: 14-17.09.2020 in Göttingen, Germany, hosted online.
   17th Horizons in Molecular Biology (2020), Poster Abstract 5: 84.

Contents

Abstract

Membranes delineate all living cells and compartmentalize eukaryotic cells into organelles. Dynamically shaping the cells and the organelles, membranes help to maintain specific micro-environments and play an important role in many physiological functions. Cryo-electron tomography (ET) is a leading technique for three-dimensional (3D) visualization and analysis of membrane morphology in a close-to-native state and molecular resolution. However, there is currently a lack of computational methods that can analyze membrane morphology directly from cryo-ET data. Adaptation of existing algorithms from other fields to cryo-ET and development of new algorithms are crucial for the analysis and interpretation of membrane segmentations from cryo-ET. During this dissertation, the following contributions were made.

1. An **open-source Python software package for membrane and surface curvature estimation**, called **PyCurv**, was created and actively maintained. The algorithms included in PyCurv were extensively benchmarked on artificial and biological data. Compared to three currently existing methods, PyCurv was **the most accurate and robust to noise not only for cryo-ET data, but also for data originating from other imaging techniques** like magnetic resonance imaging (MRI) and light microscopy. An early version of the method showed a significant **increase in endoplasmic reticulum (ER) membrane curvature in the tomograms with polyQ-expanded huntingtin (Htt) exon I fibrils**. Using a recent version of PyCurv, significant **curvature differences of cortical ER (cER) membranes** were found **in yeast cells expressing different plasma membrane (PM) tether proteins** under different conditions, highlighting **peaks of extreme curvature**.

2. An **algorithm for calculation of the density of membrane-bound macromolecules** was developed. After detection of membrane-bound ribosomes by template matching and segmentation of ER membranes in tomograms of mammalian cells with the Htt fibrils, the algorithm confirmed that **less ribosomes were bound to ER membranes near the Htt fibrils than further away from the fibrils**.

3. An **algorithm for measurement of distances between membranes in membrane contact sites (MCS)** was implemented. Applied to membrane segmentations in tomograms of yeast cells, it **determined the typical membrane distances in different MCS** and revealed significant **differences between cells expressing certain ER-PM tethering proteins**. While some of the proteins formed MCS with a shorter ER-PM distance, other proteins stabilized cER sheets with a shorter luminal thickness.

Zusammenfassung

Lebende Zellen sind von Membranen umgeben, auch die Organellen innerhalb der eukaryontischen Zellen. Membranen formen Zellen und Organellen, helfen spezifische Mikroumgebungen aufrechtzuerhalten und spielen eine wichtige Rolle bei vielen physiologischen Funktionen. Die Kryoelektronentomographie (Kryo-ET) ist eine führende Technik für die drei-dimensionale Visualisierung und Analyse der Membranmorphologie in einem beinahe natürlichem Zustand und einer molekularen Auflösung. Dennoch mangelt es derzeit an Methoden zur Analyse der Membranmorphologie direkt aus Kryo-ET-Daten. Die Anpassung vorhandener Algorithmen an Kryo-ET und die Entwicklung neuer Algorithmen sind ausschlaggebend für die Analyse und Interpretation der Membransegmentierungen aus Kryo-ET. Während dieser Dissertation wurden die folgenden Beträge geleistet.

1. Ein **Open-Source-Python-Softwarepaket zur Abschätzung der Krümmung von Membranen und anderen Oberflächen**, namens **PyCurv**, wurde erzeugt und aktiv gepflegt. Die in PyCurv enthaltenden Algorithmen wurden ausführlich auf synthetischen und biologischen Daten getestet. Verglichen mit drei derzeit vorhandenen Methoden war PyCurv **am präzisesten und robustesten gegen Rauschen für Kryo-ET-Daten, als auch für Daten aus anderen bildgebenden Verfahren** wie Magnetresonanztomographie (MRT) und Lichtmikroskopie. Eine frühe Version der Methode zeigte eine signifikante **Steigung in der Membrankrümmung des endoplasmatischen Retikulums (ER) in den Tomogrammen mit Fibrillen aus dem polyQ-expandierten Huntingtin-(Htt)-Exon-I**. Mithilfe einer neueren PyCurv-Version wurden **signifikante Unterschiede in der Membrankrümmung vom kortikalen ER (kER) in Hefezellen** erkannt, **wo verschiedene Plasmamembran-(PM)-bindende Proteine** unter verschiedenen Bedingungen **exprimiert wurden**. Bemerkenswert waren **Membran-Hügeln mit einer extremen Krümmung**.

2. Ein **Algorithmus zur Berechnung der Dichte der membrangebundenen Makromolekülen** wurde entwickelt. Nach Erkennung der membrangebundenen Ribosomen mittels Template-Matching und Segmentierung der ER-Membranen in den Tomogrammen der Säugetierzellen mit den Htt-Fibrillen, bestätigte der Algorithmus, dass **weniger Ribosomen an die ER-Membranen in der Nähe der Htt-Fibrillen gebunden waren als weiter weg davon**.

3. Ein **Algorithmus zur Berechnung der Distanzen zwischen den Membranen in den Membran-Kontakt-Stellen (MKS)** wurde implementiert. Nach dessen Anwendung auf Membransegmentierungen in Tomogrammen der Hefezellen wurden die **typischen Membrandistanzen in verschiedenen MKS erfasst** und signifikante **Unterschiede zwischen den Zellen** erkannt, **wo bestimmte ER-PM-bindende Proteine exprimiert wurden**. Manchen Proteine formten MKS mit kürzeren ER-PM-Distanzen, während andere Proteine dünne kER-Blätter stabilisierten.

List of Abbreviations

2D two-dimensional. 7, 13, 16, 24, 34

3D three dimensions. 20, 24, 25, 27

3D three-dimensional. iii, 6, 7, 13, 14, 16, 17, 19, 21, 29, 37

AP affinity propagation. 17, 36

AVV Augmented Vector Voting. 34, 35, 39–44

BAR Bin/Amphiphysin/Rvs. 5, 7

CCD charge-coupled device. 9, 12

cER cortical ER. iii, 26, 28, 31, 34–36, 42, 44

CNN convolutional neural networks. 17, 19

CTF contrast-transfer function. 9, 11

DED direct electron detector. 12

ER endoplasmic reticulum. iii, vii, 1, 6, 17, 19, 25–28, 32–35, 42–44

ET electron tomography. iii, x, 6–10, 12, 14, 19, 24, 25, 27–29, 31, 34, 37, 42

FIB focused ion beam. 7, 8, 13

HD Huntington's disease. 25–27

Htt huntingtin. iii, 25–27, 33, 34, 42, 43

IB inclusion body. 27, 43

IBs inclusion bodies. 27, 34, 42, 43

MCS membrane contact sites. iii, 26, 28, 29, 35

MRI magnetic resonance imaging. iii, 24, 29, 37

NAD nonlinear anisotropic diffusion. 15, 16

NVV Normal Vector Voting. 33–36, 42, 43

PM plasma membrane. iii, 1, 5, 7, 19, 26, 28, 34–36

QBM Quantitative Biosciences Munich. ix, x

RVV Regular Vector Voting. 35

SEM scanning electron microscope. 8

SNARE **s**oluble **N**-ethylmaleimide-sensitive factor **a**ttachment protein **re**ceptor. 7

SNR signal-to-noise ratio. 14, 15, 17, 18, 34, 36

SPA single particle analysis. 12, 16

SSVV Surface Sampling Vector Voting. 35, 39–42

TAC thesis advisory committee. ix

TEM transmission electron microscope. 7–11, 16

VPP Volta phase plate. 9, 11, 27

WBP weighted back-projection. 14

WT wild-type. 28, 42, 44

Units of measurements were abbreviated according to the international system of units.

Acknowledgments

First of all, I thank Prof. Dr. Rubén Fernández-Busnadiego, my direct PhD supervisor and thesis advisory committee (TAC) member, for all the great supervision and advice, for thorough paper and thesis revisions and for support during the hard revision times. He improved my presentation, writing and visualization skills a lot. Equally, I thank Prof. Dr. Antonio Martinez, my co-supervisor on the computational side, for joining my later TAC meetings and many of my group meetings even before changing to Ruben's group, for the collaboration on papers, especially for being the first last-author of my first first-author paper, for thorough paper and thesis revisions and for all the numerous interesting discussions in computer science and beyond. I also thank Prof. Dr. Wolfgang Baumeister, my MPI "Doktorvater", TAC member and examiner, for letting me work on my PhD thesis in his department, for giving me feedback during my TAC meetings and Ringberg talks, and for providing me financial support for several years. Many thanks to Prof. Dr. Karl-Peter Hopfner, my LMU "Doktorvater", TAC member and examiner, for agreeing to supervise my thesis without me working in his department, for the feedback during my TAC meetings and for letting me write a cumulative thesis. Special thanks to the bioinformatician Dr. Bianca Habermann for joining my first TAC meetings, one of them even after taking her new position in France, for the valuable feedback and for interesting ideas.

I acknowledge my graduate school for Quantitative Biosciences Munich (QBM) and its staff for selecting me during my application in 2015 and providing me a stipend for three years of my PhD studies, for broadening my knowledge with many courses and workshops and also for financing my attended conferences. Special thanks to Dr. Markus Hohle and Roman Wagener for fixing and exchanging my laptop several times, without a functioning laptop my project would have been impossible! Also, in addition to the numerous QBM courses in mathematics, physics and bioinformatics, I thank Markus for his help with mathematics behind curvature estimation during several private lessons.

Thanks to Dr. Felix Bäuerlein for the fruitful collaboration on our Cell paper, for teaching me how to segment membranes in Amira, as well as for his medical examination of a volleyball injury of my arm, after a correct treatment by Prof. Dr. Yoshiyuki (Fuku) Fukuda. I thank Javier Collado, another QBM student who joined the department just a month after me, for the close friendship from the beginning on. We learned many things together, for example how to load samples under liquid nitrogen and how to segment membranes in TomoSegMemTV, and collaborated on two papers. Thanks Javier for briefing me on how to fill membranes in Amira and how to submit tomogram entries to EMDB during the stressful paper revision time. I am especially grateful to Javier for teaching me how to ride a bike on the way from the institute to the subway. Also, Javier managed to convince me and Victoria Trinkaus to try some gardening at the field near the institute last year, which turned out to be a tough experience, and Javier said "I would rather finish my PhD and get a job".

I thank my (ex-)colleagues Anselm Gruber and Dr. Tillman Schäfer for giving me

cryo-ET introduction, Tillman also for sharing a tomogram with Golgi and vesicle membranes for the PLoS paper. Thanks Dr. Vladan Lucic for Python advice and for porting his Pyto software package to Python 3, which enabled me to port PyCurv as well. I thank Florian Beck for his great help with installing PyCurv on the Vis cluster. I acknowledge the director's office managers, Birgit Book and Eva Sartorius, for their reliable support with contracts, visa issues and all the other administrative questions.

Thanks to Fuku and Prof. Dr. Radostin (Rado) Danev, who became Professors in Japan, Dr. Maryam Khoshouei, who started working at Novartis in Switzerland, and Dr. Luca Zinzula for the interesting discussions including phase plate and subtomogram averaging over beer and pizza on many late Friday evenings at (back then) Rado's and Maryam's office. I also thank Rado's computational Master's student Victor Movileanu for joining PyData meetups and giving a nice talk there, for joint training sessions together with some PhD students from the Mann department and for the nice friendship. I especially want to thank an enthusiastic scientist, QBM student, PhD student representative of 2019-2020 and my close friend, Victoria (Vicky) Trinkaus, for being a nice roommate during a symposium in London and retreats at castle Ringberg, for the "despressos", for introducing me to weights lifting at the gym, for joining the MPI choir with me and for organizing many social events in our department and beyond. I very appreciate Vicky's energy and readiness to help many other people in many respects.

I thank my office (ex-)colleagues, especially Dr. Antje Aufderheide, Dr. Martin Turk, Dr. Luis Kuhn, Dr. Mauricio Toro, Dr. Peng Xu, Zhen Hou, Tapan Joshi and Patricia Dijkman for the nice working environment, interesting discussions about science, health, sports and more. Additionally, thanks to Peng, his wife Ronquin (Xiao-Xiao) Li and Zhen for letting me join the Chinese lunches and for watering my plants so many times. Also thanks to all the other (ex-)colleagues for many interesting discussions during lunches, seminars, journal clubs, retreats and other events and for the nice friendships that developed.

Thanks to Dr. Nick Del Grosso for teaching me Python programming and for his help with setting up my first GitHub repository. We also were co-organizing a Python meetup (PyData Munich) in 2018 and went to a Python conference (PyCon.DE & PyData Karlsruhe 2018) together. I thank my close friends Parastou Kohvaei and Dr. Mattias Backman for the nice time at QBM-retreats and many lunches, and together with Dr. Michael Volkmer (who worked at Dr. Bianca Habermann's group before changing to the institute's IT) for many Python meetups and gardening help. Also thanks to Dr. Roman Prytuliak (also from Dr. Bianca Habermann's group) for introducing me to Russian lunches in the Mensa, where I met many nice people.

I thank my beloved family: my parents Natalia and Vladimir Kalemanov, my sister Dr. Anna Schlösser and brother-in-law Thomas Schlösser for their support and understanding during my whole studies. Thanks to my parents-in-law Rita and Josef Salfer, to my sisters- and brothers-in-law Karin and Niklas Borchers, Michael and Barbara Salfer, who all became part of my family during my PhD studies. Last but not least, I am especially grateful to my husband, Martin Salfer, for all the scientific discussions, in particular about computer science and software development, for revisions of diverse things in German and English, for great help with Git and software diagrams, for firm support and for constant care during the whole time of my PhD studies.

1 Introduction

1.1 Biological and biochemical aspects of membrane curvature

1.1.1 Roles of membrane curvature in cellular processes

Membranes mark the limits of all cells and divide eukaryotic cells into compartments or organelles, which maintain specific environments distinct from the cytoplasm. Membranes consist of a phospholipid bilayer interspersed with other lipids, like cholesterol, as well as integral and peripheral proteins forming curved, closed surfaces (Kozlov et al., 2014). Phospholipids are amphipatic molecules with a hydrophilic head and a hydrophobic tail, consisting of two acyl chains. In aqueous solution, the hydrophobic tails stick to each other, while the hydrophilic heads face the solution, forming a bilayer. Integral proteins insert their hydrophobic domains into the lipid bilayer interior (mediated by Van-der-Waals interactions), while peripheral proteins are attracted to the bilayer surface with their hydrophilic domains (by electrostatic or hydrogen bonding forces) (Kozlov et al., 2014).

Changes in PM morphology and curvature are involved in many phenomena, e.g. endo- and exocytosis, phagocytosis and filopodia formation (Bassereau et al., 2018). Furthermore, generation and maintenance of membrane curvature of intracellular organelles is crucial for maintaining cellular functions and trafficking (McMahon and Boucrot, 2015; Bassereau et al., 2018). A common feature of intracellular organelles, e.g. ER, Golgi cisternae, mitochondria cristae and endocytic vesicles, is the large membrane curvature with radii in the range of 10–30 nm, which are only a few times larger than the 4–5 nm thicknesses of the membranes (Kozlov et al., 2014). Different organelles have characteristic shapes, which are dynamically changing according to the needs of the cell or in the process of organelle maturation (Rafelski and Marshall, 2008; McMahon and Boucrot, 2015). The shapes of the organelles are often highly complex, with a large ratio between the area and the enclosed volume (lumen), in order to facilitate the molecular exchange between the lumen and the cytosol (Kozlov et al., 2014).

To enable molecular exchange between different parts of the cell, small vesicles enclosing the required molecules by their membrane are constantly being formed and detached from organelles, transferred to a target organelle and fused with its membrane. The detachment process is called membrane scission and is crucial for budding of coated vesicles, e.g. from the ER, Golgi, endosomes or PM, and also for virus budding (Hurley and Hanson, 2010; Rossman and Lamb, 2013; McMahon and Boucrot, 2015). The opposite process is called membrane fusion (Martens et al., 2007; Martens and McMahon, 2008). Interestingly, some tethering proteins and enzymes can sense membrane curvature, mediating vesicle targeting or protein activation (McMahon and Boucrot, 2015). Furthermore, transmembrane receptors having an intrinsic shape

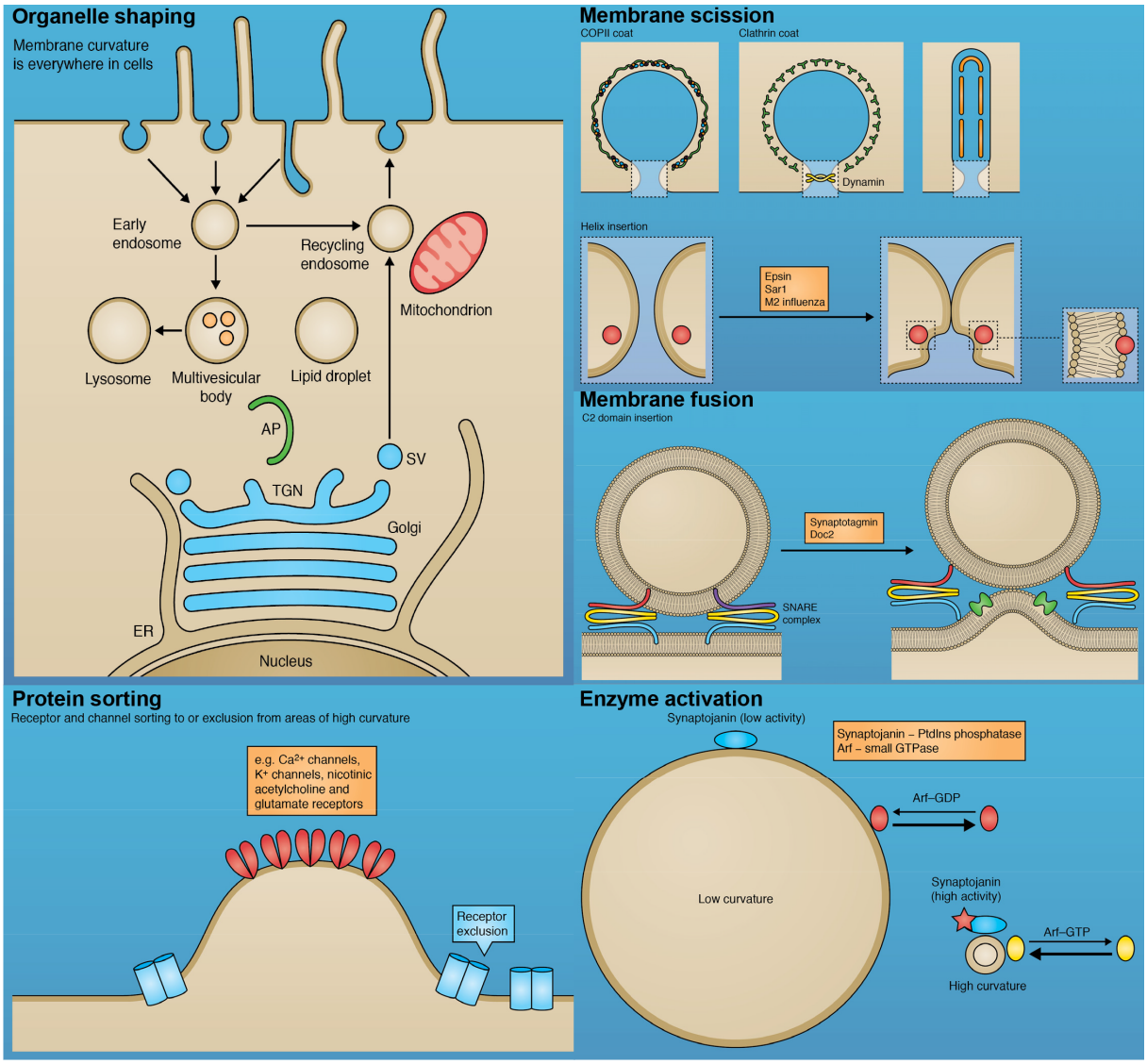

Figure 1.1: Cellular functions involving membrane curvature. Illustration of the most important cellular functions involving membrane curvature: organelle shaping, membrane scission and fusion, protein sorting and enzyme activation. Source: (McMahon and Boucrot, 2015), see for abbreviations.

are preferably sorted into membrane regions accommodating this shape. See Figure 1.1 for the illustration of the most important cellular functions involving membrane curvature.

1.1.2 Cellular mechanisms for generation, sensing and maintenance of membrane curvature

On the one hand, a pure lipid bilayer tends to be flat given the symmetry of its monolayers (if both have the same lipids) and is resistant to bending due to its elastic properties caused by the interactions between the lipid molecules in each monolayer (Kozlov et al., 2014; McMahon and Boucrot, 2015). On the other hand, any bilayer tends to be continuous without edges and holes by adopting a closed shape, which can only be achieved by bilayer bending (Helfrich, 1986; Kozlov et al., 2014). The

result of these competing phenomena is that a bilayer fragment larger than 200 nm in diameter adapts a closed spherical shape, which can only be deformed by introducing asymmetry into the bilayer or applying force to its surface (Kozlov et al., 2014). The asymmetry can be introduced either by changing the composition and/or number of lipid molecules in the two monolayers (Devaux, 2000) or by asymmetric protein crowding on the two membrane sides (Stachowiak et al., 2012; Kozlov et al., 2014; McMahon and Boucrot, 2015). Only specialized proteins have sufficient forces to curve the membrane or the ability to sense and maintain high local membrane curvature, by the mechanisms described below (Kozlov et al., 2014; McMahon and Boucrot, 2015). See Figure 1.2 for the illustration of the different mechanisms of membrane curvature generation and stabilization.

Changes in lipid composition and asymmetry

Different lipids have different shapes depending on their headgroup sizes and acyl chain saturation (McMahon and Boucrot, 2015). Clustering of many lipids with the same shapes and orientation causes the monolayer to spontaneously adopt their curvature. Cylindrical lipids (e.g. Phosphatidylcholine and phosphatidylserine) form a flat monolayer. Conical lipids with a small headgroup (e.g. phosphatidylethanolamine, phosphatic acid, diacylglycerol or cardiolipin) impose a negative curvature. A double bond induces a kink in an acyl chain (e.g in oleic acid), so that it occupies more space, also leading to a negative curvature. Inverse conical lipids with a large headgroup (e.g. lysophosphatidylcholine or phosphatidylinositol phosphates) favor a positive curvature (Chernomordik and Kozlov, 2003; Di Paolo and De Camilli, 2006; Zimmerberg and Kozlov, 2006; McMahon and Boucrot, 2015). Lipid asymmetry between the two monolayers is actively maintained by specialized proteins, e.g. by lipid flippases, lysophospholipid acyltransferases, phospholipase A or sphingomyelinases (Graham and Kozlov, 2010; McMahon and Boucrot, 2015).

Protein crowding

A higher concentration of proteins at one side of the membrane has been suggested to induce its curvature (Stachowiak et al., 2012), however the efficiency of this non-specific mechanism is very low according to theoretical predictions and experimental evidence (Kozlov et al., 2014; McMahon and Boucrot, 2015).

Clustering of shaped transmembrane domains

Transmembrane proteins (e.g. ion channels, receptors and transporters) with a conical or inverted conical shape can impose this shape on their associated membranes (Fertuck and Salpeter, 1974; MacKinnon, 2003; Unwin, 2005; Aimon et al., 2014; Fribourg et al., 2014; McMahon and Boucrot, 2015). Many integral membrane proteins cluster (directly or via connecting proteins (Boudin et al., 2000; Eckler et al., 2005)), building a local scaffold on the membranes (McMahon and Boucrot, 2015). For example, transmembrane receptors cluster in forming endocytic clathrin-coated pits, stabilizing them and so supporting the generation of membrane curvature (Ehrlich et al., 2004; McMahon and Boucrot, 2015).

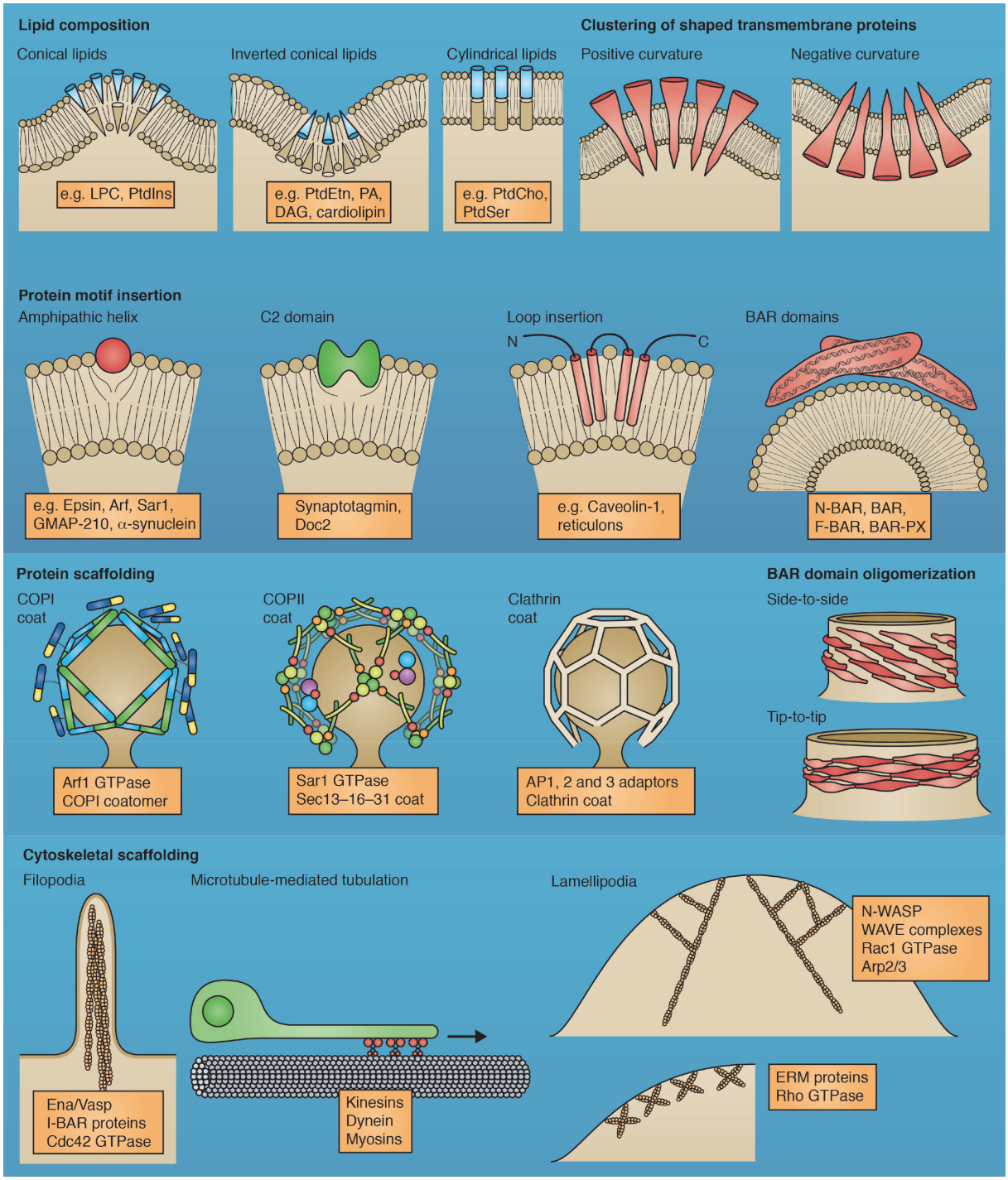

Figure 1.2: Mechanisms of membrane curvature generation and stabilization. Illustration of the main mechanisms of membrane curvature generation and stabilization: lipid composition, clustering of shaped transmembrane proteins, protein motif insertion, protein scaffolding and oligomerization as well as cytoskeletal scaffolding. Source: (McMahon and Boucrot, 2015), see for abbreviations.

Insertion of hydrophobic or amphipathic protein domains

A very efficient way of inducing local membrane curvature is a shallow insertion of a small hydrophobic or amphipathic protein domain between the lipid headgroups, acting like a wedge (Kozlov et al., 2014; McMahon and Boucrot, 2015). For example, the insertion of hydrophobic loops present at the tip of the C2 domains of synaptotagmin-1 and Doc2b (Martens et al., 2007; Hui et al., 2009; Groffen et al., 2010) induces high membrane curvature (McMahon et al., 2010; McMahon and Boucrot, 2015). Besides the shallow insertions, there are also integral insertions spanning the whole membrane thickness, e.g. transmembrane domains of ATPases or the acetylcholine receptor, which have intrinsic shapes and thus are likely to generate some local membrane curvature (Kozlov et al., 2014). The shallow protein insertions were experimentally shown (Ford et al., 2002) and predicted (Campelo et al., 2008; Lai et al., 2012; Braun et al., 2012; Fuhrmans and Marrink, 2012; Cui et al., 2013) to generate membrane curvature much more efficiently than the integral insertions (Kozlov et al., 2014).

Scaffolding by hydrophilic protein domains

Scaffolding by peripheral proteins can also efficiently generate or support membrane curvature at a microscopic level by oligomers assembled into larger, curved structures (Kozlov et al., 2014; McMahon and Boucrot, 2015). Coat proteins such as clathrin, COPI and COPII polymerize and bind via adaptor proteins to the membrane, stabilizing its spherically-shaped curvature during vesicle budding (Kirchhaussen, 2000; Jensen and Schekman, 2011; McMahon and Boucrot, 2011; Zanetti et al., 2012; Faini et al., 2013; Kozlov et al., 2014; McMahon and Boucrot, 2015). The crescent-shaped monomeric or dimeric Bin/Amphiphysin/Rvs (BAR) domains bind to membranes and favor the formation of cylindically-shaped tubules (Peter et al., 2004; Itoh and De Camilli, 2006; Frost et al., 2007; Boucrot et al., 2012; Kozlov et al., 2014; McMahon and Boucrot, 2015). Also oligomers of dynamin family proteins that are involved in endocytosis act as cylindrical scaffolds (Ferguson and De Camilli, 2012; Kozlov et al., 2014). U-shaped ATP syntase dimers assemble into helical arrays that form tubular cristae in ciliate mitochondria (Mühleip et al., 2016).

Scaffolding by cytoskeleton and molecular motors

Filopodia are formed by actin filament bundles that polymerize against tensed PM (Bornschlogl et al., 2013), whereas intracellular membrane tubes are formed by molecular motors that accumulate at the tips of microtubules and anchor to the membranes (Leduc et al., 2010; Kozlov et al., 2014). Interestingly, membrane tubes generated by pulling or pushing forces must be straight, which is normally the case for filopodia (Jaiswal et al., 2013) but not for ER and trans-Golgi tubules, which are bent (Voeltz et al., 2002; Shibata et al., 2006; Kozlov et al., 2014). Thus, it is probable that the pulling mechanism by microtubules takes place in the early stages of the tubules formation, but their membrane curvature is stabilized and completed by other mechanisms, e.g. scaffolding by reticulons and/or DP1/Yop1p proteins (Kozlov et al., 2014).

Combination of multiple mechanisms

To sum up, shallow hydrophobic insertions and strongly curved protein scaffolds are the most effective mechanisms generating membrane curvature of organelles (Kozlov et al., 2014). Usually, multiple of the aforementioned mechanisms are combined to efficiently induce membrane curvature: Insertions of domains and scaffolding can be performed by the same or different proteins involved in the same cellular process, building networks of interactions combining sensing, induction and stabilization of membrane curvature (McMahon and Gallop, 2005; McMahon and Boucrot, 2015).

1.2 Cryo-electron tomography

1.2.1 Advantages of cryo-ET for 3D visualization of membranes

Cryo-ET is since a few decades the leading technique for obtaining accurate 3D reconstructions of cells, organelles or macromolecular assemblies *in situ*, i.e. in their unperturbed environment, and at molecular resolution (Lučić et al., 2005; Beck and Baumeister, 2016). This was enabled by many technological advances in sample preparation techniques, imaging devices and computational methods (Lucic et al., 2013; Wagner et al., 2017). In cryo-ET, a cellular sample is rapidly frozen and two-dimensional images are acquired for different tilts inside an electron microscope. These images are then computationally aligned and reconstructed into a 3D volume of the cellular interior, called tomogram.

Cryo-ET is much better suited to study membrane morphology and membrane-associated complexes (Collado and Fernández-Busnadiego, 2017) than alternative related techniques. Conventional electron microscopy involves chemical fixation and dehydration of cells or tissues at room temperature, embedding into resin or plastic, sectioning into slices and staining with heavy metal salts to increase contrast. These procedures can cause distortions and rearrangements of internal membranes (Murk et al., 2003) as well as aggregation artifacts (Lučić et al., 2005). Rapid freezing/freeze-substitution involves substitution of water in cells or tissues by an organic solvent with chemical fixatives at around -80°C, also followed by resin or plastic embedding, sectioning and staining. Avoiding the dehydration procedure preserves the membranes better, however aggregation artifacts still occur (Dubochet and Sartori Blanc, 2001). In addition, the staining limits the obtained resolution beyond the molecular level (Lučić et al., 2005). The rapid freezing preparation used in cryo-ET enables *in situ* imaging of frozen-hydrated cells in a close-to-native functional state with the best structural preservation (Lučić et al., 2005; Beck and Baumeister, 2016; Collado and Fernández-Busnadiego, 2017).

Cryo-ET has been applied to study membrane morphology and curvature in reconstituted preparations (Lee, 2010; Cardone et al., 2012; Bharat et al., 2014; Chlanda et al., 2016; Chen et al., 2019) and intact cells (Yao et al., 2017; Bharat et al., 2018). Studying virus-host membrane fusion, Lee (2010) observed a funnel neck of tight curvature (15 nm-wide inner diameter) linking influenza virus and liposome membranes, Cardone et al. (2012) found that virions are capable to bind liposomes tightly enough to alter their curvature, and Chlanda et al. (2016) theoretically and experimentally determined cholesterol concentration inducing spontaneous negative curvature required for hemifusion. Studying endocytosis, Chen et al. (2019) described how the

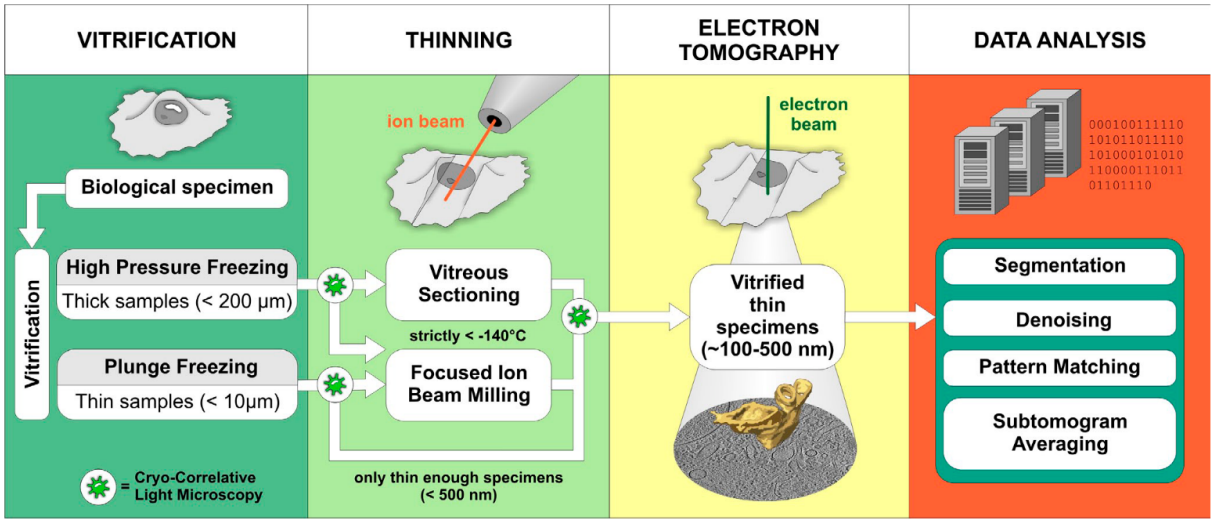

Figure 1.3: Cryo-electron tomography workflow. Schematic representation of the cryo-ET workflow, consisting of vitrification (usually by plunge freezing) and thinning (usually by cryo-FIB) of biological specimen, data acquisition by ET and data analysis procedures. Source: (Lucic et al., 2013).

vesicle curvature arises during clathrin coat assembly and its dependence on cargo recruitment. Bharat et al. (2014) studied synaptic vesicles fusion and found that **s**oluble **N**-ethylmaleimide-sensitive factor **a**ttachment protein **re**ceptor (SNARE) and regulatory proteins induce local membrane protrusions in the PM towards primed vesicles, reducing the activation energy needed for fusion. Later, Bharat et al. (2018) studied the formation of BAR-domain coats on PM in yeast, only observing dense scaffolds on highly curved membranes (30-60 nm diameter). In bacterial cell division, Yao et al. (2017) observed short FtsZ filaments forming more frequently on the outer curvature side of the cell, driving asymmetric constriction.

1.2.2 Sample preparation and data acquisition

In cryo-ET workflow (Figure 1.3), cells are first vitrified to preserve them in a nearly physiological state (Lučić et al., 2005). Vitrified cells are then usually thinned down to 100-250 nm thick lamellas by cryo-focused ion beam (FIB) milling (Rigort et al., 2012a). The grid containing the sample is then transferred to a cryo-transmission electron microscope (TEM), Figure 1.4). Next, the sample is tilted around an axis inside the TEM, acquiring two-dimensional (2D) images of a cellular region of interest at each tilt (see Section 1.2.3). Finally, the tilt series are computationally aligned and reconstructed into a tomogram, which is a 3D density map or gray-value image of the cellular interior (see Section 1.2.4).

Vitrification

The purpose of vitrification is to rapidly freeze the specimen to reach the temperature below -140°C at which water turns into vitreous ice, before damaging ice crystals can form (Lučić et al., 2005). Vitreous ice is amorphous like a liquid but more viscous, thus the specimen is preserved at a nearly physiological state. The vitrification is done by plunge-freezing for thin specimens (up to 10 μm) or by high-pressure freezing for

thick specimens (up to a few hundred μm). In plunge-freezing, a specimen is blotted on an electron microscopy grid until it is only covered by a thin film of a liquid and then plunged into liquid ethane or ethane-propane mixture. In high-pressure freezing, a specimen is pressurized while being cooled down by liquid nitrogen.

Cryo-FIB milling

To be penetrated by electrons and to reduce electron scattering interactions (see the next paragraph), the specimen must be thin enough (Amos et al., 1982). To acquire high resolution tomograms using current electron microscopes operated in intermediate voltage ranges, sample thickness should be below 500 nm, ideally in range of 100-250 nm. This thickness is only satisfied by small prokaryotic cells and peripheral regions of some eukaryotic cells. To overcome this limitation, cryo-FIB/scanning electron microscope (SEM) dual-beam microscope (Marko et al., 2006; Rigort et al., 2012a) was developed and is currently used to prepare thin slices of cells, called lamellas. The SEM is used for imaging the sample surface and the FIB for eroding or "milling" down unwanted material by ion current. The microscope is also equipped with a cryo-transfer system, a cryo-stage and a nitrogen gas cooling system for keeping the sample vitrified. To protect the front of the lamella from a successive erosion during milling, the sample is first covered with an organometallic platinum compound using a gas-injection system (Hayles et al., 2007).

The SEM is used to visualize the surface of the sample using the FIB (1-30 keV) (Bäuerlein, 2018). Inelastically scattered electrons from the beam lead to emission of low-energy secondary electrons (<50 eV) from the sample atoms, in amount mainly depending on the surface geometry. Elastically scattered electrons reflected from the sample (backscattered electrons) contribute to the contrast between areas with different chemical compositions. The FIB is usually equipped with a Gallium ion source, which is used to precisely mill down the top and the bottom parts of a target cell, leaving a thin lamella with the structure of interest. The material is removed from the cell surface by the process of sputtering (Marko et al., 2006) in several steps (usually rough milling, fine milling and polishing). It is possible to estimate the thickness profile of the lamella using the SEM (5-10 keV) and eventually correct it (Bäuerlein, 2018).

Cryo-TEM imaging

A vitrified specimen or a lamella can be imaged at high vacuum and liquid nitrogen temperature in a cryo-TEM (Figure 1.4). High vacuum inside the microscope column is needed to minimize electrons collision with gas atoms in order to keep the electron beam coherent and monochromatic. Cooling the specimen holder to a low temperature is needed to keep the vitrified specimen hydrated and solid (Castón, 2013). In our usual setting, cryo-TEM is operated at high electron voltages, usually 300 kV. The high voltage of the electron beam enables the electrons to penetrate the cellular sample.

TEM can detect electrons that are unscattered, elastically scattered (at lower-angles) or inelastically scattered. The unscattered electrons do not hit the sample and remain unchanged. The elastically scattered electrons interact with the potential field of atomic nuclei and are deflected with unchanged amplitude (brightness) and wave length (energy) but with a phase shift (difference in path length), contributing to image formation together with the unscattered electrons. The inelastically scattered electrons interact with the outer electrons of specimen atoms and transfer some of their energy to

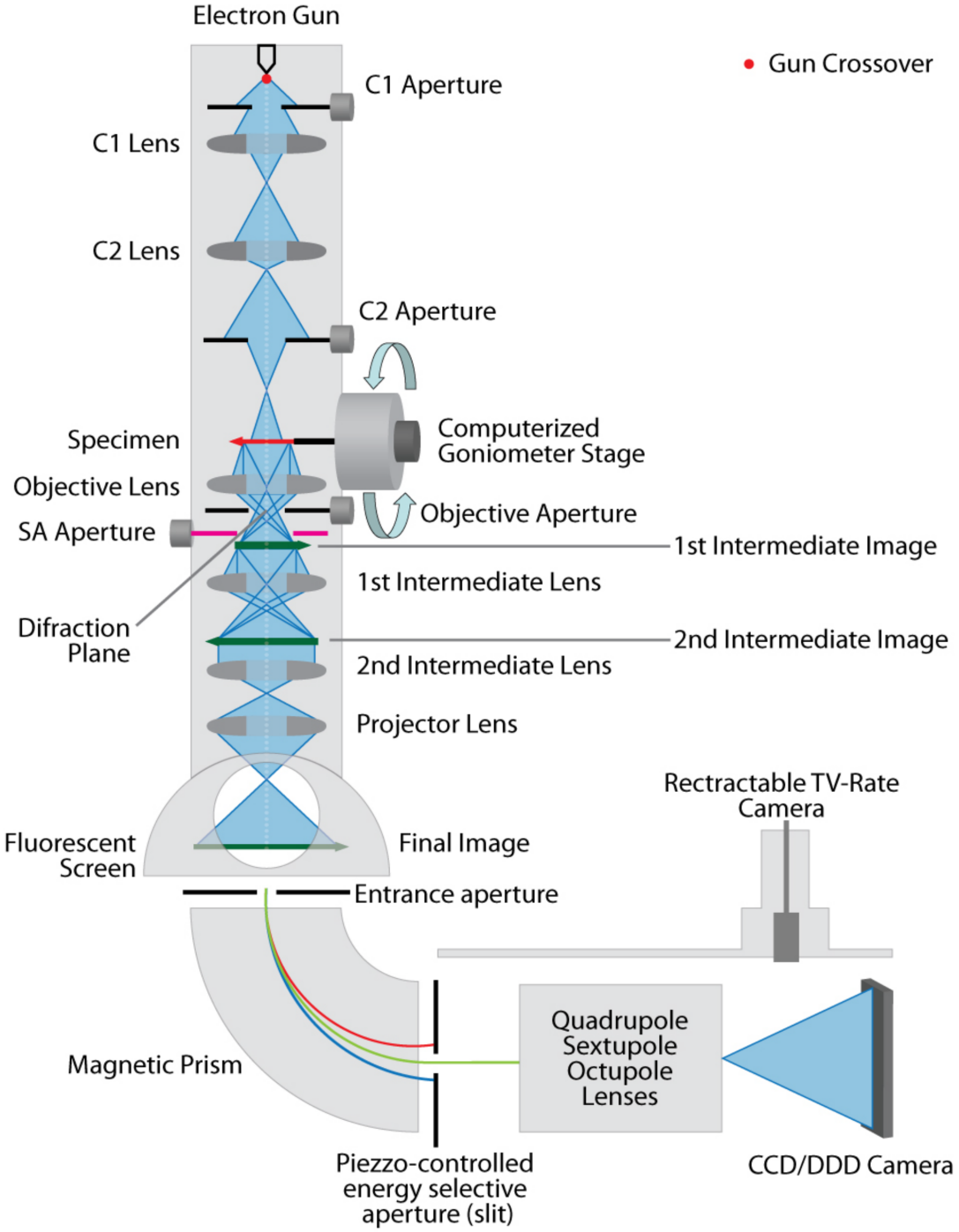

Figure 1.4: Cryo-transmission electron microscope. Schematic diagram a typical TEM system used for cryo-ET in Martinsried. Source: (Kochovski, 2014).

the atoms, causing radiation damage to the specimen. Since the inelastically scattered electrons are slowed down, they would form an image in a different plane and thus have to be filtered out. An objective lens aperture is used to block electrons scattered at large angles, i.e. elastically scattered but only a subset of inelastically scattered electrons. Since inelastically scattered electrons have a different energy, they can be filtered out using a post-column energy filter operated in "zero-loss mode" (Grimm et al., 1996, 1997).

Electron scattering results in an intensity variation between different regions in the image, known as contrast. There are two types of contrast: amplitude and phase contrast. Since a part of the scattered electrons gets filtered out by the aperture or the energy filter, some incident electrons do not reach the detector. Thus, the amplitude of the electron wave changes locally, resulting in the amplitude contrast. The phase contrast arises from the phase shift of the electron wave function while being elastically scattered from the sample. The contrast of unstained, frozen-hydrated specimens mainly arises from the phase contrast and to a lower extent from the amplitude contrast (Toyoshima and Unwin, 1988). Thus, the amplitude contrast is disregarded from now on.

The image contrast is defined by the contrast-transfer function (CTF). The CTF is an oscillating and slowly attenuating function and is mainly influenced by defocus values (Figure 1.5A): Using no or small defocus, high spatial frequencies are retained but not the low spatial frequencies, resulting in images with a very low contrast. To increase the phase contrast, defocusing of the objective lens and subsequent computational image correction for the oscillations of the CTF is common (Castón, 2013; Beck and Baumeister, 2016), e.g. using NovaCTF (Turoňová et al., 2017) or IMOD (Kremer et al., 1996) software packages. To avoid these steps and enable imaging in focus, phase plates were developed. For TEM, the Volta phase plate (VPP) (Danev et al., 2014) applies a nearly quarter-wave phase shift to the scattered electrons relative to the unscattered ones and thus inverts the contrast at the low frequencies (from sine to cosine, Figure 1.5B). The VPP is a continuous carbon film positioned at the objective aperture in the back focal plane in TEM (Fukuda et al., 2015).

The image formed on the TEM image plane is a two-dimensional projection of the electrostatic potential of the specimen convoluted with the inverse Fourier transform of the CTF (Lučić et al., 2005). The image can be viewed on a fluorescent screen, recorded analogously on a photographic film or digitally by a camera. Originally in ET, charge-coupled device (CCD) cameras were used (Krivanek and Mooney, 1993), which first converted electrons into photons by a scintillator and then detected those. However, due to backscattering of electrons into the scintillator resulting in spread of the signal, the performance of CCD cameras was not sufficient for higher spatial frequencies and acceleration voltages (Fan and Ellisman, 2000). Later on, single electron-counting detectors, or direct electron detector (DED)s, were developed, e.g. K2 Summit (Gatan Inc.) (Booth et al., 2012) that was used in these studies. A DED can directly detect electrons, resulting in substantially increased resolution and sensitivity (as measured by detective quantum efficiency) as well as a faster readout, compared to the CCD cameras and the film (Faruqi and Henderson, 2007; Mooney, 2017). Normally, beam-induced motion of the specimen leads to image blurring, see Section 1.2.3. Li et al. (2013) confirmed that the combination of rapid readout and nearly noiseless electron counting by a DED allows to correct image blurring to subpixel accuracy, restoring the intrinsic image information to a near-atomic resolution for single particle analysis

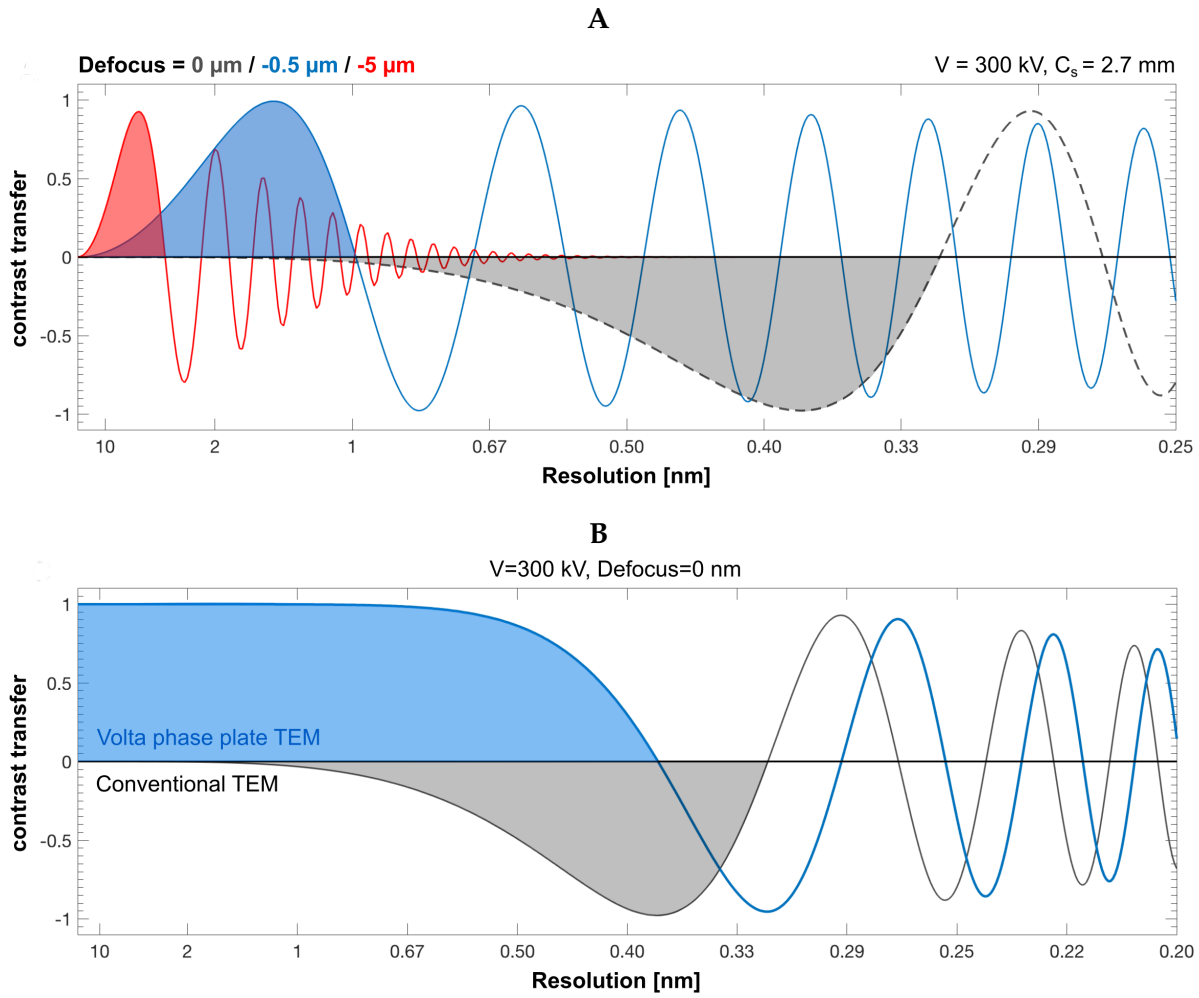

Figure 1.5: Theoretical contrast-transfer function. (**A**) The CTF depending on the defocus, three defocus values are visualized here: 0 μm (grey), -0.50 μm (blue) and -5.0 μm (red). For 0 μm defocus, low frequencies are almost completely lost and mainly high frequencies are transferred, leading to a very noisy image. Increasing the defocus improves the contrast for low frequencies (blue and red areas) but with the disadvantage of the loss of high resolution information. This is due to an intensified dampening of the CTF for higher frequencies, which is well visible for the red curve (defocus=-5.0 μm), where the oscillations vanish quickly. (**B**) The CTF at 300 kV, defocus=0 nm for conventional TEM (grey curve) and VPP TEM (blue curve). The essential difference is clearly visible for low frequencies: While low frequency information is lost with conventional TEM (grey area), there is a significant transfer of low frequency information with the VPP (blue area). At high frequencies, the CTF is comparable. Source: (Bäuerlein, 2018).

(SPA). Recently, full atomic resolution has been achieved (Nakane et al., 2020; Yip et al., 2020). A major advantage of the DEDs for cryo-ET is their ability to film multiple shortly exposed (∼200 ms) micrographs, called *frames*, which can be aligned before the tomogram reconstruction (Section 1.2.4).

1.2.3 Tilt series acquisition

In order to collect data for a tomogram, a *single-tilt series* of micrographs is recorded at different angles by tilting the specimen holder, usually from -60° to +60° at 2° angular increment. To achieve a more isotropic resolution, it is possible to record a *double-tilt series* consisting of two single tilt-series, rotating the specimen by 90° around the beam direction after the first series (Mastronarde, 1997). All tomograms used in this work were acquired by single-tilt series. There are different tilt-schemes, e.g.: *unidirectional*, *bidirectional* and *dose-symmetric*, which differ in the collection order of micrographs but all have a constant angular increment (Hagen et al., 2017). In the unidirectional tilt-scheme used in these studies, tilts are collected sequentially from one angular extreme to the other.

Due to mechanical inaccuracies of the specimen holder and the physical influence by the electron beam, the specimen moves during tilting, requiring a compensating adjustment. Since manual adjustment would overexpose the specimen to the electron beam, the automation of tilt series acquisition was crucial for minimizing the cumulative electron dose. The first developed procedures (Dierksen et al., 1992, 1993) allowed the acquisition of the first cryo-tomograms under low-dose conditions (Dierksen et al., 1995; Grimm et al., 1997). The well established SerialEM software (Mastronarde, 2005) was used in these studies.

The automated acquisition of each micrograph consists of three steps: *tracking*, *autofocusing* and *exposure* (Dierksen et al., 1992). In the tracking step, a micrograph is recorded at a very low dose and the lateral displacement of the specimen compared to the previous tilt angle is calculated. The autofocusing step adjusts the defocus according to the specimen movement in the beam direction. Both steps are performed at another location on the grid along the tilt axis to minimize the electron damage of the resulting tomogram. In the exposure step, projections of the object of interest are recorded. The beam-induced motion of the specimen cannot be avoided during the exposure step, leading to smearing of the image.

1.2.4 Frame alignment and tomogram reconstruction

After tilt-series acquisition, the frames of each tilt are aligned, reducing the motion-induced smearing and so improving the sharpness and resolution of the resulting image. To align the K2 Summit frames for the tomograms used in this work, K2Align software [1] (Li et al., 2013) was used.

To reconstruct the 3D object from its 2D projections acquired during a tilt series, the projections have to be first aligned to a common coordinate system and then combined into one tomogram (Figure 1.6). The alignment algorithm has to determine the tilt axis angle and the lateral shifts, which are not fully eliminated by the automated tracking procedure, and optionally other changes like magnification and rotation (Lučić et al., 2005). The alignment algorithms based on cross correlation (Guckenberger, 1982) and

[1] https://github.com/dtegunov/k2align

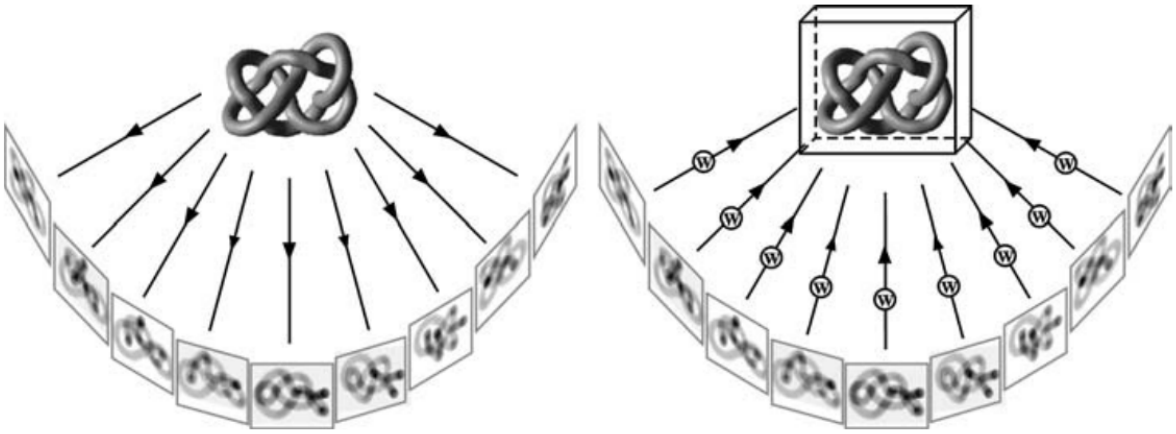

Figure 1.6: Principle of tomography. Projections of the specimen are recorded from different directions by tilting the specimen holder (left). The 3D reconstruction of the sample is obtained most commonly by backprojection into a common 3D reconstruction body (right). Source: (Lučić et al., 2005).

Fourier-space common lines (Liu et al., 1995) are usually noise sensitive and thus only useful for high-contrast or paracrystalline data (Taylor et al., 1997). Other alignment algorithms, e.g. (Han et al., 2015), require addition of fiducial markers to the specimen, which can be tracked across projections due to their high contrast. Then, the projections are aligned using a least-squares algorithm (Lučić et al., 2005; Wan and Briggs, 2016). As it is not possible to add fiducial markers under cryo conditions after FIB-milling, a cross-correlation alignment algorithm has to be used for lamellae. Such an algorithm tracks image patches along the micrographs, optimizing their alignment iteratively. This is computationally intensive but can be executed in parallel for each patch and combined using overlaps. The IMOD software package (Kremer et al., 1996) offers semi-automatic algorithms for tilt series alignment using fiducial markers or patch-tracking (the latter was used in the publications within this thesis). For alignment, user interaction is required in order to choose initial markers and discard markers or patches leading to high alignment errors.

After aligning the projections, a tomogram can be reconstructed. The mapping between the 2D projections into the 3D space can be explained in Fourier space by the central slice theorem (Figure 1.7): The Fourier transformation of a 2D projection equals to a slice in the 3D Fourier space of the imaged object (De Rosier and Klug, 1968; Crowther et al., 1970). Since interpolation in Fourier space is very computationally demanding, real space-based reconstruction algorithms are commonly used (Lučić et al., 2005; Wan and Briggs, 2016). The most common reconstruction algorithm in cryo-ET is the weighted back-projection (WBP), in which the projections are projected back to generate a 3D reconstruction of the imaged object (Wan and Briggs, 2016). Due to the tilting geometry, lower frequencies in Fourier space are sampled homogeneously up to a certain frequency (defined by Crowther et al. (1970), "Crowther criterion"), whereas higher frequencies are undersampled (Figure 1.7). Therefore, projections are weighted accordingly prior to reconstruction. Weighting is done in Fourier space either using an analytical or an exact weighting scheme (Lučić et al., 2005). The analytical weighting function grows with the frequency in the direction perpendicular to the tilt axis and approaches the exact weighting for small tilt increment. An exact

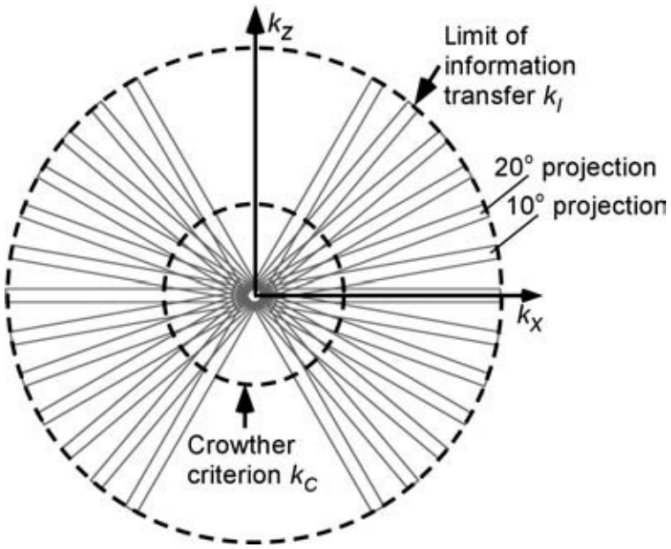

Figure 1.7: Data sampling in Fourier space. A projection of an object with thickness d corresponds to a central slice of thickness 1/d in Fourier space. Therefore, the three-dimensional information of the specimen (outside of the missing wedge) is gathered homogeneously up to frequency k_C (Crowther criterion). Source: (Lučić et al., 2005).

weighting scheme calculates the sampling density in Fourier space using the known size of the object of interest in the specimen. The IMOD software package (Kremer et al., 1996) also offers tomogram reconstruction using WBP, which was used in the publications accompanying this thesis. The reconstruction is approached differently by algebraic reconstruction technique (ART) (Gordon et al., 1970; Crowther et al., 1970), which formulate projections as a system of algebraic equations and aim to invert it approximately using an iterative algorithm. However, these algorithms lead to unsatisfactory reconstructions (Gilbert, 1972). The reconstruction is improved in the simultaneous iterative reconstruction technique (SIRT) (Gilbert, 1972), where the initial reconstruction is performed by unweighted back-projection, then the differences between the original projections and those mapped to the volume are iteratively minimized. Iterative reconstruction algorithms have two major advantages: i) They can determine proper weighting consistently and in a parameter-free manner, ii) they offer an easy interpolation of constraints; However, the established constraints are either not applicable to complex biological specimens like cells used in cryo-ET, or the improvement over WBP is marginal (Lučić et al., 2005). Moreover, while these iterative methods preserve the low-resolution signal better, they may loose the high-resolution information that is below the noise level (Wan and Briggs, 2016). A more recent iterative reconstruction method, INFR, uses nonuniform fast Fourier transform (NUFFT) and claims to yield better reconstructions than WBP, also filling up the missing wedge with meaningful low-frequency information without prior assumptions about the data (Chen and Förster, 2014). This and other new algorithms have been shown to perform better than WBP for low-resolution test data, but it remains to be shown whether these methods maintain high-resolution information as well as WBP (Wan and Briggs, 2016).

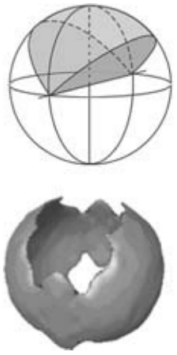

Tilt range	Single
±70°	78%
±60°	67%
±45°	50%

Figure 1.8: Missing wedge. The illustrations show schematically the sectors in the Fourier domain that remain unsampled because of the limited tilt range. In single-axis tilting, there is a *missing wedge*. The table contains percentages of the Fourier space that are covered for different tilting ranges. The missing information in real space is illustrated below. Source: (Lučić et al., 2005).

1.2.5 Limitations and artifacts of cryo-ET

Since the electron beam damages biological specimens in ice, destroying or falsifying high frequency information in projection images, those have to be recorded under low electron dose conditions (Frangakis and Förster, 2004; Lučić et al., 2005). Consequently, the resulting tomograms have a low signal-to-noise ratio (SNR).

Because in practice it is unfeasible to tilt the sample beyond ∼± 60°, in single-tilt tomography there is a wedge of unsampled information in the Fourier space. This artifact, called *missing wedge*, causes nonisotropic resolution, i.e. the features look elongated along the electron beam direction (Z-axis), and surfaces like membranes perpendicular to the tilt axis (Y-axis) are also not visible (Lučić et al., 2005). Thus, membrane regions are missing at the top and the bottom of both the Y- and the Z-axes (Figure 1.8). To avoid wrong results, the missing wedge has to be considered by computational methods that process tomograms directly or indirectly, e.g. membrane segmentation or curvature estimation (see Sections 1.3.4 and 1.4.5, respectively).

1.3 Computational methods for cryo-ET

1.3.1 Denoising algorithms

To increase the SNR, different denoising algorithms are used to identify noise and remove it from the tomogram. However, as a side effect, the algorithms also remove a certain amount of the signal.

The simplest denoising algorithms used in tomography apply linear filtering operations, e.g. low-pass filtering and median filtering in Fourier space (Lučić et al., 2005). Also Wiener deconvolution (or Wiener filter) (Wiener, 1964) is applied in Fourier space, minimizing the impact of noise at frequencies which have a poor SNR. An implementation is available[2], which was used in (Salfer et al., 2020) accompanying this thesis.

[2] https://github.com/dtegunov/tom_deconv

In real space, nonlinear filtering algorithms, e.g. nonlinear anisotropic diffusion (NAD) (Frangakis and Hegerl, 2001; Fernández and Li, 2003) and bilateral denoising (Jiang et al., 2003), can achieve a better signal preservation. NAD uses variation of the gray levels in the image and can enhance membranes (Frangakis and Förster, 2004; Lučić et al., 2005). A recent implementation (Moreno et al., 2018) allows a straightforward and fast usage of NAD, which was also used in (Salfer et al., 2020). Bilateral denoising uses gray values and their proximity and can effectively suppress noise without blurring the high resolution details (Jiang et al., 2003; Frangakis and Förster, 2004). Algorithms based on wavelet transformation (Stoschek and Hegerl, 1997), which uses the fact that the signal has characteristic features not present in the noise, preserve high-frequency spatial information better, but are very computationally expensive, and the transformation is applied to 2D slices and not to the full 3D image (Frangakis and Förster, 2004; Lučić et al., 2005). Nonlinear denoising is usually not applied for further quantitative image processing, but it may be beneficial for segmentation algorithms (Frangakis and Förster, 2004; Martinez-Sanchez et al., 2014; Lučić et al., 2016) (see Section 1.3.4).

Recently, approaches applying deep learning for image restoration have been introduced (Lehtinen et al., 2018; Krull et al., 2019; Laine et al., 2019; Batson and Royer, 2019). Adapted for cryo-TEM data, cryo-**Co**ntent-**A**ware Image **Re**storation (CARE) (Buchholz et al., 2019a,b) can train deep neural networks by using registered pairs of noisy images. Those networks can then be used to denoise single projections and whole tomographic volumes.

1.3.2 Particle picking and structural classification

Template matching is an imaging technique that correlates an image with respect to a smaller model (template) to search for coincidences (matching). In the context of biological samples, the aim is to find all occurrences of a known structure (template) in a microscopy image, also known as molecular recognition (Böhm et al., 2000; Lučić et al., 2005). The template is usually derived from a medium- or high-resolution structure obtained by X-ray crystallography or SPA (Beck and Baumeister, 2016). In "visual proteomics" (Nickell et al., 2006; Förster et al., 2010; Asano et al., 2016), a tomogram is matched against a library of templates, creating a "protein atlas" with positions and angular orientations of protein complexes inside the cell.

The standard template matching algorithm of Frangakis et al. (2002) is based on a normalized cross correlation function that normalizes the subtomograms according to local variance. The local constrained cross correlation function that accounts for the missing wedge is used in the algorithm MolMatch (Förster, 2005; Förster et al., 2010). Template matching is very computationally expensive, because many cross correlations must be performed iteratively to sample the complete rotational space of the template for each subtomogram. To reduce the computational time, MolMatch can run in parallel for overlapping subtomograms. There is an older MATLAB implementation in TOM software toolbox for tomography (Nickell et al., 2005) and a newer Python implementation in PyTOM toolbox (Hrabe et al., 2012), both were used in Bäuerlein et al. (2017) accompanying this thesis. Recent deep learning approaches use convolutional neural networks (CNN) for automated annotation of cryo-electron tomograms (Chen et al., 2017; Moebel et al., 2020), extracting macromolecular structures like ribosomes. The latter method, DeepFinder (Moebel et al., 2020), can also localize

and identify small macromolecules, several macromolecular species simultaneously or differentiate specific states of the same macromolecular species, like membrane-bound and cytosolic ribosomes.

In practice, template matching sensitivity and specificity are compromised by several factors like image SNR, macromolecular weight and crowded cellular environments. Besides the true matches (true positives), some occurrences matching the template (particles) are missed by the detection function (false negatives) and some wrong matches are found (false positives). To reduce the false negatives and increase the sensitivity, one can modify the search parameters, albeit at the cost of more false positives. To filter out the false positives and increase the specificity, the resulting particles can be classified manually and/or automatically, e.g. by multivariate statistical analysis (Frangakis et al., 2002), using constrained correlation (Förster et al., 2008), hierarchical clustering (implemented and described by Hrabe et al. (2012)), Autofocused 3D classification (Chen et al., 2014) or deep learning (CNN) (Che et al., 2018; Moebel et al., 2020). The newest CNN-based method, DeepFinder, can localize additional macromolecules that had been missed by template matching or discarded during manual classification. To find ER-bound ribosomes in Bäuerlein et al. (2017) accompanying this thesis, manual screening and distance-based filtering were followed by constrained principle component analysis and k-means clustering.

Template-based methods can only find occurrences of a known structure in a tomogram. To discover new complexes *in situ*, a template-free method for detection and classification of membrane-bound complexes, PySeg, was recently developed (Martinez-Sanchez et al., 2020). PySeg extends the segmentation method (Sousbie, 2011) based on discrete Morse theory (Milnor, 1963; Forman, 2002) combined with affinity propagation (AP) clustering algorithm (Frey and Dueck, 2007). AP clustering is unsupervised and thus does not require information on the number of optimal classes, like k-means and hierarchical clustering do, but can determine it from the data. It has been shown in (Martinez-Sanchez et al., 2020) that PySeg outperforms common template matching and clustering approaches, i.e. based on automated pattern mining (Xu et al., 2019), deep learning (Yu and Frangakis, 2011; Xu et al., 2017; Chen et al., 2017) and the difference of Gaussian picking (Voss et al., 2009) methods, for sparsely distributed small ($\sim$150 kDa) membrane associated complexes. Moreover, PySeg reduces the influence of the missing wedge and it was the only method that detected small membrane-bound complexes and provided the best resolution of class averages (Martinez-Sanchez et al., 2020). Altogether, PySeg generates sufficiently homogeneous particles sets and initial references for subsequent subtomogram averaging.

1.3.3 Subtomogram averaging

A tomogram usually contains multiple copies of the same particle in different, ideally random, orientations. However, each single subtomogram is noisy and affected by the missing wedge. Luckily, the missing information is usually not at the same location in the subtomograms. Thus, it is possible to improve the SNR and reduce the missing wedge of the target structure by averaging the subtomograms. For this, the subtomograms from the particle picking and classification procedures are iteratively aligned, refining the angular orientation of each particle, and an improved average is calculated (Lučić et al., 2005; Beck and Baumeister, 2016; Wan and Briggs, 2016). The most popular software packages implementing subtomogram alignment and

averaging algorithms are RELION (Bharat and Scheres, 2016) and emClarity (Himes and Zhang, 2018). For symmetrical structures, symmetry can be used to obtain a higher resolution (Walz et al., 1997; Förster et al., 2005). Repetitive structures, e.g. filaments, can be divided into shorter elements and averaged (Guo et al., 2018b). The obtained structures are usually in the 1-3 nm resolution range. Under favorable conditions, resolutions in the subnanometer range can be achieved (Guo et al., 2018a; O'Reilly et al., 2020), in principle even near-atomic range is possible (Beck and Baumeister, 2016).

1.3.4 Segmentation of membranes and proteins

Segmentation labels structural components present in images voxel by voxel. In tomography, segmentation defines where each structure, e.g. a certain organelle, is spatially located in the cellular subvolume and delineates its shape, which is necessary for both qualitative and quantitative tomogram interpretation. Many algorithms have been developed that can segment membranes automatically (Martinez-Sanchez et al., 2011, 2012; Mosaliganti et al., 2012; Martinez-Sanchez et al., 2014). However, in most cases a manually supervised post-processing is required to enable a quantitative analysis due to the complexity of the cellular context and the low SNR. Martinez-Sanchez et al. (2014) developed an automatic membrane segmentation method based on tensor voting, TomoSegMemTV. TomoSegMemTV accounts for distortion caused by the missing wedge by omitting the membrane regions vanished or elongated (Martinez-Sanchez et al., 2014). In the publications accompanying this thesis, we first generated membrane segmentations automatically from tomograms using TomoSegMemTV and then refined manually using Amira Software (Thermo Fisher Scientific[3]). Manually segmenting the lumen of membrane compartments was found useful for the correct membrane surface extraction (Salfer et al., 2020). A new membrane segmentation method, LimeSeg (Machado et al., 2019), which is deployed in the ImageJ environment[4] or available on GitHub[5], is based on the concept of "surfels" (**surf**ace **el**ements) rather than voxels. It provides simultaneous segmentation of numerous non overlapping objects, also highly convoluted ones, and is robust to big datasets.

Apart from membranes, there are segmentation methods for other molecular densities that are hard to detect by template matching. Rigort et al. (2012b) developed an automated segmentation method for actin filament networks in cryo-tomograms, which is integrated in the Amira software and was also used to segment other cytoskeletal filaments like microtubules (Chakraborty et al., 2020). Bäuerlein et al. (2017) (part of this thesis) applied this method to segment huntingtin fibrils. The algorithm represents filament centers by short and connected lines, which can be used to calculate filament length, orientation, density, stiffness (persistence length) and detect branching points (Rigort et al., 2012b). Lučić et al. (2016) developed a method for hierarchical detection of small, pleomorphic (i.e. variable in size and shape) membrane-bound molecular complexes in cryo-tomograms, called Pyto, which was applied to segment short filaments between synaptic vesicles (linkers) and between the vesicles and presynaptic terminal (tethers) (Fernández-Busnadiego et al., 2013; Lučić et al., 2016) as well as ER-PM contacts formed by extended synaptotagmins (Fernández-Busnadiego

[3] https://www.thermofisher.com/.../amira-life-sciences-biomedical.html
[4] http://sites.imagej.net/LimeSeg
[5] https://github.com/NicoKiaru/LimeSeg

et al., 2015). Recently, automated segmentation methods based on CNN have been developed for cryo-ET, like the method of Chen et al. (2017), which is available in the EMAN2.2[6] (Tang et al., 2007) software package. This method can be trained to segment a wide range of classes of geometrical features, like filaments, membranes and periodic arrays or isolated macromolecules. It operates on the tomogram slice by slice, is fast and largely avoids distortions due to the missing wedge.

1.4 Surface curvature estimation

Computational methods calculating quantitative descriptors, like local surface curvature, are of central importance for the interpretation of membrane segmentations. Those quantitative descriptors are a key for answering relevant biological questions.

1.4.1 Quantitative surface curvature descriptors

Surface normals, principal curvatures and principal directions

Surface curvature descriptors are studied in differential geometry and characterize the local geometry of a surface. For this, a membrane has to be first modeled as a single-layered, curved surface embedded in 3D space (Martinez-Sanchez et al., 2011). Curvature is defined locally at each point on the surface. In theory, there is an infinite number of curved lines along the surface passing through each point, leading to an infinite number of curvature values. However, at each point there are two directions, called *principal directions*, in which the bending is maximum or minimum, notated here as t_1 and t_2, respectively. The principal directions are orthogonal vectors embedded on the tangent plane to the surface at each point (do Carmo, 1976). The maximum and the minimum curvatures defined by the principal directions are called *principal curvatures* and notated here as κ_1 and κ_2, respectively.

Mean curvature, Gaussian curvature, curvedness and shape index

From the principal curvatures, different combined surface curvature measures can be computed for each point, e.g.: *mean curvature H* (Equation 1.1), *Gaussian curvature K* (Equation 1.2), *curvedness C* (Equation 1.3) and *shape index SI* (Equation 1.4) (Koenderink and van Doorn, 1992).

$$H = \frac{\kappa_1 + \kappa_2}{2} \tag{1.1}$$

$$K = \kappa_1 \kappa_2 \tag{1.2}$$

$$C = \sqrt{\frac{\kappa_1^2 + \kappa_2^2}{2}} \tag{1.3}$$

$$SI = \frac{2}{\pi} atan \frac{\kappa_1 + \kappa_2}{\kappa_1 - \kappa_2} \tag{1.4}$$

[6] http://www.EMAN2.org

1.4.2 Data structures approximating smooth surfaces

Biological membranes have to be represented in a discrete way in order to be processed computationally. There are two main categories of data structures approximating a smooth surface: polygon meshes and point-based alternatives.

Polygon and triangle meshes

Piecewise planar surfaces in three dimensions (3D) are usually represented by polygon meshes, consisting of planar faces that share their vertices and edges. Faces are simple convex polygons, most commonly triangles (Meyer et al., 2003) (Figure 1.9A), because triangle is the simplest polygon. Advantages of triangles over e.g. quadrilaterals are compactness in memory, efficiency of rendering and subdivision (Tobler and Maierhofer, 2006). Graphics hardware has been first optimized and specialized for triangle rendering (Kobbelt and Botsch, 2004; Hoppe, 1999; Sander et al., 2007; Fenney, 2018). Moreover, the triangle mesh intrinsically stores important data about the surface, e.g. surface orientation, area and connectivity information. Surface orientation is defined by triangle normal vectors (normals), which point consistently inwards or outwards the shape approximated by the mesh, depending on the convention (we used the inwards-pointing normals). Area of the triangle mesh surface is simply the sum of areas of all triangles in the mesh, which is an approximation of the area of the underlying smooth surface. The globally consistent connectivity between triangles allows to calculate shortest distances along the surface, called *geodesic distances* (Dijkstra, 1959; Kimmel and Sethian, 1998; Sun and Abidi, 2001), and find neighboring triangles within a certain geodesic distance (Page et al., 2002).

Point-based alternatives

Point-based geometry offers alternative surface representation techniques, e.g. point clouds (Figure 1.9B) and surface splats. These techniques are simpler and offer more flexibility than triangle meshes, because they neither have to store nor to maintain the globally consistent connectivity information (Kobbelt and Botsch, 2004). This can be advantageous for certain applications, e.g. efficient real time rendering or geometry manipulation of highly complex 3D models. Especially elliptical splats yield good surface approximation since they can be aligned to the principal directions of the underlying surface.

In this thesis, a graph-based representation of triangle meshes was developed and used in our algorithms. The possible advantage of using a point-based data structure is discussed in Section 3.2.

1.4.3 Curvature estimation algorithms

Curvature estimation algorithms can be classified into three main categories: *discrete*, *analytical* and *tensor voting-based*.

Discrete

The first category of discrete curvature estimation algorithms uses discretized formulae of differential geometry. These formulae try to approximate the underlying surface

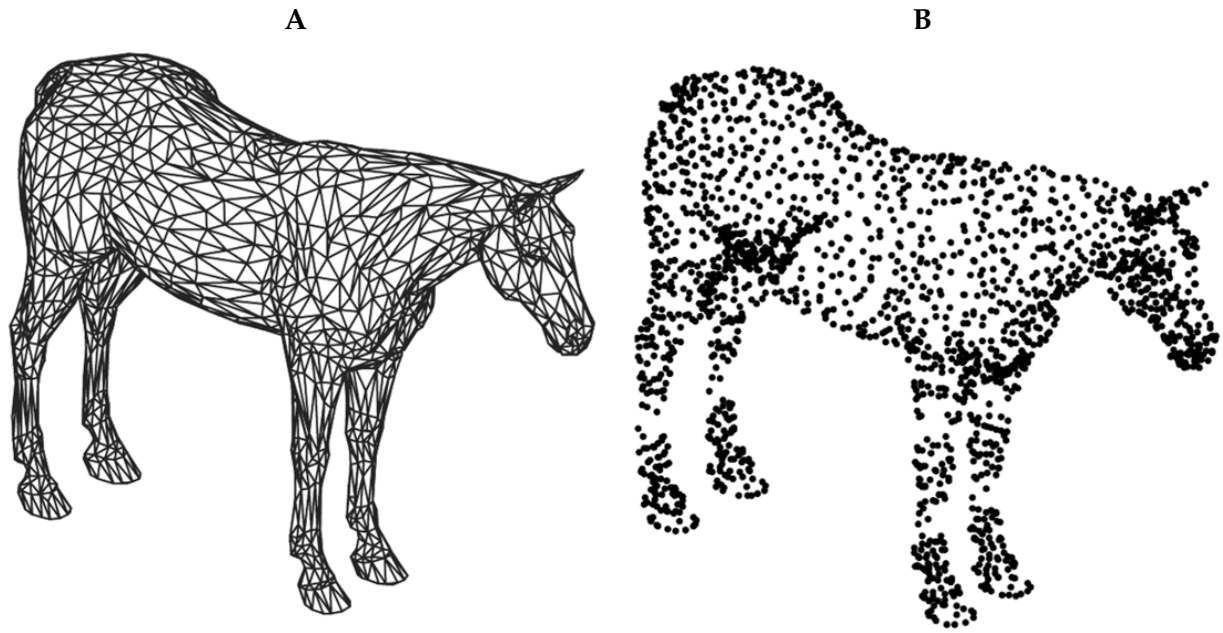

Figure 1.9: Data structures approximating smooth surfaces. (**A**) Triangular mesh and (**B**) point cloud representing a horse. Source: Discrete geometry Lecture 2 by Alexander and Michael Bronstein (https://slideplayer.com/slide/4789180/).

from the given triangle mesh (Polthier and Schmies, 1998; Desbrun et al., 1999; Meyer et al., 2003; Szilvási-Nagy, 2008). However, the approximation is often not precise for noisy, coarsely triangulated surfaces, as usually only a 1-ring neighborhood is used, i.e. directly neighboring triangle vertices sharing an edge with the central vertex (Razdan and Bae, 2005). An exception is the method of Szilvási-Nagy (2008), which uses a user-defined neighborhood of an arbitrary size. The popular method of Meyer et al. (2003) estimates Gauss curvature (K) using the discretized Gauss-Bonnet theorem (Polthier and Schmies, 1998) and mean curvature (H) using the discrete Laplace-Bertrami operator (also used for fairing irregular meshes by Desbrun et al. (1999)). The principal directions are estimated using least-square fitting of an ellipse, the so called curvature tensor. However, the directions are not robust for coarse, triangulated surfaces and therefore not recommended to use for the computation of principal curvatures. Thus, the principal curvatures are derived from the Gauss and mean curvatures.

Analytical

The second category are analytical algorithms that either fit surfaces (Goldfeather and Interrante, 2004; Razdan and Bae, 2005) or curvature tensors (Taubin, 1995; Theisel et al., 2004; Rusinkiewicz, 2004) to local patches of the mesh containing a central vertex and a small neighborhood of triangles around it. Subsequently, the algorithms derive principal curvatures and directions from the fitted model. The drawback of the surface fitting algorithms is their computational complexity, since the fitting process includes an optimization step. This optimization improves their robustness to noise but not their susceptibility to surface discontinuities (Page et al., 2002). The difference between the algorithms is in the number of fitted parameters, which usually correlates with

the goodness of the fit. For example, Goldfeather and Interrante (2004) proposed three principal direction approximation methods and found that their cubic-order method additionally using the normal vectors at adjacent vertices outperforms the other two quadratic-order methods, especially on irregular meshes. An interesting algorithm is the biquadratic Bézier method of Razdan and Bae (2005), which has an advantage of a more flexible surface fit (at a cost of more parameters to fit), as it uses 2-ring neighborhood and outperforms the cubic-order method (Goldfeather and Interrante, 2004). In the subcategory of the curvature tensor algorithms, Taubin (1995) defines a symmetric matrix with eigenvectors corresponding to the principal directions and eigenvalues from which the principal curvatures can be obtained by fixed homogeneous linear transformations. He estimates this matrix per triangle vertex using vertex pairs sharing an edge (1-ring neighborhood).

Tensor voting-based

Algorithms using 2-ring neighborhood or also the neighboring normals proved superior over algorithms using only 1-ring neighborhood. Especially, 1-ring neighborhood is not sufficient for noisy data (Razdan and Bae, 2005). The higher the resolution of scanned surfaces, the bigger the neighborhood yielding the best results, because it compensates the scanning errors (Magid et al., 2007). There is a category of curvature estimation algorithms incorporating a bigger neighborhood to fit a curvature tensor (Tang and Medioni, 1999; Page et al., 2002; Tong and Tang, 2005). These algorithms are based on Medioni's tensor voting theory (Medioni et al., 2000) for discerning shape features in a point cloud. Tang and Medioni (1999) robustly estimated curvature sign and principal directions from noisy point cloud data, and Tong and Tang (2005) extended this method to estimate also the magnitude of principal curvatures. Page et al. (2002) combined the discrete formulation from Taubin (1995) with the voting scheme from Tang and Medioni (1999) and used a geodesic neighborhood of triangles to robustly estimate normal vectors, principal directions and curvatures for each triangle vertex. However, we found that the algorithm of Page et al. (2002) leads to wrong curvature sign estimation for non-convex surfaces (Salfer et al., 2020). To sum up, all tensor voting-based algorithms aim to increase the robustness of principal directions and curvatures estimation for noisy surfaces with discontinuities.

Triangle vertex vs. face-based

Most of the algorithms estimate curvature at triangle vertices, but some operate on triangle faces (Theisel et al., 2004; Rusinkiewicz, 2004; Szilvási-Nagy, 2008) (Figure 1.10). Theisel et al. (2004) estimate curvature tensor as a smooth function on each triangle, using triangle normals linearly interpolated from vertex normals (Figure 1.10). The method slightly outperforms the cubic-order method of Goldfeather and Interrante (2004). A method of Rusinkiewicz (2004) estimates first the triangle normals using the vertex normals from 1-ring neighborhood, then the curvatures for each triangle face using the triangle edges (Figure 1.10) and least squares fitting of the curvature tensor, and finally averages curvatures for each triangle vertex from the adjacent triangles. This algorithm is efficient, robust, free of degenerate configurations, where other algorithms fail, and is accurate even on irregularly tessellated and moderately noisy meshes. A discrete method of Szilvási-Nagy (2008) estimates normal, principal and Gaussian curvatures on triangle barycenters (Figure 1.10) using a user-defined

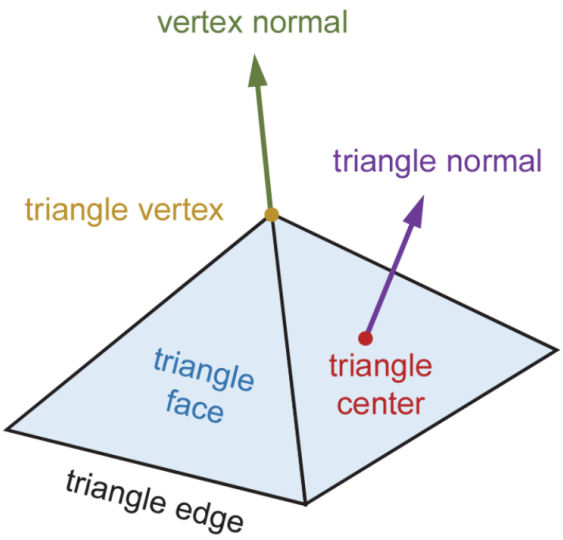

Figure 1.10: Triangle mesh geometry. Schematic representation of two neighboring triangles from an arbitrary triangle mesh, showing the basic components: triangle face, edge, vertex, barycenter ("center") as well as vertex and triangle normal vectors ("normal").

geodesic radius. The method is not dependent on estimated normal vectors, and the defined osculating circle approximates the underlying surface in third order. The method works in regions with long, narrow triangles where vertex-based methods fail. To sum up, face-based curvature estimation algorithms yield more robust results than vertex-based algorithms on irregularly tessellated and moderately noisy meshes.

1.4.4 Curvature estimation methods in biological imaging

Curvature estimation methods were mainly developed for analysis of MRI data, especially for the human brain. The widely used software package FreeSurfer (Dale et al., 1999) includes a curvature estimation module (Pienaar et al., 2008) that was used to analyze human brain development. Additionally, a "Gaussian-curvature-based variable-radius filter" was introduced in order to analyze curvatures of brains of different sizes. Mindboggle (Klein et al., 2017) is a newer open source brain morphometry software, which was applied to the largest dataset of manually labeled and publicly available brain images (Mindboggle-101 (Klein and Tourville, 2012; Klein, 2016)[7]) to demonstrate its use in studies of shape variation in healthy and diseased humans. Both methods are based on discrete curvature estimation algorithms operating on triangle vertices using a small neighborhood of triangles. Studying human fetal brain development, Hu et al. (2012) estimated the principle curvatures (κ_1 and κ_2) by a voxel intensity-based method (Thirion and Gourdon, 1993), then used the shape index (SI) to locale the gyral nodes and sulcal pits and the curvedness (C) to quantify the sharpness of the cortical surfaces. For MRI heart data, curvature of the interventricular septum was estimated using smoothing 2D spline surfaces and differential geometry operators (Moses and Axel, 2004).

[7] http://mindboggle.info/data.html, https://osf.io/nhtur/

For fluorescence microscopy data, custom software based on cubic B-splines, which are splines comprised of piecewise degree-3 Bézier curves, was used to quantify the absolute curvature of curved microtubules (Bechstedt et al., 2014). However, this algorithm is only applicable for linear structures but not to surfaces. Curvatures of *C. elegans* cellular membranes were estimated based on local surface fitting using smooth point cloud surfaces (Xu et al., 2018). Another local surface fitting method, included in Amira Software, was recently used to estimate the curvedness (C) at contact zones in cultured mouse cerebellar neurons from block-face EM data (Hoffman et al., 2020).

To achieve robust results on the noisy images using nearly all the methods mentioned above (except for the one from Hu et al. (2012), which avoids surface modeling), the surfaces had to be strongly smoothed. How problematic smoothing can be depends on the relative size of the feature of interest compared to the pixel size.

To define constriction sites at tomographic cross-sections of dividing bacterial cells, Yao et al. (2017) wrote a Python software tool[8] that finds curvature maxima and the radius of curvature of the inner membrane by fitting a centripetal natural cubic spline. Also analyzing tomographic slices, Chen et al. (2019) fitted a spline curve to membrane profiles of clathrin-coated pits and estimated their curvature according to Boutin (2000). However useful for these specific cases, these methods are not capable of measuring curvature of arbitrary membranes in 3D. The aforementioned methods applying smoothing on surfaces are not suitable for cryo-ET data, as this would lead to the loss of small structural details in nanometer range, eliminating high curvature information. Thus, another solution has to be found to enable a reliable curvature estimation on noisy surfaces, as will be discussed below.

1.4.5 Limiting factors for membrane curvature estimation in cryo-ET

Quantization noise

The first step towards membrane curvature estimation in tomograms is membrane segmentation. Besides the errors possibly generated during the automated and manual membrane segmentation process, discretization of segmented data using binary voxels (1 membrane and 0 background) is the major limiting factor for membrane curvature estimation. This binary discretization is known as quantization noise (Magid et al., 2007). The second step towards membrane curvature estimation is surface extraction from the segmentation. The surface should ideally be smooth and free from artifacts. However, surface extraction algorithms would need gray-level values to achieve sub-voxel precision, i.e. to extract smooth surfaces. For this reason, the quantization noise present in the segmentations leads to step-wise surfaces. Thus, curvature estimation algorithms for cryo-ET should be robust to noisy surfaces. As seen in Section 1.4.3, the algorithms based on tensor voting are the most successful in coping with noisy, coarsely triangulated surfaces and thus look the most promising for cryo-ET.

[8] https://github.com/jewettaij/sabl_mpl/

Missing wedge and surface borders

Another limiting factor for curvature estimation of membranes from cryo-tomograms is the missing wedge (described in Section 1.2.5), which causes features to appear elongated in the beam direction and surfaces to be partially missing. The elongated or missing membrane regions in a tomogram are also missing in the automated segmentation (see Section 1.3.4) and should also be omitted during the manual refinement. Consequently, it is not possible to estimate curvature covering the whole membrane, the missing regions will remain undersampled. Since closed surfaces cannot be fully recovered, membrane surfaces in cryo-ET will always have borders. As seen in Section 1.4.3, curvature estimation on discrete surfaces requires a certain neighborhood around each point, thus curvature estimation at and near surface borders would also be affected, unfortunately especially in tensor voting-based algorithms that use a bigger neighborhood.

1.5 Motivation

Cryo-ET combined with segmentation methods is a powerful technique to visualize biological membranes in 3D, in a close-to-native state and at molecular resolution (Section 1.2.1 and 1.3.4). However, computational methods specialized on membrane morphology analysis did not exist or were unable to cope with imaging artifacts present in cryo-ET data, especially surface noise and holes (Section 1.2.5). Therefore, the general aim of my dissertation was to develop algorithms that help quantitatively analyze membrane biology from cryo-ET membrane segmentations.

The main aim was to estimate membrane curvature. Analyzing Huntington's disease (HD) model cells expressing exon I of polyQ-expanded Htt gene using cryo-ET, we observed that Htt fibrils interacted with and deformed cellular endomembranes, especially ER. We hypothesized that Htt fibrils induce high membrane curvature, perhaps leading to ER membrane disruption (Bäuerlein et al., 2017). Furthermore, we wanted to compare curvature of cER membranes in different tether protein mutants in yeast to better understand the contribution of the individual protein families to cER membrane morphology. For example, we wanted to visualize and analyze peaks of extreme curvature on the cER membrane facing the PM, which were more frequently observed in cells expressing only the tricalbin family tethers than in the wild type cells (Collado et al., 2019). Since existing publicly available curvature estimation methods were based on discrete approaches using only a small neighborhood of triangles (Section 1.4.3 and 1.4.4), these methods were sensitive to surface noise present in cryo-ET data (Section 1.4.5). Approaches based on tensor voting and geodesic neighborhood found in the literature (Page et al., 2002; Tong and Tang, 2005) seemed promising but the code was not publicly available. Therefore, we wanted to implement and adapt these algorithms to our data. Moreover, algorithms facilitating calculation of geodesic distances and filtering of surface borders had to be developed.

A secondary aim was to develop a method for calculation of density of membrane-bound ribosomes. In tomograms of the HD model cells mentioned above, there seemed to be less ribosomes on ER near Htt fibrils than further away from the fibrils (Bäuerlein et al., 2017). In order to help to test this hypothesis, the idea was to find membrane-bound ribosomes by template matching, map them to the ER membrane segmentation represented by a graph and calculate their density on the membrane using geodesic

distances.

Another secondary aim was to measure distances between membranes in different MCS and in different ER-PM tether protein mutants in yeast, to better understand the contribution of the individual protein families to intermembrane distances (Collado et al., 2019). For this, we wanted to implement an algorithm using the membrane surface graph representation and the surface normals estimation from the curvature estimation method.

2 Publications

2.1 In situ architecture and cellular interactions of polyQ inclusions

Felix J.B. Bäuerlein, Itika Saha*, Archana Mishra*, Maria Kalemanov, Antonio Martínez-Sánchez, Rüdiger Klein, Irina Dudanova, Mark S. Hipp, F. Ulrich Hartl, Wolfgang Baumeister & Rubén Fernández-Busnadiego, ***Cell***, 171: 179-187, 2017, DOI, URL.
* These authors contributed equally

Summary

In many neurodegenerative diseases, a certain protein aggregates into soluble oligomers and large insoluble inclusion bodies (IBs). Whereas the oligomers are known to be cytotoxic, little is known about the IBs contribution to pathology. Here, we analyzed the architecture of IBs and their cellular interactions *in situ* and in 3D using VPP cryo-ET and light microscopy.

Primary mouse neurons and human HeLa cells were transfected with different constructs of polyQ-expanded Htt exon 1, which is found in IBs in HD patient neurons and recapitulates HD-like symptoms in mice. All the construct types formed nearly spherical and mostly cytosolic IBs that consisted of a dense network of radially arranged fibrils. Large molecules like cytosolic ribosomes were abundant at the inclusion body (IB) periphery but were mostly excluded from its core.

We observed that fibrils in the outer IB periphery closely contacted organellar membranes, especially ER, and vesicles. ER membranes close to the fibrils were almost devoid of ribosomes, indicating reduction of translation. The interactions with fibrils often co-localized with ER and vesicle membrane deformations of extremely high curvature. To quantify membrane curvature at nanometric scale, we developed a previously lacking method for cryo-ET. According to our estimation, the ER curvature was significantly higher at the IB interface than in distal areas or in cells without IBs, suggesting that Htt fibrils can deform membranes. Moreover, some ER chaperones and components of ER-associated degradation machinery accumulated in the ER around the IBs, indicating ER stress. Furthermore, ER dynamics were largely reduced around IBs. Altogether, these findings suggest that the abnormal interactions between Htt fibrils and cellular endomembranes can contribute to HD pathology.

Author contribution

To quantitatively describe membrane-fibrils interactions, I segmented the membranes, analyzed ER-bound ribosomes by template matching and calculated their density on the membranes by applying a newly developed method. Moreover, I proposed and implemented a new method for curvature estimation and analyzed curvature of ER and vesicle membranes. Finally, I contributed to writing and revising the manuscript.

Article

Cell

In Situ Architecture and Cellular Interactions of PolyQ Inclusions

Graphical Abstract

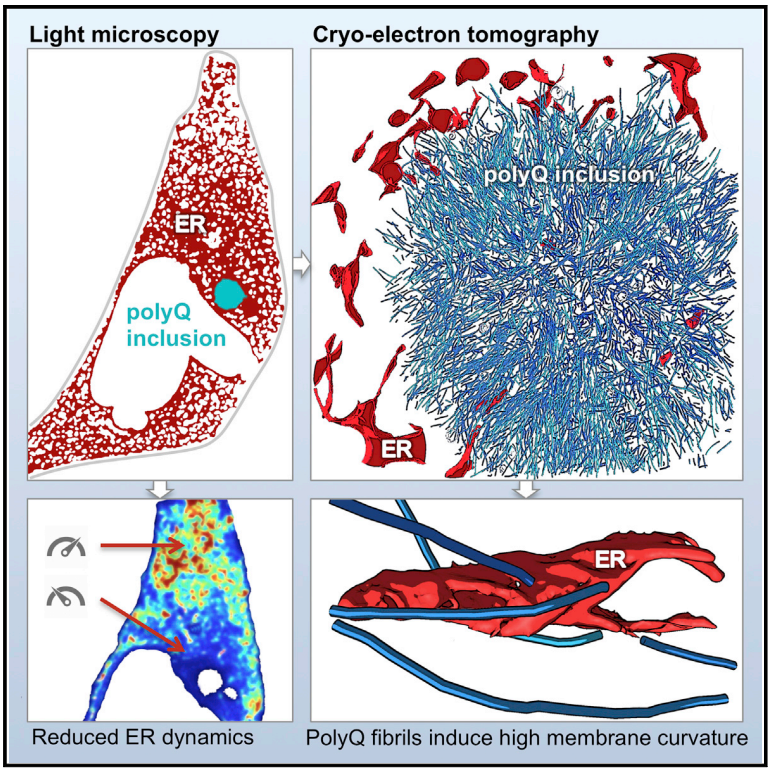

Authors

Felix J.B. Bäuerlein, Itika Saha, Archana Mishra, ..., F. Ulrich Hartl, Wolfgang Baumeister, Rubén Fernández-Busnadiego

Correspondence

uhartl@biochem.mpg.de (F.U.H.), baumeist@biochem.mpg.de (W.B.)

In Brief

Cryo-electron tomography shows that fibrils from polyglutamine inclusions distort organellar membranes and perturb membrane dynamics.

Highlights

- Polyglutamine inclusions in intact neurons visualized with cryo-electron tomography
- PolyQ inclusions in neurons consist of amyloid-like fibrils
- PolyQ fibrils interact with cellular endomembranes
- PolyQ fibrils deform ER membranes and alter ER organization and dynamics

Bäuerlein et al., 2017, Cell *171*, 179–187
September 21, 2017
http://dx.doi.org/10.1016/j.cell.2017.08.009

CellPress

Article

Cell

In Situ Architecture and Cellular Interactions of PolyQ Inclusions

Felix J.B. Bäuerlein,[1] Itika Saha,[2,6] Archana Mishra,[3,6] Maria Kalemanov,[1,4] Antonio Martínez-Sánchez,[1] Rüdiger Klein,[3,5] Irina Dudanova,[3] Mark S. Hipp,[2,5] F. Ulrich Hartl,[2,5,*] Wolfgang Baumeister,[1,7,*] and Rubén Fernández-Busnadiego[1]

[1]Department of Molecular Structural Biology, Max Planck Institute of Biochemistry, 82152 Martinsried, Germany
[2]Department of Cellular Biochemistry, Max Planck Institute of Biochemistry, 82152 Martinsried, Germany
[3]Department of Molecules, Signaling, and Development, Max Planck Institute of Neurobiology, 82152 Martinsried, Germany
[4]Graduate School of Quantitative Biosciences Munich, 81337 Munich, Germany
[5]Munich Cluster for Systems Neurology (SyNergy), 80336 Munich, Germany
[6]These authors contributed equally
[7]Lead Contact
*Correspondence: uhartl@biochem.mpg.de (F.U.H.), baumeist@biochem.mpg.de (W.B.)
http://dx.doi.org/10.1016/j.cell.2017.08.009

SUMMARY

Expression of many disease-related aggregation-prone proteins results in cytotoxicity and the formation of large intracellular inclusion bodies. To gain insight into the role of inclusions in pathology and the in situ structure of protein aggregates inside cells, we employ advanced cryo-electron tomography methods to analyze the structure of inclusions formed by polyglutamine (polyQ)-expanded huntingtin exon 1 within their intact cellular context. In primary mouse neurons and immortalized human cells, polyQ inclusions consist of amyloid-like fibrils that interact with cellular endomembranes, particularly of the endoplasmic reticulum (ER). Interactions with these fibrils lead to membrane deformation, the local impairment of ER organization, and profound alterations in ER membrane dynamics at the inclusion periphery. These results suggest that aberrant interactions between fibrils and endomembranes contribute to the deleterious cellular effects of protein aggregation.

INTRODUCTION

Protein aggregation is a hallmark of many neurodegenerative disorders, including Huntington's disease (HD), amyotrophic lateral sclerosis, and Parkinson's disease (Hipp et al., 2014; Ross and Poirier, 2004). Soluble oligomeric aggregates have been linked to toxicity in many of these proteinopathies, whereas the large insoluble inclusions found in the brains of patients and in animal and cellular models are often regarded as oligomer-sequestering protective entities (Arrasate and Finkbeiner, 2012; Bucciantini et al., 2002; Haass and Selkoe, 2007). However, the exact contribution of inclusions to pathology remains poorly characterized, and detailed structural information on inclusion body (IB) organization in unperturbed cellular environments is missing. The traditional methods of sample preparation including chemical fixation, dehydration, and heavy metal staining are not compatible with high-resolution structural studies.

Recent technical advances make cryo-electron tomography (cryo-ET) ideally suited to address the challenge of studying IB structures in situ, enabling the analysis of their interactions with their cellular environment. Cryo-focused ion beam milling (cryo-FIB) opens windows into the interior of frozen-hydrated vitrified cells by producing thin lamellas that can be studied in three dimensions (3D) by cryo-ET (Mahamid et al., 2016; Rigort et al., 2012a). Furthermore, cryo-ET imaging capabilities have been dramatically expanded by the introduction of direct electron detectors (Li et al., 2013) and the Volta phase plate, which enables imaging close to focus with maximum contrast (Asano et al., 2015; Danev et al., 2014; Mahamid et al., 2016). Thus, cryo-ET allows the 3D visualization of pristinely preserved cells at molecular resolution.

Here, we capitalize on these developments to dissect IB architecture within unstained, frozen-hydrated, vitrified mammalian cells, using polyglutamine (polyQ)-expanded huntingtin (Htt) exon 1 as a model aggregating protein. The expansion of a polyQ stretch in the N-terminal region of Htt renders the mutant protein highly aggregation-prone and leads to HD in humans (Finkbeiner, 2011; Macdonald, 1993; Scherzinger et al., 1997). PolyQ-expanded Htt oligomers have been implicated in the misregulation of, among others, transcription, vesicular traffic, autophagy, and the function of the endoplasmic reticulum (ER) and mitochondria (Arrasate and Finkbeiner, 2012), but it is not known whether inclusions play any role in these phenomena. Furthermore, several other neurodegenerative disorders including spinal and bulbar muscular atrophy and spinocerebellar ataxias are also caused by polyQ expansions in otherwise non-related proteins (Orr and Zoghbi, 2007). Our results show that inclusions of polyQ-expanded Htt exon 1 are formed by fibrils that impinge on cellular membranes, especially those of the ER. These interactions result in membrane deformation and possibly rupture, as well as impaired ER organization and dynamics around inclusion bodies.

RESULTS

3D Architecture of Htt97Q Inclusion Bodies

Inclusion bodies in HD patient neurons are formed by N-terminal fragments of Htt harboring the polyQ-expanded exon 1,

expression of which suffices to recapitulate HD-like symptoms in mice (Davies et al., 1997; DiFiglia et al., 1997; Mangiarini et al., 1996; Yamamoto et al., 2000). We transfected mouse primary neurons with GFP-tagged Htt exon 1 containing 97 Q (Htt97Q-GFP). Non-apoptotic cells containing inclusions were identified by live imaging and subsequently vitrified by plunge freezing following a short incubation in medium containing 10% glycerol to ensure full vitrification. Correlative microscopy allowed us to target inclusions for cryo-FIB milling to yield 150- to 250-nm-thick cellular lamellas that were imaged in 3D by Volta phase plate cryo-ET (Figure S1). Htt97Q-GFP inclusions were roughly spherical, ~3 μm in diameter and mostly cytosolic, although nuclear inclusions were also found. Both cytosolic and nuclear inclusions consisted of a network of amyloid-like fibrils with a diameter of 7–8 nm and length of 125 ± 81 nm (mean ± SD) (Figures 1A, 1B, 1E, 2A, and 2B). Thus, despite the similarity in fibril length, the cellular organization of Htt97Q-GFP fibrils was very different from the bundles of parallel fibrils formed by Sup35 yeast prions (Kawai-Noma et al., 2010; Saibil et al., 2012). The analysis of fibril curvature provided insights into fibril flexibility. We calculated an average fibril persistence length of 2.6 ± 0.1 μm (mean ± SD) and a Young's modulus of 52 ± 2 MPa (mean ± SD) (Figure S2A), in the range of other amyloid fibrils or actin (Mahamid et al., 2016; Wegmann et al., 2010). Despite the dense appearance of the network, the fibrils occupied less than 3% of the IB volume (Figure 1F).

In situ fibrils were morphologically similar to those formed in vitro, but did not associate laterally to form wider ribbons (Scherzinger et al., 1997) (Figure 1A, inset). Interestingly, Htt97Q-GFP fibrils were decorated by regularly spaced globular densities of ~6 nm in diameter consistent in size with GFP dimers. To further investigate the nature of these densities, cells were co-transfected with untagged 97Q Htt exon 1 (Htt97Q) and mCherry-ubiquitin. The latter can be conjugated to target proteins in a manner similar to wild-type ubiquitin (Qian et al., 2002) and its recruitment to inclusion bodies (Hipp et al., 2012) served as a surrogate fluorescent marker for Htt97Q inclusions. Given the relatively low transfection rates obtained in neurons, these and further experiments were carried out in HeLa cells to increase the number of cells amenable to cryo-ET analysis. Htt97Q and Htt97Q-GFP inclusions in HeLa cells were almost identical to those in neurons in terms of overall architecture and fibril morphology (Figures 1E–1H and 3A–3E). Both in neurons and HeLa cells the fibrils were radially arranged in most, but not all inclusions (Figures 1A, 1B, 2, and 3A–3C). Although Htt97Q-GFP and untagged Htt97Q fibrils were similar in diameter and length (Figure 1E), untagged Htt97Q fibrils were not decorated by additional densities (Figure 1H). This demonstrates that the fibrils consisted of Htt97Q, and suggests a molecular organization in which the polyQ regions form the fibril core and the more flexible C-terminal sequence protrudes outward (Bugg et al., 2012; Isas et al., 2015; Lin et al., 2017). The presence of GFP resulted in a 50% reduction in fibril density within the IB (Figure 1F) and a 25% increase in fibril stiffness (Figures S2A–S2C).

Htt97Q and Htt97Q-GFP fibrils were always observed as part of inclusions, suggesting that inclusions are the main sites of fibril growth in the cell (Ossato et al., 2010). Although only a small fraction of IB volume was occupied by fibrils (Figure 1F), the core of the aggregates was mostly devoid of large macromolecules such as ribosomes, which were abundant at the IB periphery (Figures 1A and 1B).

Htt97Q Fibrils Impinge on Cellular Endomembranes

For all cytosolic inclusions analyzed (N = 5 inclusions, neurons, Htt97Q-GFP; N = 10, HeLa, Htt97Q-GFP; N = 8, HeLa, Htt97Q; Table S1), fibrils in extended areas of the IB periphery visibly contacted the membranes of various organelles. These included mitochondria, lysosomes and, most prominently, the ER (Figures 1A, 1B, 3, S3B, and S3D; Movie S1), but no observable association with autophagic structures. The electron densities of membranes and fibrils often appeared continuous at points of contact (Figures 1D, 3D, and S3D), indicating that the fibril-membrane distance was shorter than the pixel size (1.7 or 2.8 nm). Ribosome-free ER tubes often protruded into the IB, apparently interacting extensively with the fibrillar network (Figures 1B–1D, 3B, 3C, and 3G). Both the ends and sides of fibrils directly touched the membranes, and these regions displayed extremely high membrane curvature (Figures 1C, 1D, and 3D–3F). A systematic analysis showed that ER membrane curvature was higher at the IB interface than in more distal areas, and also compared to ER membranes in cells expressing diffuse Htt97Q-GFP without visible inclusions or non-pathogenic Htt25Q-GFP (Figures S2D and S4).

A heterogeneous population of vesicles was embedded in most cytosolic inclusions (100% of inclusions, neurons, and Htt97Q-GFP; 94%, HeLa and Htt97Q-GFP; 82%, HeLa and Htt97Q) at sites of interaction with organelles (Figures 1A, 1B, 1D, and 3A–3F). Many of these vesicles were highly irregular in shape and were often in contact with fibrils at regions of high membrane curvature, suggesting that they resulted from the disruption of organellar membranes following interaction with the fibrils (Figures 1D and 3D–3F). Ribosomes were bound to the membranes of some of these vesicles, suggesting that they originated from ruptured ER membranes (Figures 3E and 3F). Interestingly, similar membrane deformations at contact regions with amyloid fibrils leading to membrane disruption were previously observed in vitro with liposomes (Milanesi et al., 2012).

Comparable IB architecture and membrane interactions were found in cells expressing Htt64Q-GFP (Figures 2C and 2D), arguing against a strong influence of the exact length of the expanded polyQ tract on fibril arrangement and cellular interactions. Htt97Q and Htt97Q-GFP nuclear inclusions were similar in overall architecture to cytosolic ones but did not contain vesicles and did not contact the inner nuclear membrane (Figures 2A and 2B), indicating differential mechanisms of cellular interaction (Benn et al., 2005; Gu et al., 2015; Liu et al., 2015). In summary, the fibrils forming cytosolic polyQ inclusions have the potential to deform and perhaps disrupt cellular membranes in their proximity, particularly those of the ER, both in mouse neurons and in human cells.

Htt97Q Inclusions Alter ER Organization and Dynamics

Light microscopy in HeLa cells confirmed the association of Htt97Q-GFP inclusions with the ER (Figure 4A). Interestingly, some inclusions contained puncta positive for ER markers but disconnected from the ER network (Figure 4B), in line with the assumption that some of the vesicles found within inclusions

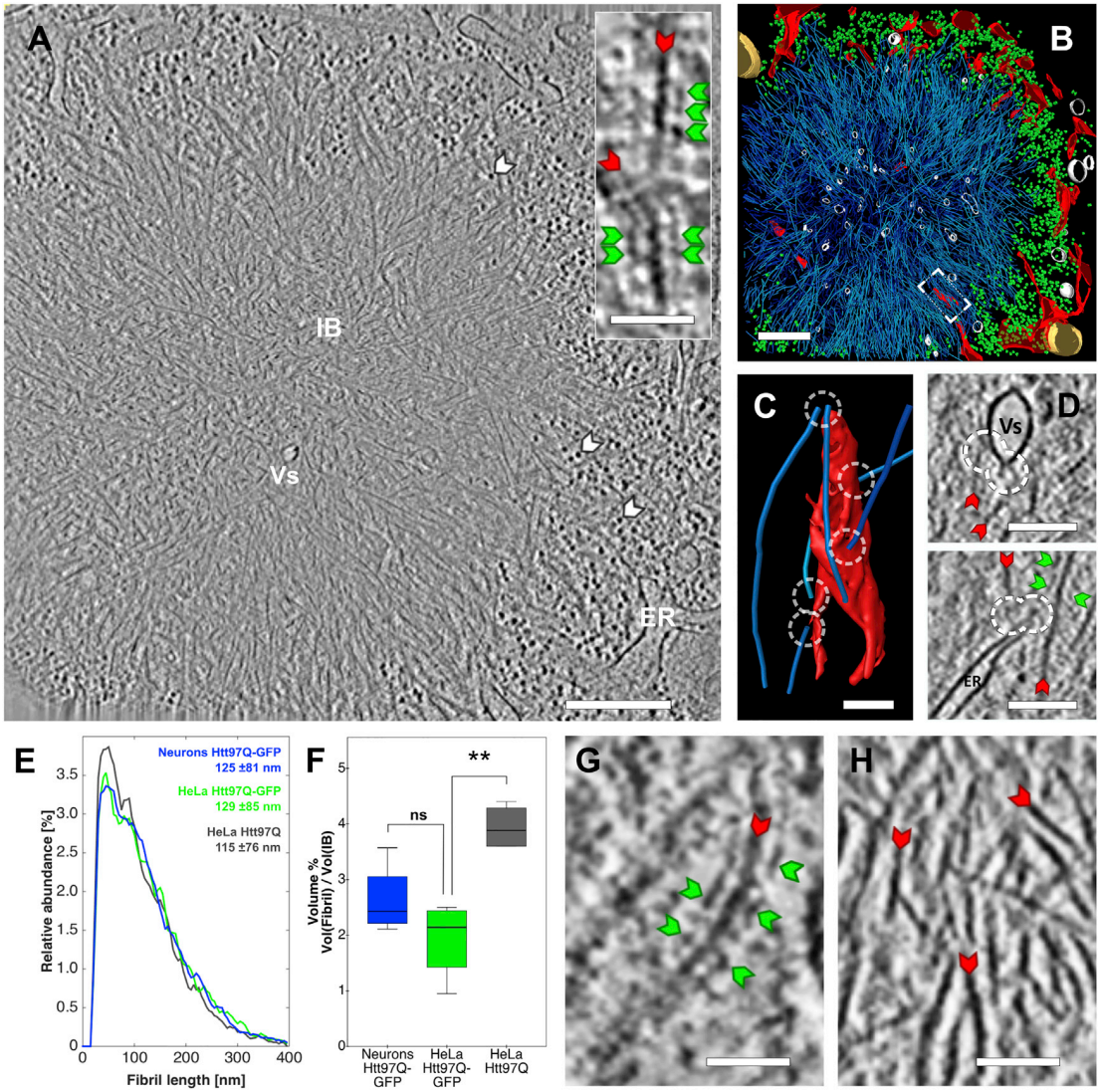

Figure 1. Cytosolic Inclusions of Htt97Q-GFP Contain Amyloid-like Fibrils

(A) Tomographic slice of an IB in an Htt97Q-GFP-transfected mouse primary neuron. The cytoplasmic electron dense particles represent ribosomes (white arrowheads). ER, endoplasmic reticulum; IB, Htt97Q-GFP inclusion body; Vs, vesicle. Inset: high-magnification image of Htt97Q-GFP fibrils (red arrowheads) decorated by globular densities (green arrowheads).

(B) 3D rendering of the tomogram shown in (A). ER membranes (red), Htt97Q-GFP fibrils (cyan), ribosomes (green), vesicles (white), and mitochondria (gold). Note that the core of the IB is largely devoid of ribosomes, which are abundant at the IB periphery. Scale bars, 400 nm in (A) and (B) and 30 nm in (A) (inset).

(C) Magnified rendering of the region marked in (B) showing interaction sites (white circles) between Htt97Q-GFP fibrils and the ER membrane. Scale bar, 50 nm.

(D) Magnified tomographic slices showing Htt97Q-GFP fibrils (red arrowheads) decorated by globular densities (green arrowheads) interacting with cellular membranes in Htt97Q-GFP-transfected neurons. Scale bars, 100 nm.

(E) Histograms of fibril length in mouse neurons expressing Htt97Q-GFP (blue), HeLa cells expressing Htt97Q-GFP (green), and HeLa cells expressing Htt97Q (gray) (number of fibrils: n = 11,481 neurons and Htt97Q-GFP; n = 7,648 HeLa and Htt97Q-GFP; n = 12,465 HeLa and Htt97Q; 4 tomograms for all conditions).

(F) Percentage of IB volume occupied by fibrils. The boxes and whiskers, respectively, indicate confidence intervals of 50% and 95% around the mean (solid line inside each box). ** indicates $p < 0.01$; ns, not significant in an ANOVA analysis with Bonferroni post hoc test.

(G) Magnified tomographic slice of an Htt97Q-GFP-transfected HeLa cell showing an Htt97Q-GFP fibril (red arrowhead) decorated by globular densities (green arrowheads).

(H) Magnified tomographic slice of an Htt97Q-transfected HeLa cell showing Htt97Q fibrils.

Scale bars, 50 nm in (G) and (H). Tomographic slices are 2.8-nm (A and D) or 1.7-nm (G and H) thick. The number of experiments and cells analyzed per condition is shown in Table S1.

See also Figures S1, S2, and S4 and Table S1.

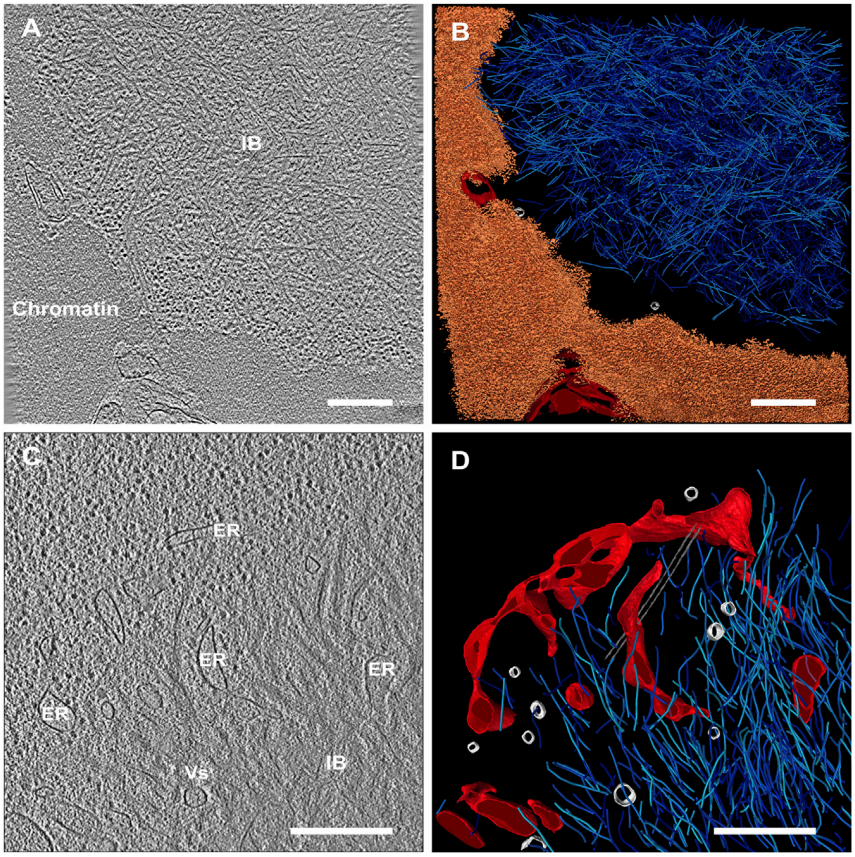

Figure 2. Nuclear Htt97Q-GFP Inclusions in Neurons and Cytosolic Htt64Q-GFP Inclusions in HeLa Cells

(A) 1.7-nm thick tomographic slice of a nuclear IB in an Htt97Q-GFP-transfected neuron. IB, Htt97Q-GFP inclusion body.

(B) 3D rendering of the tomogram shown in (A). Chromatin (orange), nuclear envelope membranes (red), vesicles in the periphery of the IB (white), and Htt97Q-GFP fibrils (cyan). Scale bars, 400 nm in (A) and (B).

(C) 2.5-nm-thick tomographic slice showing an IB in an Htt64Q-GFP-transfected HeLa cell. ER, endoplasmic reticulum; IB, Htt64Q-GFP inclusion body; Vs, vesicle.

(D) 3D rendering of the tomogram shown in (C). ER membranes (red), Htt64Q-GFP fibrils (cyan), and microtubule (gray parallel lines).

Scale bars, 250 nm in (C) and (D). The number of experiments and cells analyzed per condition is shown in Table S1.

See also Figures S2 and S4 and Table S1.

by cryo-ET originated from ruptured ER membranes. Occasionally, puncta positive for mitochondrial markers were also observed inside Htt97Q-GFP inclusions (Figure S3A), but this was not the case for other organelles, such as the Golgi apparatus (Figure S3C). Thus, our light and electron microscopy data indicate that the polyQ Htt exon 1 fibrils of inclusion bodies interact most extensively with ER membranes.

We further investigated the consequences of this membrane interaction by immunostaining for a variety of ER-resident proteins. Interestingly, some ER chaperones (e.g. calnexin) and components of the ER-associated degradation (ERAD) machinery (e.g., Erlin-2, Sel1L) were enriched in the ER domain surrounding the inclusions, whereas other ER proteins and ERAD components (e.g., BiP, calreticulin, PDI, or p97) did not show this pattern (Figure S3E; data not shown). In contrast, the translocase component Sec61 was largely excluded from the IB vicinity, consistent with the observation by cryo-ET that ER membranes in contact with the IB were essentially devoid of ribosomes (Figures 1C, 3B, 3C, and 3G). Thus, some, but not all, of the components of the so-called "ER quality control compartment" (Leitman et al., 2013a) accumulated around Htt97Q-GFP inclusions. Strikingly, live cell imaging revealed a complete "freezing" of ER dynamics in the vicinity of Htt97Q-GFP inclusions (Figures 4C–4F and S3F–S3H; Movie S2). This effect was not merely steric, as the ER was highly dynamic around other large cellular structures or the nucleus (Figures 4C and 4D).

Altogether, these data suggest that the interaction of Htt97Q-GFP fibrils with ER membranes alters cell physiology by locally impairing ER organization and dynamics.

DISCUSSION

While polyQ-expanded Htt exon 1 forms fibrils in vitro (Scherzinger et al., 1997), it has remained controversial whether Htt in cellular inclusions is present in granular or fibrillar form (Finkbeiner, 2011; Qin et al., 2004; Waelter et al., 2001). Importantly, fibril formation is thought to be required for neurodegeneration in HD mice (Gu et al., 2009). Our cryo-ET data conclusively show that in vitrified frozen hydrated murine neurons and human cells, inclusions of polyQ-expanded Htt exon 1 do consist of fibrils. The high resolution of our images allowed us to resolve additional densities decorating the fibrils formed by a GFP-labeled Htt97Q construct, and to quantify the changes in fibril density and rigidity induced by the GFP tag. Htt97Q fibrils were substantially thinner than those found in heavy-metal stained preparations (Qin et al., 2004), and sufficiently stiff to deform membranes (Roux, 2013). The structure of in situ fibrils is consistent with that proposed by recent NMR studies, in which the polyQ stretch forms the amyloid core and the flanking regions protrude outward in a bottlebrush fashion (Isas et al., 2015; Lin et al., 2017). However, our data do not allow the molecular organization of the fibril core to be resolved, possibly due to its structural heterogeneity (Hoop et al., 2016; Lin et al., 2017). A comparative cryo-ET analysis of endogenous polyQ inclusions in brain tissue is not yet technically feasible and remains a goal for future research.

Wild-type Htt is known to interact with cellular membranes (Kegel-Gleason, 2013), and fibrils of polyQ-expanded Htt exon 1 and other amyloids can cause membrane disruption in vitro (Milanesi et al., 2012; Pieri et al., 2012). Our results suggest that as a

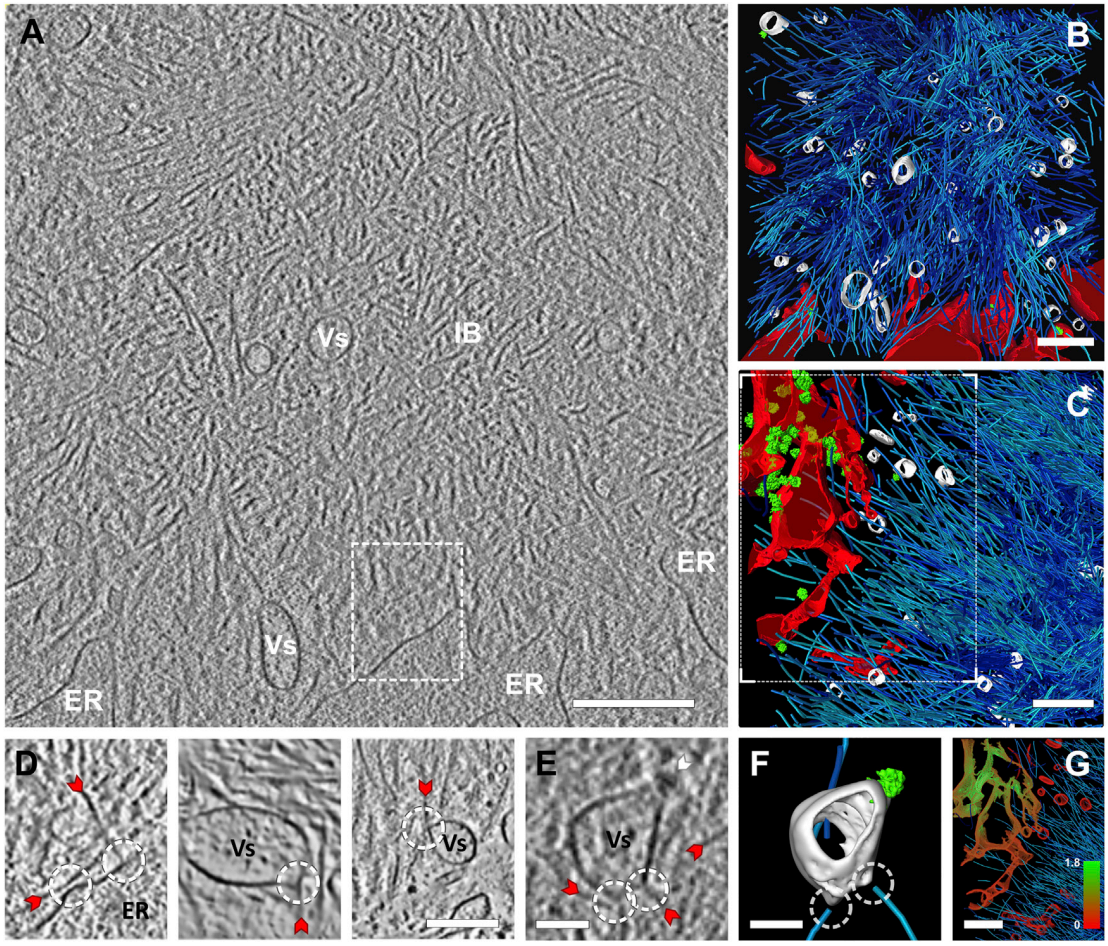

Figure 3. Htt97Q Inclusions Interact with Cellular Membranes

(A) Tomographic slice from the interaction zone between an IB and cellular membranes in an Htt97Q-transfected HeLa cell. ER, endoplasmic reticulum; IB, Htt97Q inclusion body; Vs, vesicles.

(B) 3D rendering of the tomogram shown in (A). ER membranes (red), ER-bound ribosomes (green), Htt97Q fibrils (cyan), and vesicles inside the IB (white).

(C) 3D rendering of ER membranes and ER-bound ribosomes in the vicinity of Htt97Q fibrils in a different cell. Note that ER-bound ribosomes are depleted from ER membranes directly interacting with Htt97Q fibrils but are abundant in more distal areas (see also G). Scale bars, 250 nm in (A)–(C).

(D) Magnified tomographic slices showing the sides and ends of Htt97Q (left and middle) and Htt97Q-GFP (right) fibrils (red arrowheads) interacting with cellular membranes (white circles). The left panel shows the area boxed in (A) in a different tomographic slice.

(E) Magnified tomographic slice of a putative membrane-bound ribosome (white arrowhead) on a small vesicle contacted (white circles) by the Htt97Q-GFP fibrils of an IB.

(F) 3D rendering of the vesicle shown in (E). Note the high curvature of the vesicle membrane at the sites of interaction with fibrils. Scale bars, 100 nm in (D)–(F).

(G) Visualization of the density of membrane-bound ribosomes in the area boxed in (C). Ribosome density is indicated by color and is lower (red) on ER membranes in direct contact with fibrils. Scale bar, 250 nm. Tomographic slices are 1.7-nm thick. The number of experiments and cells analyzed per condition is shown in Table S1.

See also Figures S2, S3, and S4, Table S1, and Movie S1.

cytopathological consequence of these phenomena, the fibrils of Htt exon 1 inclusions impinge on and possibly disrupt cellular endomembranes, most prominently those of the ER. As a result, inclusions drive a reorganization of the ER network in their periphery. Fibril-membrane interactions are thought to be largely lipid-mediated (Burke et al., 2013; Kegel et al., 2005; Trevino et al., 2012), and whether any specificity for ER membranes exists (Atwal et al., 2007) remains to be determined. Although it is possible that oligomers dissociating from fibril ends (Carulla et al., 2005; Martins et al., 2008) contribute to these effects, high concentrations of soluble Htt97Q-GFP did not disturb membrane morphology in the absence of inclusions. Thus, fibrils appear to be necessary for membrane deformation.

The region of the ER surrounding the inclusions showed dramatically reduced membrane dynamics, suggesting that a wide variety of cellular processes that depend on the dynamic behavior of the ER (Zhang and Hu, 2016) might be affected as a consequence. Moreover, translation is halted in these regions, as ER membranes contacting fibrils lacked ribosomes and the Sec61 translocon. The accumulation of ERAD factors and ER

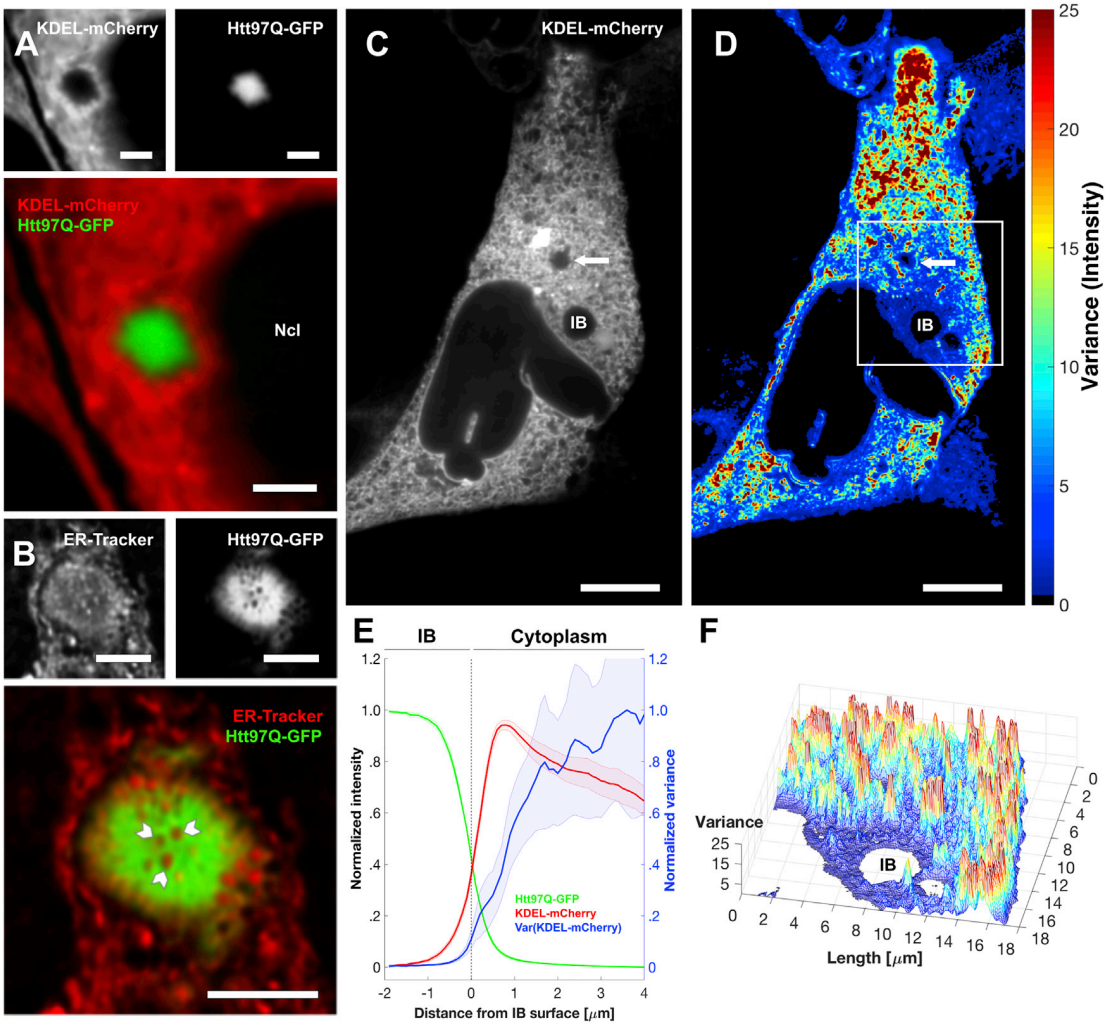

Figure 4. Htt97Q-GFP Inclusions Locally Alter ER Organization and Dynamics

(A) HeLa cell co-expressing Htt97Q-GFP (green) and the ER luminal marker KDEL-mCherry (red). Note the accumulation of ER around the IB. Ncl, nucleus.

(B) HeLa cell expressing Htt97Q-GFP (green) and labeled with ER-Tracker (red). White arrowheads mark ER-positive structures inside the IB. Scale bars, 5 μm in (A) and (B).

(C) Additional example of a HeLa cell co-expressing Htt97Q-GFP and KDEL-mCherry. A white arrow points to an Htt97Q-GFP-negative large cytoplasmic structure around which ER dynamics are normal. IB, Htt97Q-GFP inclusion body.

(D) ER dynamics of the cell shown in (C) quantified as the variance of KDEL-mCherry pixel intensity over time for 20 s. Scale bars, 10 μm in (C) and (D).

(E) Quantification of ER membrane dynamics in the vicinity of Htt97Q-GFP inclusions (n = 44 HeLa cells). Note the substantial accumulation of ER (red curve; radial average of KDEL-mCherry pixel intensity) at the IB periphery (x = 0). Membrane dynamics, assessed by the variance of KDEL-mCherry pixel intensity over time (blue curve), were markedly slower in this ER domain than in more distal regions. Radial averages (solid lines) and 95% confidence intervals (shaded areas) are shown. See Figures S3F–3H for individual traces.

(F) 3D representation of the boxed region in (D) around the IB.

See also Figure S3 and Movie S2.

chaperones suggests that cytosolic inclusions locally induce misfolding of ER luminal proteins causing ER stress. These results are consistent with previous findings that polyQ expression compromises ER function by perturbing ERAD, ER Ca^{2+} signaling and the ER redox state, leading to ER stress in cellular and animal models (Duennwald and Lindquist, 2008; Higo et al., 2010; Jiang et al., 2016; Kirstein et al., 2015; Kouroku et al., 2002; Lajoie and Snapp, 2011; Leitman et al., 2013b; Tang et al., 2003). ER stress markers are upregulated in Htt knockin mice and HD patients, and alleviating ER stress is beneficial in various HD models (Carnemolla et al., 2009; Lee et al., 2012; Leitman et al., 2014; Vidal et al., 2012). Thus, beyond the toxic role of oligomeric aggregate species, our data suggest that the formation of large fibrillar inclusions (Benn et al., 2005; Liu et al., 2015; Ramdzan et al., 2017; Woerner et al., 2016) also contributes to cytopathology.

STAR★METHODS

Detailed methods are provided in the online version of this paper and include the following:

- KEY RESOURCES TABLE
- CONTACT FOR REAGENT AND RESOURCE SHARING
- EXPERIMENTAL MODEL AND SUBJECT DETAILS
  - Cell Culture
  - Hippocampal Neuron Culture and Transfection
- METHOD DETAILS
  - Plasmids and Antibodies
  - Immunofluorescence
  - Correlative Light Microscopy and Live Cell Imaging
  - Cell Vitrification
  - Cryo-focused Ion Beam Milling
  - Cryo-electron Tomography
  - Tomogram Reconstruction and Analysis
- QUANTIFICATION AND STATISTICAL ANALYSIS
  - Persistence Length Analysis
  - Ribosome Template Matching and Calculation of ER-bound Ribosome Density
  - Determination of ER Membrane Curvature
  - Statistical Analysis
- DATA AND SOFTWARE AVAILABILITY

SUPPLEMENTAL INFORMATION

Supplemental Information includes four figures, one table, and two movies and can be found with this article online at http://dx.doi.org/10.1016/j.cell.2017.08.009.

A video abstract is available at http://dx.doi.org/10.1016/j.cell.2017.08.009#mmc4.

AUTHOR CONTRIBUTIONS

F.J.B.B. performed all electron and light microscopy experiments, analyzed the data, and prepared the figures. I.S. and A.M. performed the cell culture experiments. M.K. and A.M.-S. contributed to the computational analysis of cryo-ET data. R.K., I.D., M.S.H., F.U.H., W.B., and R.F.-B. designed the research. I.D., M.S.H., and R.F.-B. supervised the experiments. M.S.H., F.U.H., W.B., and R.F.-B. wrote the manuscript with contributions from the other authors.

ACKNOWLEDGMENTS

This research has received funding from the European Commission (FP7 GA ERC-2012-SyG_318987–ToPAG) and the Munich Cluster for Systems Neurology (EXC 010 SyNergy). M.K. was supported by the Graduate School of Quantitative Biosciences Munich (GSC-1006). We thank Radostin Danev, Günter Pfeifer, and Jürgen Plitzko for electron microscopy support; Tom Gaitanos and Tim Laugks for assistance with light microscopy; Stefan Pfeffer for advice in data analysis; and Eri Sakata for discussions and critically reading the manuscript.

Received: March 31, 2017
Revised: June 30, 2017
Accepted: August 7, 2017
Published: September 7, 2017

REFERENCES

Anger, A.M., Armache, J.P., Berninghausen, O., Habeck, M., Subklewe, M., Wilson, D.N., and Beckmann, R. (2013). Structures of the human and Drosophila 80S ribosome. Nature *497*, 80–85.

Arrasate, M., and Finkbeiner, S. (2012). Protein aggregates in Huntington's disease. Exp. Neurol. *238*, 1–11.

Asano, S., Fukuda, Y., Beck, F., Aufderheide, A., Förster, F., Danev, R., and Baumeister, W. (2015). Proteasomes. A molecular census of 26S proteasomes in intact neurons. Science *347*, 439–442.

Atwal, R.S., Xia, J., Pinchev, D., Taylor, J., Epand, R.M., and Truant, R. (2007). Huntingtin has a membrane association signal that can modulate huntingtin aggregation, nuclear entry and toxicity. Hum. Mol. Genet. *16*, 2600–2615.

Bence, N.F., Sampat, R.M., and Kopito, R.R. (2001). Impairment of the ubiquitin-proteasome system by protein aggregation. Science *292*, 1552–1555.

Benn, C.L., Landles, C., Li, H., Strand, A.D., Woodman, B., Sathasivam, K., Li, S.H., Ghazi-Noori, S., Hockly, E., Faruque, S.M., et al. (2005). Contribution of nuclear and extranuclear polyQ to neurological phenotypes in mouse models of Huntington's disease. Hum. Mol. Genet. *14*, 3065–3078.

Bucciantini, M., Giannoni, E., Chiti, F., Baroni, F., Formigli, L., Zurdo, J., Taddei, N., Ramponi, G., Dobson, C.M., and Stefani, M. (2002). Inherent toxicity of aggregates implies a common mechanism for protein misfolding diseases. Nature *416*, 507–511.

Bugg, C.W., Isas, J.M., Fischer, T., Patterson, P.H., and Langen, R. (2012). Structural features and domain organization of huntingtin fibrils. J. Biol. Chem. *287*, 31739–31746.

Burke, K.A., Hensal, K.M., Umbaugh, C.S., Chaibva, M., and Legleiter, J. (2013). Huntingtin disrupts lipid bilayers in a polyQ-length dependent manner. Biochim. Biophys. Acta *1828*, 1953–1961.

Carnemolla, A., Fossale, E., Agostoni, E., Michelazzi, S., Calligaris, R., De Maso, L., Del Sal, G., MacDonald, M.E., and Persichetti, F. (2009). Rrs1 is involved in endoplasmic reticulum stress response in Huntington disease. J. Biol. Chem. *284*, 18167–18173.

Carulla, N., Caddy, G.L., Hall, D.R., Zurdo, J., Gairí, M., Feliz, M., Giralt, E., Robinson, C.V., and Dobson, C.M. (2005). Molecular recycling within amyloid fibrils. Nature *436*, 554–558.

Danev, R., Buijsse, B., Khoshouei, M., Plitzko, J.M., and Baumeister, W. (2014). Volta potential phase plate for in-focus phase contrast transmission electron microscopy. Proc. Natl. Acad. Sci. USA *111*, 15635–15640.

Davies, S.W., Turmaine, M., Cozens, B.A., DiFiglia, M., Sharp, A.H., Ross, C.A., Scherzinger, E., Wanker, E.E., Mangiarini, L., and Bates, G.P. (1997). Formation of neuronal intranuclear inclusions underlies the neurological dysfunction in mice transgenic for the HD mutation. Cell *90*, 537–548.

Deo, N. (2016). Graph Theory with Applications to Engineering and Computer Science (Dover Publications).

DiFiglia, M., Sapp, E., Chase, K.O., Davies, S.W., Bates, G.P., Vonsattel, J.P., and Aronin, N. (1997). Aggregation of huntingtin in neuronal intranuclear inclusions and dystrophic neurites in brain. Science *277*, 1990–1993.

Duennwald, M.L., and Lindquist, S. (2008). Impaired ERAD and ER stress are early and specific events in polyglutamine toxicity. Genes Dev. *22*, 3308–3319.

Fernandez, J.J., Laugks, U., Schaffer, M., Bäuerlein, F.J., Khoshouei, M., Baumeister, W., and Lucic, V. (2016). Removing contamination-induced reconstruction artifacts from cryo-electron tomograms. Biophys. J. *110*, 850–859.

Finkbeiner, S. (2011). Huntington's disease. Cold Spring Harb. Perspect. Biol. *3*, 3.

Fukuda, Y., Laugks, U., Lučić, V., Baumeister, W., and Danev, R. (2015). Electron cryotomography of vitrified cells with a Volta phase plate. J. Struct. Biol. *190*, 143–154.

Gu, X., Greiner, E.R., Mishra, R., Kodali, R., Osmand, A., Finkbeiner, S., Steffan, J.S., Thompson, L.M., Wetzel, R., and Yang, X.W. (2009). Serines 13 and 16 are critical determinants of full-length human mutant huntingtin induced disease pathogenesis in HD mice. Neuron *64*, 828–840.

Gu, X., Cantle, J.P., Greiner, E.R., Lee, C.Y., Barth, A.M., Gao, F., Park, C.S., Zhang, Z., Sandoval-Miller, S., Zhang, R.L., et al. (2015). N17 Modifies mutant Huntingtin nuclear pathogenesis and severity of disease in HD BAC transgenic mice. Neuron *85*, 726–741.

Haass, C., and Selkoe, D.J. (2007). Soluble protein oligomers in neurodegeneration: lessons from the Alzheimer's amyloid beta-peptide. Nat. Rev. Mol. Cell Biol. *8*, 101–112.

Higo, T., Hamada, K., Hisatsune, C., Nukina, N., Hashikawa, T., Hattori, M., Nakamura, T., and Mikoshiba, K. (2010). Mechanism of ER stress-induced brain damage by IP(3) receptor. Neuron *68*, 865–878.

Hipp, M.S., Patel, C.N., Bersuker, K., Riley, B.E., Kaiser, S.E., Shaler, T.A., Brandeis, M., and Kopito, R.R. (2012). Indirect inhibition of 26S proteasome activity in a cellular model of Huntington's disease. J. Cell Biol. *196*, 573–587.

Hipp, M.S., Park, S.H., and Hartl, F.U. (2014). Proteostasis impairment in protein-misfolding and -aggregation diseases. Trends Cell Biol. *24*, 506–514.

Holmberg, C.I., Staniszewski, K.E., Mensah, K.N., Matouschek, A., and Morimoto, R.I. (2004). Inefficient degradation of truncated polyglutamine proteins by the proteasome. EMBO J. *23*, 4307–4318.

Hoop, C.L., Lin, H.K., Kar, K., Magyarfalvi, G., Lamley, J.M., Boatz, J.C., Mandal, A., Lewandowski, J.R., Wetzel, R., and van der Wel, P.C. (2016). Huntingtin exon 1 fibrils feature an interdigitated β-hairpin-based polyglutamine core. Proc. Natl. Acad. Sci. USA *113*, 1546–1551.

Hrabe, T., Chen, Y., Pfeffer, S., Cuellar, L.K., Mangold, A.V., and Förster, F. (2012). PyTom: a python-based toolbox for localization of macromolecules in cryo-electron tomograms and subtomogram analysis. J. Struct. Biol. *178*, 177–188.

Isas, J.M., Langen, R., and Siemer, A.B. (2015). Solid-state nuclear magnetic resonance on the static and dynamic domains of huntingtin exon-1 fibrils. Biochemistry *54*, 3942–3949.

Jiang, Y., Chadwick, S.R., and Lajoie, P. (2016). Endoplasmic reticulum stress: the cause and solution to Huntington's disease? Brain Res. *1648* (Pt B), 650–657.

Kawai-Noma, S., Pack, C.G., Kojidani, T., Asakawa, H., Hiraoka, Y., Kinjo, M., Haraguchi, T., Taguchi, H., and Hirata, A. (2010). In vivo evidence for the fibrillar structures of Sup35 prions in yeast cells. J. Cell Biol. *190*, 223–231.

Kegel, K.B., Sapp, E., Yoder, J., Cuiffo, B., Sobin, L., Kim, Y.J., Qin, Z.H., Hayden, M.R., Aronin, N., Scott, D.L., et al. (2005). Huntingtin associates with acidic phospholipids at the plasma membrane. J. Biol. Chem. *280*, 36464–36473.

Kegel-Gleason, K.B. (2013). Huntingtin interactions with membrane phospholipids: strategic targets for therapeutic intervention? J. Huntingtons Dis. *2*, 239–250.

Kirstein, J., Morito, D., Kakihana, T., Sugihara, M., Minnen, A., Hipp, M.S., Nussbaum-Krammer, C., Kasturi, P., Hartl, F.U., Nagata, K., and Morimoto, R.I. (2015). Proteotoxic stress and ageing triggers the loss of redox homeostasis across cellular compartments. EMBO J. *34*, 2334–2349.

Koenderink, J.J., and van Doorn, A.J. (1992). Surface shape and curvature scales. Image Vis. Comput. *10*, 557–564.

Kouroku, Y., Fujita, E., Jimbo, A., Kikuchi, T., Yamagata, T., Momoi, M.Y., Kominami, E., Kuida, K., Sakamaki, K., Yonehara, S., and Momoi, T. (2002). Polyglutamine aggregates stimulate ER stress signals and caspase-12 activation. Hum. Mol. Genet. *11*, 1505–1515.

Kremer, J.R., Mastronarde, D.N., and McIntosh, J.R. (1996). Computer visualization of three-dimensional image data using IMOD. J. Struct. Biol. *116*, 71–76.

Lajoie, P., and Snapp, E.L. (2011). Changes in BiP availability reveal hypersensitivity to acute endoplasmic reticulum stress in cells expressing mutant huntingtin. J. Cell Sci. *124*, 3332–3343.

Lee, H., Noh, J.Y., Oh, Y., Kim, Y., Chang, J.W., Chung, C.W., Lee, S.T., Kim, M., Ryu, H., and Jung, Y.K. (2012). IRE1 plays an essential role in ER stress-mediated aggregation of mutant huntingtin via the inhibition of autophagy flux. Hum. Mol. Genet. *21*, 101–114.

Leitman, J., Ron, E., Ogen-Shtern, N., and Lederkremer, G.Z. (2013a). Compartmentalization of endoplasmic reticulum quality control and ER-associated degradation factors. DNA Cell Biol. *32*, 2–7.

Leitman, J., Ulrich Hartl, F., and Lederkremer, G.Z. (2013b). Soluble forms of polyQ-expanded huntingtin rather than large aggregates cause endoplasmic reticulum stress. Nat. Commun. *4*, 2753.

Leitman, J., Barak, B., Benyair, R., Shenkman, M., Ashery, U., Hartl, F.U., and Lederkremer, G.Z. (2014). ER stress-induced eIF2-alpha phosphorylation underlies sensitivity of striatal neurons to pathogenic huntingtin. PLoS ONE *9*, e90803.

Li, X., Mooney, P., Zheng, S., Booth, C.R., Braunfeld, M.B., Gubbens, S., Agard, D.A., and Cheng, Y. (2013). Electron counting and beam-induced motion correction enable near-atomic-resolution single-particle cryo-EM. Nat. Methods *10*, 584–590.

Lin, H.K., Boatz, J.C., Krabbendam, I.E., Kodali, R., Hou, Z., Wetzel, R., Dolga, A.M., Poirier, M.A., and van der Wel, P.C.A. (2017). Fibril polymorphism affects immobilized non-amyloid flanking domains of huntingtin exon1 rather than its polyglutamine core. Nat. Commun. *8*, 15462.

Liu, K.Y., Shyu, Y.C., Barbaro, B.A., Lin, Y.T., Chern, Y., Thompson, L.M., James Shen, C.K., and Marsh, J.L. (2015). Disruption of the nuclear membrane by perinuclear inclusions of mutant huntingtin causes cell-cycle re-entry and striatal cell death in mouse and cell models of Huntington's disease. Hum. Mol. Genet. *24*, 1602–1616.

Macdonald, M.; The Huntington's Disease Collaborative Research Group (1993). A novel gene containing a trinucleotide repeat that is expanded and unstable on Huntington's disease chromosomes. Cell *72*, 971–983.

Mahamid, J., Pfeffer, S., Schaffer, M., Villa, E., Danev, R., Cuellar, L.K., Förster, F., Hyman, A.A., Plitzko, J.M., and Baumeister, W. (2016). Visualizing the molecular sociology at the HeLa cell nuclear periphery. Science *351*, 969–972.

Mangiarini, L., Sathasivam, K., Seller, M., Cozens, B., Harper, A., Hetherington, C., Lawton, M., Trottier, Y., Lehrach, H., Davies, S.W., and Bates, G.P. (1996). Exon 1 of the HD gene with an expanded CAG repeat is sufficient to cause a progressive neurological phenotype in transgenic mice. Cell *87*, 493–506.

Martinez-Sanchez, A., Garcia, I., Asano, S., Lucic, V., and Fernandez, J.J. (2014). Robust membrane detection based on tensor voting for electron tomography. J. Struct. Biol. *186*, 49–61.

Martins, I.C., Kuperstein, I., Wilkinson, H., Maes, E., Vanbrabant, M., Jonckheere, W., Van Gelder, P., Hartmann, D., D'Hooge, R., De Strooper, B., et al. (2008). Lipids revert inert Abeta amyloid fibrils to neurotoxic protofibrils that affect learning in mice. EMBO J. *27*, 224–233.

Mastronarde, D.N. (2005). Automated electron microscope tomography using robust prediction of specimen movements. J. Struct. Biol. *152*, 36–51.

Milanesi, L., Sheynis, T., Xue, W.F., Orlova, E.V., Hellewell, A.L., Jelinek, R., Hewitt, E.W., Radford, S.E., and Saibil, H.R. (2012). Direct three-dimensional visualization of membrane disruption by amyloid fibrils. Proc. Natl. Acad. Sci. USA *109*, 20455–20460.

Nagashima, H., and Asakura, S. (1980). Dark-field light microscopic study of the flexibility of F-actin complexes. J. Mol. Biol. *136*, 169–182.

Nickell, S., Förster, F., Linaroudis, A., Net, W.D., Beck, F., Hegerl, R., Baumeister, W., and Plitzko, J.M. (2005). TOM software toolbox: acquisition and analysis for electron tomography. J. Struct. Biol. *149*, 227–234.

Orr, H.T., and Zoghbi, H.Y. (2007). Trinucleotide repeat disorders. Annu. Rev. Neurosci. *30*, 575–621.

Ossato, G., Digman, M.A., Aiken, C., Lukacsovich, T., Marsh, J.L., and Gratton, E. (2010). A two-step path to inclusion formation of huntingtin peptides revealed by number and brightness analysis. Biophys. J. *98*, 3078–3085.

Page, D.L., Sun, Y., Koschan, A.F., Paik, J., and Abidi, M.A. (2002). Normal vector voting: crease detection and curvature estimation on large, noisy meshes. Graph. Models *64*, 199–229.

Pfeffer, S., Brandt, F., Hrabe, T., Lang, S., Eibauer, M., Zimmermann, R., and Förster, F. (2012). Structure and 3D arrangement of endoplasmic reticulum membrane-associated ribosomes. Structure *20*, 1508–1518.

Pieri, L., Madiona, K., Bousset, L., and Melki, R. (2012). Fibrillar α-synuclein and huntingtin exon 1 assemblies are toxic to the cells. Biophys. J. *102*, 2894–2905.

Qian, S.B., Ott, D.E., Schubert, U., Bennink, J.R., and Yewdell, J.W. (2002). Fusion proteins with COOH-terminal ubiquitin are stable and maintain dual functionality in vivo. J. Biol. Chem. *277*, 38818–38826.

Qin, Z.H., Wang, Y., Sapp, E., Cuiffo, B., Wanker, E., Hayden, M.R., Kegel, K.B., Aronin, N., and DiFiglia, M. (2004). Huntingtin bodies sequester vesicle-associated proteins by a polyproline-dependent interaction. J. Neurosci. *24*, 269–281.

Ramdzan, Y.M., Trubetskov, M.M., Ormsby, A.R., Newcombe, E.A., Sui, X., Tobin, M.J., Bongiovanni, M.N., Gras, S.L., Dewson, G., Miller, J.M.L., et al. (2017). Huntingtin inclusions trigger cellular quiescence, deactivate apoptosis, and lead to delayed necrosis. Cell Rep. *19*, 919–927.

Rigort, A., Bäuerlein, F.J., Villa, E., Eibauer, M., Laugks, T., Baumeister, W., and Plitzko, J.M. (2012a). Focused ion beam micromachining of eukaryotic cells for cryoelectron tomography. Proc. Natl. Acad. Sci. USA *109*, 4449–4454.

Rigort, A., Günther, D., Hegerl, R., Baum, D., Weber, B., Prohaska, S., Medalia, O., Baumeister, W., and Hege, H.C. (2012b). Automated segmentation of electron tomograms for a quantitative description of actin filament networks. J. Struct. Biol. *177*, 135–144.

Ross, C.A., and Poirier, M.A. (2004). Protein aggregation and neurodegenerative disease. Nat. Med. *10* (*Suppl*), S10–S17.

Roux, A. (2013). The physics of membrane tubes: soft templates for studying cellular membranes. Soft Matter *9*, 6726–6736.

Saibil, H.R., Seybert, A., Habermann, A., Winkler, J., Eltsov, M., Perkovic, M., Castaño-Diez, D., Scheffer, M.P., Haselmann, U., Chlanda, P., et al. (2012). Heritable yeast prions have a highly organized three-dimensional architecture with interfiber structures. Proc. Natl. Acad. Sci. USA *109*, 14906–14911.

Schaffar, G., Breuer, P., Boteva, R., Behrends, C., Tzvetkov, N., Strippel, N., Sakahira, H., Siegers, K., Hayer-Hartl, M., and Hartl, F.U. (2004). Cellular toxicity of polyglutamine expansion proteins: mechanism of transcription factor deactivation. Mol. Cell *15*, 95–105.

Scherzinger, E., Lurz, R., Turmaine, M., Mangiarini, L., Hollenbach, B., Hasenbank, R., Bates, G.P., Davies, S.W., Lehrach, H., and Wanker, E.E. (1997). Huntingtin-encoded polyglutamine expansions form amyloid-like protein aggregates in vitro and in vivo. Cell *90*, 549–558.

Schindelin, J., Arganda-Carreras, I., Frise, E., Kaynig, V., Longair, M., Pietzsch, T., Preibisch, S., Rueden, C., Saalfeld, S., Schmid, B., et al. (2012). Fiji: an open-source platform for biological-image analysis. Nat. Methods *9*, 676–682.

Tang, T.S., Tu, H., Chan, E.Y., Maximov, A., Wang, Z., Wellington, C.L., Hayden, M.R., and Bezprozvanny, I. (2003). Huntingtin and huntingtin-associated protein 1 influence neuronal calcium signaling mediated by inositol-(1,4,5) triphosphate receptor type 1. Neuron *39*, 227–239.

Trevino, R.S., Lauckner, J.E., Sourigues, Y., Pearce, M.M., Bousset, L., Melki, R., and Kopito, R.R. (2012). Fibrillar structure and charge determine the interaction of polyglutamine protein aggregates with the cell surface. J. Biol. Chem. *287*, 29722–29728.

Vidal, R.L., Figueroa, A., Court, F.A., Thielen, P., Molina, C., Wirth, C., Caballero, B., Kiffin, R., Segura-Aguilar, J., Cuervo, A.M., et al. (2012). Targeting the UPR transcription factor XBP1 protects against Huntington's disease through the regulation of FoxO1 and autophagy. Hum. Mol. Genet. *21*, 2245–2262.

Waelter, S., Boeddrich, A., Lurz, R., Scherzinger, E., Lueder, G., Lehrach, H., and Wanker, E.E. (2001). Accumulation of mutant huntingtin fragments in aggresome-like inclusion bodies as a result of insufficient protein degradation. Mol. Biol. Cell *12*, 1393–1407.

Wegmann, S., Jung, Y.J., Chinnathambi, S., Mandelkow, E.M., Mandelkow, E., and Muller, D.J. (2010). Human Tau isoforms assemble into ribbon-like fibrils that display polymorphic structure and stability. J. Biol. Chem. *285*, 27302–27313.

Woerner, A.C., Frottin, F., Hornburg, D., Feng, L.R., Meissner, F., Patra, M., Tatzelt, J., Mann, M., Winklhofer, K.F., Hartl, F.U., and Hipp, M.S. (2016). Cytoplasmic protein aggregates interfere with nucleocytoplasmic transport of protein and RNA. Science *351*, 173–176.

Yamamoto, A., Lucas, J.J., and Hen, R. (2000). Reversal of neuropathology and motor dysfunction in a conditional model of Huntington's disease. Cell *101*, 57–66.

Zhang, H., and Hu, J. (2016). Shaping the endoplasmic reticulum into a social network. Trends Cell Biol. *26*, 934–943.

STAR★METHODS

KEY RESOURCES TABLE

REAGENT or RESOURCE	SOURCE	IDENTIFIER
Antibodies		
Rabbit polyclonal anti-GRP78 BiP	Abcam	Cat# ab21685; RRID: AB_2119834
Rabbit polyclonal anti-Calnexin	AbCam	Cat# ab10286; RRID: AB_2069009
Chicken polyclonal anti-Calreticulin	AbCam	Cat# ab14234; RRID: AB_2228460
Rabbit polyclonal anti-Giantin	AbCam	Cat# ab24586; RRID: AB_448163
Rabbit monoclonal anti-PDIA6	AbCam	Cat# ab154820
Rabbit monoclonal anti-Sec61A	AbCam	Cat# ab183046; RRID: AB_2620158
Rabbit polyclonal anti-SEL1L	Sigma	Cat# S3699; RRID: AB_1856660
Rabbit monoclonal anti- SPFH2/ERLIN2	AbCam	Cat# ab128924; RRID: AB_11150974
Rabbit polyclonal anti-VCP	Cell Signaling	Cat# 2648; RRID: AB_2214632
Goat anti-Rabbit Cy3	Dianova	Cat# 111-165-045; RRID: AB_2338003
Goat anti-Chicken Alexa Flour 633	Thermo Fisher Scientific	Cat# A-21103; RRID: AB_2535756
Chemicals, Peptides, and Recombinant Proteins		
Dulbecco's modified Eagle medium (DMEM)	Biochrom	Cat# F0435
Fetal Bovine Serum (FBS)	GIBCO	Cat# 10270-106
L-Glutamine	GIBCO	Cat# 25030-024
Penicillin / Streptomycin	GIBCO	Cat# 15140-122
Non-essential amino acids	GIBCO	Cat# 11140-035
Trypsin	GIBCO	Cat# 12605-010
PBS	GIBCO	Cat# 20012-068
Lipofectamine 2000	Thermo Fisher Scientific	Cat# 11668027
16% Formaldehyde	Thermo Fisher Scientific	Cat# 28908
Fluorescence mounting medium	Dako	Cat# S3023
Poly-D-Lysine hydrobromide	Sigma-Aldrich	Cat# P7886
Laminin Mouse Protein, Natural	Thermo Fisher Scientific	Cat# 23017015
Neurobasal Medium	Thermo Fisher Scientific	Cat# 21103-049
B27 Serum-free Supplement	Thermo Fisher Scientific	Cat# 17504044
L-Glutamine (100x)	Thermo Fisher Scientific	Cat# 25030081
Trypsin-EDTA	Thermo Fisher Scientific	Cat# 25200056
DNA-InTM Neuro	MTI-GlobalStem	Cat# GST-2101
Triton X-100	Sigma-Aldrich	Cat# T9284
DAPI	Thermo Fisher Scientific	Cat# D1306
Critical Commercial Assays		
Annexin V, Alexa Fluor 594 conjugate	Thermo Fisher Scientific	Cat# A13203
ER-Tracker Red	Thermo Fisher Scientific	Cat# E34250
Mito-Tracker Red	Thermo Fisher Scientific	Cat# M22425
Deposited Data		
Cryo-EM structure of membrane-bound ribosome	Pfeffer et al., 2012	EMDB: 2099
Cryo-EM structure of non membrane-bound ribosome	Anger et al., 2013	EMDB: 5592
Experimental Models: Cell Lines		
Human: HeLa cells	ATCC	ATCC CCL-2; RRID: CVCL_0030
Experimental Models: Organisms/Strains		
Mouse primary neuronal culture: C57BL/6 (E17)	MPI-Biochemistry	RRID: CVCL_9115

(*Continued on next page*)

Continued

REAGENT or RESOURCE	SOURCE	IDENTIFIER
Recombinant DNA		
Plasmid: Htt25Q-GFP	Bence et al., 2001	N/A
Plasmid: Htt97Q-GFP	Bence et al., 2001	N/A
Plasmid: Htt97Q	Schaffar et al., 2004	N/A
Plasmid: Htt64Q-GFP	Holmberg et al., 2004	N/A
Plasmid: mCherry-Ubiquitin	Eric J. Bennett and Ron R. Kopito	N/A
Plasmid: KDEL-mCherry	This study	N/A
Software and Algorithms		
Fiji	Schindelin et al., 2012	https://fiji.sc/ RRID: SCR_002285
SerialEM	Mastronarde, 2005	http://bio3d.colorado.edu/SerialEM/
MaskTomRec	Fernandez et al., 2016	https://sites.google.com/site/3demimageprocessing/masktomrec
TomoSegMemTV	Martinez-Sanchez et al., 2014	https://sites.google.com/site/3demimageprocessing/tomosegmemtv
Amira	N/A	https://www.fei.com/software/amira-3d-for-life-sciences/ RRID: SCR_014305
Amira XTracing Module	Rigort et al., 2012b	http://www.zib.de/software/actin-segmentation
Pytom	Hrabe et al., 2012	http://pytom.org/
TOM toolbox	Nickell et al., 2005	https://www.biochem.mpg.de/tom
VTK	N/A	http://www.vtk.org RRID: SCR_015013
MATLAB and Python scripts used to calculate the density of membrane-bound ribosomes and measure ER membrane curvature	This study	https://github.com/anmartinezs/polyqIB
MATLAB scripts used for the analysis of light microscopy data and quantification of fibril persistence length and ER membrane curvature measurements	This study	https://github.com/FJBauerlein/Huntington
Other		
ibidi 35 mm μ-Dishes	ibidi	Cat# 81158
Poly-L-Lysine coverslips	NeuVitro	Cat# GG-12-PLL
Quantifoil grids 200 mesh Gold R2/1	Quantifoil Micro Tools	N/A
Whatman paper #1	Sigma-Aldrich	Cat# WHA10010155

CONTACT FOR REAGENT AND RESOURCE SHARING

Further information and requests for resources and reagents should be directed to and will be fulfilled by the Lead Contact, Wolfgang Baumeister (baumeist@biochem.mpg.de).

EXPERIMENTAL MODEL AND SUBJECT DETAILS

Cell Culture

HeLa cells (female; ATCC CCL-2; RRID: CVCL_0030) were freshly obtained from ATCC and no unusual DAPI staining was observed, indicating no mycoplasma contamination. Cells were seeded on holey carbon-coated 200 mesh gold EM grids (Quantifoil Micro Tools, Jena, Germany) within ibidi μ-dishes (ibidi, Munich) containing Dulbecco's MEM (Biochrom) supplemented with 10% fetal bovine serum, 2mM L-Glutamine, 100 Units/mL penicillin, 100μg/mL streptomycin and non-essential amino acids cocktail (GIBCO) and cultured at 37°C with 10% CO_2. The cells were transfected by lipofection using Lipofectamine 2000 (Invitrogen) with either Htt25Q-GFP, Htt64Q-GFP, Htt97Q-GFP or Htt97Q together with mCherry-ubiquitin as per manufacturer's protocol. In co-transfected cells mCherry-ubiquitin formed a ring around Htt97Q inclusions that facilitated correlative microscopy (Hipp et al., 2012). 30 min prior to imaging the cells were stained with Annexin V conjugated to Alexa Fluor 594 (LifeTechnologies) to exclude cells undergoing apoptosis from further analysis.

Hippocampal Neuron Culture and Transfection

Holey carbon-coated 200 mesh gold EM grids were sterilized in ethanol for 10 min, washed several times in double distilled water and transferred to culture dishes containing water. Grids and dishes were coated with poly-D-lysine (Sigma-Aldrich; 1 mg/ml in borate buffer) and laminin (Thermo Fisher; 7.5 μg/ml in PBS) for 24 hr each, washed with PBS three times and placed in neurobasal medium supplemented with B27 containing 0.5 mM Glutamine (all reagents from Thermo Fisher). During washes and medium exchange steps, grids were transferred into another dish containing appropriate liquid to prevent grids from drying.

Mice (C57BL/6 background, either sex; RRID:CVCL_9115) were housed in an specific pathogen free facility with 12:12 hr light/dark cycle and food/water available ad libitum. All animal experiments were performed in compliance with institutional policies approved by the government of upper Bavaria. For preparation of neurons, hippocampi from embryonic day 17 mice were separated from diencephalic structures and digested individually with 0.25% trypsin containing 1 mM 2,2′,2″,2‴-(ethane-1,2-diyldinitrilo) tetraacetic acid (EDTA) for 20 min at 37°C. Neurons were plated on the coated grids within 24-well plates (60,000 per well). After 6 days in culture at 37°C in 5% CO_2, neurons were transfected with Htt97Q-GFP using DNA-In *Neuro* (GlobalStem) according to the manufacturer's protocol.

METHOD DETAILS

Plasmids and Antibodies

The plasmids expressing myc-tagged Htt25Q exon 1-GFP, Htt64Q exon 1-GFP, Htt97Q exon 1 and Htt97Q exon 1-GFP have been described previously (Bence et al., 2001; Holmberg et al., 2004; Schaffar et al., 2004; Woerner et al., 2016). The plasmid expressing mCherry-Ubiquitin was a kind gift from Eric J. Bennett and Ron R. Kopito. To generate the KDEL-mCherry construct (kind gift from Lisa Vincenz-Donnelly), the signal peptide of human pulmonary surfactant-associated protein B (MAESHLLQWLLLLLPTLCGPGTA) followed by one alanine residue and a myc tag was fused upstream to mCherry by PCR amplification. A C-terminal KDEL sequence, as well as a 5′ BamH1 and a 3′ Not1 digestion site were also added by PCR amplification. The purified PCR product was then inserted into the pcDNA3.1+ plasmid via BamH1/Not1.

The following primary antibodies were used for immunofluorescence: BiP (AbCam ab21685; RRID: AB_2119834), calnexin (AbCam ab10286; RRID: AB_2069009), calreticulin (AbCam ab14234; RRID: AB_2228460), giantin (AbCam ab24586; RRID: AB_448163), p97/VCP (Cell Signaling 2468; RRID: AB_2214632), PDIA6 (AbCam ab154820), Sec61A (AbCam ab183046; RRID: AB_2620158), SEL1L (Sigma S3699; RRID: AB_1856660) and SPFH2/ERLIN2 (AbCam ab128924; RRID: AB_11150974). The following secondary antibodies were used: Anti-Rabbit Cy3 (Dianova 111-165-045) and Anti-Chicken Alexa Fluor 633 conjugate (Thermo Fisher Scientific A21103; RRID: AB_2535756).

Immunofluorescence

HeLa cells were seeded on poly-L-lysine coated glass coverslips (NeuVitro), transfected with Htt97Q-GFP and fixed 24-48 hr post-transfection using 4% formaldehyde in PBS for 10 min, permeabilized with 0.1% (v/v) Triton X-100 in PBS (GIBCO) for 5 min and blocked in 5% milk in PBS for 1 hr at room temperature. The cells were then washed and primary antibodies were applied overnight at a dilution of 1:500 to 1:1000 in blocking solution at 4°C, washed in PBS and incubated with secondary antibodies at a dilution of 1:5000 in PBS at room temperature for 1-2 hr. Coverslips were stained with 500 nM DAPI in PBS for 5 min, washed several times with PBS and mounted in fluorescence mounting medium (Dako).

To investigate the identity of the membranous structures contained inside inclusions, HeLa cells were transfected with Htt97Q-GFP and loaded with either ER-Tracker Red or Mito-Tracker Red (Thermo Fischer) 24h after transfection. The cells were subsequently fixed and imaged as described below.

Correlative Light Microscopy and Live Cell Imaging

To locate cells containing polyQ inclusions and suitable for cryo-ET, cells were imaged in an atmosphere of 37°C and 10% CO_2 using a CorrSight light microscope (FEI, Hillsboro, USA) equipped with bright field and spinning disc confocal laser illumination (405/488/561/640 nm), 20x (air, NA 0.8) and 63x (oil, NA 1.4) Plan Achromat objectives (Carl Zeiss, Jena, Germany) and a 1344 × 1024 pixel camera with a pixel size of 6.4 μm (Hamamatsu Digital Camera C10600 ORCA-R2).

For correlative microscopy a map of the EM grid was acquired with 20x magnification (object pixel size 323 nm) in spinning disc confocal mode. Htt97Q and Htt97Q-GFP-expressing HeLa cells and primary neurons were imaged 24 hr after transfection, as this yielded the best compromise between cell death and formation of IB. Protein expression was allowed for 48-72h in Htt64Q-GFP-expressing HeLa cells, as IB formation was slower.

For investigation of ER dynamics, HeLa cells were co-transfected with Htt97Q-GFP and KDEL-mCherry and imaged at 5-10 Hz with 63x magnification (object pixel size 102 nm) in spinning disk confocal mode for 20-30 s. The z slice containing the maximum IB diameter was analyzed further for each movie. Movies were first bleach-corrected using the exponential fit tool of Fiji (Schindelin et al., 2012; RRID:SCR_002285) and further processed using in-house MATLAB (MathWorks) scripts (available at https://github.com/FJBauerlein/Huntington). The IB boundary (x = 0 in Figures 4E and S3F–S3H) was estimated as the line where Htt97Q-GFP intensity dropped to 40% of its maximum value in each IB. A radial average of KDEL-mCherry pixel intensity was calculated from this mask within the cytoplasm. The radial variance of KDEL-mCherry pixel intensity was calculated over time, and normalized by pixel intensity

to account for different KDEL-mCherry expression levels in different cells. The maximum of the curve was scaled to 1. The normalized variance was used as readout for ER membrane dynamics (blue curves in Figures 4E and S3H).

Cell Vitrification

After light microscopy the cells were incubated for 1-5 min in DMEM containing 10% glycerol as a cryo-protectant to ensure full vitrification. The grids were then mounted on a manual plunger, blotted from the back side using Whatman paper #1 (Sigma-Aldrich) and plunged into a 2:1 ethane:propane mixture cooled down to liquid nitrogen temperature.

Cryo-focused Ion Beam Milling

To prepare thin electron transparent lamellae containing polyQ inclusions and surrounding cellular structures, plunge-frozen grids were first mounted into Autogrid frames (FEI). Autogrids were mounted into a dual-beam Quanta 3D focused ion beam (FIB) / scanning electron microscope (SEM) (FEI) using a custom-built transfer shuttle and a cryo-transfer system (PP3000T, Quorum). The samples were kept at −180°C throughout FIB milling by the microscope's cryo-stage. To target cells containing inclusions an overview map of the EM grid was acquired by SEM at 10 kV at 100x magnification (object pixel size 1.1 μm) and correlated with the light microscopy map using MAPS software (FEI). Thereby, the fluorescence signal was overlaid on the correlated SEM micrograph. For Htt97Q/mCherry-ubiquitin co-transfected cells a custom-made MATLAB algorithm (available at https://github.com/FJBauerlein/Huntington) was applied to the correlated light microscopy/SEM image to select inclusions as ring-shaped structures and classify them according to their size and usability in terms of distance to the grid bars. To protect the milling front of the lamellae, gaseous organic platinum was frozen on top of the grid using a gas injection system. 15-30 μm wide lamellae were prepared in target cells using a Ga^+ ion beam at 30 kV at shallow angles (8-14°) in four consecutive steps: initially cells were abrased in 500 nm steps from the top down with 500-1000 pA and imaged consecutively by SEM at 2.5 kV, 4.1 pA in integration mode to identify inclusions. Further rectangular patterns were defined above and below the intended lamella with 2 μm spacing for the rough milling step (ion beam current of 500-1000 pA), followed by fine milling with 800 nm spacing (200 pA) and a final polishing step down to the final lamella thickness of 150-250 nm (50 pA). To reduce lamella charging during phase plate cryo-ET data acquisition a thin layer of pure metallic Pt was sputtered onto the lamella under cryo conditions at the PP3000T transfer system with the following parameters: 5 mA sputtering current, 500 V between stage and sputtering target and 10 s of exposure at $4.5x10^{-2}$ mbar.

Cryo-electron Tomography

Cryo-FIB lamellas were imaged using a Titan cryo-transmission electron microscope (FEI) equipped with a field emission gun operated at 300 kV, a Volta phase plate (Danev et al., 2014), a post-column energy filter (Gatan, Pleasanton, CA, USA) operated at zero-loss and a K2 Summit direct electron detector (Gatan). Low-magnification images of lamellas were recorded at 11,500x (object pixel size 1.312 nm) and stitched using ICE (Microsoft Research) to produce complete lamella overviews. Phase plate alignment and operation was carried out as described (Fukuda et al., 2015). Upon phase plate conditioning, high-magnification (19,500x, object pixel size 0.710 nm for Figure 1A; 33,000x, object pixel size 0.421 nm for all other tomograms) tilt series were recorded at locations of interest using the SerialEM (Mastronarde, 2005) low dose acquisition scheme with a tilt increment of 2°, typically spanning an angular range from −52° to 70°. Target defocus was set to −0.5 μm. The K2 camera was operated in dose fractionation mode recording frames every 0.2 s. For each tilt series, a new spot on the phase plate was selected. The total dose was limited to 70-150 $e^-/Å^2$.

Tomogram Reconstruction and Analysis

K2 camera frames were aligned using in-house software (available at https://github.com/dtegunov/k2align) following previously developed procedures (Li et al., 2013). In brief, the relative shifts of the image between camera frames due to stage drift and beam-induced motion were measured and corrected. A band-pass filter (0.001 - 0.250 of Nyquist frequency) was applied to aid alignment. Hot pixels were corrected and frames with empty regions resulting from camera readout errors were discarded. For each exposure, the aligned frames were added to provide a corrected image. The resulting corrected tilt series were aligned using the patch tracking option of the IMOD package (Kremer et al., 1996) and reconstructed by weighted back projection. After reconstruction, the tilt series were cleaned of surface contamination (ice crystals and sputtered metallic Pt) using the MaskTomRec software (Fernandez et al., 2016), re-aligned and reconstructed again.

Membranes were automatically segmented using the TomoSegMemTV package (Martinez-Sanchez et al., 2014) and refined manually when necessary using Amira (FEI Visualization Sciences Group; RRID:SCR_014305). PolyQ fibrils were automatically detected using the XTracing Module in Amira (Rigort et al., 2012b). In brief, tomograms were denoised by a non-local means filter and searched for a cylindrical template of 8 nm in diameter and 42 nm in length. The resulting cross-correlation fields were thresholded at an empirical value of 0.68-0.72 that produced optimal numbers of true positives and negatives. The thresholded correlation fields were used as starting point for the filament tracing process. The length and orientation distribution of the resulting fibrils was then measured. The total volume occupied by fibrils was calculated by multiplying the total length of all fibrils by πr^2, where r is the radius of the fibrils, here 4 nm. The fraction of IB occupied by fibrils was determined by dividing the total fibril volume by the volume of a manually traced envelope of the IB.

QUANTIFICATION AND STATISTICAL ANALYSIS

Persistence Length Analysis

The persistence length (L_P) was determined using an in-house script (available at https://github.com/FJBauerlein/Huntington). L_P is a measure of the stiffness of polymers that can be defined as the average distance for which a filament is not bent. It is calculated as the expectation value of cos θ, where θ is the angle between two tangents to the fibril at positions 0 and l (Nagashima and Asakura, 1980):

$$\cos(\theta_0 - \theta_l) = e^{-\left(l/L_p\right)}$$

Intuitively, the larger θ (i.e., the smaller L_P) the more flexible is the fibril.

The Young's modulus E defines the relation between applied force and deformation of the fibril and can be calculated from L_P as:

$$E = \frac{L_P k_B T}{I}$$

where k_B is the Boltzmann constant (1.38×10^{-23} m^2 kg s^{-2} K^{-1}), T is the absolute temperature (here 295 K) and I is the momentum of inertia, which for a solid rod can be calculated from its radius r as:

$$I = \frac{\pi r^4}{4}$$

The force necessary to deform the cell membrane into filopodia-like extensions or to drive membrane fission by dynamin has been estimated in the order of 20 pN (Roux, 2013), which would result in only a 1% axial deformation of an Htt97Q fibril according to:

$$E = \frac{\sigma(\varepsilon)}{\varepsilon} = \frac{F/A_0}{\Delta L/L_0}$$

where σ is the stress applied (force F divided by the cross section of the fibril A_0) and ε the resulting strain or deformation (the increase in length ΔL divided by the initial length L_0). Therefore, we conclude that Htt97Q fibrils could easily withstand or exert the forces necessary to deform cellular membranes without rupturing.

Ribosome Template Matching and Calculation of ER-bound Ribosome Density

ER-bound ribosomes were analyzed by template matching using PyTom and TOM software (Hrabe et al., 2012; Nickell et al., 2005). In brief, tomograms were searched for the structure of a membrane-bound ribosome (Pfeffer et al., 2012) (Electron Microscopy Data Bank, EMDB: 2099) downsampled to 40 Å resolution in a volume limited to < 100 nm distance from previously segmented ER membranes. The top cross-correlation hits were screened visually and further filtered to discard ribosomes whose center was located more than 18 nm away from the ER membrane. The remaining particles were aligned by real space alignment and classified into six groups using constrained principle component analysis and k-means clustering. One of those classes yielded non-membrane bound ribosomes and was discarded, whereas the others contained mainly true positives and were pooled.

Each membrane-bound ribosome center coordinate was mapped to a central voxel on the membrane plane of the ribosome template and overlapped with the membrane segmentation using in-house MATLAB scripts to discard particles with wrong orientation. The membrane segmentation was transformed into a graph (Deo, 2016) using the graph-tool python library (https://git.skewed.de/count0/graph-tool) as follows: All voxels of the ER or vesicle membranes were added to the set of vertices. Then, all pairs of vertices representing neighboring voxels were connected by edges, resulting in a fully connected graph. The shortest distances via the membrane (geodesic distance) from each membrane voxel to the ribosome center voxels on the membrane (d) were calculated using the graph-tool python library. The ribosome density (D) for each membrane voxel was defined as:

$$D = \sum_{(reachable\ ribosomes)} \frac{1}{d+1}$$

Thus, for every membrane voxel, the higher the number of reachable ribosomes and the shorter the distances to them, the higher D value. These procedures are available at https://github.com/anmartinezs/polyqIB.

The cytosolic ribosomes shown in Figure 1B were detected by template matching using the structure of a cytosolic ribosome (Anger et al., 2013) (EMDB: 5592).

Determination of ER Membrane Curvature

First, ER membrane segmentations were pre-processed with morphological operations to remove small holes. The segmentations were then transformed into a signed, single-layer surface (a mesh of connected triangles) using in-house python software. This procedure was based on the Visualization Toolkit library (http://www.vtk.org; RRID:SCR_015013) implementation of Hoppe's surface

reconstruction algorithm (http://hhoppe.com/proj/thesis/). To recover surface mesh topology, a graph was constructed using the graph-tool python library, so that every vertex of the graph represented the center of a surface triangle, and every edge of the graph connected two adjacent triangles. The graph was then used to estimate geodesic distances between triangles as the shortest paths along graph edges. For each triangle, a local neighborhood was defined by all triangles within 9 nm center-to-center distance. For each neighborhood, the maximal and minimal principal curvatures (κ_1 and κ_2, respectively) were estimated by an in-house implementation of the normal vector voting algorithm (Page et al., 2002). To represent surface curvature as a single scalar value for every triangle, principal curvatures were combined by computing curvedness (Koenderink and van Doorn, 1992), defined as:

$$Curvedness = \sqrt{\frac{\kappa_1^2 + \kappa_2^2}{2}}$$

These procedures are available at https://github.com/anmartinezs/polyqIB.

Statistical Analysis

The number of cells analyzed for each condition is shown in Table S1. Tomograms of poor technical quality or showing signs of cell death were excluded. For optimal fibril tracing and subsequent analysis (fibril length, density, persistence length, Young's modulus), the 4 tomograms with best signal-to-noise ratio were selected for each condition as this procedure can be affected by noise (Rigort et al., 2012b). This resulted in a large number of fibrils analyzed: n = 11,481, neurons, Htt97Q-GFP; n = 7,648, HeLa, Htt97Q-GFP; n = 12,465, HeLa, Htt97Q. For the fibril density analysis, statistical significance was calculated by ANOVA analysis with Bonferroni post hoc-test. The distributions of ER membrane curvature in the vicinity of inclusions and in control cells were compared by the Kolmogorov–Smirnov test. The red line in Figure S2D was calculated as the IB/control ratio of curvedness for each bin and smoothed using robust LOESS. ER dynamics were analyzed in 44 cells from 2 independent experiments. The analysis included all cells in which IB size was in the range of those observed by cryo-ET, which was the case for the large majority of IB-containing cells.

DATA AND SOFTWARE AVAILABILITY

The MATLAB and Python scripts used to calculate the density of membrane-bound ribosomes and measure ER membrane curvature are available at https://github.com/anmartinezs/polyqIB.

The MATLAB scripts used for the analysis of light microscopy data and quantification of fibril persistence length and ER membrane curvature measurements are available at https://github.com/FJBauerlein/Huntington.

Cell

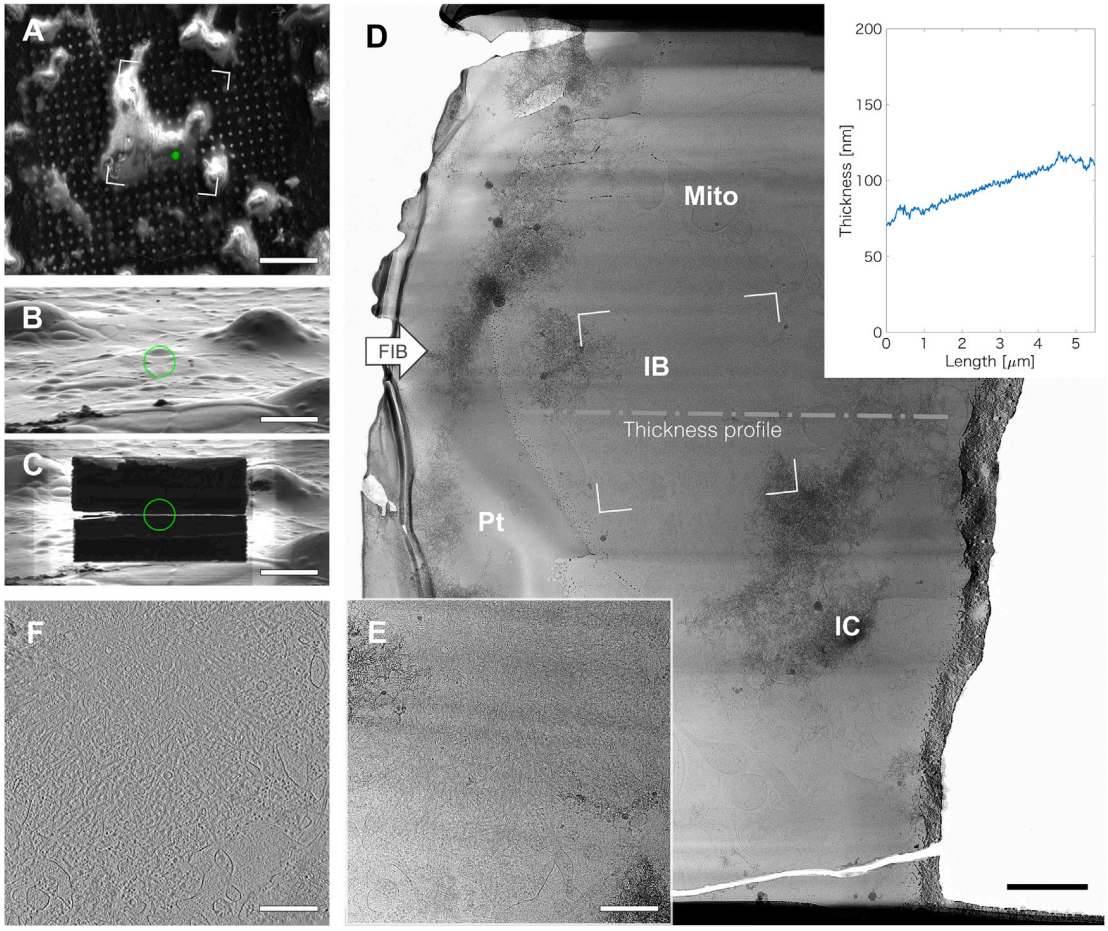

Figure S1. Correlative Light and Electron Microscopy Workflow, Related to Figure 1

(A) Lamellas were prepared in a dual beam focused ion beam/scanning electron microscope (SEM). (A) shows an overlay of live cell imaging and cryo-SEM images of primary neurons growing on an EM grid and containing an Htt97Q-GFP IB (green). Scale bar, 50 μm.

(B and C) Side view of (A) imaged with the ion beam with low current before (B) and after (C) lamella preparation. Green circles mark the coordinates of the IB obtained from correlation with the light microscopy image. The SEM and ion beam images are taken from different angles dictated by the geometry of the electron and ion columns within the microscope chamber. With low currents, the ion beam generates secondary electrons that can be used for imaging (B, C). With higher currents, the ion beam removes material from the cell allowing lamella production (C). Scale bars, 5 μm.

(D) Lamellas were transferred to a cryo-transmission electron microscope (TEM) for high-resolution imaging. (D) displays a TEM overview of the lamella shown in (C). The lamella is a slab of the cell, and therefore appears as a line when imaged from the milling direction with the ion beam (C), or as a plane when imaged in the TEM (D) from an angle roughly perpendicular to the milling direction (arrow). IC, ice crystal contamination deposited on top of the lamella; Mito, mitochondria; Pt, remainder of the organometallic platinum layer evaporated on the cells prior to FIB milling. Scale bar, 1 μm. Inset: Thickness profile along the line marked in the main panel, calculated from the intensity ratio between images recorded with and without energy filtering.

(E) Magnification of the region boxed in (D) containing the Htt97Q-GFP IB.

(F) 2.5 nm-thick slice of a tomogram recorded in the region shown in (E). Scale bars, 500 nm in (E) and (F).

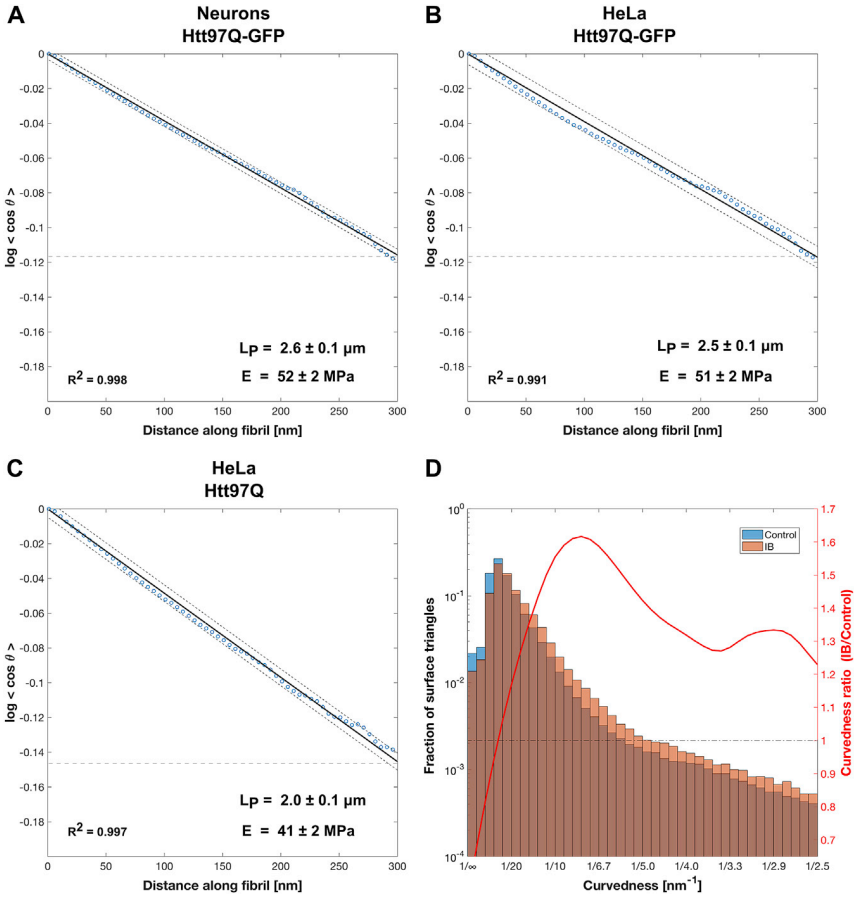

Figure S2. Analysis of PolyQ Fibril Persistence Length and ER Membrane Curvature, Related to Figures 1, 2, and 3

(A–C) Linear fit for the total persistence length for all tomograms analyzed (Number of fibrils: n = 11,481, neurons; Htt97Q-GFP; n = 7,648, HeLa; Htt97Q-GFP; n = 12,465, HeLa; Htt97Q; 4 tomograms for all conditions). The blue circles represent the original data. 95% confidence interval (dotted lines) and the values of the persistence length (L_p), Young's modulus (E) and coefficients of determination (R^2) are indicated. The dashed horizontal lines mark the values of the fitting line at a distance along the filament of 300 nm as indication of the slope of the line, from which L_p is calculated. Note that the values are almost identical for Htt97Q-GFP in HeLa cells and neurons, but different from Htt97Q in HeLa cells.

(D) Histograms of ER membrane curvedness values as a measure of curvature. Curvedness was calculated for ER membranes in the vicinity of inclusions (n = 4 tomograms, including two Htt97Q inclusions in HeLa cells, one Htt97Q-GFP IB in a neuron and one Htt64Q-GFP IB in a HeLa cell) and in control conditions (n = 3 tomograms, including one of a Htt97Q-GFP IB-containing HeLa cell in an area distal from the IB, one of a HeLa cell expressing diffuse Htt97Q-GFP without visible IB and one of a HeLa cell expressing non-pathogenic Htt25Q-GFP; see Figure S4). The distributions of curvedness around inclusions and in control cells were significantly different ($p < 0.001$ by Kolmogorov–Smirnov test). The red line shows the ratio between ER membrane curvatures around inclusions and in control cells. Note that sites with curvatures above 1/10 nm^{-1} were 20%–60% more abundant in the vicinity of inclusions.

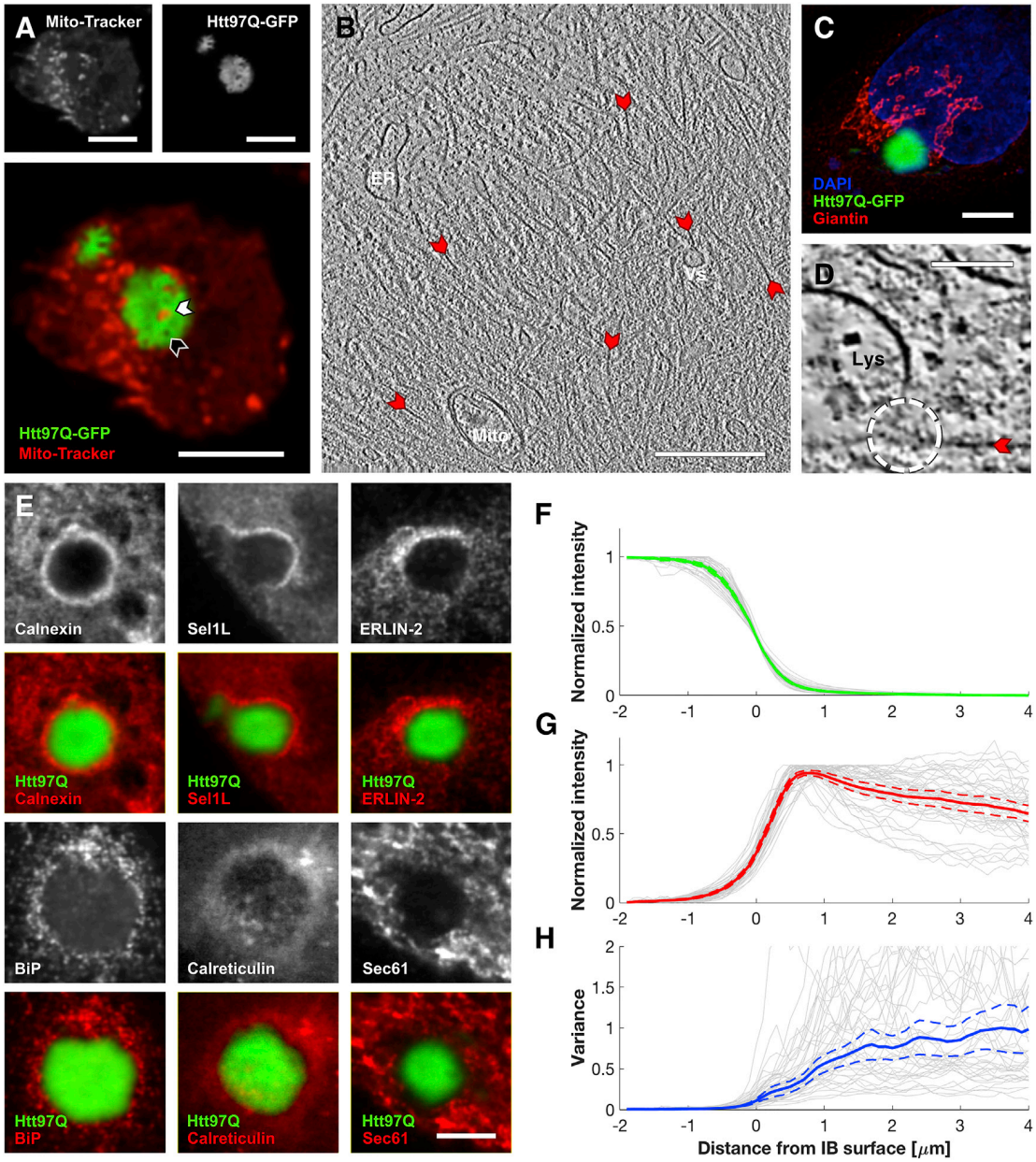

Figure S3. Interactions of Htt97Q-GFP Inclusions with Various Organelles in HeLa Cells, Related to Figures 3 and 4

(A) HeLa cell expressing Htt97Q-GFP (green) and loaded with Mito-Tracker (red). Note the mitochondria-positive structure inside the IB (white arrowhead). Other empty regions inside the IB are Mito-Tracker negative (black arrowhead) and may correspond to other organelles. Scale bars, 5 μm.

(B) Tomographic slice showing a mitochondrion (Mito) embedded inside an IB in an Htt97Q-GFP-transfected HeLa cell. ER, endoplasmic reticulum; red arrowheads, Htt97Q-GFP fibrils; Vs, vesicle. Scale bar, 250 nm.

(C) HeLa cell expressing Htt97Q-GFP (green) and stained with antibodies against the Golgi marker giantin (red). Scale bar, 5 μm.

(D) Tomographic slice on the interaction (white circle) between an Htt97Q-GFP fibril and the membrane of a lysosome (Lys). Scale bar, 100 nm.

(E) HeLa cells expressing Htt97Q-GFP (green) and stained with antibodies against the ER proteins (red) calnexin, SEL1L, ERLIN2, BiP, calreticulin and Sec61. Scale bar, 5 μm.

(F–H) Individual traces (gray), radial averages (solid lines) and 95% confidence intervals (dashed lines) of Htt97Q-GFP IB intensity (F), KDEL-mCherry ER intensity (G) and the variance of KDEL-mCherry intensity over time (H) for all live cell movies analyzed (n = 44) in Figure 4E. Tomographic slices are 2.5 nm (B) or 1.7 nm (D) thick.

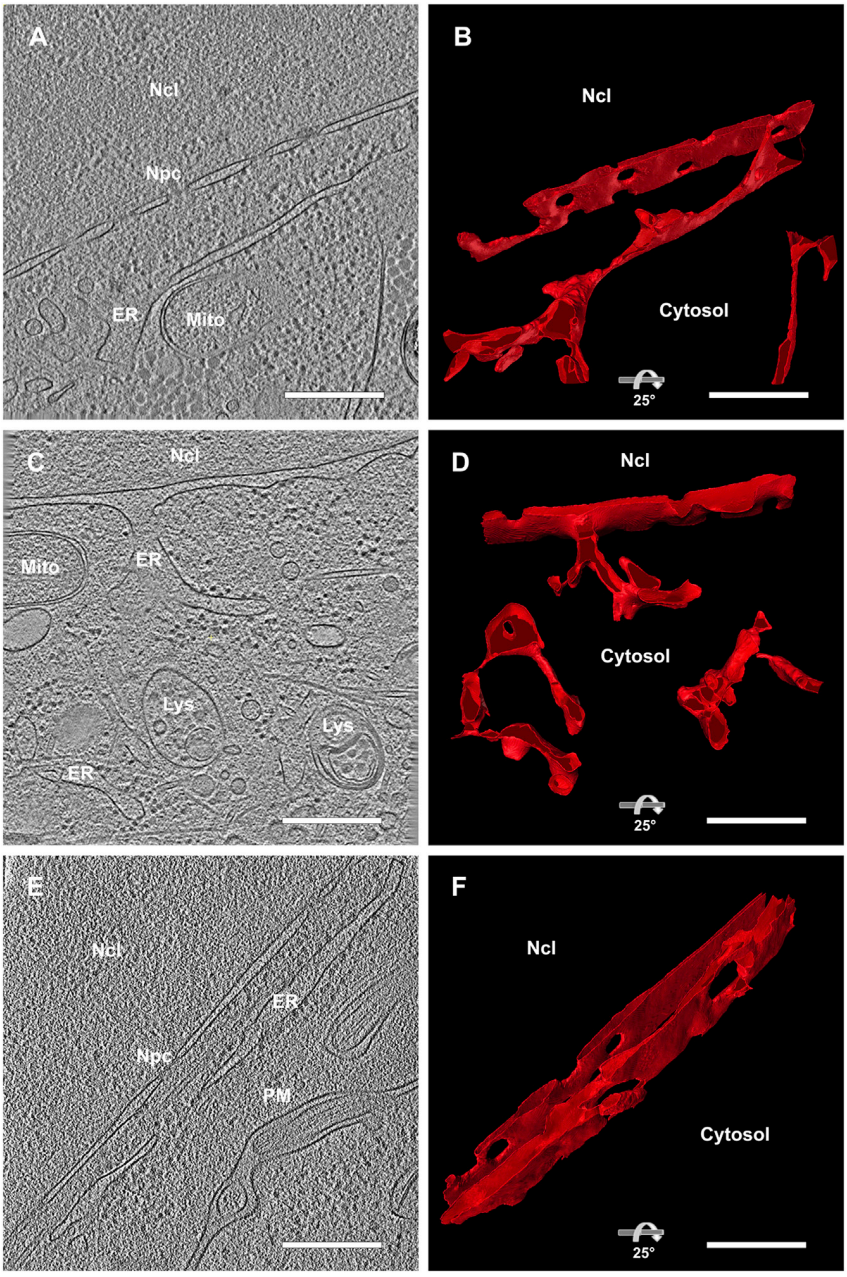

Figure S4. Normal Perinuclear ER Morphology in HeLa Cells in the Absence of PolyQ Inclusions, Related to Figures 1, 2, and 3

(A) Tomographic slice of an area of the nuclear periphery distal from the IB in a HeLa cell containing an Htt97Q-GFP IB.

(C) Tomographic slice of the nuclear periphery of a HeLa cell expressing diffuse Htt97Q-GFP and no visible IB.

(E) Tomographic slice of the nuclear periphery of a HeLa cell expressing Htt25Q-GFP.

(B, D, F) 3D renderings of the tomograms shown in (A), (C), and (E) respectively, tilted 25° along the x axis. ER membranes (red). In all cases, note the smooth ER membranes, in contrast to the deformed ER membranes observed in the vicinity of polyQ inclusions (Figures 1, 2, and 3). ER, Endoplasmic reticulum; Lys, Lysosome; Mito, Mitochondria; Ncl, Nucleus, Npc: nuclear pore complex, PM: plasma membrane. Tomographic slices are 2.5 nm thick. Scale bars, 400 nm. The number of experiments and cells analyzed per condition is shown in Table S1.

2.2 Tricalbin-mediated contact sites control ER curvature to maintain plasma membrane integrity

Javier Collado, Maria Kalemanov*, Felix Campelo*, Clélia Bourgoint*, Ffion Thomas, Robbie Loewith, Antonio Martínez-Sánchez, Wolfgang Baumeister, Christopher J. Stefan & Rubén Fernández-Busnadiego, ***Dev Cell***, 51: 476-487, 2019, DOI, URL.
* These authors contributed equally

Summary

MCS control lipid exchange in all eukaryotic cells. As most PM lipids are synthesized in the ER, ER-PM MCS are critical modulators of lipid homeostasis, and their disruption is linked to multiple diseases. ER-PM MCS are particularly abundant in yeast, where several tethering proteins are important for cER formation, especially Ist2, Scs2/22 and Tcb1/2/3. Deletion of all six proteins largely reduces the extent of ER-PM MCS. Here, we investigated the effects of these tethers on the cER morphology using cryo-ET with new computational methods, functional assays and theoretical modeling.

We observed that the cER of wild-type (WT) cells had a variable morphology with both sheets and tubules and a broad distribution of distances to PM and luminal thicknesses. Cells expressing only Ist2 or Scs2/22 still had substantial total levels of cER, whereas Tcb1/2/3-only cell had markedly less cER than the WT. The cER morphology was similar to WT in Ist2-only cells but with slightly shorter ER-PM distances, whereas it was strikingly different in Scs2/22-only cells, which consisted almost exclusively of extended and significantly narrower sheets but had a broader range of ER-PM distances. In Tcb1/2/3-only cells, cER contained mostly tubules and the overall ER-PM distance was significantly shorter. Estimated cER membrane curvature was significantly lower in Scs2/22-only cells but higher in Tcb1/2/3 cells.

Peaks of very high curvature were found on the cER membrane side facing the PM: occasionally in WT, more frequently in Tcb1/2/3-only cells but not in the other mutants lacking Tcb1/2/3. Peaks with comparable morphology and frequency to WT were found in *tcb1*Δ and *tcb2*Δ, but not in *tcb3*Δ and *tcb1/2*Δ cells. Thus, Tcb3 and either Tcb1 or Tcb2 are necessary for the formation of cER peaks. As Tcbs contain C2 domains that can induce membrane curvature and SMP domain that can transport lipids, Tcbs could reduce the cER-to-PM distance and disturb the cER lipid bilayer in order to facilitate lipid extraction, as confirmed by modeling. It was shown that both SMP and C2 domains are required for cER peak formation. Upon heat stress, PM integrity was compromised in all mutants lacking cER peaks, but not in WT cells, thanks to the increase in the density of cER peaks. We propose the following model: upon heat stress, Ca^{2+} enters the cells through the damaged PM and induces cER peak formation, which increase the lipid transfer from cER to PM, enabling its repair.

Author contribution

To investigate cER morphology, I developed methods for membrane curvature determination and intermembrane distances measurements and applied them to the experimental cryo-ET data. I performed statistical analysis of the measurements, including cER peak morphology and density as well as PM integrity assays, and visualized the results. Finally, I contributed to writing and revising the manuscript.

Article

Developmental Cell

Tricalbin-Mediated Contact Sites Control ER Curvature to Maintain Plasma Membrane Integrity

Graphical Abstract

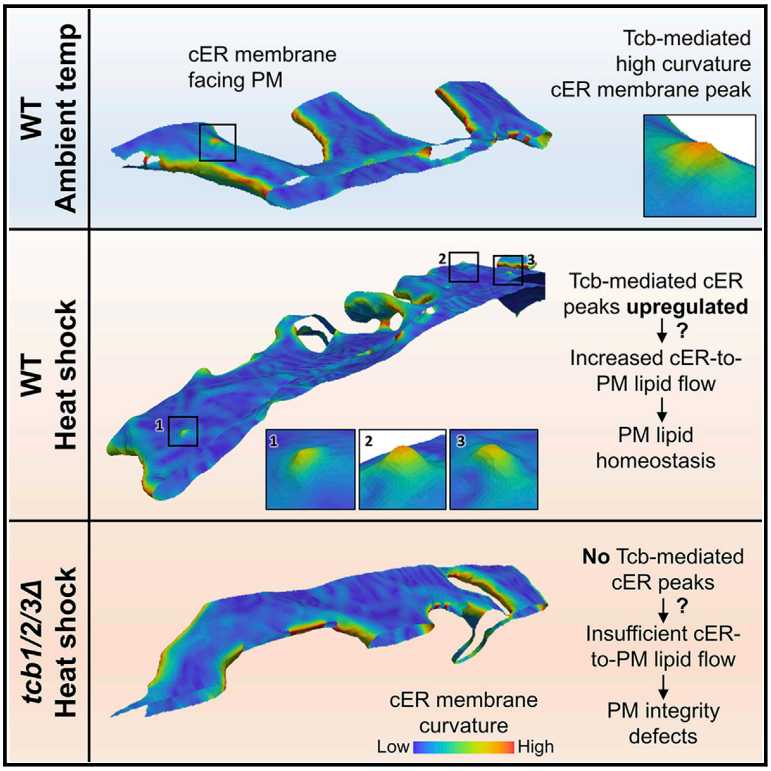

Highlights

- Tethers of ER-plasma membrane (PM) contact sites shape cortical ER (cER) morphology
- Tricalbins create peaks of extreme curvature on the cER membrane facing the PM
- cER peaks are important to maintain PM integrity under heat stress
- cER peaks may facilitate ER-to-PM lipid transport

Authors

Javier Collado, Maria Kalemanov, Felix Campelo, ..., Wolfgang Baumeister, Christopher J. Stefan, Rubén Fernández-Busnadiego

Correspondence

ruben.fernandezbusnadiego@med.uni-goettingen.de

In Brief

Using cryo-electron tomography, Collado et al. show that tricalbins generate peaks of extreme curvature on the cortical ER (cER) membrane at ER-plasma membrane (PM) contact sites. Functional assays and theoretical modeling indicate that cER peaks are important to maintain PM integrity under heat stress, possibly by facilitating cER-to-PM lipid transport.

Collado et al., 2019, Developmental Cell *51*, 476–487
November 18, 2019
https://doi.org/10.1016/j.devcel.2019.10.018

CellPress

CellPress

Developmental Cell
Article

Tricalbin-Mediated Contact Sites Control ER Curvature to Maintain Plasma Membrane Integrity

Javier Collado,[1,2,3] Maria Kalemanov,[1,3,9] Felix Campelo,[4,9] Clélia Bourgoint,[5,9] Ffion Thomas,[6] Robbie Loewith,[5,7] Antonio Martínez-Sánchez,[1] Wolfgang Baumeister,[1] Christopher J. Stefan,[6] and Rubén Fernández-Busnadiego[1,2,8,10,*]

[1]Department of Molecular Structural Biology, Max Planck Institute of Biochemistry, Martinsried 82152, Germany
[2]Institute of Neuropathology, University Medical Center Göttingen, Göttingen 37099, Germany
[3]Graduate School of Quantitative Biosciences Munich, Munich 81337, Germany
[4]ICFO, Institut de Ciencies Fotoniques, The Barcelona Institute of Science and Technology, Castelldefels 08860, Spain
[5]Department of Molecular Biology, University of Geneva, Geneva 1211, Switzerland
[6]MRC Laboratory for Molecular Cell Biology, University College London, London, WC1E 6BT, UK
[7]Swiss National Centre for Competence in Research, Program Chemical Biology, Geneva 1211, Switzerland
[8]Cluster of Excellence "Multiscale Bioimaging: from Molecular Machines to Networks of Excitable Cells" (MBExC), University of Göttingen, Göttingen, Germany
[9]These authors contributed equally
[10]Lead Contact
*Correspondence: ruben.fernandezbusnadiego@med.uni-goettingen.de
https://doi.org/10.1016/j.devcel.2019.10.018

SUMMARY

Membrane contact sites (MCS) between the endoplasmic reticulum (ER) and the plasma membrane (PM) play fundamental roles in all eukaryotic cells. ER-PM MCS are particularly abundant in *Saccharomyces cerevisiae*, where approximately half of the PM surface is covered by cortical ER (cER). Several proteins, including Ist2, Scs2/22, and Tcb1/2/3 are implicated in cER formation, but the specific roles of these molecules are poorly understood. Here, we use cryo-electron tomography to show that ER-PM tethers are key determinants of cER morphology. Notably, Tcb proteins (tricalbins) form peaks of extreme curvature on the cER membrane facing the PM. Combined modeling and functional assays suggest that Tcb-mediated cER peaks facilitate the transport of lipids between the cER and the PM, which is necessary to maintain PM integrity under heat stress. ER peaks were also present at other MCS, implying that membrane curvature enforcement may be a widespread mechanism to regulate MCS function.

INTRODUCTION

Endoplasmic reticulum (ER)-plasma membrane (PM) membrane contact sites (MCS) are critical modulators of Ca^{2+} and lipid homeostasis in eukaryotic cells (Balla, 2018; Chang et al., 2017; Cockcroft and Raghu, 2018; Saheki and De Camilli, 2017a; Stefan, 2018). These structures, where the ER and the PM come into close apposition (10 – 30 nm), mediate store-operated Ca^{2+} entry (Carrasco and Meyer, 2011), insulin secretion by pancreatic beta cells (Lees et al., 2017), and excitation-contraction coupling in striated muscle (Bers, 2002). Consequently, dysregulation of ER-PM MCS is linked to multiple human diseases (Lacruz and Feske, 2015; Landstrom et al., 2014; Ríos et al., 2015).

ER-PM MCS are particularly abundant in the yeast *Saccharomyces cerevisiae*, where nearly half of the PM surface area is covered by cortical ER (cER) (Manford et al., 2012; Pichler et al., 2001; Quon et al., 2018; Toulmay and Prinz, 2012; West et al., 2011). The loss of six proteins (Ist2, Scs2/22, and Tcb1/2/3; "Δtether" cells) dramatically reduces the extent of ER-PM association, indicating that these proteins are important ER-PM tethers (Manford et al., 2012). Additional proteins, including Ice2 and the yeast StARkin orthologs, are also implicated in cER-PM function in *S. cerevisiae* (Gatta et al., 2015; Quon et al., 2018). Loss of cER triggers PM lipid imbalance (Manford et al., 2012; Quon et al., 2018), highlighting the physiological importance of these membrane junctions.

Ist2 is a member of the anoctamin/TMEM16 protein family (Whitlock and Hartzell, 2017). Ist2 resides on the ER membrane and consists of eight transmembrane domains plus a long C-terminal cytoplasmic tail that binds PM lipids (Figure 2A), thereby tethering the ER and the PM (Fischer et al., 2009; Jüschke et al., 2005; Maass et al., 2009; Manford et al., 2012). Deletion of Ist2 results in reduced cER levels, whereas Ist2 overexpression leads to increased ER-PM MCS (Manford et al., 2012; Wolf et al., 2012).

Scs2/22 are orthologs of the mammalian VAMP-associated proteins (VAPs), a family of ER-resident proteins widely implicated in MCS formation (Murphy and Levine, 2016; Stefan et al., 2011). Both Scs2 and Scs22 are C-terminally anchored to the ER by a transmembrane segment and contain an N-terminal major sperm protein (MSP) domain (Figure 2A). Scs2/22 function as ER-PM tethers thanks to the binding of their MSP domain to PM proteins containing FFAT or FFAT-like motifs (Manford et al., 2012; Murphy and Levine, 2016). A strong reduction in cER levels is observed in Scs2/22 knockout (KO) cells (Loewen et al., 2007; Manford et al., 2012).

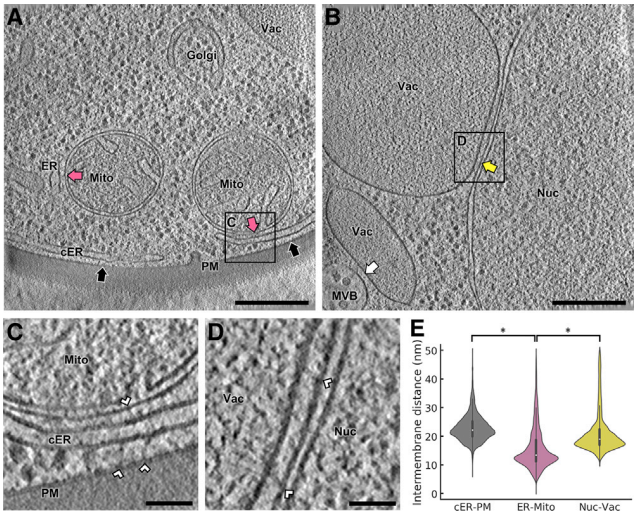

Figure 1. Cryo-ET Imaging of MCS in WT *S. cerevisiae*

(A) 1.4 nm-thick tomographic slice showing cER-PM MCS (black arrows) and ER-mitochondria MCS (purple arrows). The boxed area is magnified in (C). ER: endoplasmic reticulum; cER: cortical ER; Golgi: Golgi apparatus; Mito: mitochondrion; PM: plasma membrane; Vac: vacuole.

(B) 1.4 nm-thick tomographic slice showing a nucleus-vacuole junction (yellow arrow) and a multivesicular body-vacuole MCS (white arrow). The boxed area is magnified in (D). MVB: multivesicular body; Nuc: nucleus.

(C) Magnification of the area boxed in (A). White arrowheads: intermembrane tethers.

(D) Magnification of the area boxed in (B).

(E) Violin plots showing the distribution of intermembrane distances of cER-PM, ER-mitochondrion and nucleus-vacuole MCS. The plots show the complete distribution of values including all MCS analyzed. A white dot represents the median, a black slab the interquartile range, and a black line 1.5x the interquartile range. * indicates $p < 0.05$ by unpaired t test. N = 6 (cER-PM), 5 (ER-mitochondria) and 5 (nucleus-vacuole) MCS in WT cells. Scale bars: 300 nm (A, B), 50 nm (C, D). See also Figure S2; Table S1.

The tricalbin proteins (Tcb1/2/3) are orthologs of the mammalian extended-synaptotagmins (E-Syts) and the plant synaptotagmins (SYTs) (Pérez-Sancho et al., 2016; Saheki and De Camilli, 2017b). Tcbs are likely anchored to the ER membrane by a hairpin sequence (Giordano et al., 2013; Saheki and De Camilli, 2017b) (Figure 2A) similar to those found in ER morphogenetic proteins such as reticulons (Hu et al., 2011). Tcbs harbor a synaptotagmin-like, mitochondrial, and lipid-binding protein (SMP) domain that can bind and transport lipids (Lee and Hong, 2006; Saheki et al., 2016; Schauder et al., 2014; Toulmay and Prinz, 2012; Yu et al., 2016). SMP domains have been found in multiple MCS-resident proteins and likely play a key role in the intermembrane exchange of lipids at these sites (Reinisch and De Camilli, 2016). C-terminal to the SMP domain, Tcbs contain a variable number of C2 domains (four in Tcb1/2 and five in Tcb3), some of which can bind membrane phospholipids in a manner either dependent upon or independent of Ca^{2+} (Creutz et al., 2004; Rizo and Südhof, 1998; Schulz and Creutz, 2004). Both the SMP and the C2 domains are required for Tcb targeting to ER-PM MCS (Manford et al., 2012; Toulmay and Prinz, 2012), and tethering likely takes place via PM binding by C2 domains (Giordano et al., 2013).

Although Ist2, Scs2/22, and Tcb1/2/3 are involved in the appropriate formation of cER, the exact functions of these proteins at ER-PM MCS are poorly understood. First, whereas Ist2 and Scs2/22 are important ER-PM tethers, their relative contributions to cER generation remain unclear. The functions of Tcbs are even more mysterious: Tcbs are bona fide ER-PM tethers, because cER levels are significantly higher in mutants expressing Tcbs but lacking Ist2 and Scs2/22 than in Δtether cells (Manford et al., 2012). However, loss of Tcbs on their own does not result in a substantial reduction in the amount of cER (Manford et al., 2012; Toulmay and Prinz, 2012), suggesting that the main role of Tcbs is not the mechanical anchoring of the ER to the PM. More broadly, the physiological functions of the mammalian E-Syts remain similarly unclear (Sclip et al., 2016; Tremblay and Moss, 2016), although their capacity to shuttle lipids at ER-PM MCS has been demonstrated (Bian et al., 2018; Saheki et al., 2016; Yu et al., 2016).

Here, we aimed to dissect the functional roles of Ist2, Scs2/22, and Tcb1/2/3 at ER-PM MCS. To this end, we used cryo-electron tomography (cryo-ET) to study the fine structure of the cER within mutant cells lacking specific tethers. Thanks to the advent of cryo-focused ion beam (cryo-FIB) technology and direct electron detectors, cryo-ET allows high resolution 3D imaging of a virtually unperturbed cell interior at molecular resolution (Beck and Baumeister, 2016; Rigort et al., 2012; Wagner et al., 2017). Given the narrow intermembrane space of MCS, these structures are particularly sensitive to alterations introduced by classical EM procedures such as chemical fixation, dehydration, and heavy-metal staining, which can alter membrane morphology. Therefore, cryo-ET is especially suited for the high-resolution study of native MCS architecture (Collado and Fernández-Busnadiego, 2017; Fernández-Busnadiego et al., 2015). Our results show that, besides simply anchoring the ER to the PM, each family of tethers uniquely contributes to shaping the cER. In particular, Scs2/22 are associated with cER sheets, whereas Tcbs favor cER tubules. Notably, Tcbs are necessary for the generation of peaks of extreme curvature at the cER membrane that contribute to maintaining PM integrity, possibly by facilitating the transport of cER lipids to the PM.

RESULTS

MCS Architecture in *S. cerevisiae*

To study MCS architecture *in situ* by cryo-ET, *S. cerevisiae* cells were vitrified on EM grids and thinned down to 100–200-nm-thick lamellae using cryo-FIB. Lamellae were loaded into a cryo-TEM (Figure S1), and tomograms were acquired at suitable cellular locations. Cryo-tomograms of various MCS (Figures 1A and 1B) revealed abundant proteinaceous densities of diverse morphologies bridging the gap between the membranes (Figures 1C and 1D; Figure S2A). Interestingly, distance measurements showed a characteristic intermembrane spacing for different MCS. For example, while average nucleus-vacuole distance was 21 ± 7 nm (mean ± STD, N = 5 nucleus-vacuole MCS; Figure 1E), ER-mitochondria junctions were significantly narrower (16 ± 7 nm; mean ± STD, N = 5 ER-mitochondria MCS; $p < 0.05$ by unpaired t test; Figure 1E).

To gain further insights into the molecular determinants of MCS structure and function, we focused on ER-PM MCS,

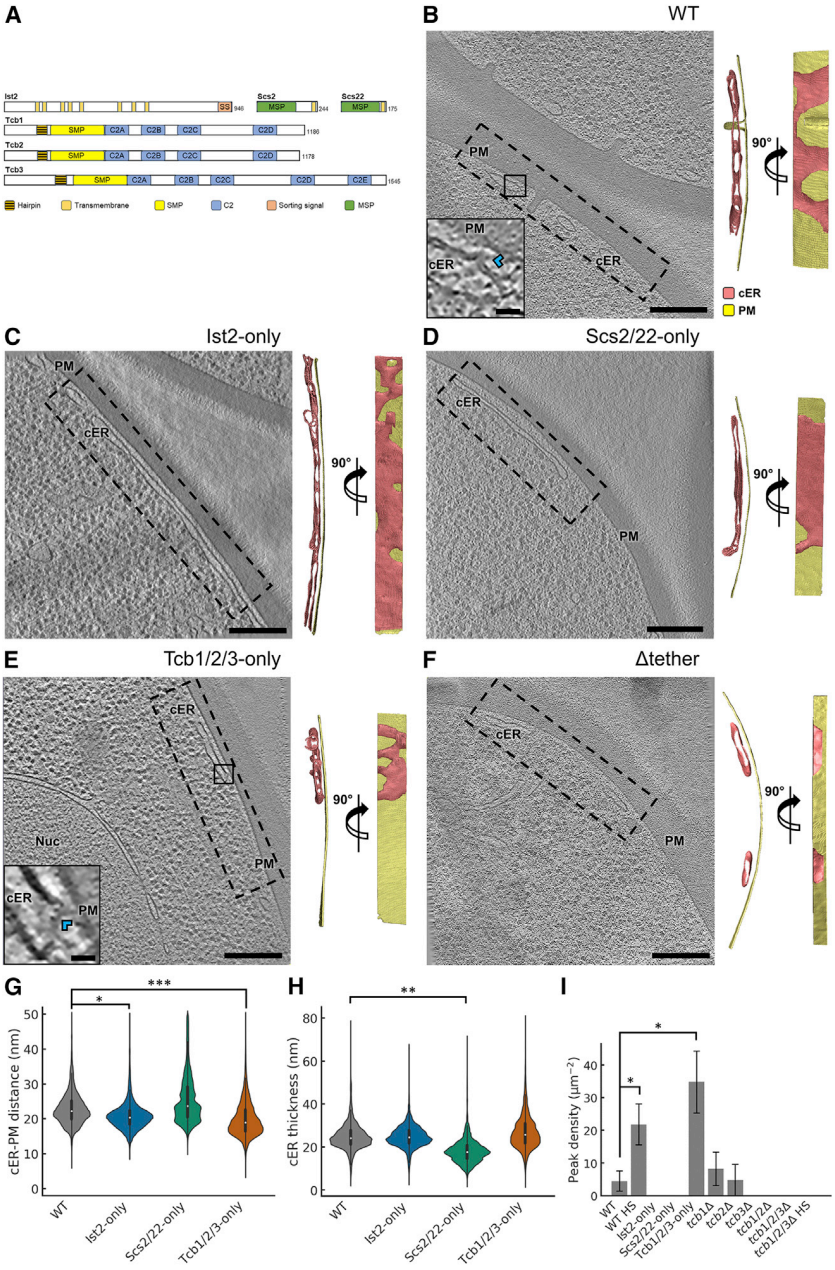

Figure 2. cER Morphology in ER-PM MCS Tether Mutants

(A) Domain structure of the main ER-PM tethers. Ist2 is an ER multipass transmembrane protein with a long and presumably unstructured cytosolic tail. The C-terminal sorting signal (SS) binds the PM. Scs2 and Scs22 are ER transmembrane proteins containing an N-terminal MSP domain. Tcb proteins are anchored to the ER membrane by a hairpin sequence. In their cytoplasmic C-terminus, Tcbs contain an SMP domain and a variable number of C2 domains. Panels B through F show 1.4-nm-thick tomographic slices of cER in the indicated strains (left) and 3D renderings in two perpendicular orientations upon a 90° rotation along an axis parallel to the PM (right). cER: cortical ER (pink); Nuc: nucleus; PM: plasma membrane (gold). (B) WT cell, (C) Ist2-only cell, (D) Scs2/22-only cell, (E) Tcb1/2/3-only cell, (F) Δtether cell. Insets in (B) and (E) show cER peaks (blue arrowheads). Scale bars: 300 nm (main panels); 25 nm (insets). Panels G, H, and I show quantifications of cER-PM distance (G), cER thickness (H) and cER peak density per μm^2 of cER membrane area (I). In G and H the violin plots show the complete distribution of values for all MCS analyzed. A white dot represents the median, a black slab the interquartile range, and a black line 1.5 times the interquartile range. Panel I shows average values (gray bars) and SE (error bars). HS: heat shock (42°C for 10 min). *, **, and *** indicate, respectively, $p < 0.05$, $p < 0.01$ and $p < 0.01$ by unpaired t test (G, H) or Mann-Whitney U test (I). N = 6 (WT), 7 (WT HS), 5 (Ist2-only), 5(Scs2/22-only), 9 (Tcb1/2/3-only), 5 (*tcb1Δ*), 5 (*tcb2Δ*), 5 (*tcb3Δ*), 5 (*tcb1/2Δ*), 5 (*tcb1/2/3Δ*), and 5 (*tcb1/2/3Δ* HS) cER-PM MCS. See also Figures S1 and S2; Table S1.

perhaps the most abundant MCS in *S. cerevisiae* (Manford et al., 2012; Pichler et al., 2001; Quon et al., 2018; West et al., 2011). Cryo-ET analysis showed that the cER of wild-type (WT) cells consisted of both membrane sheets and tubules (Figure 2B), with an average thickness of 24 ± 6 nm (mean ± STD, N = 6 cER-PM MCS; Figure 2H). For 95% of the MCS area, ER-PM distance ranged from 16 to 34 nm, with an average of 23 ± 5 nm (mean ± STD; Figures 1E and 2G). Thus, in WT cells the cER had a variable morphology and a relatively broad distribution of distances to the PM.

ER-PM Tethers Control cER Morphology

Because the simultaneous deletion of Ist2, Scs2/22, and Tcb1/2/3 largely abolishes ER-PM MCS (Manford et al., 2012), we sought to understand the individual contribution of each of these protein families to ER-PM tethering. To that end, we performed cryo-ET imaging of ER-PM MCS in mutant cells expressing only one family of tethers. These data confirmed previous observations (Loewen et al., 2007; Manford et al., 2012; Toulmay and Prinz, 2012; Wolf et al., 2012) that total levels of cER were still substantial in cells expressing only Ist2 (*scs2/22Δ tcb1/2/3Δ*; "Ist2-only" cells; Figure S1B) or the VAP orthologues Scs2 and Scs22 (*ist2Δ tcb1/2/3Δ*; "Scs2/22-only" cells; Figure S1C). However, cER levels in cells expressing only Tcb1/2/3 (*ist2Δ scs2/22Δ*; "Tcb1/2/3-only" cells; Figure S1D) were markedly lower than in WT (Figure S1A), although higher than in Δtether cells (Figure S1E), in agreement with previous results (Manford et al., 2012).

Next, we investigated the fine morphology of the cER in these mutants. In Ist2-only cells, the cER was a mixture of membrane sheets and tubules similar to WT cells (Figures 2B and 2C). Although average ER-PM distance was slightly shorter than WT (21 ± 4 nm, mean ± STD, N = 5 cER-PM MCS; $p < 0.05$ by unpaired t test; Figure 2G), cER thickness (25 ± 6 nm, mean ± STD; Figure 2H) was comparable to WT, suggesting that Ist2 is

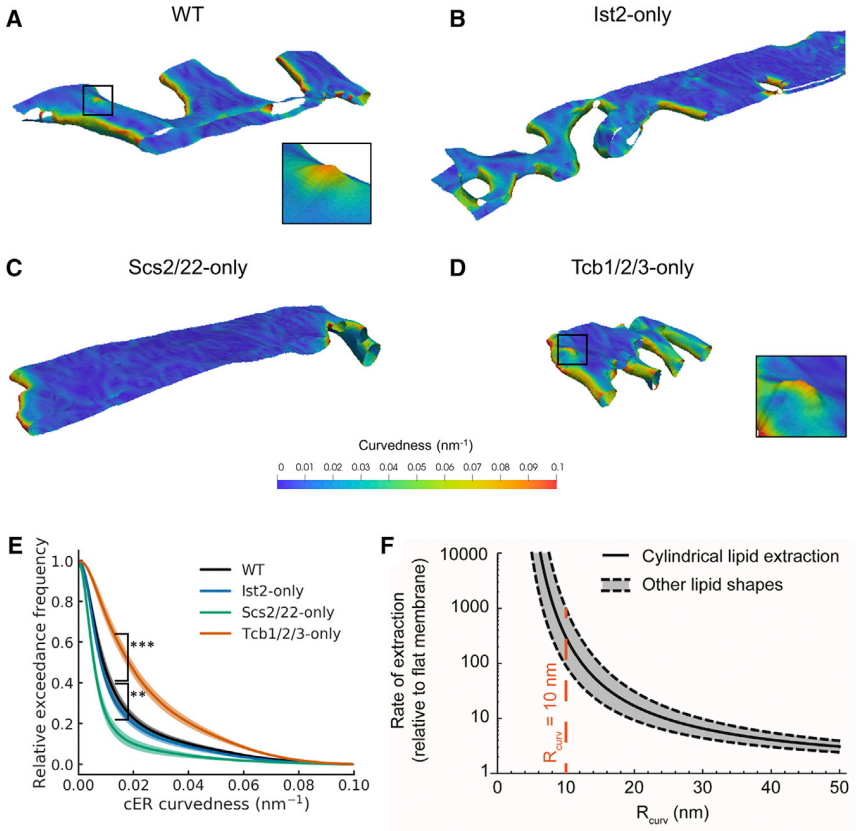

Figure 3. Quantification of cER Curvature

(A–D) 3D visualizations of cER curvedness in the indicated strains. Insets in (A) and (D) show cER peaks. (A) WT cell, (B) Ist2-only cell, (C) Scs2/22-only cell, (D) Tcb1/2/3-only cell. (E) Quantification of cER curvedness, shown as an exceedance plot. The shaded lines represent the average across all MCS ± SE for each bin (1 nm^{-1}.). ** and *** indicate, respectively, $p < 0.01$ and $p < 0.001$ by unpaired t test. N = 6 (WT), 7 (WT HS), 5 (Ist2-only), 5 (Scs2/22-only), and 9 (Tcb1/2/3-only) cER-PM MCS. (F) Enhancement of the rate of lipid extraction by membrane curvature according to a theoretical model. The plot shows the rate of extraction computed for a standard cylindrical lipid (black curve) as well as for lipids of other shapes, such as conical or inverted conical lipids (gray-shaded area between the dashed, black curves). The value of the radius of curvature of the experimentally observed cER peaks is denoted by the dashed red line. $1/R_{curv}$ is equivalent to the curvedness for $\kappa_1=\kappa_2$. See also Figures S3 and S4; Table S1.

an important contributor to the morphology of the cER in WT cells.

Interestingly, cER morphology in Scs2/22-only cells was dramatically different from WT. In these mutants, cER tubules were rarely observed, as the cER consisted almost exclusively of extended sheets (Figure 2D). Average ER-PM distance in these cells spread across a wider range of values (26 ± 7 nm, mean ± STD, N = 5 cER-PM MCS; Figure 2G). On the other hand, the ER sheets observed in Scs2/22-only cells were significantly narrower than WT (18 ± 6 nm, mean ± STD; $p < 0.01$ by unpaired t test; Figure 2H). These data show that while Scs2/22 are not very effective in controlling ER-PM distance, they are important determinants of cER width.

In contrast to Scs2/22-only cells, the cER was formed mainly by membrane tubules in Tcb1/2/3-only cells (Figure 2E). Interestingly, in these cells we also observed abundant peaks of very high curvature on the membrane of the cER facing the PM (Figure 2E, inset; Figure S2B). These peaks had a radius of ~10 nm at their base and protruded ~7 nm from the cER membrane (Figure S2C). The cER came into very close proximity of the PM at cER peaks, narrowing to distances of 7–8 nm (Figure S2C). Overall, the average cER-PM distance was significantly shorter in Tcb1/2/3-only (20 ± 5 nm, mean ± STD; N = 9 cER-PM MCS; $p < 0.001$ by unpaired t test; Figure 2G) than in WT cells (23 ± 5 nm, mean ± STD). Whereas cER peaks were not found in Ist2-only (Figures 2C and 2I), Scs2/22-only (Figures 2D and 2I), or Δtether (Figure 2F) cells, they were also present in WT cells, albeit at a lower frequency (Figure 2B, inset; Figure 2I; $p < 0.05$ by Mann-Whitney U test; Figure S2B). The cER peaks in WT cells were morphologically indistinguishable from those found in Tcb1/2/3-only cells (Figure S2C). Therefore, the formation of high curvature peaks at the cER is likely controlled by the Tcb proteins. Because the peaks were only found on the part of the cER membrane opposed to the PM, these structures may be involved in intermembrane exchange.

Altogether, these data show that each of the ER-PM tethers play key and yet distinct roles in controlling cER morphology, especially in terms of membrane curvature.

Quantitative Analysis of cER Membrane Curvature

Membrane curvature plays a major role in a wide variety of cellular processes (Kozlov et al., 2014) and is a fundamental determinant of ER morphology (Hu et al., 2011). Therefore, we further analyzed the cER membrane curvature alterations observed in the different ER-PM tether mutants. To that end, we implemented an algorithm allowing a quantitative determination of membrane curvature in cryo-ET data (Kalemanov et al., 2019). A global analysis was consistent with the visual impression that the average cER curvature observed in Scs2/22-only cells was lower than in WT ($p < 0.01$ by unpaired t test; Figures 3A, 3C, and 3E), indicating the higher prevalence of cER sheets. Conversely, the curvature of the cER membrane in Tcb1/2/3-only cells was significantly higher than WT ($p < 0.001$ by unpaired t test; Figures 3A, 3D, and 3E), reflecting the more tubular cER morphology in these cells. Local mapping of the curvature in cER membrane renderings highlighted the presence of peaks of extreme curvature (curvature radius ≤ 10 nm; Figure 3A, inset) in WT cells. These structures were enriched in Tcb1/2/3-only cells compared to WT (Figure 2I; Figure 3D, inset), and absent in *tcb1/2/3Δ* mutants (N = 5 cER-PM MCS; Figures 2I and 4E) and cells expressing only Scs2/22 or Ist2 (Figures 2I, 3B, and

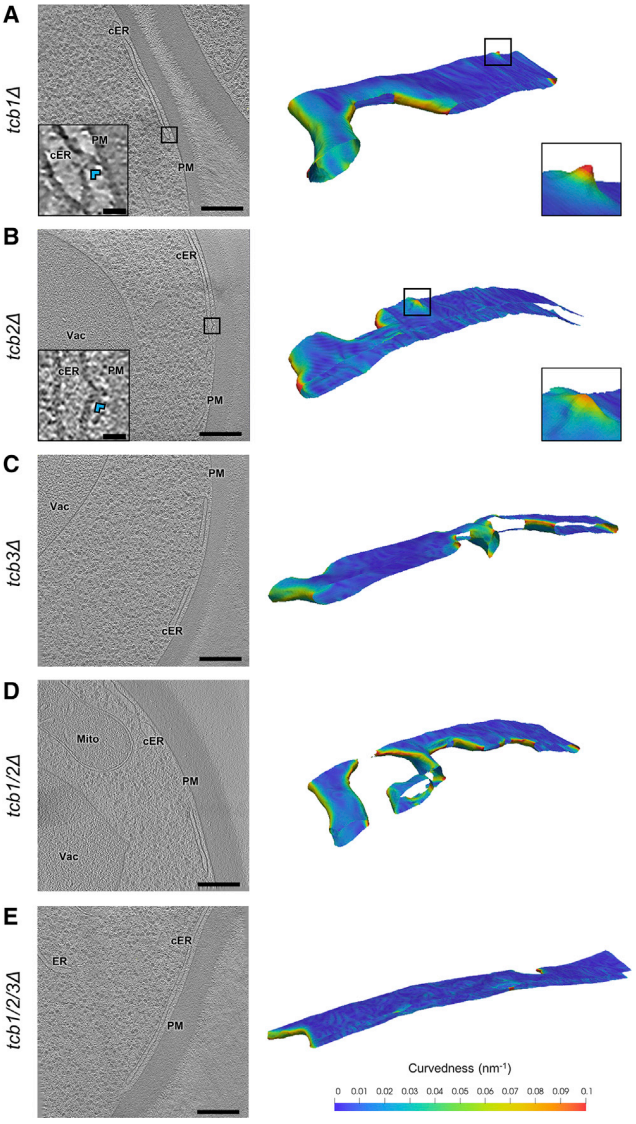

Figure 4. cER Peaks in Tcb Mutants

(A–E) 1.4-nm-thick tomographic slices of cER in the indicated strains (left) and 3D renderings of cER curvature (right). (A) *tcb1Δ*, (B) *tcb2Δ*, (C) *tcb3Δ*, (D) *tcb1/2Δ*, (E) *tcb1/2/3Δ* cell. cER: cortical ER; Mito: mitochondrion; PM: plasma membrane; Vac: vacuole. Insets in (A) and (B) show cER peaks (blue arrowheads). Scale bars for tomographic slices: 300 nm (main panels), 25 nm (insets). See also Figure S2; Table S1.

3C). Therefore, this analysis reinforced the notion that Tcb1/2/3 are necessary for the generation of high curvature peaks on the side of the cER membrane directly facing the PM.

To address the molecular basis of this phenomenon, we next investigated which Tcb proteins were required for cER peak formation by conducting cryo-ET of cells lacking specific Tcbs in the presence of all other ER-PM tethers. In *tcb1Δ* (N = 5 cER-PM MCS; Figures 4A and S2B) and *tcb2Δ* cells (N = 5 cER-PM MCS; Figures 4B and S2B), cER peaks were similar in frequency to WT cells (Figure 2I). cER peaks in these strains were also morphologically comparable to WT (Figure S2C). In contrast, no cER peaks were observed in *tcb3Δ* (N = 5 cER-PM MCS; Figures 2I and 4C) and *tcb1/2Δ* cells (N = 5 cER-PM MCS; Figures 2I and 4D). Therefore, the expression of Tcb3 and either Tcb1 or Tcb2 seems necessary for the efficient formation of cER peaks, consistent with reports that Tcbs (and E-Syts) can form heterodimers (Creutz et al., 2004; Giordano et al., 2013; Idevall-Hagren et al., 2015; Schulz and Creutz, 2004).

cER Peaks May Facilitate Lipid Transfer

Next, we investigated the biological function of Tcb-mediated cER peaks. Tcbs contain modules that can sense or induce membrane curvature (hairpin anchor, multiple C2 domains) and transport lipids (SMP domain) (Creutz et al., 2004; Lee and Hong, 2006; Manford et al., 2012; Martens et al., 2007; Schauder et al., 2014; Toulmay and Prinz, 2012). Tcbs may combine both their curvature-generation and lipid-transport properties by controlling the formation of cER peaks, which could facilitate cER-to-PM lipid transport by (1) reducing the physical distance between cER and PM, and/or (2) disturbing the cER lipid bilayer to facilitate lipid extraction and at the same time imposing cER-to-PM directionality on the transfer process.

To address this possibility, we used a semi-quantitative model (Campelo and Kozlov, 2014) to calculate how the induction of cER membrane curvature may facilitate the lipid-transfer process. We assume that this task is performed by a lipid-transport module such as the SMP domain of Tcbs. The total free energy required for lipid extraction by a lipid-transport protein (LTP) can be expressed as the sum of two components. The first one is independent from membrane geometry, incorporating electrostatic interactions and membrane-independent interactions between the lipid and the LTP. The second component is determined by the elastic stresses imposed on the membrane by its geometry prior to LTP binding, and by how these stresses change as a result of the lipid rearrangements caused by a partial insertion of the LTP into the membrane. In turn, membrane geometry can be determined by its lipid composition and/or by external factors such as curvature-generating proteins (Campelo et al., 2008). We focused on this last scenario, as it is unlikely that physiological lipid compositions result in the extreme membrane curvatures of cER peaks (Campelo et al., 2008; Sorre et al., 2009). With these premises, our calculations showed that the energy barrier for lipid extraction is reduced by ~6 k_BT when the radius of curvature of the membrane is 10 nm (Figure S3), as observed in Tcb-induced cER peaks. This is of similar magnitude to the facilitation of sterol extraction from a flat membrane by an LTP in comparison to its spontaneous desorption, estimated to be ~2–3 k_BT (Dittman and Menon, 2017), and would result in a ~500-fold acceleration of the transfer reaction (Figure 3F). Therefore, our model predicts that cER peaks greatly facilitate lipid extraction by lipid transport modules.

cER Peaks Maintain PM Integrity

The synthesis of certain PM lipids—including phosphatidylinositol, phosphatidylserine, and sterols—is enhanced at the cER (Pichler et al., 2001). Interestingly, *tcb1/2/3Δ* cells show PM integrity defects upon heat stress (Omnus et al., 2016), a situation in which substantial traffic of lipids between the ER and the PM may be necessary to repair heat-induced alterations. Because Tcbs are required for the formation of cER peaks that may facilitate ER-PM lipid transfer, it is possible that cER peaks

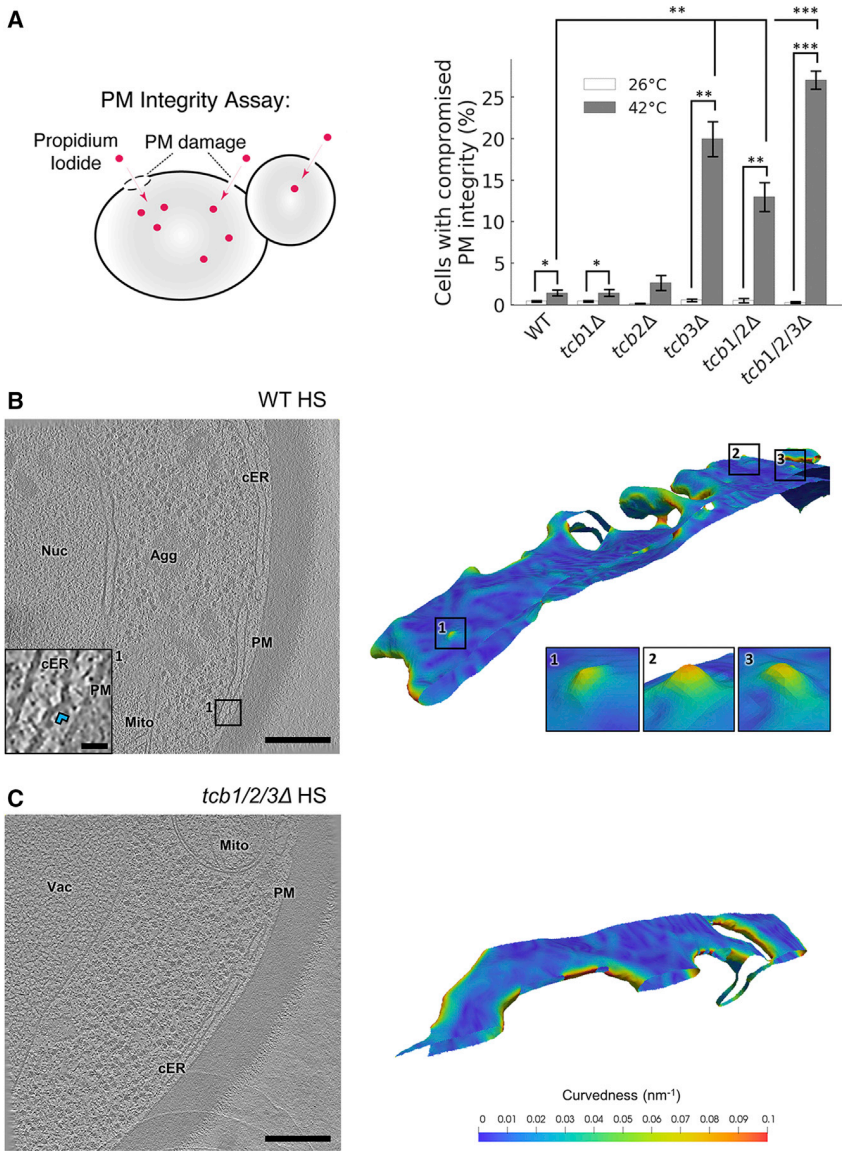

Figure 5. PM Integrity and cER Curvature under Heat Stress

(A) Schematic of the propidium iodide assay to assess PM integrity (left) and PM integrity measurements of Tcb deletion mutants upon 10-min incubation at 42°C (right). The entry of propidium iodide in cells with compromised PM integrity was measured by flow cytometry. The plot shows average values (white/gray bars) for each condition ± SE (error bars). *, **, and ***, respectively, indicate $p < 0.05$, $p < 0.01$, and $p < 0.001$ by Mann-Whitney U test (for *tcb1Δ* 26°C data, which was not normally distributed) or unpaired t test (for all other conditions). Four independent biological repeats were performed for all conditions. (B and C) 1.4-nm-thick tomographic slices of cER in the indicated strains (left) and 3D renderings of cER curvature (right). Agg: aggregate; cER: cortical ER; Mito: mitochondrion; Nuc: nucleus; PM: plasma membrane; Vac: vacuole. (B) WT cell under heat stress (HS). Insets show cER peaks (blue arrowhead in the tomographic slice inset). (C) *tcb1/2/3Δ* cell under heat stress. Scale bars: 300 nm (main panels), 25 nm (inset). See also Figures S2 and S4; Table S1.

are important to maintain PM integrity under heat-stress conditions.

To test this hypothesis, we performed PM integrity assays in the different Tcb mutants. Cells were subjected to 42°C for 10 min, and PM integrity was monitored by measuring the entry of extracellular propidium iodide into cells using flow cytometry (Figure 5A). Because this dye is membrane impermeable, it only enters cells with compromised PM integrity (Zhao et al., 2013). Remarkably, these experiments revealed PM integrity defects for all conditions in which cER peaks were not observed (*tcb3Δ*, *tcb1/2Δ* cells, $p < 0.01$ by unpaired t test; *tcb1/2/3Δ* cells, $p < 0.001$ by unpaired t test; Figure 5A), whereas PM integrity in Tcb mutants showing cER peaks (*tcb1Δ, tcb2Δ*) was comparable to WT. Thus, there was a strong correlation between the absence of Tcb-induced cER peaks and PM integrity defects.

However, the density of cER peaks was relatively low in WT cells under nonstress conditions (Figures 2B, 2I, and 3A); cER peak area was equivalent to 0.15% of the total cER area facing the PM in WT cells. Could these rare structures play an important role in maintaining PM integrity under heat-shock conditions? To address this question, we performed cryo-ET on heat-shocked cells. As expected, cells showed abundant amorphous aggregates in various cellular locations (Miller et al., 2015; Wagner et al., 2017) (Figure 5B). Also, heat-shocked WT cells showed a strong increase in the number of cER peaks (N = 7 cER-PM MCS; $p < 0.05$ by Mann-Whitney U test; Figures 2I and 5B), whereas these structures were absent in heat-shocked *tcb1/2/3Δ* cells (N = 5 cER-PM MCS; Figures 2I and 5C). Therefore, the Tcb-dependent formation of cER peaks is induced by conditions that challenge PM integrity, such as heat shock.

Of note, deletion of all Tcbs (*tcb1/2/3Δ*) did not result in integrity defects as pronounced as Δtether (Figure S4A), and even in the presence of Tcbs, tether mutants with severely impaired cER formation (*scs2/22Δ*, Tcb1/2/3-only; Manford et al., 2012) also suffered from PM integrity defects (Figure S4A). Therefore, non-Tcb enriched areas of the cER may also be important for PM integrity.

We investigated this issue combining theoretical modeling with our experimental measures of peak size and abundance. We assume that the cER membrane is completely flat outside of cER peaks, and that LTPs are homogenously distributed at the cER-PM interface. Taking into account the much higher rate of lipid transfer predicted at cER peaks, our model indicates that the total number of lipids extracted from cER peaks in WT cells (0.15% of total cER membrane area) is roughly equivalent

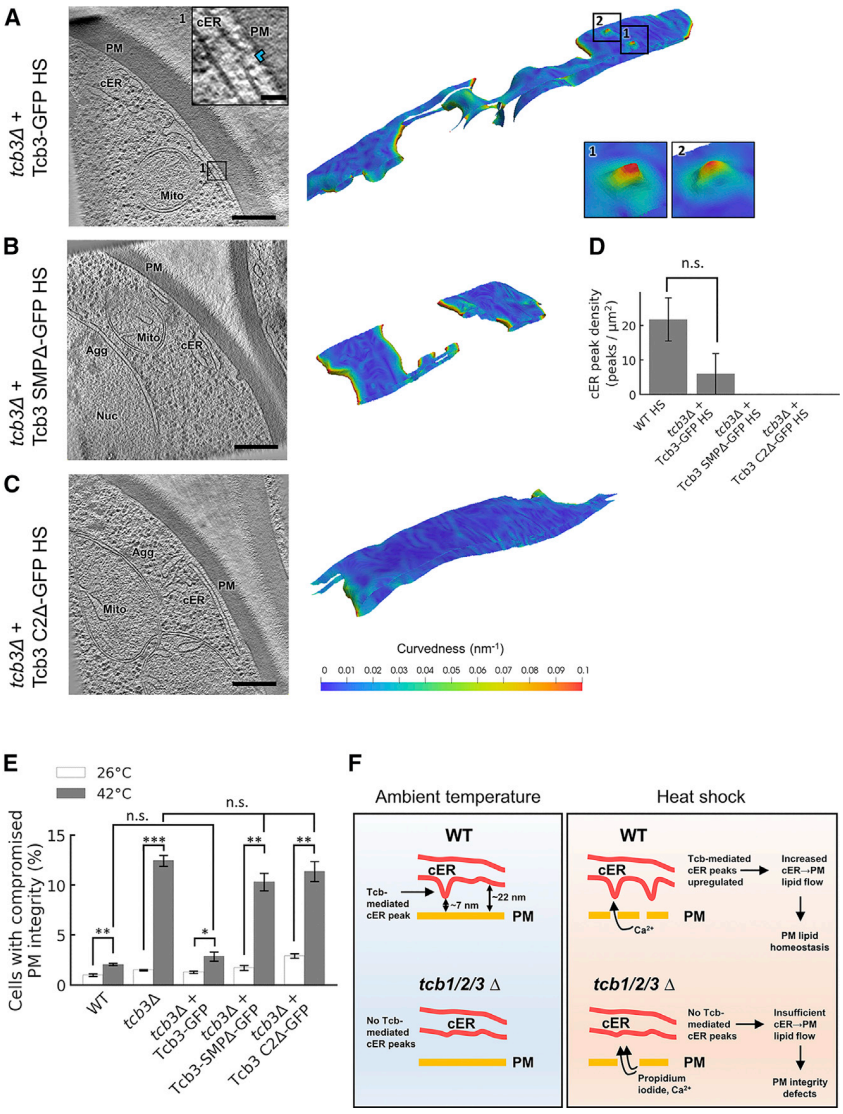

Figure 6. cER Peaks and PM Integrity in Heat-Shocked Tcb3 Truncation Mutants

(A–C) 1.4-nm-thick tomographic slices of cER in the indicated strains (left) and 3D renderings of cER curvature (right). Agg: aggregate; cER: cortical ER; Mito: mitochondrion; Nuc: nucleus; PM: plasma membrane. (A) *tcb3Δ* + Tcb3-GFP HS, (B) *tcb3Δ* + Tcb3 SMPΔ- GFP HS, (C) *tcb3Δ* + Tcb3 C2Δ-GFP HS. Insets show cER peaks (blue arrowhead in the tomographic slice inset). Scale bars for tomographic slices: 300 nm (main panels); 25 nm (insets). The contrast of the tomographic slices in (A), (B), and (C) was enhanced using a deconvolution filter. (D) cER peak density per μm^2 of cER membrane area showing average values (gray bars) ± SE (error bars). N = 7 (WT HS), 3 (*tcb3Δ* + Tcb3-GFP HS), 3 (*tcb3Δ* + Tcb3 SMPΔ-GFP HS), and 3 (*tcb3Δ* + Tcb3 C2Δ-GFP HS) ER-PM MCS. n.s. indicates $p > 0.05$ by Mann-Whitney U test. (E) PM integrity assay of *tcb3Δ* cells complemented with Tcb3 truncation mutants upon 10-min incubation at 42°C. The plot shows average values (white/gray bars) for each condition ± SE (error bars). n.s., *, **, and ***, respectively, indicate $p > 0.05$, $p < 0.05$, $p < 0.01$, and $p < 0.001$ by unpaired t test. Four independent biological repeats were performed for all conditions. (F) Model for the function of cER peaks in maintaining PM integrity. In WT cells, Tcbs generate membrane peaks of extreme curvature on the cER membrane. This may facilitate the extraction of cER lipids and their delivery to the PM (top left). The generation of cER peaks is the main structural role of Tcbs at ER-PM MCS, as overall ER-PM tethering is not substantially affected by Tcb1/2/3 deletion. However, *tcb1/2/3Δ* cells lack cER peaks (bottom left). Under heat stress, influx of extracellular Ca^{2+} through a damaged PM drives the localized formation of additional Tcb-mediated cER peaks, which in turn facilitate sufficient delivery of cER lipids to the PM to maintain PM integrity (top right). Absence of cER peaks in heat stressed *tcb1/2/3Δ* cells leads to PM integrity defects allowing influx of propidium iodide (bottom right). See also Figure S4; Table S1.

to that of the flat parts (99.85% of total cER membrane area) (Figure S4B). Thus, lipid transfer at flat cER membranes may not be negligible. Nevertheless, in heat-shocked WT cells the observed ~6-fold increase in cER peak density would translate into a ~5-fold more lipids transferred from cER peaks than from the flat portions of the cER (Figure S4B). This analysis also shows that increasing cER peak density can only substantially increase lipid flows when the total levels of cER are high, possibly explaining the PM integrity defects observed in mutants with less cER such as *scs2/22Δ* or Tcb1/2/3-only (Figure S4A).

Tcb3 SMP and C2 Domains Are Necessary for cER Peak Formation

The higher density of cER peaks observed in heat-shocked WT cells provided a higher dynamic range to investigate by cryo-ET the specific roles of Tcb3 domains in cER peak formation at 42°C. We investigated GFP-tagged Tcb3 constructs, either full length (Tcb3-GFP), lacking the SMP domain (Tcb3 SMPΔ-GFP), or all C2 domains (Tcb3 C2Δ-GFP). In agreement with previous studies (Manford et al., 2012; Toulmay and Prinz, 2012), both truncations localized to the cER, although substantially higher fluorescence was detected in the nuclear ER compared to full-length Tcb3-GFP (Figure S4C).

We then inquired to what extent these Tcb3 constructs could rescue the defects observed in *tcb3Δ* cells in terms of cER peak formation (Figures 2I and 4C) and PM integrity (Figure 5A). Interestingly, cryo-ET imaging of heat-shocked cells and PM integrity assays revealed that neither truncation was able to complement *tcb3Δ* mutants (Figures 6B–6E), while substantial recovery was observed by expression of full-length Tcb3-GFP (Figures 6A, 6D, and 6E). These experiments indicate that the Tcb3 SMP and C2 domains are involved in cER peak formation and reinforce the correlation between PM integrity at elevated temperatures and the presence of Tcb-mediated cER peaks.

Altogether, these data indicate that (1) Tcbs are necessary for the formation of cER peaks; (2) cER peaks may facilitate ER-to-PM lipid transfer; and (3) cER peaks are important to maintain PM integrity under heat stress, a condition in which the PM

may require substantial lipid influx to restore its lipid homeostasis. Interestingly, similar high curvature peaks were observed at other ER-mediated MCS such as ER-mitochondria MCS (Figure S2D), suggesting that the induction of membrane curvature may be a general mechanism to facilitate intermembrane lipid exchange at various MCS.

DISCUSSION

ER-PM Tethers Shape the cER

MCS exist between essentially all cellular membranes, and a great number of MCS-resident proteins and tethers have been identified. However, the functions of many of these molecules remain poorly understood (Bohnert and Schuldiner, 2018; Shai et al., 2018; Valm et al., 2017; Wu et al., 2018). For example, it is unclear why so many ER-PM tethers exist in *S. cerevisiae* (Gatta et al., 2015; Manford et al., 2012; Quon et al., 2018), as well as the possible functions of these proteins beyond the mechanical anchoring of the membranes. Here, we employed state-of-the-art *in situ* imaging by cryo-ET to reveal that ER-PM tethers are critical determinants of cER morphology and MCS function.

Our data confirm that Ist2 is an important ER-PM tether (Lavieu et al., 2010; Manford et al., 2012; Wolf et al., 2012). The distribution of ER-PM distances was particularly narrow in Ist2-only cells, indicating that Ist2 is very effective in maintaining an ER-PM separation of about 21 nm. This is surprising, because Ist2 bridges the ER and the PM by a 340-amino-acid-long linker that is predicted to be unstructured. This linker is probably not fully extended, as this would allow it to span up to 120 nm, but how it can precisely regulate intermembrane distance requires further investigation.

ER-PM distances were more broadly distributed in Scs2/22-only cells, possibly due to the promiscuous interactions of Scs2/22 with different FFAT/FFAT-like motif proteins at the PM (Murphy and Levine, 2016). Strikingly, the cER in these cells consisted almost exclusively of extended, narrow sheets. How such sheets are formed remains to be established, as direct interactions of Scs2/22 in *trans* across the ER lumen appear unlikely, given their short luminal sequences. In contrast to Scs2/22-only cells, the cER was mainly formed by tubules in Tcb1/2/3-only cells. This phenomenon may rely on the hairpin sequence that anchors Tcbs to the ER membrane. Tcb hairpin sequences could sense and/or generate membrane curvature as in reticulons and other ER morphogenetic proteins (Hu et al., 2011).

Alternatively, it is also possible that the cER morphologies observed in the different ER-PM tether mutants arise from the dysregulation of additional ER-PM MCS factors (Quon et al., 2018), other ER morphogenetic proteins, or lipids. However, WT cER also consists of a mixture of sheets and tubules, which could plausibly arise as a combination of the morphologies of the individual ER-PM tether mutants. Therefore, it is possible that the different families of tethers are enriched in partially segregated cER subdomains, consistent with their punctate localization observed by light microscopy (Creutz et al., 2004; Manford et al., 2012; Toulmay and Prinz, 2012; Wolf et al., 2012). Similarly, in plant and mammalian cells, different ER-PM tethers are known to co-exist at the same MCS but form separate subdomains (Giordano et al., 2013; Siao et al., 2016). Therefore, native ER-PM MCS may be established as a juxtaposition of molecular territories enriched in different tethers.

Tcbs Form Highly Curved Peaks at the cER Membrane

Besides being generally tubular, the cER in Tcb1/2/3-only cells was enriched in membrane peaks of extreme (< 10-nm radius) membrane curvature, one of the highest observed in a cell (Antonny, 2011). cER peaks were also present in WT cells at a lower frequency, suggesting that Tcbs generate these structures also in the WT case. In fact, our study of Tcb-deletion mutants indicated that the efficient formation of cER peaks requires expression of Tcb3 and Tcb1 or Tcb2, consistent with biochemical evidence that Tcbs/E-Syts form heterodimers (Creutz et al., 2004; Giordano et al., 2013; Idevall-Hagren et al., 2015; Schulz and Creutz, 2004). Given that the SMP domain is important for dimerization (Schauder et al., 2014), disruption of Tcb3-Tcb1/2 heterodimers may explain the lack of cER peaks in *tcb3Δ* cells expressing Tcb3 SMPΔ-GFP.

A Tcb3 truncation lacking all C2 domains also failed to rescue cER peak formation in *tcb3Δ* cells. On one hand, it is possible that C2 domains are also involved in Tcb dimerization or oligomerization (Zanetti et al., 2016). Additionally, binding of at least some C2 domains to the cER membrane may play an active role in curvature generation, by analogy with other multi-C2 domain proteins. For example, the C2 domains of mammalian SYT1 bind the PM in a Ca^{2+}-dependent manner, generating curvature in the PM (Martens et al., 2007). Although C2 domains generally prefer negatively charged membranes such as the PM, binding of E-Syt C2 domains to the ER membrane has been speculated (Min et al., 2007; Schauder et al., 2014). The exact mechanisms by which Tcb SMP and C2 domains could generate cER peaks, perhaps synergistically with the hairpin sequence, require further investigation.

Bona fide membrane curvature generators such as reticulons have also been implicated in ER-PM MCS formation (Caldieri et al., 2017), and there is increasing evidence for important roles of curvature-sensing and/or generating proteins at other MCS (Ackema et al., 2016; de Saint-Jean et al., 2011; Ho and Stroupe, 2016; Moser von Filseck et al., 2015; Voss et al., 2012), consistent with our observations of high curvature peaks at, e.g., ER-mitochondria MCS. Thus, membrane curvature may be an important regulator of MCS function (Henne et al., 2015).

cER Peaks Are Important for PM Integrity under Stress

Most MCS harbor an intense nonvesicular exchange of lipids (Cockcroft and Raghu, 2018; Lees et al., 2017; Saheki et al., 2016), which is especially important at ER-PM MCS because most PM lipids are synthesized in the ER. Moreover, the E-Syts, mammalian orthologs of Tcbs, are directly implicated in ER-PM lipid transfer, as their SMP domain mediates lipid binding and transport (Bian et al., 2018; Saheki et al., 2016; Schauder et al., 2014; Yu et al., 2016). Because Tcb-induced cER peaks always faced the PM, we hypothesized that these peaks could play a role in an ER-PM lipid transfer.

Consistent with this idea, our semi-quantitative modeling indicated that cER peaks can dramatically enhance the rate of lipid extraction from the cER by facilitating the shallow insertion of lipid-transport modules into the lipid bilayer, in agreement with experimental studies (Machida and Ohnishi, 1980; Moser von

Filseck et al., 2015). cER peaks also shorten cER-PM distance and can impose cER-to-PM directionality on the lipid transfer process. Thus, cER-to-PM lipid transfer may be greatly enhanced by Tcb-mediated cER peaks. It is also attractive to speculate that Tcb SMP domains may play an active role in such lipid transfer process.

The physiological roles of the Tcb protein family remain enigmatic. On one hand, these molecules are highly conserved and therefore likely to play important functions. However, no major alterations were discovered in yeast cells lacking all Tcbs (Manford et al., 2012; Toulmay and Prinz, 2012), nor in mammalian cells or mice lacking all three E-Syts (Saheki et al., 2016; Sclip et al., 2016; Tremblay and Moss, 2016). E-Syt triple knockout cells did display an accumulation of diacylglycerol at the PM upon phospholipase C activation (Saheki et al., 2016), suggesting that the main function of E-Syts/Tcbs is to respond to stimuli that perturb lipid homeostasis (Stefan, 2018).

Our data suggest that one of such stimulus is heat stress. Although Tcb1/2/3 deletion does not substantially reduce the levels of cER, heat-shocked *tcb1/2/3Δ* cells suffer from PM integrity defects (Omnus et al., 2016). Furthermore, our functional assays of Tcb mutants showed a strong correlation between the absence of cER peaks and PM integrity defects upon heat stress. Although the exact mechanisms by which heat stress compromises PM integrity remain to be established, heat alters PM protein and lipid homeostasis, as well as the physico-chemical properties of the bilayer (Fan and Evans, 2015; Verghese et al., 2012; Zhao et al., 2013). PM repair likely involves the addition of new lipids (Vaughan et al., 2014), and ER-PM MCS regulate phospholipid biogenesis (Pichler et al., 2001; Tavassoli et al., 2013). Thus, under conditions of PM damage, Tcb-mediated cER peaks could maintain PM integrity by ensuring sufficient flow of lipids synthesized in the cER toward the PM.

Consistently, we observed a substantial increase in the number of cER peaks in WT cells under heat stress. Since membrane binding of some Tcb C2 domains is regulated by Ca^{2+} (Schulz and Creutz, 2004), the formation of new cER peaks upon heat stress could be driven by the influx of extracellular Ca^{2+} through a damaged PM (Andrews and Corrotte, 2018; Jimenez and Perez, 2017). Ca^{2+} influx may trigger the binding of Tcb C2 domains to the cER membrane, inducing cER membrane curvature in a way similar to mammalian SYTs (Martens et al., 2007). At the same time, the cER is highly dynamic and explores most of the cellular PM over a few minutes, possibly monitoring PM status (Omnus et al., 2016). Thus, Ca^{2+} signals at sites of PM damage may trigger formation of Tcb-mediated cER peaks exactly where they are needed to locally enhance PM repair (Figure 6F). This mechanism may act in parallel or synergistically with other pathways to maintain PM homeostasis (Andrews and Corrotte, 2018; Jimenez and Perez, 2017; Omnus et al., 2016; Zhao et al., 2013).

In fact, our calculations show that besides cER peaks, high levels of cER may also be important for PM integrity, suggesting that optimal cER-PM lipid flow requires joint efforts by Tcbs and other tethers. Although our model indicates that the capacity to extract lipids from cER peaks is much higher than from flat membranes, lipid currents from cER peaks and flat areas appear comparable in WT cells, given the minute fraction of cER area occupied by peaks. However, lipid currents from cER peaks may dominate upon heat shock due to the increase in cER peak density, possibly explaining why the phenotypes of Tcb mutants only become apparent under stress conditions.

The important role of Tcbs in maintaining PM integrity upon stress agrees with findings on the plant SYTs, which also act as ER-PM tethers and are important factors protecting PM integrity from different stresses (Kawamura and Uemura, 2003; Lee et al., 2019; Pérez-Sancho et al., 2015; Schapire et al., 2008; Yamazaki et al., 2008). Other mammalian multi-C2 domain proteins like SYT7 and dysferlin are directly implicated in PM repair (Andrews and Corrotte, 2018; Jimenez and Perez, 2017). As with yeast Tcbs, membrane binding by some C2 domains of plant SYTs and mammalian E-Syts is regulated by Ca^{2+} (Giordano et al., 2013; Idevall-Hagren et al., 2015; Pérez-Sancho et al., 2015). Therefore, we propose that a crucial function of yeast Tcbs, plant SYTs, and possibly mammalian E-Syts is to respond to the influx of extracellular Ca^{2+} through a damaged PM by forming cER peaks, which may enhance the cER-to-PM lipid transfer necessary for PM repair. Further work should experimentally determine the extent and composition of these lipid flows.

STAR★METHODS

Detailed methods are provided in the online version of this paper and include the following:

- KEY RESOURCES TABLE
- LEAD CONTACT AND MATERIAL AVAILABILITY
- EXPERIMENTAL MODEL AND SUBJECT DETAILS
  - Yeast Strains and Cell Culture
  - Plasmid Construction
- METHOD DETAILS
  - Light Microscopy
  - Cell Vitrification
  - Cryo-Focused Ion Beam Milling
  - Cryo-Electron Tomography
  - Membrane Segmentation and Surface Generation
  - Membrane Curvature Determination
  - Intermembrane Distance Measurements
  - cER Peak Morphology and Density Quantification
  - Membrane Modeling
  - Calculation of Lipid Extraction Currents
  - PM Integrity Assays
- QUANTIFICATION AND STATISTICAL ANALYSIS
- DATA AND CODE AVAILABILITY

SUPPLEMENTAL INFORMATION

Supplemental Information can be found online at https://doi.org/10.1016/j.devcel.2019.10.018.

ACKNOWLEDGMENTS

We thank Philipp Erdmann, Günter Pfeifer, Jürgen Plitzko, and Miroslava Schaffer for electron microscopy support, and the Imaging Facility of the Max Planck Institute of Biochemistry for light microscopy support. We are grateful to Scott Emr for strains as well as Markus Hohle, Vladan Lucic, Eri

Sakata, and Florian Wilfling for helpful discussions. We also thank Patrick C. Hoffmann and Wanda Kukulski for sharing unpublished results. J.C. and M.K. were supported by the Graduate School of Quantitative Biosciences Munich. J.C., M.K., A.M.-S., W.B. and R.F.-B. have received funding from the European Commission (FP7 GA ERC-2012-SyG_318987–ToPAG). R.F.-B. acknowledges funding from the Deutsche Forschungsgemeinschaft (DFG, German Research Foundation) through Germany's Excellence Strategy - EXC 2067/1- 390729940 and SFB1190/P22. F.C. acknowledges financial support from the Spanish Ministry of Economy and Competitiveness ("Severo Ochoa" program for Centres of Excellence in R&D (SEV-2015-0522, FIS2015-63550-R, FIS2017-89560-R, BFU2015-73288-JIN, RYC-2017-22227, and AEI/FEDER/UE), Fundació Privada Cellex, and from the Generalitat de Catalunya through the CERCA program. R.L. acknowledges funding from the European Commission (ERC AdG TENDO - 834394), the Swiss National Science Foundation (31003A_179517), the Swiss National Centre for Competence in Research in Chemical Biology (51NF40-185898), and the Canton of Geneva. C.J.S. is supported by MRC funding to the MRC LMCB University Unit at UCL, award code MC_UU_00012/6.

AUTHOR CONTRIBUTIONS

J.C. performed electron microscopy experiments and contributed to computational data analysis. M.K. and A.M.S. developed software procedures for data analysis. M.K. performed computational and statistical analysis of the data. F.C. performed theoretical modeling. C.B. carried out molecular biology and light microscopy experiments. F.T. and C.J.S. constructed strains, plasmids, and performed plasma membrane integrity assays. R.F.-B. supervised electron microscopy experiments and data analysis. J.C., F.C., C.B., R.L., W.B., C.J.S., and R.F.-B. designed the research. R.F.-B. wrote the manuscript with contributions from all authors.

DECLARATION OF INTERESTS

The authors declare no competing interests.

Received: March 28, 2019
Revised: September 23, 2019
Accepted: October 16, 2019
Published: November 18, 2019

REFERENCES

Ackema, K.B., Prescianotto-Baschong, C., Hench, J., Wang, S.C., Chia, Z.H., Mergentaler, H., Bard, F., Frank, S., and Spang, A. (2016). Sar1, a novel regulator of ER-mitochondrial contact sites- sar1. PLoS One *11*, e0154280.

Ahrens, J., Geveci, B., and Law, C. (2005). ParaView: an end-user tool for large data visualization. In Visualization Handbook (Elsevier).

Andrews, N.W., and Corrotte, M. (2018). Plasma membrane repair. Curr. Biol. *28*, R392–R397.

Antonny, B. (2011). Mechanisms of membrane curvature sensing. Annu. Rev. Biochem. *80*, 101–123.

Balla, T. (2018). Ca(2+) and lipid signals hold hands at endoplasmic reticulum-plasma membrane contact sites. J. Physiol. (Lond.) *596*, 2709–2716.

Beck, M., and Baumeister, W. (2016). Cryo-electron tomography: can it reveal the molecular sociology of cells in atomic detail? Trends Cell Biol. *26*, 825–837.

Bers, D.M. (2002). Cardiac excitation-contraction coupling. Nature *415*, 198–205.

Bian, X., Saheki, Y., and De Camilli, P. (2018). Ca(2+) releases E-Syt1 autoinhibition to couple ER-plasma membrane tethering with lipid transport. EMBO J. *37*, 219–234.

Bohnert, M., and Schuldiner, M. (2018). Stepping outside the comfort zone of membrane contact site research. Nat. Rev. Mol. Cell Biol. *19*, 483–484.

Caldieri, G., Barbieri, E., Nappo, G., Raimondi, A., Bonora, M., Conte, A., Verhoef, L.G.G.C., Confalonieri, S., Malabarba, M.G., Bianchi, F., et al. (2017). Reticulon 3-dependent ER-PM contact sites control EGFR nonclathrin endocytosis. Science *356*, 617–624.

Campelo, F., and Kozlov, M.M. (2014). Sensing membrane stresses by protein insertions. PLoS Comput. Biol. *10*, e1003556.

Campelo, F., McMahon, H.T., and Kozlov, M.M. (2008). The hydrophobic insertion mechanism of membrane curvature generation by proteins. Biophys. J. *95*, 2325–2339.

Carrasco, S., and Meyer, T. (2011). STIM proteins and the endoplasmic reticulum-plasma membrane junctions. Annu. Rev. Biochem. *80*, 973–1000.

Chang, C.L., Chen, Y.J., and Liou, J. (2017). ER-plasma membrane junctions: why and how do we study them? Biochim. Biophys. Acta Mol. Cell Res. *1864*, 1494–1506.

Cockcroft, S., and Raghu, P. (2018). Phospholipid transport protein function at organelle contact sites. Curr. Opin. Cell Biol. *53*, 52–60.

Collado, J., and Fernández-Busnadiego, R. (2017). Deciphering the molecular architecture of membrane contact sites by cryo-electron tomography. Biochim. Biophys. Acta Mol. Cell Res. *1864*, 1507–1512.

Creutz, C.E., Snyder, S.L., and Schulz, T.A. (2004). Characterization of the yeast tricalbins: membrane-bound multi-C2-domain proteins that form complexes involved in membrane trafficking. Cell. Mol. Life Sci. *61*, 1208–1220.

de Saint-Jean, M., Delfosse, V., Douguet, D., Chicanne, G., Payrastre, B., Bourguet, W., Antonny, B., and Drin, G. (2011). Osh4p exchanges sterols for phosphatidylinositol 4-phosphate between lipid bilayers. J. Cell Biol. *195*, 965–978.

Dittman, J.S., and Menon, A.K. (2017). Speed limits for nonvesicular intracellular sterol transport. Trends Biochem. Sci. *42*, 90–97.

Fan, W., and Evans, R.M. (2015). Turning up the heat on membrane fluidity. Cell *161*, 962–963.

Fernández, J.J., and Li, S. (2003). An improved algorithm for anisotropic nonlinear diffusion for denoising cryo-tomograms. J. Struct. Biol. *144*, 152–161.

Fernández-Busnadiego, R., Saheki, Y., and De Camilli, P. (2015). Three-dimensional architecture of extended synaptotagmin-mediated endoplasmic reticulum-plasma membrane contact sites. Proc. Natl. Acad. Sci. USA *112*, E2004–E2013.

Fischer, M.A., Temmerman, K., Ercan, E., Nickel, W., and Seedorf, M. (2009). Binding of plasma membrane lipids recruits the yeast integral membrane protein Ist2 to the cortical ER. Traffic *10*, 1084–1097.

Gatta, A.T., Wong, L.H., Sere, Y.Y., Calderón-Noreña, D.M., Cockcroft, S., Menon, A.K., and Levine, T.P. (2015). A new family of StART domain proteins at membrane contact sites has a role in ER-PM sterol transport. ELife *4*.

Gibson, D.G., Young, L., Chuang, R.Y., Venter, J.C., Hutchison, C.A., 3rd, and Smith, H.O. (2009). Enzymatic assembly of DNA molecules up to several hundred kilobases. Nat. Methods *6*, 343–345.

Giordano, F., Saheki, Y., Idevall-Hagren, O., Colombo, S.F., Pirruccello, M., Milosevic, I., Gracheva, E.O., Bagriantsev, S.N., Borgese, N., and De Camilli, P. (2013). PI(4,5)P2-dependent and Ca2+-regulated ER-PM interactions mediated by the Extended Synaptotagmins. Cell *153*, 1494–1509.

Hagen, W.J.H., Wan, W., and Briggs, J.A.G. (2017). Implementation of a cryo-electron tomography tilt-scheme optimized for high resolution subtomogram averaging. J. Struct. Biol. *197*, 191–198.

Helfrich, W. (1973). Elastic properties of lipid bilayers: theory and possible experiments. Z. Naturforsch. C Biochem. Biophys. Biol. Virol. *28*, 693–703.

Henne, W.M., Liou, J., and Emr, S.D. (2015). Molecular mechanisms of inter-organelle ER-PM contact sites. Curr. Opin. Cell Biol. *35*, 123–130.

Ho, R., and Stroupe, C. (2016). The HOPS/class C Vps complex tethers high-curvature membranes via a direct protein-membrane interaction. Traffic *17*, 1078–1090.

Hu, J., Prinz, W.A., and Rapoport, T.A. (2011). Weaving the web of ER tubules. Cell *147*, 1226–1231.

Idevall-Hagren, O., Lü, A., Xie, B., and De Camilli, P. (2015). Triggered Ca2+ influx is required for extended synaptotagmin 1-induced ER-plasma membrane tethering. EMBO J. *34*, 2291–2305.

Jimenez, A.J., and Perez, F. (2017). Plasma membrane repair: the adaptable cell life-insurance. Curr. Opin. Cell Biol. *47*, 99–107.

Jüschke, C., Wächter, A., Schwappach, B., and Seedorf, M. (2005). SEC18/NSF-independent, protein-sorting pathway from the yeast cortical ER to the plasma membrane. J. Cell Biol. *169*, 613–622.

Kalemanov, M., Collado, J.F., Baumeister, W., Fernández-Busnadiego, R., and Martínez-Sánchez, A. (2019). Estimation of membrane curvature for cryo-electron tomography. bioRxiv, 579060.

Kawamura, Y., and Uemura, M. (2003). Mass spectrometric approach for identifying putative plasma membrane proteins of Arabidopsis leaves associated with cold acclimation. Plant J. *36*, 141–154.

Koenderink, J.J., and van Doorn, A.J. (1992). Surface shape and curvature scales. Image Vis. Comput. *10*, 557–564.

Kozlov, M.M., Campelo, F., Liska, N., Chernomordik, L.V., Marrink, S.J., and McMahon, H.T. (2014). Mechanisms shaping cell membranes. Curr. Opin. Cell Biol. *29*, 53–60.

Kremer, J.R., Mastronarde, D.N., and McIntosh, J.R. (1996). Computer visualization of three-dimensional image data using IMOD. J. Struct. Biol. *116*, 71–76.

Lacruz, R.S., and Feske, S. (2015). Diseases caused by mutations in ORAI1 and STIM1. Ann. N. Y. Acad. Sci. *1356*, 45–79.

Landstrom, A.P., Beavers, D.L., and Wehrens, X.H. (2014). The junctophilin family of proteins: from bench to bedside. Trends Mol. Med. *20*, 353–362.

Lavieu, G., Orci, L., Shi, L., Geiling, M., Ravazzola, M., Wieland, F., Cosson, P., and Rothman, J.E. (2010). Induction of cortical endoplasmic reticulum by dimerization of a coatomer-binding peptide anchored to endoplasmic reticulum membranes. Proc. Natl. Acad. Sci. USA *107*, 6876–6881.

Lee, E., Vanneste, S., Pérez-Sancho, J., Benitez-Fuente, F., Strelau, M., Macho, A.P., Botella, M.A., Friml, J., and Rosado, A. (2019). Ionic stress enhances ER-PM connectivity via phosphoinositide-associated SYT1 contact site expansion in Arabidopsis. Proc. Natl. Acad. Sci. USA *116*, 1420–1429.

Lee, I., and Hong, W. (2006). Diverse membrane-associated proteins contain a novel SMP domain. FASEB J. *20*, 202–206.

Lees, J.A., Messa, M., Sun, E.W., Wheeler, H., Torta, F., Wenk, M.R., De Camilli, P., and Reinisch, K.M. (2017). Lipid transport by TMEM24 at ER-plasma membrane contacts regulates pulsatile insulin secretion. Science *355*.

Li, X., Mooney, P., Zheng, S., Booth, C.R., Braunfeld, M.B., Gubbens, S., Agard, D.A., and Cheng, Y. (2013). Electron counting and beam-induced motion correction enable near-atomic-resolution single-particle cryo-EM. Nat. Methods *10*, 584–590.

Loewen, C.J., Young, B.P., Tavassoli, S., and Levine, T.P. (2007). Inheritance of cortical ER in yeast is required for normal septin organization. J. Cell Biol. *179*, 467–483.

Longtine, M.S., McKenzie, A., 3rd, Demarini, D.J., Shah, N.G., Wach, A., Brachat, A., Philippsen, P., and Pringle, J.R. (1998). Additional modules for versatile and economical PCR-based gene deletion and modification in Saccharomyces cerevisiae. Yeast *14*, 953–961.

Lorensen, W.E., and Cline, H.E. (1987). Marching cubes: A high resolution 3D surface construction algorithm. SIGGRAPH Comput. Graph. Proceedings of the 14th SIGGRAPH 1987 (ACM) *21*, 163–169.

Lučić, V., Fernández-Busnadiego, R., Laugks, U., and Baumeister, W. (2016). Hierarchical detection and analysis of macromolecular complexes in cryo-electron tomograms using Pyto software. J. Struct. Biol. *196*, 503–514.

Maass, K., Fischer, M.A., Seiler, M., Temmerman, K., Nickel, W., and Seedorf, M. (2009). A signal comprising a basic cluster and an amphipathic alpha-helix interacts with lipids and is required for the transport of Ist2 to the yeast cortical ER. J. Cell Sci. *122*, 625–635.

Machida, K., and Ohnishi, S.I. (1980). Effect of bilayer membrane curvature on activity of phosphatidylcholine exchange protein. Biochim. Biophys. Acta *596*, 201–209.

Manford, A.G., Stefan, C.J., Yuan, H.L., Macgurn, J.A., and Emr, S.D. (2012). ER-to-plasma membrane tethering proteins regulate cell signaling and ER morphology. Dev. Cell *23*, 1129–1140.

Martens, S., Kozlov, M.M., and McMahon, H.T. (2007). How synaptotagmin promotes membrane fusion. Science *316*, 1205–1208.

Martinez-Sanchez, A., Garcia, I., Asano, S., Lucic, V., and Fernandez, J.J. (2014). Robust membrane detection based on tensor voting for electron tomography. J. Struct. Biol. *186*, 49–61.

Mastronarde, D.N. (2005). Automated electron microscope tomography using robust prediction of specimen movements. J. Struct. Biol. *152*, 36–51.

Miller, S.B., Mogk, A., and Bukau, B. (2015). Spatially organized aggregation of misfolded proteins as cellular stress defense strategy. J. Mol. Biol. *427*, 1564–1574.

Min, S.W., Chang, W.P., and Südhof, T.C. (2007). E-Syts, a family of membranous Ca2+-sensor proteins with multiple C2 domains. Proc. Natl. Acad. Sci. USA *104*, 3823–3828.

Moser von Filseck, J., Vanni, S., Mesmin, B., Antonny, B., and Drin, G. (2015). A phosphatidylinositol-4-phosphate powered exchange mechanism to create a lipid gradient between membranes. Nat. Commun. *6*, 6671.

Murphy, S.E., and Levine, T.P. (2016). VAP, a Versatile Access Point for the endoplasmic reticulum: review and analysis of FFAT-like motifs in the VAPome. Biochim. Biophys. Acta *1861*, 952–961.

Nickell, S., Förster, F., Linaroudis, A., Net, W.D., Beck, F., Hegerl, R., Baumeister, W., and Plitzko, J.M. (2005). TOM software toolbox: acquisition and analysis for electron tomography. J. Struct. Biol. *149*, 227–234.

Niggemann, G., Kummrow, M., and Helfrich, W. (1995). The bending rigidity of phosphatidylcholine bilayers - dependences on experimental-method, sample cell sealing and temperature. J. Phys. II France *5*, 413–425.

Omnus, D.J., Manford, A.G., Bader, J.M., Emr, S.D., and Stefan, C.J. (2016). Phosphoinositide kinase signaling controls ER-PM cross-talk. Mol. Biol. Cell *27*, 1170–1180.

Peixoto, T.P. (2017). The graph-tool python library. figshare. 106084/m9figshare1164194.

Pérez-Sancho, J., Tilsner, J., Samuels, A.L., Botella, M.A., Bayer, E.M., and Rosado, A. (2016). Stitching organelles: organization and function of specialized membrane contact sites in plants. Trends Cell Biol. *26*, 705–717.

Pérez-Sancho, J., Vanneste, S., Lee, E., McFarlane, H.E., Esteban Del Valle, A., Valpuesta, V., Friml, J., Botella, M.A., and Rosado, A. (2015). The Arabidopsis synaptotagmin1 is enriched in endoplasmic reticulum-plasma membrane contact sites and confers cellular resistance to mechanical stresses. Plant Physiol. *168*, 132–143.

Pichler, H., Gaigg, B., Hrastnik, C., Achleitner, G., Kohlwein, S.D., Zellnig, G., Perktold, A., and Daum, G. (2001). A subfraction of the yeast endoplasmic reticulum associates with the plasma membrane and has a high capacity to synthesize lipids. Eur. J. Biochem. *268*, 2351–2361.

Quon, E., Sere, Y.Y., Chauhan, N., Johansen, J., Sullivan, D.P., Dittman, J.S., Rice, W.J., Chan, R.B., Di Paolo, G., Beh, C.T., et al. (2018). Endoplasmic reticulum-plasma membrane contact sites integrate sterol and phospholipid regulation. PLOS Biol. *16*, e2003864.

Reinisch, K.M., and De Camilli, P. (2016). SMP-domain proteins at membrane contact sites: structure and function. Biochim. Biophys. Acta *1861*, 924–927.

Rigort, A., Bäuerlein, F.J., Villa, E., Eibauer, M., Laugks, T., Baumeister, W., and Plitzko, J.M. (2012). Focused ion beam micromachining of eukaryotic cells for cryoelectron tomography. Proc. Natl. Acad. Sci. USA *109*, 4449–4454.

Ríos, E., Figueroa, L., Manno, C., Kraeva, N., and Riazi, S. (2015). The couplonopathies: A comparative approach to a class of diseases of skeletal and cardiac muscle. J. Gen. Physiol. *145*, 459–474.

Rizo, J., and Südhof, T.C. (1998). C2-domains, structure and function of a universal Ca2+-binding domain. J. Biol. Chem. *273*, 15879–15882.

Robinson, J.S., Klionsky, D.J., Banta, L.M., and Emr, S.D. (1988). Protein sorting in Saccharomyces cerevisiae: isolation of mutants defective in the delivery and processing of multiple vacuolar hydrolases. Mol. Cell. Biol. *8*, 4936–4948.

Saheki, Y., Bian, X., Schauder, C.M., Sawaki, Y., Surma, M.A., Klose, C., Pincet, F., Reinisch, K.M., and De Camilli, P. (2016). Control of plasma membrane lipid homeostasis by the extended synaptotagmins. Nat. Cell Biol. *18*, 504–515.

Saheki, Y., and De Camilli, P. (2017a). Endoplasmic reticulum-plasma membrane contact sites. Annu. Rev. Biochem. *86*, 659–684.

Saheki, Y., and De Camilli, P. (2017b). The extended-synaptotagmins. Biochim. Biophys. Acta Mol. Cell Res. *1864*, 1490–1493.

Schapire, A.L., Voigt, B., Jasik, J., Rosado, A., Lopez-Cobollo, R., Menzel, D., Salinas, J., Mancuso, S., Valpuesta, V., Baluska, F., et al. (2008). Arabidopsis synaptotagmin 1 is required for the maintenance of plasma membrane integrity and cell viability. Plant Cell *20*, 3374–3388.

Schauder, C.M., Wu, X., Saheki, Y., Narayanaswamy, P., Torta, F., Wenk, M.R., De Camilli, P., and Reinisch, K.M. (2014). Structure of a lipid-bound extended synaptotagmin indicates a role in lipid transfer. Nature *510*, 552–555.

Schroeder, W., Martin, K.M., and Lorensen, W.E. (2006). The visualization toolkit: an object-oriented approach to 3d graphics (Kitware).

Schulz, T.A., and Creutz, C.E. (2004). The tricalbin C2 domains: lipid-binding properties of a novel, synaptotagmin-like yeast protein family. Biochemistry *43*, 3987–3995.

Sclip, A., Bacaj, T., Giam, L.R., and Südhof, T.C. (2016). Extended synaptotagmin (ESyt) triple knock-out mice are viable and fertile without obvious endoplasmic reticulum dysfunction. PLoS One *11*, e0158295.

Shai, N., Yifrach, E., van Roermund, C.W.T., Cohen, N., Bibi, C., IJlst, L., Cavellini, L., Meurisse, J., Schuster, R., Zada, L., et al. (2018). Systematic mapping of contact sites reveals tethers and a function for the peroxisome-mitochondria contact. Nat. Commun. *9*, 1761.

Siao, W., Wang, P., Voigt, B., Hussey, P.J., and Baluska, F. (2016). Arabidopsis SYT1 maintains stability of cortical endoplasmic reticulum networks and VAP27-1-enriched endoplasmic reticulum-plasma membrane contact sites. J. Exp. Bot. *67*, 6161–6171.

Sorre, B., Callan-Jones, A., Manneville, J.B., Nassoy, P., Joanny, J.F., Prost, J., Goud, B., and Bassereau, P. (2009). Curvature-driven lipid sorting needs proximity to a demixing point and is aided by proteins. Proc. Natl. Acad. Sci. USA *106*, 5622–5626.

Stefan, C.J. (2018). Building ER-PM contacts: keeping calm and ready on alarm. Curr. Opin. Cell Biol. *53*, 1–8.

Stefan, C.J., Manford, A.G., Baird, D., Yamada-Hanff, J., Mao, Y., and Emr, S.D. (2011). Osh proteins regulate phosphoinositide metabolism at ER-plasma membrane contact sites. Cell *144*, 389–401.

Szule, J.A., Fuller, N.L., and Rand, R.P. (2002). The effects of acyl chain length and saturation of diacylglycerols and phosphatidylcholines on membrane monolayer curvature. Biophys. J. *83*, 977–984.

Tavassoli, S., Chao, J.T., Young, B.P., Cox, R.C., Prinz, W.A., de Kroon, A.I., and Loewen, C.J. (2013). Plasma membrane–endoplasmic reticulum contact sites regulate phosphatidylcholine synthesis. EMBO Rep. *14*, 434–440.

Toulmay, A., and Prinz, W.A. (2012). A conserved membrane-binding domain targets proteins to organelle contact sites. J. Cell Sci. *125*, 49–58.

Tremblay, M.G., and Moss, T. (2016). Loss of all 3 Extended Synaptotagmins does not affect normal mouse development, viability or fertility. Cell Cycle *15*, 2360–2366.

Valm, A.M., Cohen, S., Legant, W.R., Melunis, J., Hershberg, U., Wait, E., Cohen, A.R., Davidson, M.W., Betzig, E., and Lippincott-Schwartz, J. (2017). Applying systems-level spectral imaging and analysis to reveal the organelle interactome. Nature *546*, 162–167.

Vaughan, E.M., You, J.S., Elsie Yu, H.Y., Lasek, A., Vitale, N., Hornberger, T.A., and Bement, W.M. (2014). Lipid domain-dependent regulation of single-cell wound repair. Mol. Biol. Cell *25*, 1867–1876.

Verghese, J., Abrams, J., Wang, Y., and Morano, K.A. (2012). Biology of the heat shock response and protein chaperones: budding yeast (Saccharomyces cerevisiae) as a model system. Microbiol. Mol. Biol. Rev. *76*, 115–158.

Voss, C., Lahiri, S., Young, B.P., Loewen, C.J., and Prinz, W.A. (2012). ER-shaping proteins facilitate lipid exchange between the ER and mitochondria in S. cerevisiae. J. Cell Sci. *125*, 4791–4799.

Wagner, J., Schaffer, M., and Fernández-Busnadiego, R. (2017). Cryo-electron tomography-the cell biology that came in from the cold. FEBS Lett. *591*, 2520–2533.

West, M., Zurek, N., Hoenger, A., and Voeltz, G.K. (2011). A 3D analysis of yeast ER structure reveals how ER domains are organized by membrane curvature. J. Cell Biol. *193*, 333–346.

Whitlock, J.M., and Hartzell, H.C. (2017). Anoctamins/TMEM16 proteins: chloride channels flirting with lipids and extracellular vesicles. Annu. Rev. Physiol. *79*, 119–143.

Wolf, W., Kilic, A., Schrul, B., Lorenz, H., Schwappach, B., and Seedorf, M. (2012). Yeast Ist2 recruits the endoplasmic reticulum to the plasma membrane and creates a ribosome-free membrane microcompartment. PLoS One *7*, e39703.

Wong, L.H., Čopič, A., and Levine, T.P. (2017). Advances on the transfer of lipids by lipid transfer proteins. Trends Biochem. Sci. *42*, 516–530.

Wu, H., Carvalho, P., and Voeltz, G.K. (2018). Here, there, and everywhere: the importance of ER membrane contact sites. Science *361*.

Yamazaki, T., Kawamura, Y., Minami, A., and Uemura, M. (2008). Calcium-dependent freezing tolerance in Arabidopsis involves membrane resealing via synaptotagmin SYT1. Plant Cell *20*, 3389–3404.

Yu, H., Liu, Y., Gulbranson, D.R., Paine, A., Rathore, S.S., and Shen, J. (2016). Extended synaptotagmins are Ca2+-dependent lipid transfer proteins at membrane contact sites. Proc. Natl. Acad. Sci. USA *113*, 4362–4367.

Zanetti, M.N., Bello, O.D., Wang, J., Coleman, J., Cai, Y., Sindelar, C.V., Rothman, J.E., and Krishnakumar, S.S. (2016). Ring-like oligomers of Synaptotagmins and related C2 domain proteins. ELife *5*, e17262.

Zhao, Y., Macgurn, J.A., Liu, M., and Emr, S. (2013). The ART-Rsp5 ubiquitin ligase network comprises a plasma membrane quality control system that protects yeast cells from proteotoxic stress. ELife *2*, e00459.

Zimmerberg, J., and Kozlov, M.M. (2006). How proteins produce cellular membrane curvature. Nat. Rev. Mol. Cell Biol. *7*, 9–19.

STAR★METHODS

KEY RESOURCES TABLE

REAGENT or RESOURCE	SOURCE	IDENTIFIER
Bacterial and Virus Strains		
Max Efficiency® DH5alpha	Invitrogen	Cat# 18258-012
Chemicals, Peptides, and Recombinant Proteins		
Phusion® HF DNA Polymerase	NEB	Cat# M0530
DpnI	NEB	Cat# R0176
Propidium Iodide	Invitrogen	Cat# P3566
Critical Commercial Assays		
QIAprep® Spin MiniPrep Kit	Qiagen	Cat# 27106
Deposited Data		
Cryo-Electron Tomogram of cER-PM MCS in a Heat-Shocked WT *S. cerevisiae* Cell	This study	EMDB ID: EMD-10378
Cryo-Electron Tomogram of cER-PM MCS in a Heat-Shocked WT *S. cerevisiae* Cell (NAD Filtered)	This study	EMDB ID: EMD-10379
Experimental Models: Organisms/Strains		
S. cerevisiae: Strain Background SEY6210: *MATα leu2-3,112 ura3-52 his3-Δ200 trp1-Δ901 lys2-801 suc2-Δ9*	(Robinson et al., 1988)	ATCC: 96099
S. cerevisiae: Strain Background SEY6210.1: *MAT**a** leu2-3, 112 ura3-52 his3-Δ200 trp1 Δ901 lys2 801 suc2-Δ9*	(Robinson et al., 1988)	SEY6210.1
S. cerevisiae: Strain ANDY117: SEY6210 *tcb1*Δ::KANMX6	(Manford et al., 2012)	ANDY117
S. cerevisiae: Strain ANDY118: SEY6210.1 *tcb1*Δ::*KANMX6*	(Manford et al., 2012)	ANDY118
S. cerevisiae: Strain ANDY120: SEY6210.1 *tcb2*Δ::KANMX6	(Manford et al., 2012)	ANDY120
S. cerevisiae: Strain YCS2359: SEY6210.1 *tcb3*Δ::HISMX6	This study	YCS2359
S. cerevisiae: Strain YCS2430: SEY6210.1 *tcb1*Δ::KANMX6 *tcb2*Δ::KANMX6	This study	YCS2429
S. cerevisiae: Strain ANDY214: SEY6210.1 *tcb1*Δ::KANMX6 *tcb2*Δ::KANMX6 *tcb3*Δ::HISMX6	(Manford et al., 2012)	ANDY214
S. cerevisiae: Strain DBY356: SEY6210.1 *scs2*Δ::*TRP1 scs22*Δ:: *HISMX6*	(Stefan et al., 2011)	DBY356
S. cerevisiae: Strain ANDY113 SEY6210.1 *ist2*Δ::*HISMX6*	(Manford et al., 2012)	ANDY113
S. cerevisiae: Strain ANDY129: SEY6210.1 *ist2*Δ::HISMX6 *scs2*Δ::TRP1 *scs22*Δ::HISMX6	(Manford et al., 2012)	ANDY129
S. cerevisiae: Strain ANDY176: SEY6210.1 *ist2*Δ::HISMX6 *tcb1*Δ::KANMX6 *tcb2*Δ::KANMX6 *tcb3*Δ::HISMX6	(Manford et al., 2012)	ANDY176
S. cerevisiae: Strain ANDY196: SEY6210.1 *scs2*Δ::TRP1 *scs22*Δ::HISMX6 *tcb1*Δ::KANMX6 *tcb2*Δ::KANMX6 *tcb3*Δ::HISMX6	(Manford et al., 2012)	ANDY196
S. cerevisiae: Strain ANDY198: SEY6210.1 *ist2*Δ::HISMX6 *scs2*Δ::TRP1 *scs22*Δ::HISMX6 *tcb1*Δ::KANMX6 *tcb2*Δ:: KANMX6 *tcb3*Δ::HISMX6	(Manford et al., 2012)	ANDY198
Oligonucleotides		
Fwd deltaTCB3_SMP: AAGAAACCTTGTCG GATCGCGACATTATGGCTGCTCAATCAAAAGAAG	metabion	N/A
Rv deltaTCB3_SMP: GCGATCCGACAAGGTTTCTT	metabion	N/A
Fwd TCB3-1: ATGACTGGCATCAAAGCTCAAGT	metabion	N/A

(*Continued on next page*)

Continued

REAGENT or RESOURCE	SOURCE	IDENTIFIER
Recombinant DNA		
Plasmid: pRS415-TCB3-GFP-TADH1	(Manford et al., 2012)	pAM43
Plasmid: pRS415-Tcb3 (1–491)-GFP-TADH1	(Manford et al., 2012)	pAM44
Plasmid: pRS415-TCB3 SMPΔ-GFP-TADH1	This study	pCB2
Software and Algorithms		
Amira	Thermo Fisher Scientific	https://www.fei.com/software/amira-3d-for-life-sciences/ RRID:SCR_014305
BD FACSDiva	BD Biosciences	https://www.bdbiosciences.com/en-us RRID:SCR_001456
Fiji/ImageJ	NIH	https://imagej.net/Fiji#Downloads RRID:SCR_002285
Graph-Tool 2.2.44	(Peixoto, 2017)	https://graph-tool.skewed.de
IMOD	(Kremer et al., 1996)	http://bio3d.colorado.edu/imod/ RRID:SCR_003297
K2Align	Dimitry Tegunov	https://github.com/dtegunov/k2align
Mathematica 9.0	Wolfram Research, Inc.	https://www.wolfram.com/mathematica RRID:SCR_014448
MATLAB	MathWorks	https://www.mathworks.com/ RRID:SCR_001622
ParaView 5.5.2	(Ahrens et al., 2005)	https://www.paraview.org RRID:SCR_002516
Pyto	(Lučić et al., 2016)	N/A
Python 2.7.16 and 3.6.5	N/A	https://www.python.org RRID:SCR_008394
Python 2.7 Packages Installed via Pip or Anaconda: matplotlib-1.5.1, networkx-1.11, nibabel-2.4.0, numpy-1.11.3, skimage-0.12.3, scipy-0.18.1, pandas-0.19.2, pathlib2-2.2.0, pathos-0.2.2.1, pytest-4.6.2	N/A	https://pypi.org https://www.anaconda.com RRID:SCR_008624 RRID:SCR_002498 RRID:SCR_008633 RRID:SCR_008058
Python 3 Packages Installed via Anaconda: matplotlib-3.0.2, numpy-1.15.2, pandas-0.23.0, scipy-1.1.0, seaborn-0.8.1, Statsmodels-0.9.0	N/A	https://www.anaconda.com RRID:SCR_016074
Python Software to Estimate Membrane Curvature and Calculate Distances between Membranes	This study and (Kalemanov et al., 2019)	https://github.com/kalemaria/pycurv
SerialEM	(Mastronarde, 2005)	http://bio3d.colorado.edu/SerialEM/ RRID:SCR_017293
TOM Toolbox	(Nickell et al., 2005)	https://www.biochem.mpg.de/tom
tom_deconv	Dimitry Tegunov	https://github.com/dtegunov/tom_deconv
TomSegMemTV	(Martinez-Sanchez et al., 2014)	https://sites.google.com/site/3demimageprocessing/tomosegmemtv
TOMOAND	(Fernández and Li, 2003)	https://sites.google.com/site/3demimageprocessing/tomoand
VTK 6.3.0	(Schroeder et al., 2006)	http://www.vtk.org RRID: SCR_015013
Other		
Quantifoil grids 200 Mesh Copper R2/1	Quantifoil MicroTools	N/A
Whatman Filter Paper 597	Sigma Aldrich	Cat# WHA10311814
Cover Glasses	Carl Zeiss	Cat# 474030-9000-000

LEAD CONTACT AND MATERIAL AVAILABILITY

Further information and requests for resources and reagents should be directed to and will be fulfilled by the Lead Contact, Ruben Fernandez-Busnadiego (ruben.fernandezbusnadiego@med.uni-goettingen.de). Strains and plasmids are available from the authors upon request.

EXPERIMENTAL MODEL AND SUBJECT DETAILS

Yeast Strains and Cell Culture

The yeast strains used in this study are listed in the Key Resources Table.

All strains analyzed were previously reported (Manford et al., 2012; Robinson et al., 1988; Stefan et al., 2011), except YCS2359 (*tcb3*Δ) and YCS2429 (*tcb1*Δ *tcb2*Δ), which were created for this study. Chromosomal deletion of the *TCB3* gene was performed as previously described (Longtine et al., 1998). The *tcb1*Δ *tcb2*Δ double mutant strain (YCS2429) is a segregant from a genetic cross of *tcb1*Δ (ANDY117) and *tcb2*Δ (ANDY120) single mutant strains.

Yeast colonies grown on YPD plates were inoculated in liquid YPD and incubated at 30°C until reaching 0.6 OD_{600}.

Plasmid Construction

The constructs used in this study are listed in the Key Resources Table.

Plasmids pAM43 and pAM44 were previously reported (Manford et al., 2012). For plasmid pCB2, the deletion of the SMP domain of TCB3 (272–479 aa) was created by linearizing the pAM43 vector using the Phusion® HF DNA polymerase (NEB). The sequences of the two oligos used were: 5′- AAGAAACCTTGTCGGATCGCGACATTATGGCTGCTCAATCAAAAGAAG - 3′ and 5′- GCGATCCGA CAAGGTTTCTT -3′. The resulting PCR product was treated with DnpI restriction enzyme (NEB) and later purified using the phenol-chloroform protocol. The vector was re-circularized using Gibson strategy (Gibson et al., 2009) as described in https://openwetware.org/wiki/Gibson_Assembly. The complete reaction was transformed in Max Efficiency® DH5alpha (Invitrogen) and platted on an LB plate containing 100 μg/mL ampicillin. The plasmid was extracted using QIAprep® Spin Miniprep Kit (Qiagen) and sequenced by Microsynth with the oligo : 5′- ATGACTGGCATCAAAGCTCAAGT- 3′.Plasmids were transformed into the strains of interest.

Cells carrying plasmids were grown in complete synthetic media buffered at pH 6.25 with Soerensen buffer, lacking leucine to maintain plasmid selection and with 2% glucose as carbon source.

METHOD DETAILS

Light Microscopy

Cells were grown in the appropriate liquid media and diluted the following day. Recovered cells reaching the exponential phase (OD_{600}=0.6-0.8) were briefly spun down, and confocal Z-stack images were acquired with an LSM780 microscope (Zeiss) at 63× magnification. The images were analyzed using Fiji software (NIH).

Cell Vitrification

Cryo-EM grids (R2/1, Cu 200 mesh grid, Quantifoil microtools) were glow discharged using a plasma cleaner (PDC-3XG, Harrick) for 30 s and mounted on a Vitrobot Mark IV (FEI).

A 3.5 μl drop of yeast culture was deposited on the carbon side of the grid before being blotted from the back using filter paper (Whattman 597) at force setting 9 for 10 s. The grids were immediately plunged into a liquid ethane/propane mixture at liquid nitrogen temperature and stored in grid boxes submerged in liquid nitrogen until usage.

Cryo-Focused Ion Beam Milling

Vitrified grids were mounted into Autogrid carriers (FEI), held in place by a copper ring. They were subsequently inserted in a dual-beam Quanta 3D cryo-FIB / scanning electron microscope (SEM) (FEI) using a transfer shuttle and a cryo-transfer system (PP3000T, Quorum). Inside the microscope, the sample was kept at -180°C using a cryo-stage throughout the milling process.

To protect the sample from unwanted damage by the ion beam, a layer of organic platinum was deposited on top of the grid using a gas injection system from a 13.5 mm distance for 9 s.

Small groups of cells located near the center of the grid square were targeted for milling. Milling was done at a 20° tilt. Several sequential steps were taken, starting with the Ga^{2+} ion beam at 30 kV and 500 pA beam current for rough milling, down to 30 kV and 30 pA for fine milling.

The final lamellae were around 14 μm wide and 150–250 nm thick. SEM imaging at 5 kV and 13 pA was used to monitor the milling process. The final thickness was reached when the lamellae lacked contrast at 3 kV and 10 pA.

Cryo-Electron Tomography

Cryo-FIB lamellae were imaged at liquid nitrogen temperature in a Polara (*tcb3Δ* + Tcb3 SMPΔ-GFP, *tcb3Δ* + Tcb3 C2Δ-GFP, *tcb3Δ* + Tcb3-GFP cells, as well as one experiment of *tcb1/2/3Δ, tcb3Δ and tcb1Δ* cells) or Titan Krios (all other cases) cryo-electron

microscopes (FEI) equipped with 300 kV field emission guns, post column energy filters (Gatan) and K2 Summit direct electron detectors (Gatan).

Low magnification (4500 ×, 27-Å pixel size in Polara; 3600 ×, 40-Å pixel size in Titan Krios; -100 μm defocus) images of the lamellae were taken to identify regions of interest. Tilt series were recorded using SerialEM software (Mastronarde, 2005) at higher magnification (34,000 ×, 3.509-Å pixel size in Polara; 42,000 ×, 3.42-Å pixel size in Titan Krios; -5 μm defocus), typically from -46° to +64° with increments of 2°. For one experiment of the *tcb1/2/3Δ*, *tcb3Δ* and *tcb1Δ* conditions, tilt series were recorded in Polara at 22,500 x (0.522-Å pixel size) using -5 μm defocus.

The cameras were operated in dose fractionation mode, producing frames every 0.2 s. 1/cos scheme was used to increase the exposure time at higher tilt angles, resulting in exposure times of 1–2 s per projection image. Tilt series acquired in the Titan Krios for the *tcb1/2/3Δ*, Δtether, WT heat shock and *tcb1/2/3Δ* heat shock conditions were recorded using a dose-symmetric scheme (Hagen et al., 2017). All other tilt series were acquired using a unidirectional scheme. In all cases, the total dose per tilt series was ~120 $e^-/Å^2$.

K2 frames were aligned using in house software (K2Align) based on previous research (Li et al., 2013) and available at https://github.com/dtegunov/k2align. The tilt series were aligned using patch-tracking and reconstructed by weighted back projection in IMOD (Kremer et al., 1996). Tomograms were binned twice, to a final voxel size of ~1.4 nm (2.1 nm for the tilt series recorded at 22,500 x). For visualization, the tomographic slices shown in all figures except Figures S2A, S2D, 6A, 6B, and 6C were denoised using a non-linear anisotropic filter (Fernández and Li, 2003). The contrast of Figures S2A, S2D, 6A, 6B, and 6C was enhanced using a deconvolution filter (https://github.com/dtegunov/tom_deconv) executed in MATLAB (MathWorks) using the functionalities of the TOM toolbox (Nickell et al., 2005).

Membrane Segmentation and Surface Generation

Membranes were automatically segmented along their middle line using TomoSegMemTV (Martinez-Sanchez et al., 2014), and refined manually using Amira (FEI). The intermembrane volumes were manually segmented. Segmentations consisted of binary voxel masks, which were smoothed using a Gaussian kernel with σ of 1 voxel. From these segmentations, isosurfaces were generated using the Marching Cubes algorithm (Lorensen and Cline, 1987) with an isosurface level of 0.7. Finally, isosurfaces were transformed into single-layer triangle mesh surfaces delineating the membranes. On average, surface triangles had an area of 0.6 ± 0. 4 nm^2 (mean ± SD) for the PM and 0.7 ± 0. 4 nm^2 (mean ± SD) for the cER membrane.

Membrane Curvature Determination

Curvature was estimated locally for each surface triangle using a novel algorithm (Kalemanov et al., 2019). Briefly, we used tensor voting with a neighborhood of triangles defined by the *RadiusHit* parameter to denoise the surface normal vectors and then estimate the principal directions and curvatures for each surface triangle center. The maximal (κ_1) and the minimal (κ_2) principal curvatures were combined into a single scalar value for each triangle by calculating curvedness (Koenderink and van Doorn, 1992):

$$Curvedness = \sqrt{\frac{\kappa_1^2 + \kappa_2^2}{2}}.$$

A *RadiusHit* value of 10 nm was used, limiting the size of the smallest feature measured reliably to a radius of 10 nm, i.e. a curvedness of 0.1 nm^{-1}. Higher values were excluded from the analysis. Values within 1 nm to the surface border were removed, as curvature estimation was not reliable in these areas. The total number of cER triangles where curvature was measured in each condition is shown in Table S1. Membrane curvature was visualized using ParaView (Ahrens et al., 2005).

Intermembrane Distance Measurements

To calculate distances between two membranes, surfaces following the cytosolic side of all membranes were generated. Denoised normal vectors from the first surface (PM in ER-PM MCS, mitochondria in ER-mitochondria MCS, vacuole in nucleus-vacuole MCS) were generated (see above) and extended until their intersection with the second surface. The Euclidean distance between the source triangle center and the intersection point was calculated as the intermembrane distance. These measurements were performed for all triangles of the first surface for which a normal vector intersected with the second surface within 50 nm (Table S1 shows the total number of measurements for each condition).

To calculate cER thickness, a surface following the luminal side of the cER membrane was generated. Denoised PM surface normal vectors were extended until their first and second intersections with the cER membrane surface. The Euclidean distance between the intersections was calculated as the cER thickness. These measurements were performed for all triangles of the PM for which cER thickness was within 80 nm (Table S1 shows the total number of measurements for each condition).

Intermembrane distances at ER-PM, ER-mitochondria and nucleus-vacuole MCS were defined as the distances between the cytosolic leaflets of the membranes. cER thickness was calculated as the distance between the luminal leaflets of the cER membrane. Given that the triangle-mesh surfaces go through the centers of the voxels on the edge of the segmentations, one voxel was added to all distances for correction.

cER Peak Morphology and Density Quantification

Measurements of cER peak height, radius and distance to the PM were done in tomographic slices using the measuring tool built in IMOD. The cER peak density was calculated per MCS by dividing the number of cER peaks by half of the cER surface area, since cER peaks were found only on the side of cER facing the PM. The cER surface area was calculated by summing up the areas of all triangles in the cER surface (the total cER surface area for each condition is shown in Table S1).

Membrane Modeling

To compute the change in the free energy barrier associated to the extraction of a lipid from a highly curved membrane as compared to the extraction from a flat membrane, we consider that the extraction is performed by a lipid transport protein (LTP). The lipid extraction reaction undergoes a series of steps, initiated by the binding and partial insertion of the LTP into the membrane (absorption), followed by the lipid extraction and detachment of the protein-lipid complex from the membrane (desorption) (Dittman and Menon, 2017; Wong et al., 2017). Hence, the total free energy required for lipid extraction, ε_{extr}, corresponds to the change of the free energy of the system (including both the membrane and the LTP) resulting from the extraction of lipids by one lipid transfer reaction of a single LTP.

We can split this free energy of lipid extraction in two terms. The first one, denoted by ε_0, corresponds to contributions independent from membrane stress, such as hydrogen bonding and electrostatic interactions occurring during protein insertion, as well as LTP-lipid chemical interactions occurring both within the membrane and in solution. The second term, denoted by ε_{el}, corresponds to the elastic contribution dependent on membrane stress (Campelo and Kozlov, 2014). We denote by $\Delta\varepsilon_{extr}$ the change in the free energy of lipid extraction from a highly curved membrane (associated with a total curvature $J = 2/R$, where R is the radius of curvature, and the local curvature at the tip of the peak is considered to be locally spherical; $1/R$ is equivalent to the curvedness for κ_1=κ_2) with respect to the extraction from a flat membrane ($J = 0$). Since ε_0 is independent of the curvature or elastic stresses within the membrane, it follows that $\Delta\varepsilon_{extr}(J) = \Delta\varepsilon_{el}(J) = \varepsilon_{el}(J) - \varepsilon^0_{el}$, where $\varepsilon^0_{el} = \varepsilon_{el}(J = 0)$.

To calculate the elastic part of the free energy of lipid extraction as a function of the membrane curvature, $\varepsilon_{el}(J)$, we consider that the main contributions to this energy arise from the shallow insertion of a domain of the LTP into the cytoplasmic leaflet of the cER membrane, $\varepsilon_{el,prot}(J)$, and from the elastic energy relaxation of the extracted lipids, $\varepsilon_{el,lip}(J)$.

We consider an elastic model of the lipid monolayer as a three-dimensional, anisotropic elastic material (Campelo et al., 2008) to compute the internal strains and stresses generated by the partial insertion of the LTP into the membrane, and hence the accumulated elastic energy, $\varepsilon_{el,prot}(J)$ (Campelo and Kozlov, 2014; Campelo et al., 2008). One can define the curvature sensitivity parameter, α_J, which accounts for the ability of a given protein domain to sense membrane curvature, and depends on the way the membrane curvature has been generated (Campelo and Kozlov, 2014). It has been computationally shown that the elastic energy of insertion can be written as $\varepsilon_{el,prot}(J) = \varepsilon^0_{el,prot} - \alpha_J J$, which allow us to write, $\Delta\varepsilon_{extr,prot}(J) = -\alpha_J J$, given that $\varepsilon^0_{el,prot}$ is the curvature-independent part of the protein insertion energy.

To compute the elastic energy relaxation of the lipid (or lipids) extracted by the LTP, we use the Helfrich model of membrane curvature energy (Helfrich, 1973). According to this model, we can express the change in the free energy relaxation of N lipids, each of which having a cross-sectional surface area, $a_0 \approx 0.6\ nm^2$, and an effective spontaneous curvature (Zimmerberg and Kozlov, 2006), ζ_s, as $\Delta\varepsilon_{extr,lip}(J) = \varepsilon_{extr,lip}(J) - \varepsilon_{extr,lip}(J = 0) = -\frac{\kappa_m}{2} N a_0 \left(J^2 - 2\,J\,\zeta_s\right)$, where $\kappa_m \approx 10\ k_BT$ is the bending rigidity of a single monolayer (Niggemann et al., 1995). k_BT is the product of the Boltzmann constant and the absolute temperature. We do not consider here a possible dependence of the lipid free energy change on the lateral tension of the membrane, since we assume that there is no membrane tension gradient appearing as a result of membrane bending and therefore the membrane is under the same lateral tension regardless of its curvature.

In total, we can write down the free energy change for lipid extraction by an LTP as a function of the curvature of the donor membrane as

$$\Delta\varepsilon_{extr}(J) = -\alpha_J J - \frac{\kappa_m}{2} N a_0 \left(J^2 - 2\,J\,\zeta_s\right) \qquad \text{(Equation 1)}$$

From the free energy change for lipid extraction, we can estimate the change in the rate of lipid extraction from a curved membrane relative to the flat membrane. Assuming Arrhenius kinetics, the rate of lipid extraction can be written as $r(J) = Ae^{-\varepsilon_{extr}(J)/k_BT}$, where A is the Arrhenius prefactor, which we consider to be curvature-independent (Dittman and Menon, 2017). Hence, the change in the rate of lipid extraction from a curved membrane relative to the flat membrane can be written as

$$\frac{r(J)}{r(0)} = e^{\frac{-\Delta\varepsilon_{extr}(J)}{k_BT}} \qquad \text{(Equation 2)}$$

The value of the curvature sensitivity parameter can be computationally calculated (Campelo and Kozlov, 2014), and depends on different parameters, in particular, on the size and depth of the insertion. Importantly, it depends on the way the membrane curvature has been generated. For membrane curvature generated by an externally applied torque (e.g. by protein scaffolds or by protein insertions), a cylindrical insertion of radius 0.5 nm, length 2 nm, and inserted 0.8 nm into the monolayer, the curvature sensitivity parameter has been calculated to be $\alpha_J = 28\ k_BT\ nm$ (Campelo and Kozlov, 2014). Depending on the geometrical parameters, the curvature sensitivity can range between $\alpha_J \approx 10$–$50\ k_BT\ nm$ (Campelo and Kozlov, 2014).

The relative dependence of the two contributions to the free energy change in Equation (1) can be quantitated by the ratio $r_{p/l} = \frac{\Delta\varepsilon_{extr,prot}(J)}{\Delta\varepsilon_{extr,lip}(J)} = \frac{2\alpha_J}{\kappa_m N a_0}\frac{1}{J-2\zeta_s}$. For the characteristic parameters mentioned above ($\alpha_J = 28\ k_BT\ nm$; $\kappa_m = 10\ k_BT$; $a_0 = 0.6\ nm^2$; $N = 1$; $J = 2/10\ nm^{-1}$), the relative contribution to the extraction free energy of the protein insertion elastic energy is much higher than that of the lipid curvature stress for a wide range of lipid spontaneous curvatures (Figure S3A). The lipid bending stress only dominates for protein insertions with a relatively low curvature sensitivity extracting many lipids with a very large negative spontaneous curvature (conical lipids such as diacylglycerol, which has a spontaneous curvature $\zeta_{s,DAG} \approx -1\ nm^{-1}$ (Szule et al., 2002)) (Figure S3B).

The plots of the calculated lipid extraction energy changes as a function of the membrane curvature, J, and of the curvature sensitivity parameter, α_J, for the extraction of both cylindrical ($\zeta_s = 0\ nm^{-1}$) and highly conical ($\zeta_s = -1\ nm^{-1}$) lipids are shown in Figure S3C. In addition, we present the computed values of the lipid extraction energy from a highly curved cER peak (radius of curvature $R_{curv} = 10\ nm$) as a function of the curvature sensitivity parameter for a cylindrical lipid (Figure S3D) and as a function of the lipid spontaneous curvature for $\alpha_J = 28\ k_BT\ nm$ (Figure S3E). Altogether, we can conclude that, for standard physiological conditions, the extraction of lipids by LTPs is more efficient when occurring from highly curved membranes because these proteins have a better insertion affinity into highly bent membranes associated with a large bending moment in the monolayer facing the PM.

Calculation of Lipid Extraction Currents

We define the lipid current as the total number of lipids extracted along the entire cER membrane per unit time, $I = \int r(J)dA$, where the local extraction rate, $r(J)$, is integrated along the entire cER membrane, which has a total surface area A_{cER}. We consider that the cER membrane is formed by (i) highly curved peaks of constant curvature, J, with an area A_{peak}, and (ii) a flat region of zero curvature, with an area $A_{flat} = A_{cER} - A_{peak}$. Hence, the total lipid current is the sum of the lipid currents coming from the peaks and the flat part, $I = I_{peak} + I_{flat}$, where the peak current is $I_{peak} = r(J)A_{peak}$, and the flat current, $I_{flat} = r(0)A_{flat} = r(0)(A_{cER} - A_{peak})$.

We can relate A_{peak} to the experimentally measured peak number density, ϕ_{peak}, (Figure 2I) as $A_{peak} = \phi_{peak}A_{cER}a_{peak}$, where a_{peak} is the average surface area of a single cER peak, which can be estimated from our cryo-tomograms to be $a_{peak} \approx 400\ nm^2$ (by modeling the peak as a conic structure of base radius $\approx 10\ nm$ and height of $\approx 7\ nm$, and hence average total curvature, $J = 0.2\ nm^{-1}$). Moreover, if we define the standard lipid current as the lipid current for a flat cER having a total surface area A^0_{cER} and with no peaks, $I_0 = r(0)A^0_{cER}$, we can express the peak, flat, and total lipid currents, respectively, as

$$I_{peak} = I_0\frac{A_{cER}}{A^0_{cER}}\frac{r(J)}{r(0)}\phi_{peak}a_{peak}, \qquad \text{(Equation 3a)}$$

$$I_{flat} = I_0\frac{A_{cER}}{A^0_{cER}}(1 - \phi_{peak}a_{peak}), \qquad \text{(Equation 3b)}$$

$$I = I_0\frac{A_{cER}}{A^0_{cER}}\left[1 + \left(\frac{r(J)}{r(0)} - 1\right)\phi_{peak}a_{peak}\right]. \qquad \text{(Equation 3c)}$$

In Figure S4B we plot the total lipid current relative to the standard lipid current, I/I_0,as a function of the peak density, ϕ_{peak}, and of the relative cER surface area $\overline{A}_{cER} = \frac{A_{cER}}{A^0_{cER}}$, for the computed value of the lipid extraction rate at the peaks, $\frac{r(J)}{r(0)} = 500$. We can see that the total amount of lipids being extracted from the cER depends not only on the number density of peaks per unit area, ϕ_{peak} (horizontal axis in Figure S4B), but also on the total amount of cER surface area (plotted relative to WT levels in Figure S4B, vertical axis). When heat shocking WT cells, peak density increases from $\approx 4\ \mu m^{-2}$ to $\approx 22\ \mu m^{-2}$ (Figure 2I), and the total lipid current concomitantly increases about 3-fold.

It is also informative to evaluate the relative contribution to the lipid current between the peaks and the flat part, which, from Equations (3a) and (3b), is

$$I_{peak}\Big/I_{flat} = \frac{r(J)}{r(0)}\frac{\phi_{peak}a_{peak}}{1 - \phi_{peak}a_{peak}}. \qquad \text{(Equation 4)}$$

Using the experimentally determined density of cER peaks, $I_{peak}/I_{flat}(WT) \approx 0.8$, whereas $I_{peak}/I_{flat}(WT\ HS) \approx 4.4$. Therefore, in WT cells the total number of lipids extracted from cER peaks is roughly equivalent to that of the flat parts, but lipid extraction from cER peaks becomes dominant upon heat shock due to the observed increase in cER peak density (Figure S4B).

PM Integrity Assays

Cells were grown at 26°C to mid-log phase in rich media (YPD) or selective drop out media (YND) as required. Cells were shifted to 42°C for 10 min and ($1OD_{600}$ equivalents) were collected, resuspended in PBS, and incubated with propidium iodide (Invitrogen) for 10 min. Cells were then washed twice with ddH_2O and analyzed by flow cytometry (BD LSR II). For each condition, 10,000 cells were measured. Background was determined by analyzing each of the cell strains prior to staining with propidium iodide. Four

independent biological repeats were performed for all conditions. We noted that PM integrity defects were enhanced in mutant cells grown in YPD compared to YND, consistent previous results (Omnus et al., 2016).

QUANTIFICATION AND STATISTICAL ANALYSIS

For intermembrane distances (Figures 1E and 2G), cER thickness (Figure 2H) and cER curvedness (Figure 3E), a large number of measurements (Table S1) was performed automatically for surface triangles (see above). The figures show the complete distribution of values as violin plots (Figures 1E, 2G, and 2H) or histograms (Figure 3E), including all measurements for all MCS analyzed. For violin plots, a white dot represents the median, a black slab the interquartile range, and a black line 1.5x the interquartile range. The histogram in Figure 3E shows the relative frequency of exceedance (calculated as 1 – cumulative relative frequency) of cER curvedness averaged across MCS for each bin (solid line) ± SE (shaded area). Bin width was 1 nm^{-1}. The frequency was weighted by triangle area and normalized to the total surface area.

Because measurements of neighboring triangles are not statistically independent from each other, statistical comparisons between conditions were performed using the mean of the measurements for each MCS. Consequently, in the text we report N as the number of MCS analyzed. In all cases, normality was assessed using Shapiro-Wilks test. To estimate statistical significance we used t-test for normally distributed samples and Mann-Whitney-U test for non-normally distributed samples.

Figure 2I shows mean peak density per μm^2 cER surface area for each condition ± SE. cER peak morphology measurements (Figure S2C) were displayed by box plots. For PM integrity assays (Figures 5A, 6E, and S4A), average values from four independent experiments were analyzed. Bar plots show mean values for each condition ± SE.

These data were statistically analyzed as reported above. The number of independent biological experiments, MCS studied and measurements performed are reported in Table S1.

DATA AND CODE AVAILABILITY

The tomogram displayed in Figure 5A showing cER-PM MCS in a heat-shocked WT cell has been deposited at the Electron Microscopy Data Base (EMDB) with accession numbers EMD-10378 (raw tomogram) and EMD-10379 (tomogram filtered by non-linear anisotropic diffusion, as in Figure 5A).

The Python software used to estimate membrane curvature and calculate distances between membranes is available at https://github.com/kalemaria/pycurv. The software depends on the following external packages: Pyto (Lučić et al., 2016), Graph-tool (Peixoto, 2017) and VTK (Schroeder et al., 2006). Graph-tool and VTK are respectively available at https://graph-tool.skewed.de/ and https://vtk.org/.

Developmental Cell, Volume *51*

Supplemental Information

Tricalbin-Mediated Contact Sites Control ER Curvature to Maintain Plasma Membrane Integrity

Javier Collado, Maria Kalemanov, Felix Campelo, Clélia Bourgoint, Ffion Thomas, Robbie Loewith, Antonio Martínez-Sánchez, Wolfgang Baumeister, Christopher J. Stefan, and Rubén Fernández-Busnadiego

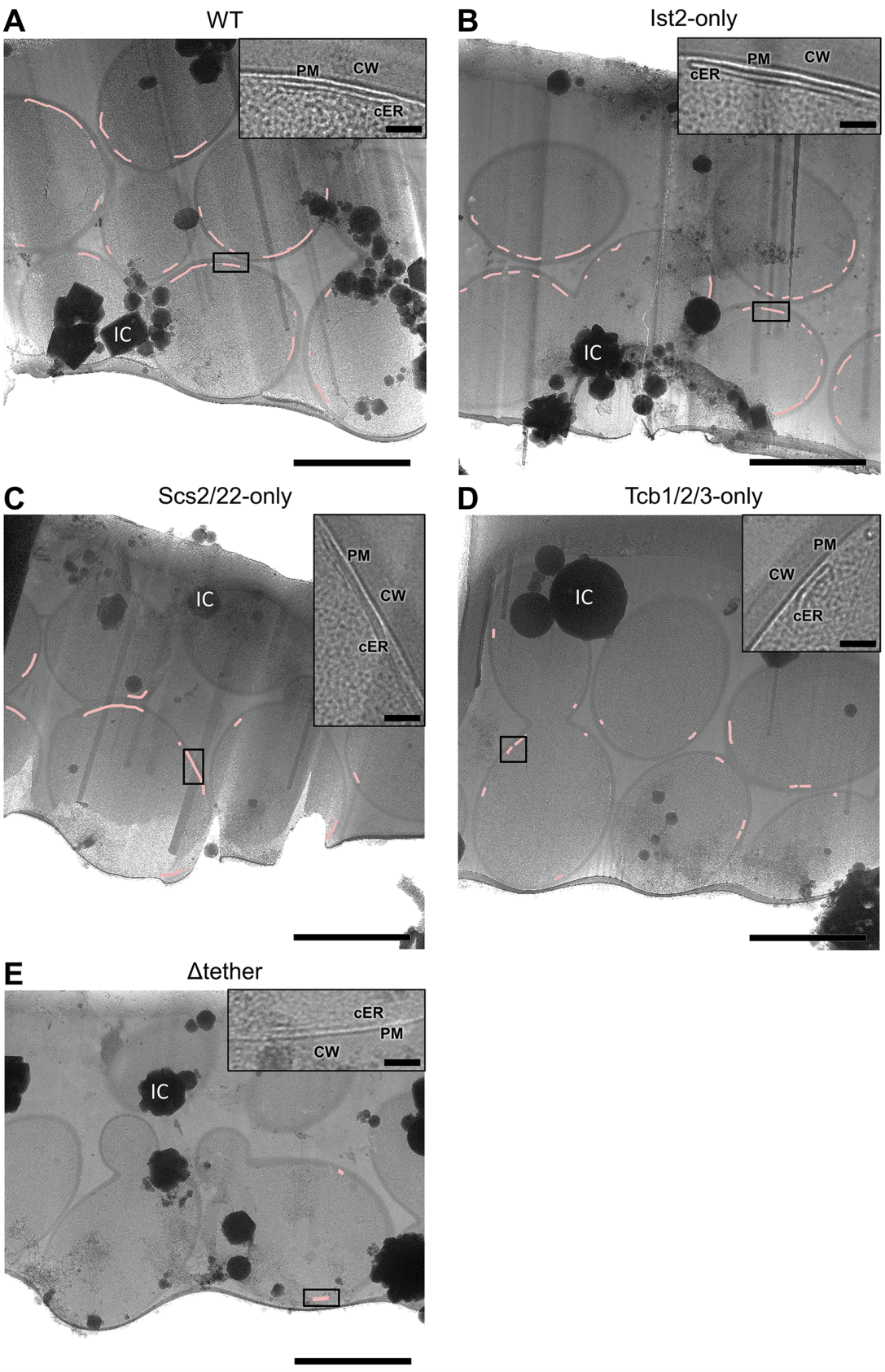
A
WT
PM
CW
cER
IC
B
Ist2-only
PM
CW
cER
IC
C
Scs2/22-only
IC
PM
CW
cER
D
Tcb1/2/3-only
IC
PM
CW
cER
E
Δtether
cER
PM
CW
IC

Figure S 1: Cryo-EM Overview Images of Cryo-FIB Lamellae. Related to Figure 2. Panels (A-E) show low magnification cryo-EM images of cryo-FIB lamellae milled through groups of cells. The profile of individual cells is marked by their cell wall. Pink lines mark cER (magnified in insets). CW: cell wall; cER: cortical ER; IC: ice crystal surface contamination; PM: plasma membrane. (**A**) WT cells, (**B**) Ist2-only cells, (**C**) Scs2/22-only cells, (**D**) Tcb1/2/3-only cells, (**E**) ∆tether cells. Scale bars: 3 µm (main panels), 500 nm (insets).

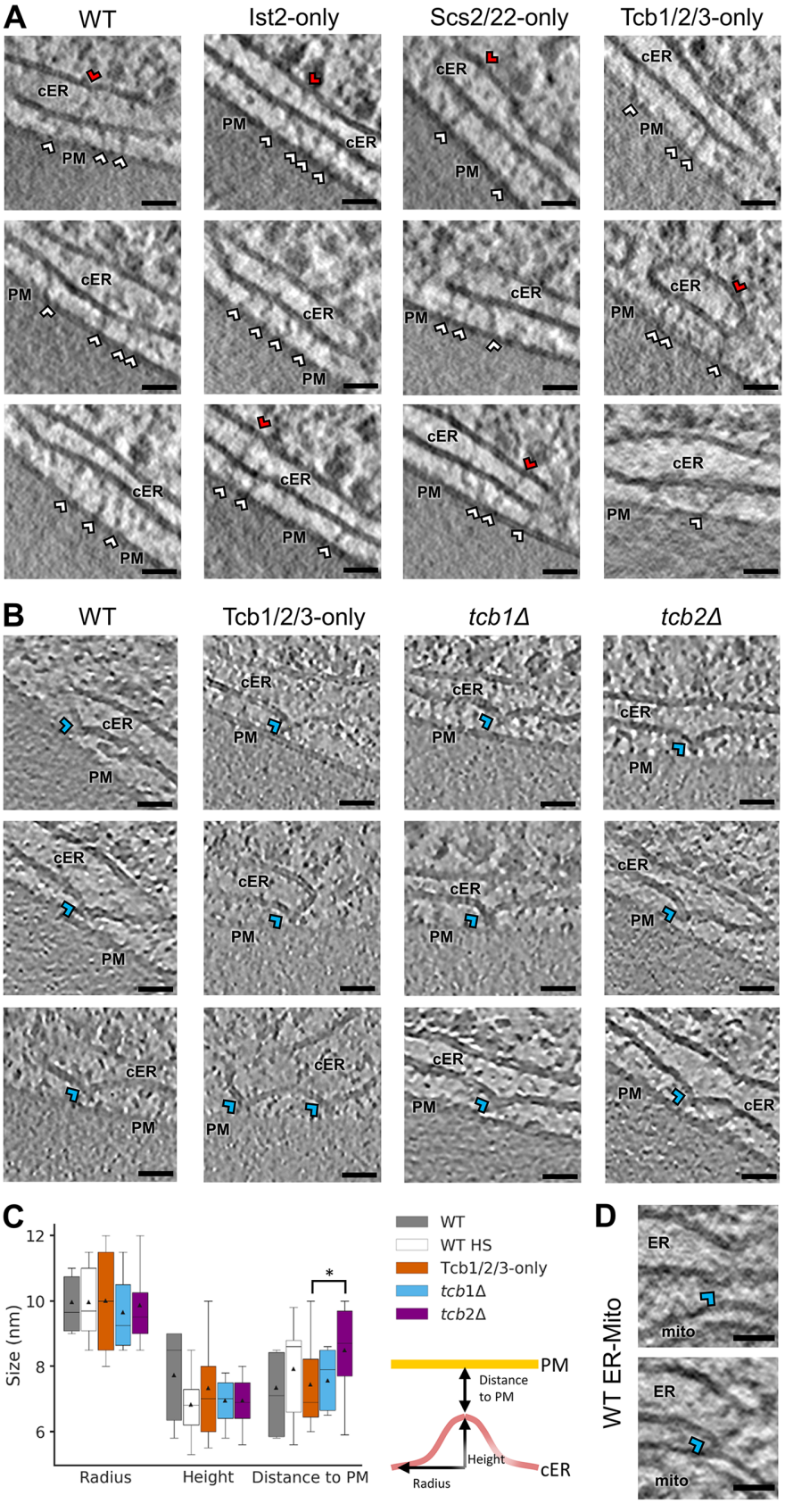
A
WT
Ist2-only
Scs2/22-only
Tcb1/2/3-only
cER
PM
B
WT
Tcb1/2/3-only
tcb1Δ
tcb2Δ
C
Size (nm)
12
10
8
6
Radius
Height
Distance to PM
*
WT
WT HS
Tcb1/2/3-only
tcb1Δ
tcb2Δ
PM
Distance to PM
Height
Radius
cER
D
WT ER-Mito
ER
mito

Figure S 2: High Magnification Images of ER-PM MCS. Related to Figure 1, Figure 2, Figure 4 and Figure 5. Gallery of magnified (**A**) tether structures and (**B**) cER peaks found in the different strains. White arrowheads: ER-PM tethers; red arrowheads: intraluminal cER tethers; blue arrowheads: cER peaks. cER: cortical ER; PM: plasma membrane. The images show 1.4 nm-thick tomographic slices. (**C**) Quantification of cER peak morphology in terms of radius, height and distance to the PM. All strains in which cER peaks were found are displayed except *tcb3Δ* + Tcb3-GFP. Boxes represent all measurements per strain: 6 (WT), 21 (WT HS), 24 (Tcb1/2/3-only), 7 (*tcb1*Δ) and 15 (*tcb2*Δ) cER peaks. The horizontal lines of each box represent 75% (top), 50% (middle) and 25% (bottom) of the values, whiskers 95% (top) and 5% (bottom), and a black triangle the average value. N = 6 (WT), 7 (WT HS), 16 (Tcb1/2/3-only), 5 (*tcb1*Δ) and 10 (*tcb2*Δ) cER-PM MCS (cER peak morphology was analyzed in 7 additional Tcb1/2/3-only and 5 *tcb2Δ* tomograms that were not used for other quantifications). * indicates $p < 0.05$ by unpaired t-test. (**D**) ER peaks (blue arrowheads) at ER-mitochondria MCS in WT cells. mito: mitochondrion. The contrast of the images in (A) and (D) was enhanced using a deconvolution filter. Scale bars: 25 nm.

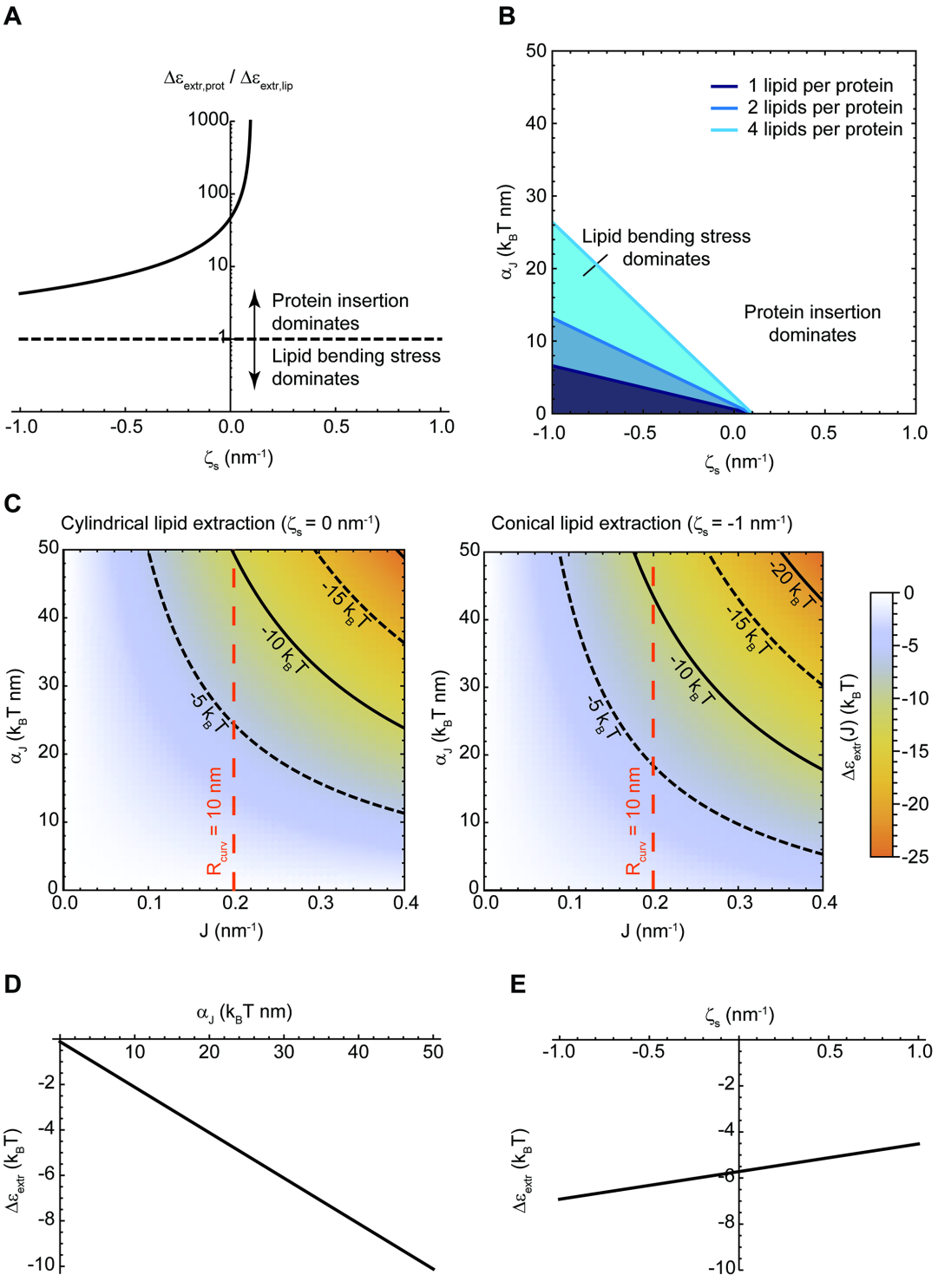

Figure S 3: Theoretical Model of How cER Peaks May Facilitate the Extraction of Lipids from the cER Membrane. Related to Figure 3 and STAR Methods. (**A**) Contribution of the protein insertion energy, $\Delta\varepsilon_{extr,prot}(J)$, to the total free energy change for lipid extraction relative to the elastic energy

relaxation of lipid extraction, $\Delta\varepsilon_{extr,lip}(J)$, for different values of the effective spontaneous curvature of the extracted lipids, ζ_s. When the relative contribution is larger than one, protein insertion energy dominates, whereas when the ratio is smaller than one, the elastic (bending) stress of the lipids dominates. (**B**) Transition line separating the regime of protein insertion domination (white region) from the regime of lipid bending stress domination (blue-shaded regions) for different values of the effective spontaneous curvature of the extracted lipids, ζ_s, and of the protein curvature sensitivity, α_J. The three lines correspond to the transition lines for extraction of 1, 2, or 4 lipids per protein (dark to light blue lines, see legend). (**C**) Energy barrier of lipid extraction from a curved membrane relative to a flat membrane (color code), $\Delta\varepsilon_{extr}(J)$, as a function of the total curvature of the membrane, J, and of the protein curvature sensitivity, α_J. (Left) Extraction of a cylindrical lipid with no effective spontaneous curvature, $\zeta_s = 0$. (Right) Extraction of a conical lipid with a large negative effective spontaneous curvature, $\zeta_s = -1\ nm^{-1}$. Isoenergy lines are plotted on both graphs (solid and dashed black lines), as well as a dashed red line marking the experimentally observed total curvature of the cER peaks. k_BT is the product of the Boltzmann constant and the absolute temperature. (**D**) Energy barrier for extraction of a cylindrical lipid ($\zeta_s = 0$) from a cER peak ($J = 0.2\ nm^{-1}$) relative to a flat membrane, $\Delta\varepsilon_{extr}$, as a function of the protein curvature sensitivity, α_J. (**E**) Energy barrier for lipid extraction from a cER peak ($J = 0.2\ nm^{-1}$) relative to a flat membrane, $\Delta\varepsilon_{extr}$, as a function of the effective spontaneous curvature of the extracted lipids, ζ_s, for the case of a lipid transfer protein with a curvature sensitivity, $\alpha_J = 28\ k_BT\ nm$.

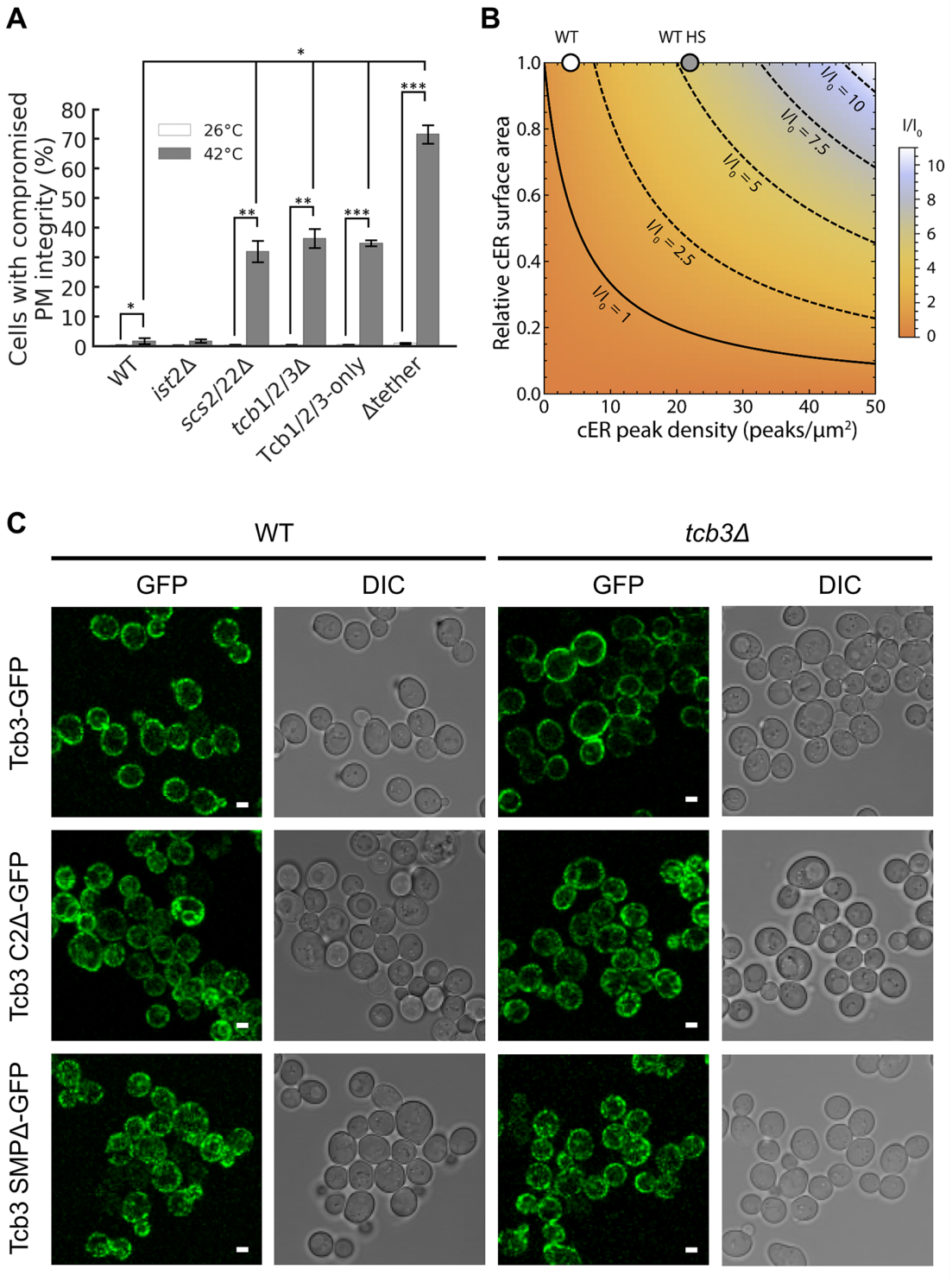

Figure S 4: PM Integrity Assays in Other Tether Mutants, Relative Contribution of cER Peaks and Flat Membranes to Lipid Transfer, and Localization of Tcb3 Truncations. Related to Figure 3, Figure 5, Figure 6 and STAR Methods. (**A**) PM integrity measurements of Ist2, Scs2/22, Tcb and

Δtether mutants upon 10 min incubation at 42 °C (right). The plot shows average values (white/grey bars) for each condition ± SE (error bars). *, ** and *** respectively indicate $p < 0.05$, $p < 0.01$ and $p < 0.001$ by Mann-Whitney-U test (for WT 42 °C data, which was not normally distributed) or unpaired t-test (for all other conditions). Four independent biological repeats were performed for all conditions. (**B**) Plot of I/I_0 (color coded), the lipid extraction current from cER peaks and flat parts of the cER membrane ($I=I_{peak} + I_{flat}$) relative the current from a completely flat membrane (I_0). The calculation was performed considering a 500 fold facilitation of lipid extraction by cER peak formation (Figure 3F) and modeling the peak as a conic structure of base radius of ~10 nm and height of ~7 nm (Figure S 2C). The X-axis shows the density of cER peaks, which is experimentally determined from cryo-ET data. The Y-axis shows the area of cER relative to WT, i.e. = 1 for WT cells and < 1 for conditions with reduced total levels of cER (e.g. Tcb1/2/3-only). The graph shows that for WT cells, the lipid flows from cER peaks and flat membranes are roughly equivalent ($I/I_0 \approx 1.8$; white circle). However, lipid flow from cER peaks dominates in heat-shocked WT cells (WT HS) due to the observed ~6-fold increase in cER peak density ($I/I_0 \approx 5.4$; grey circle). Note that increasing cER peak density can only substantially increase I/I_0 when total levels of cER are high. (**C**) Light microscopy imaging by GFP fluorescence (mid-section confocal images; left) and DIC (right) of WT and *tcb3Δ* cells expressing the following constructs: full length Tcb3-GFP, Tcb3 C2Δ-GFP and Tcb3 SMPΔ-GFP. Scale bars: 2 µm.

Condition	Number of experiments	Number of MCS	Total number of intermembrane distance measurements	Total number of cER thickness measurements	Total number of cER curvature measurements	Total cER area analyzed (μm²)
WT	2	6	685,160	531,487	2,612,817	1.7
WT HS	2	7	-	-	-	1.7
Ist2-only	2	5	663,763	525,115	2,327,393	1.5
Scs2/22-only	2	5	478,590	388,246	1,824,833	1.1
Tcb1/2/3-only	3	9	552,956	368,510	2,053,182	1.3
Δtether	1	4	-	-	-	0.16
tcb1Δ	2	5	-	-	-	0.9
tcb2Δ	2	5	-	-	-	0.7
tcb3Δ	2	5	-	-	-	0.8
tcb1/2Δ	2	5	-	-	-	0.8
tcb1/2/3Δ	2	5	-	-	-	1.4
tcb1/2/3Δ HS	2	5	-	-	-	0.7
tcb3Δ + Tcb3-GFP HS	2	3	-	-	-	0.3
tcb3Δ + Tcb3-SMPΔ-GFP HS	2	3	-	-	-	0.4
tcb3Δ + Tcb3-C2Δ-GFP HS	2	3	-	-	-	0.4
ER-Mito	3	5	81,124	-	-	-
Nuc-Vac	2	5	362,899	-	-	-

Table S 1: Statistics of Cryo-ET Experiments. Related to Figure 1, Figure 2, Figure 3, Figure 4, Figure 5 and Figure 6. The column “Number of MCS” refers to ER-PM MCS in all cases except ER-mitochondria (ER-Mito) and nucleus-vacuole (Nuc-Vac) MCS. In the following columns, “total” indicates aggregated values for all tomograms analyzed in each condition. The total number of intermembrane distance measurements reflects the number of triangles from the first membrane (PM in ER-PM MCS, mitochondria in ER-mitochondria MCS, vacuole in nucleus-vacuole MCS) from which normal vectors

intersected the second membrane. The total number of cER thickness measurements reflects the number of triangles from the PM from which normal vectors intersected the cER membrane twice. The total number of cER curvature measurements reflects the number of triangles of the cER membrane. The total cER area analyzed is the sum of the area of all cER triangles. For the calculation of cER peak density, the number of cER peaks per condition was divided by half of the total cER area, as cER peaks were only found on the side of the cER membrane facing the PM. For simplicity, values are only shown for the conditions plotted (Figure 1E, Figure 2G, H, I, Figure 3E and Figure 6D).

2.3 Reliable estimation of membrane curvature for cryo-electron tomography

Maria Salfer, Javier Collado, Wolfgang Baumeister, Rubén Fernández-Busnadiego & Antonio Martínez-Sánchez, ***PLoS Comput Biol***, 2020, DOI, URL.

Summary

Membrane curvature is crucial for many cellular functions like cell division, organelle shaping and MCS. Cryo-ET is a leading technique for 3D visualization and analysis of membrane morphology in a close-to-native state and molecular resolution. However, different artifacts are introduced during image acquisition and tomogram analysis, such as quantization noise and membrane holes. Available curvature estimation methods cannot cope with some of these artifacts and thus cannot be applied directly to membrane segmentations from cryo-ET. In this publication, we present PyCurv: a software package for reliable estimation of curvature of membranes and other biological surfaces from cryo-ET and other imaging techniques. This package generalizes and improves the algorithms for curvature estimation developed in Sections 2.1 and 2.2.

The PyCurv workflow consists of the following steps. (1) From a membrane segmentation, a single-layered, signed triangle mesh surface is extracted. (2) A spatially embedded graph is generated to facilitate the calculation of geodesic neighborhood and distances. (3) Surface normals are denoised for each triangle center using a geodesic neighborhood of triangles defined by a parameter corresponding to the radius of the smallest feature of interest. (4) The denoised normals and the geodesic neighborhood are used to estimate the principal directions, principal curvatures and combined measures such as curvedness. We developed four algorithms that are based on tensor voting, aiming to increase the sensitivity to small membrane details visible by cryo-ET and the robustness to quantization noise.

First, we extensively evaluated the performance of our algorithms on synthetic surfaces in comparison with three currently existing methods. Then, we applied our best algorithm and the existing ones to biological membranes from cryo-ET data. Moreover, we applied PyCurv to surfaces of *C. elegans* embryo cells from confocal light microscopy and human brain cortex from MRI. Among all algorithms analyzed, PyCurv was the most accurate and robust to noise not only for cryo-ET data, but also for data originating from other imaging techniques. To conclude, PyCurv is a versatile open-source software package that can be used to reliably estimate membrane and surface curvature in a large variety of applications.

Author contribution

I contributed to find the best solution for membrane curvature estimation using cryo-ET data. I developed and implemented the PyCurv algorithms, including benchmarking on synthetic data and comparison to the three existing ones. I applied all algorithms to new biological data from cryo-ET, light microscopy and MRI, visualized and analyzed the results. I wrote and revised the manuscript, prepared the figures and a video according to the requirements of the co-authors. I publicly shared the PyCurv code, documentation and example data on GitHub. Finally, I deposited the used tomogram and segmentation files into the EM Data Bank with the help from co-authors.

PLOS COMPUTATIONAL BIOLOGY

RESEARCH ARTICLE

Reliable estimation of membrane curvature for cryo-electron tomography

Maria Salfer[1,2], **Javier F. Collado**[1,2,3], **Wolfgang Baumeister**[1], **Rubén Fernández-Busnadiego**[1,3,4], **Antonio Martínez-Sánchez**[1,3,4]*

1 Department of Molecular Structural Biology, Max Planck Institute of Biochemistry, Martinsried, Germany, **2** Graduate School of Quantitative Biosciences Munich, Munich, Germany, **3** Institute of Neuropathology, University Medical Center Göttingen, Göttingen, Germany, **4** Cluster of Excellence "Multiscale Bioimaging: from Molecular Machines to Networks of Excitable Cells" (MBExC), University of Göttingen, Germany

* martinez@biochem.mpg.de, antonio.martnezsanchez@med.uni-goettingen.de

OPEN ACCESS

Citation: Salfer M, Collado JF, Baumeister W, Fernández-Busnadiego R, Martínez-Sánchez A (2020) Reliable estimation of membrane curvature for cryo-electron tomography. PLoS Comput Biol 16(8): e1007962. https://doi.org/10.1371/journal.pcbi.1007962

Editor: Jeffrey J. Saucerman, University of Virginia, UNITED STATES

Received: October 30, 2019

Accepted: May 18, 2020

Published: August 10, 2020

Data Availability Statement: The algorithms and experimental data are publicly available in a software package called PyCurv at https://github.com/kalemaria/pycurv. Tomograms and segmentations in Figs 2, 11 and 12 have been deposited EM Data Bank (EMD-10767, EMD-10765, and EMD-10766).

Funding: MS and JC have been supported by the Graduate School of Quantitative Biosciences Munich GSC-1006 (http://qbm.genzentrum.lmu.de). MS, JC, WB, RF-B, and AM-S have received

Abstract

Curvature is a fundamental morphological descriptor of cellular membranes. Cryo-electron tomography (cryo-ET) is particularly well-suited to visualize and analyze membrane morphology in a close-to-native state and molecular resolution. However, current curvature estimation methods cannot be applied directly to membrane segmentations in cryo-ET, as these methods cannot cope with some of the artifacts introduced during image acquisition and membrane segmentation, such as quantization noise and open borders. Here, we developed and implemented a Python package for membrane curvature estimation from tomogram segmentations, which we named PyCurv. From a membrane segmentation, a signed surface (triangle mesh) is first extracted. The triangle mesh is then represented by a graph, which facilitates finding neighboring triangles and the calculation of geodesic distances necessary for local curvature estimation. PyCurv estimates curvature based on tensor voting. Beside curvatures, this algorithm also provides robust estimations of surface normals and principal directions. We tested PyCurv and three well-established methods on benchmark surfaces and biological data. This revealed the superior performance of PyCurv not only for cryo-ET, but also for data generated by other techniques such as light microscopy and magnetic resonance imaging. Altogether, PyCurv is a versatile open-source software to reliably estimate curvature of membranes and other surfaces in a wide variety of applications.

Author summary

Membrane curvature plays a central role in many cellular processes like cell division, organelle shaping and membrane contact sites. While cryo-electron tomography (cryo-ET) allows the visualization of cellular membranes in 3D at molecular resolution and close-to-native conditions, there is a lack of computational methods to quantify membrane curvature from cryo-ET data. Therefore, we developed a computational procedure for membrane curvature estimation from tomogram segmentations and implemented it in a software package called PyCurv. PyCurv converts a membrane segmentation, i.e. a set

funds from the European Research Council FP7 GA ERC-2012- 387 SyG_318987-ToPAG (http://erc.europa.eu). AM-S and RF-B were supported by the Deutsche Forschungsgemeinschaft (DFG, German Research Foundation) under Germany's Excellence Strategy - EXC 2067/1-390729940 and the Lower Saxony Ministry of Science and Culture. The funders had no role in study design, data collection and analysis, decision to publish, or preparation of the manuscript.

Competing interests: The authors have declared that no competing interests exist.

of voxels, into a surface, i.e. a mesh of triangles. PyCurv uses the local geometrical information to reliably estimate the local surface orientation, the principal (maximum and minimum) curvatures and their directions. PyCurv outperforms well-established curvature estimation methods, and it can also be applied to data generated by other imaging techniques.

This is a *PLOS Computational Biology* Methods paper.

Introduction

Membranes define the limits of the cells and encompass compartments within eukaryotic cells, helping to maintain specific micro-environments with different shapes and functions. Membrane curvature is important for many cellular processes, including organelle shaping, vesicle formation, scission and fusion, protein sorting and enzyme activation [1, 2]. There is a plethora of cellular mechanisms for generation, sensing and maintenance of local membrane curvature, e.g. clustering of conical lipids or transmembrane proteins, insertion of specific protein domains as well as larger scale scaffolding by e.g. cytoskeletal filaments [1, 3].

Cryo-electron tomography (cryo-ET) enables an accurate three-dimensional (3D) visualization and analysis of the subcellular architecture at molecular resolution [4–6] and is particularly well-suited to study membrane morphology. While other transmission electron microscopy (TEM) techniques may cause membrane deformations by chemical fixation and dehydration, cryo-ET allows imaging of fully hydrated vitrified cells in a close-to-native state with minimal structural perturbations [7]. The nominal resolution of tomograms can reach ∼2-4 Å per voxel, but tomograms are usually binned for membrane segmentation to enhance contrast, resulting in voxel sizes of ∼0.8-1.6 nm. Subtomogram averaging allows to routinely obtain structures in the 10-20 Å resolution range, although higher resolutions are in principle attainable [8]. Cryo-ET can be used to study membrane morphology and curvature in reconstituted preparations [9–13] and intact cells [14, 15]. We have recently employed cryo-ET to visualize peaks of extreme curvature on the cortical endoplasmic reticulum (cER) membrane facing the plasma membrane (PM). These high curvature structures are formed by Tcb proteins and help to maintain PM integrity under heat stress [16]. We have also used cryo-ET to show that polyQ-expanded huntingtin exon I fibrils induce high curvature in the endoplasmic reticulum (ER) membrane, perhaps leading to ER membrane disruption [17]. Since we lacked a method to reliably quantify membrane curvature in noisy cryo-ET data, we developed a new method, which we formally describe in this paper.

In cryo-ET, the vitreous sample is tilted around an axis inside the electron microscope, while 2D images of a cellular region of interest are acquired for each tilt. The tilt series are then computationally aligned and reconstructed into a tomogram, which is a 3D gray-value image of the cellular interior. Because in practice it is unfeasible to tilt the sample beyond $\sim \pm 60^{\circ}$, in single-tilt tomography there is a wedge of missing information in the Fourier space. This artifact, called *missing wedge* [4], causes the features to look smeared out along the electron beam direction (Z-axis), while surfaces perpendicular to the tilt axis (Y-axis) are not visible. Thus, missing membrane regions appear at the top and the bottom of both the Y- and Z-axes. Nevertheless, the missing wedge does not affect the automatically segmented membrane, the

elongated regions are just omitted [18, 19]. Moreover in cryo-ET, the cells are illuminated by only a low dose of electrons, resulting in tomograms of low signal-to-noise ratio. Segmentation, i.e. voxel labeling of structural components present in tomograms, is necessary for tomogram interpretation. Available software packages can assist membrane segmentation [18, 20–22], but in most cases human supervision is still necessary due to the complexity of the cellular context and the low signal-to-noise ratio.

Currently, the interpretation of membrane segmentations is limited by the lack of computational methods to measure quantitative descriptors. Here, we quantitatively determine local curvature descriptors of cellular membranes from tomogram segmentations. A membrane can be modeled as a surface [23], so that curvature descriptors characterize its local geometry. For a surface embedded in a 3D space, principal curvatures measure the maximum and minimum bending at each point, while the principal directions define the directions of the principal curvatures as orthogonal vectors embedded on the tangent plane to the surface at each point [24]. From the principal curvatures, both extrinsic (mean) and intrinsic (Gaussian) surface curvatures can be computed for each point.

An oriented triangle mesh is the most common way to represent discrete surfaces [25]. However, triangle mesh generation from a set of voxels [26] is not trivial because of the presence of holes in membrane segmentations. Besides the errors generated during membrane segmentation, quantization noise [27] is the limiting factor for describing local membrane geometry. The term quantization noise includes here all accuracy limiting factors induced by the discretization of segmented data using binary voxels (1 membrane and 0 background). This binary discretization leads to step-wise surfaces, since surface extraction algorithms would need gray levels to achieve subvoxel precision.

Curvature estimation algorithms can be divided into three main categories: discrete, analytical and based on tensor voting. Discrete algorithms use discretized formulae of differential geometry, approximating a surface from a mesh [25, 28–31]. However, the majority of those algorithms use only a 1-ring neighborhood, i.e. triangle vertices sharing an edge with the central vertex, and therefore are not robust for coarsely triangulated, noisy surfaces [32]. An exception is [31], which uses a geodesic neighborhood of a certain size. Moreover, discrete algorithms do not directly estimate the principal directions or principal curvatures [33]. Analytical algorithms fit surfaces [32, 34] or curvature tensors [35–37] to local patches of the mesh, defined by a central vertex and a small neighborhood around it, and derive principal curvatures and directions from their model. The surface fitting algorithms are more robust to noise but more susceptible to surface discontinuities [33]. The last category of algorithms applies Medioni's tensor voting theory [38] on a neighborhood of an arbitrary size to fit curvature tensors, increasing the robustness of principal directions and curvatures estimation for noisy surfaces with discontinuities [33, 39, 40]. However, [33] leads to wrong curvature sign estimation for non-convex surfaces, while [39, 40] were designed for point clouds instead of triangle meshes. While most of the algorithms operate on triangle vertices because the computation of distances on surfaces is straightforward, some operate on triangle faces [31, 36, 37], exhibiting a more robust behavior on irregularly tessellated and moderately noisy meshes.

Discrete curvature estimation algorithms are included in two software packages for analysis of magnetic resonance imaging (MRI) data of the human brain: the widely used FreeSurfer [41] and the newer Mindboggle [42]. Curvature of the interventricular septum in the heart from MRI was estimated in 3D using smoothing 2D spline surfaces and differential geometry operators [43]. However, those algorithms require strong smoothing of surfaces to achieve robust results, which would lead to a loss of high resolution details present in cryo-ET data.

For microscopy data, there is software to study curvature of linear cellular structures like microtubules [44], which is not applicable to surfaces. For fluorescence microscopy data,

smooth point cloud surfaces of cellular membranes were reconstructed and their curvatures estimated based on local surface fitting [45]. Hoffman et al. [46] also used a local surface fitting method to estimate membrane curvature from block-face electron microscopy data. However, also these methods employ strong smoothing of surfaces, eliminating small structural details. In cryo-ET, some membrane curvature approximation methods have been already proposed [9, 14], but they only work on 2D slices and are not capable of measuring curvature on arbitrary membranes in 3D.

Here, we developed and implemented a method for robust membrane curvature estimation from tomogram segmentations. In brief, the workflow has the following steps. (1) From a segmentation, a single-layered, signed triangle mesh surface is extracted. (2) To extract the surface topology, we generate a spatially embedded graph. Graph vertices depict triangle centers and graph edges connect the centers of triangle pairs sharing an edge or a vertex. (3) Local curvature descriptors are computed for every triangle center. We propose different procedures that combine two established tensor voting-based algorithms [33, 40] but operate on triangle faces, aiming to increase the robustness to membrane geometries present in cryo-ET and to minimize the impact of quantization noise. Extensive evaluation of our algorithms and comparison with three well-established ones [30, 41, 42] on synthetic and biological surfaces proved the superiority of our approach in terms of accuracy and robustness to noise for cryo-ET and other imaging techniques.

Materials and methods

Cryo-ET data collection and segmentation

As real-world test input files for PyCurv, in this study we used membrane segmentations from *in situ* cryo-ET data collected from vitrified cells: a human HeLa cell [17], yeast *Saccharomyces cerevisiae* (EMD-10767 and EMD-10765) and a primary mouse neuron (EMD-10766). The cells were milled down to 150-250 nm thick lamellas using cryo-focused ion beam [16, 54] and imaged using a Titan Krios cryo-electron microscope (FEI), equipped with a K2 Summit direct electron detector (Gatan), operated in dose fractionation mode. Tilt series were recorded using SerialEM software [55] at magnifications of 33,000 X (pixel size of 4.21 Å) for the HeLa cell and the mouse neuron and 42,000 X (pixel size of 3.42 Å) for yeast, typically from -50˚ to +60˚ with increments of 2˚. The K2 frames were aligned using K2Align software [56]. Tilt series were aligned using patch-tracking and weighted back projection provided by the IMOD software package [57]. The tomograms were binned 4 times to improve contrast prior to segmentation, thus the voxel size of the final segmentations was 1.684 nm (HeLa cell and mouse neuron) and 1.368 nm (yeast). The contrast of one tomogram of yeast (EMD-10767) was enhanced prior to segmentation using an anisotropic filter [58], while the contrast of the other tomogram of yeast (EMD-10765) and the one of the mouse neuron was enhanced using a deconvolution filter executed in MATLAB (MathWorks) using the functionalities of the TOM toolbox [59]. Membrane segmentations were generated automatically from tomograms using TomoSegMemTV [18] using parameters `s` = 10 and `t` = 0.3 (HeLa cell), `s` = 12 and `t` = 4 (yeast) and `s` = 10 and `t` = 3 (mouse neuron) and further refined manually using Amira Software (ThermoFisher Scientific). The lumen of membrane compartments was then filled manually.

Data preprocessing algorithms

The first steps of the PyCurv workflow (Fig 1A) are the conversion of the input segmentation into a surface and the extraction of its associated graph.

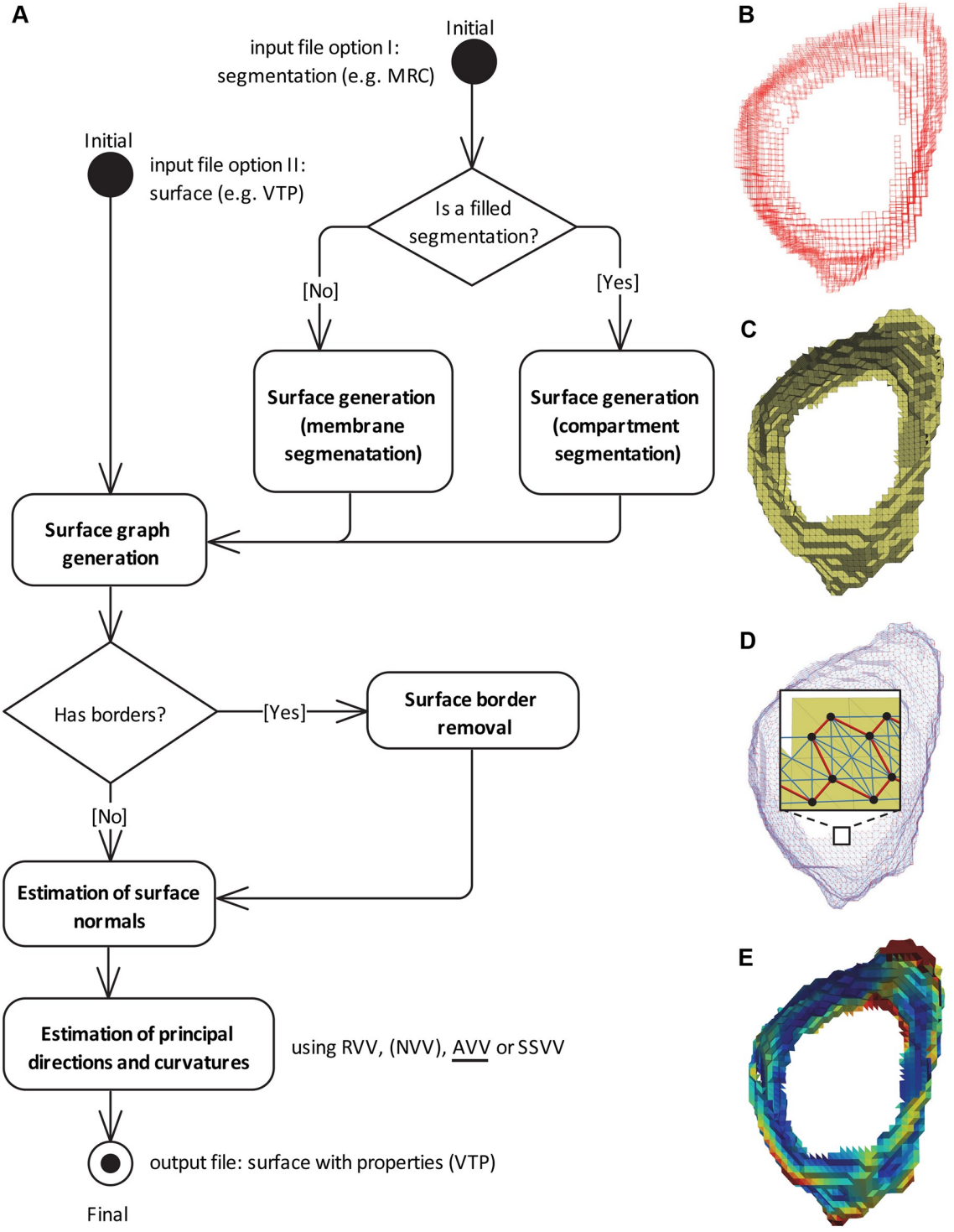

Fig 1. PyCurv workflow. (**A**) UML activity diagram of the PyCurv workflow. If the input segmentation (in e.g. MRC format) is filled, the surface is generated using the *compartment segmentation*, otherwise using the *membrane segmentation* algorithm. This step is omitted if the input is a surface (in e.g. VTP format). From the surface, a graph is generated. If the graph has surface borders, they are removed. Then, surface normals are estimated at each triangle center. Finally, principle directions and curvatures are estimated and different combined curvature measures calculated using one of the tensor voting-based algorithms: RVV (Regular Vector Voting), NVV (Normal Vector Voting, only for evaluation), AVV (Augmented Vector Voting, default algorithm) or SSVV (Surface Sampling Vector Voting). The

output is a surface with all the calculated values stored as triangle properties (VTP format). All the processing steps (rounded rectangles) are implemented in PyCurv. (**B**) Voxels of a segmentation of a vesicle from a cryo-electron tomogram of a human HeLa cell [17]. (**C**) A surface (triangle mesh) generated from the membrane segmentation shown in (A). (**D**) Surface graph generated from the surface shown in (B); the inset shows a magnified region of the graph mapped on top of the triangle mesh (triangles: yellow, graph vertices: black dots, strong edges: red lines, weak edges: light blue lines). (**E**) The output surface with estimated normals, principal directions and curvatures as well as several combined curvature measures. Here, curvedness is shown. See also the video in S1 Video.

https://doi.org/10.1371/journal.pcbi.1007962.g001

Surface generation. A surface can be extracted using PyCurv from two types of input segmentations, a *membrane segmentation* or a *compartment segmentation*. This step is not required if the input is directly a surface (Fig 1A).

Using the *membrane segmentation* surface generation algorithm, the segmented membrane of interest (Fig 2B) from the binned tomogram (Fig 2A) was used as the input for an algorithm [26] that reconstructs signed, single-layered triangle-mesh surfaces from an unorganized set of points, here the membrane voxels (Fig 1B). This algorithm was designed for closed surfaces without boundaries. However, most segmented membranes in cryo-ET are open, e.g. due to noise or missing wedge artifacts. Attempting to close the surface, the algorithm generated large artefactual surface regions beyond the segmentation (Fig 2D, transparent white). These regions were largely discarded by applying a mask with the membrane segmentation (Fig 2D, yellow). Since the masking was done with a distance threshold of three voxels in order to bridge upon small holes in the segmentation, additional three voxels-wide border remained. This additional border was removed in the final cleaning step (see Surface graph generation). We use the convention that normal vectors ("normals") point inwards in a convex surface. However, since membrane segmentations have boundaries, the algorithm [26] sometimes mistakenly initiates normals on both sides (Fig 2D, red arrows). As a result, ridge-like patches appear along the surface (Fig 2E), leading to holes in the cleaned surface (Fig 2F). In some cases, the surface reconstruction can be improved by closing small holes in the segmentation using morphological operators.

The *compartment segmentation* surface generation algorithm requires additional segmentation of the inner volume of a compartment enclosed by a membrane (Fig 2C). This unequivocally defines the orientation of the membrane by closing its holes. After joining the membrane and its inner volume masks, we generate an isosurface around the resulting volume using the Marching Cubes algorithm [47]. Finally, we apply a mask using the original membrane segmentation to keep only the surface region going through the membrane (again, except for the additional border that is cleaned in the end). The surface orientation is recovered perfectly in our experiments (Fig 2G). In some cases, especially where the membrane segmentation was manually refined, Marching Cubes produces triangles standing out perpendicularly to the surface (Fig 2H), leading to holes in the cleaned surface (Fig 2I). To correct those artifacts and exploit the subvoxel precision offered by Marching Cubes, the compartment segmentation mask was slightly smoothed using a Gaussian kernel with $\sigma = 1$ voxel before extracting the surface (Fig 2J–2L).

In summary, although compartment segmentations require more human intervention, they ensure smoother and well oriented surfaces. Thus, we choose this algorithm as the default for the subsequent data processing.

Surface graph generation. Curvature is a local property. Thus, for a triangle-mesh surface, curvature has to be estimated using a local neighborhood of triangles. If the neighborhood is too small, one would measure only noise created by the steps between voxels. If the neighborhood is too large, one would underestimate the curvature.

To estimate geodesic distances within membrane surfaces, we use the graph-tool python library [48] to map the triangle mesh (Fig 1A and 1C) into a spatially embedded graph, here

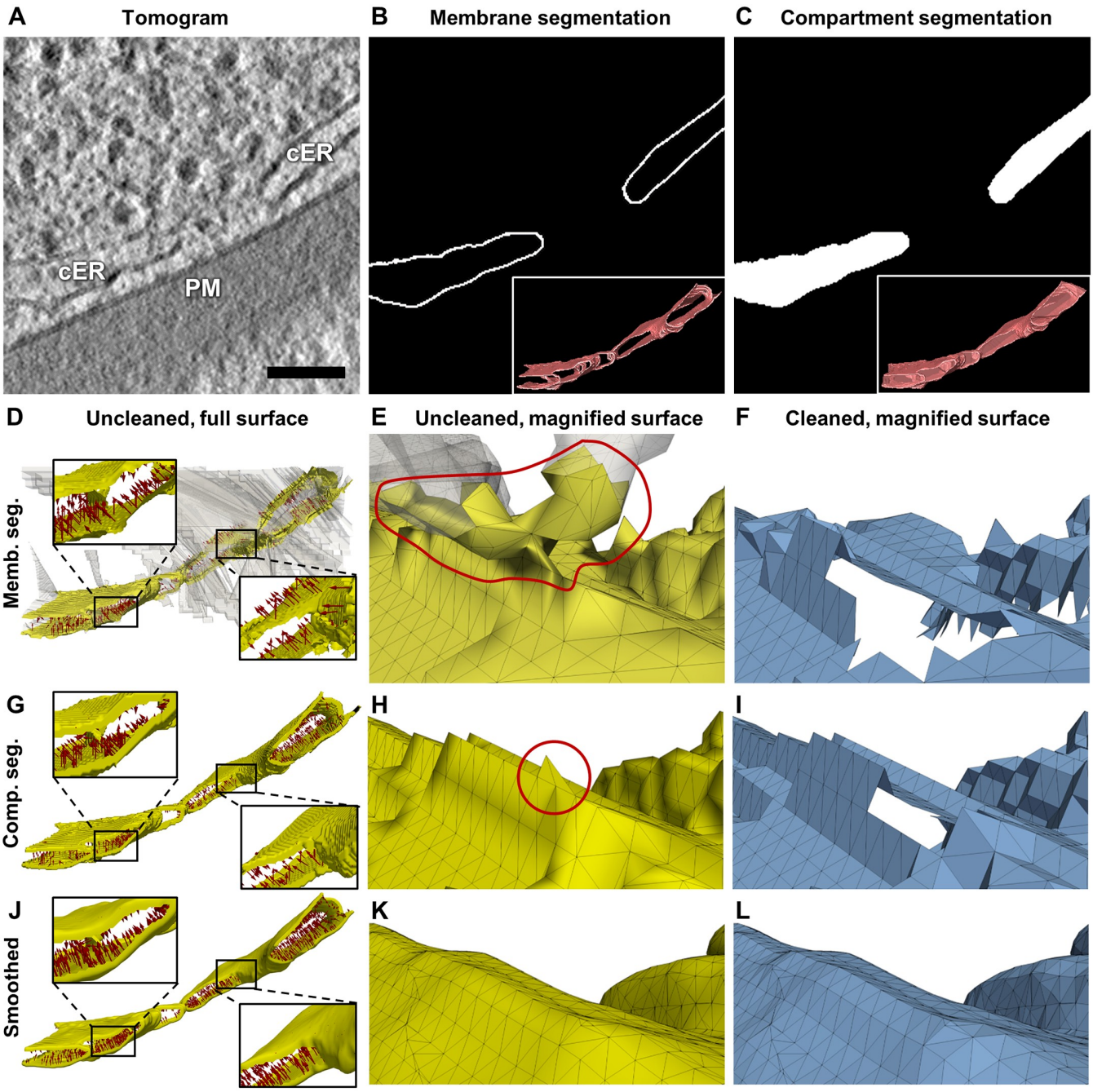

Fig 2. Surface generation from *membrane* and *compartment segmentations*. (**A**) A filtered tomographic slice showing the cortical endoplasmic reticulum (cER) and plasma membrane (PM) of a yeast cell (scale bar: 100 nm). Panels (B-C) show the same slice as in (A) with (**B**) the *membrane segmentation* of the cER and (**C**) the *compartment segmentation* of the cER; the insets show 3D renderings of the full segmentations (including all tomographic slices). Panels (D-F) show a surface generated from the cER *membrane segmentation* shown in (B): (**D**) The unmasked artefactual surface is shown in transparent white. The masked but uncleaned surface is shown in yellow with normals (every 100th) as red arrows. Some of the normals erroneously point outside the cER lumen (see right inset). (**E**) A different view of the uncleaned surface shown in (D), magnified. The red line marks an artifact. (**F**) The same magnified view as in (E) showing the cleaned surface in blue with a hole resulting from removing the artifact shown in (E). Panels (G-L) show surfaces generated using the *compartment segmentation* shown in (C), (G-I) without and (J-L) with Gaussian smoothing; the views are the same as in panels (D-F) column-wise: (**G**, **J**) Using the *compartment segmentation*, all normals point inside the cER lumen (see the insets). (**H**) Without smoothing, triangles sticking out (red circle) in the uncleaned surface lead to a hole in the cleaned surface shown in (**I**). (**K**-**L**) The cleaned smoothed surface is free from artifacts. The tomogram and segmentation are deposited in EM Data Bank (EMD-10767). See also the video in S1 Video.

https://doi.org/10.1371/journal.pcbi.1007962.g002

referred as *surface graph*. First, graph vertices are associated to triangle centroid coordinates. Second, pairs of triangles sharing two triangle vertices are connected by *strong* edges, while those sharing only one triangle vertex are connected by *weak* edges (Fig 1D). To approximate the shortest paths along the surface between the centers of a source triangle and a target triangle, the graph is traversed starting from the source vertex along all its edges until the target vertex is found, using the Dijkstra algorithm [49]. Using both strong and weak edges increases the number of possible paths and thus improves the estimation of the shortest path. The geodesic distance is computed by summing up the lengths of the edges comprising the shortest path.

Another application of the surface graph is to remove surface borders to avoid wrong curvature estimations in these regions. Using the surface graph, we can detect triangles at borders because they have less than three strong edges. Then, triangles up to a certain geodesic distance from the border can be found and filtered out from the surface.

Curvature estimation algorithms

We estimate membrane curvature from surface graphs (Fig 1A). This algorithm combines two previously published algorithms that are based on tensor voting and curvature tensor theory [33, 40], to increase the precision of curvature estimation for noisy surfaces. To estimate principal curvatures, principal directions have to be estimated. For the estimation of principal directions, surface normals are required. Surface normals are robustly estimated by averaging normals of triangles within a geodesic neighborhood.

Parameters defining the geodesic neighborhood. Similarly to [40], here we define a `radius_hit` (`rh`) parameter to approximate the highest curvature value we can estimate reliably, i.e. $\mathtt{rh}^{-1}$. For each surface triangle center, we define its local neighborhood as

$$g_{max} = \frac{\pi \cdot \mathtt{rh}}{2}, \tag{1}$$

where g_{max} defines the maximum geodesic distance. In Eq 1, g_{max} is approximated by one quarter of a circle perimeter with radius equal to `rh` (Fig 3A).

Estimation of surface normals. Normals computed directly from the triangle mesh are corrupted by quantization noise. To avoid this, we have adapted the first step of the algorithm proposed in [33], but estimating the normals for each triangle center instead of defining new normals at each triangle vertex.

For each triangle centroid (or graph vertex) v, the normal votes of all triangles within its geodesic neighborhood are collected and the weighted covariance matrix sum V_v is calculated. More precisely, a normal vote $\vec{n}_i$ of a neighboring triangle (whose center c_i is lying within g_{max} of vertex v) is calculated using the normal $\vec{n}_{\mathrm{c}_i}$ assigned to this triangle:

$$\vec{n}_i = \vec{n}_{\mathrm{c}_i} + 2\cos\theta_i \frac{\vec{\mathrm{vc}}_i}{\|\vec{\mathrm{vc}}_i\|}, \tag{2}$$

where $\cos\theta_i = -\frac{\vec{n}^t_{\mathrm{c}_i}\vec{\mathrm{vc}}_i}{\|\vec{\mathrm{vc}}_i\|}$, $\vec{n}^t_{\mathrm{c}_i}$ is the transposed vector $\vec{n}_{\mathrm{c}_i}$, $\vec{\mathrm{vc}}_i = \mathrm{c}_i - \mathrm{v}$ and $0 \le \theta_i \le \pi$. This formula fits a smooth curve from c_i to v, allowing the normal vote $\vec{n}_i$ to follow this curve, so that the angle θ_i between $\vec{n}_i$ and $\vec{\mathrm{vc}}_i$ is equal to the angle between $\vec{n}_{\mathrm{c}_i}$ and $-\vec{\mathrm{vc}}_i$. According to the perceptual continuity constrain [38], the most appropriate curve is the shortest circular arc (Fig 3B). Then, each vote is represented by a covariance matrix $V_i = \vec{n}^t_i\vec{n}_i$, and votes from the geodesic neighborhood are collected as a weighted matrix sum V_v:

$$V_\mathrm{v} = \sum w_i V_i, \tag{3}$$

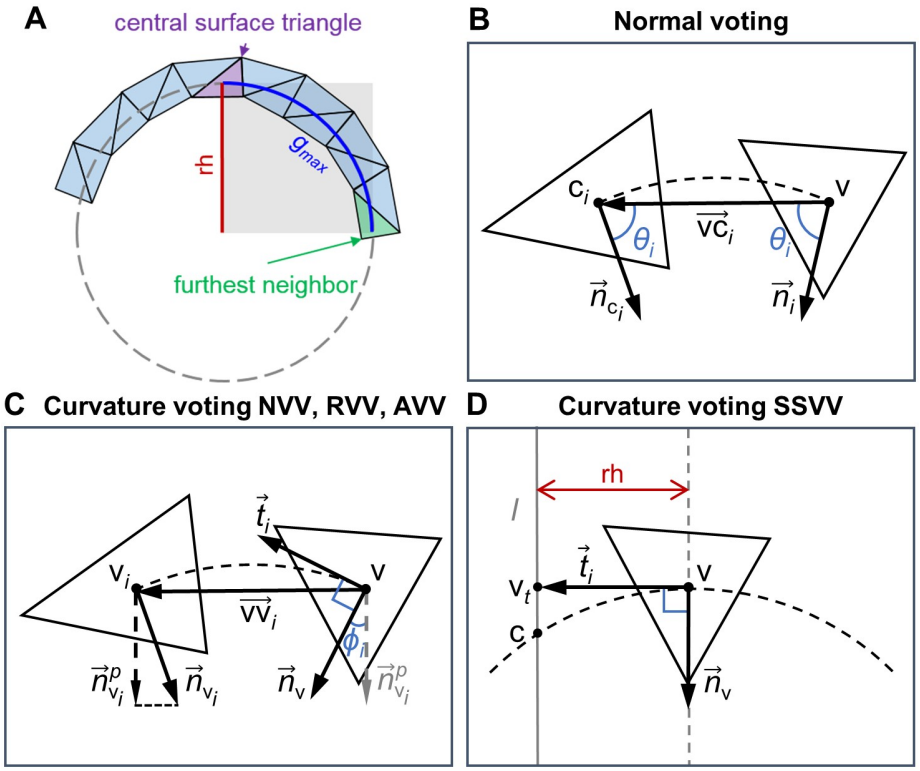

Fig 3. Neighborhood parameters and voting geometry. (**A**) Schematic illustrating the `rh` and g_{max} parameters. g_{max} is one quarter of the circle perimeter with radius equal to `rh`. g_{max} defines the maximum geodesic distance from a surface triangle center to the centers of its neighboring triangles, approximated by the shortest path along the edges of the surface graph. (**B**) Collection of normal votes in all proposed algorithms based on [33]. The rectangle denotes the plane containing the circular arc (dashed line) between the neighboring triangle centers v and c_i, the normal vector $\vec{n}_{c_i}$ at c_i and the normal vote $\vec{n}_i$ at v. (**C**) Collection of curvature votes for the NVV, RVV and AVV algorithms based on [33]. The rectangle denotes the arc plane containing the triangle center v, its estimated normal $\vec{n}_v$, its tangent $\vec{t}_i$ towards neighboring triangle center v_i and the projection $\vec{n}^p_{v_i}$ of the estimated normal $\vec{n}_{v_i}$ at v_i. (**D**) Collection of curvature votes in the SSVV algorithm based on [40]. The rectangle denotes the plane containing the tangent vector $\vec{t}_i$ at v of length = `rh`, ending with the point v_t, and the normal vector $\vec{n}_v$ at v. The line *l*, crossing v_t and parallel to $\vec{n}_v$, intersects the surface (dashed) at point c.

https://doi.org/10.1371/journal.pcbi.1007962.g003

where w_i is a weighting term calculated as follows:

$$w_i = \frac{a_i}{a_{max}} exp\left(-\frac{g_i}{\sigma}\right). \quad (4)$$

The weight of the vote of a neighboring triangle increases linearly with its surface area a_i, but decreases exponentially with its geodesic distance g_i to v. a_{max} is the area of the largest triangle in the whole surface and σ is an exponential decay parameter, which is set to fulfill $3\sigma = g_{max}$, so that votes beyond the geodesic neighborhood have almost no influence and can be ignored.

The votes collected into the matrix V_v are used for estimating the correct normal vector for the triangle represented by vertex v. This is done by eigen-decomposition of V_v, which generates three real eigenvalues $e_1 \geq e_2 \geq e_3$ with corresponding eigenvectors $\vec{e}_1$, $\vec{e}_2$ and $\vec{e}_3$. The normal direction is equal in its absolute value to that of the first eigenvector. During construction of V_v, the sign of normal votes is lost when V_i is computed. The correct orientation can be recovered from the original normal $\vec{n}$, as the original surface was already oriented. Therefore,

the estimated normal is correctly oriented by:

$$\vec{n}_{\mathrm{v}} = \begin{cases} \vec{e}_1 & \text{if } cos(\vec{n}^t\vec{e}_1) > cos(-\vec{n}^t\vec{e}_1) \\ -\vec{e}_1 & \text{otherwise.} \end{cases} \tag{5}$$

Estimation of principal directions and curvatures. For each graph vertex v, we use the estimated normals $\vec{n}_{\mathrm{v}_i}$ of its geodesic neighbors v_i in order to cast curvature votes. The curvature votes are summed into a curvature tensor. The resulting curvature tensor is decomposed to find the principal directions and curvatures at vertex v. Below, we describe the basic curvature estimation algorithm as an adaptation of [33] and [40].

Each neighboring vertex v_i casts a vote to the central vertex v, where the votes are collected into a 3x3 symmetric matrix B_{v} [35]:

$$B_{\mathrm{v}} = \frac{1}{2\pi}\sum w_i\kappa_i\vec{t}_i\vec{t}_i^{\,t}. \tag{6}$$

For each v_i, three variables are computed:

1. Weight w_i depending on the geodesic distance between v_i and v, as defined in Eq 4 but without normalizing by relative triangle area:

$$w_i = exp\left(-\frac{g_i}{\sigma}\right). \tag{7}$$

   Also, all weights around the vertex v are constrained by $\sum w_i = 2\pi$.

2. Tangent $\vec{t}_i$ from v in the direction of the arc connecting v and v_i (using the estimated normal $\vec{n}_{\mathrm{v}}$ at v) (Fig 3C):

$$\vec{t}_i = \frac{\vec{t'}_i}{\|\vec{t'}_i\|}, \quad \vec{t'}_i = \vec{\mathrm{vv}}_i - (\vec{n}_{\mathrm{v}}^t\vec{\mathrm{vv}}_i)\vec{n}_{\mathrm{v}}. \tag{8}$$

3. Normal curvature κ_i [40]:

$$|\kappa_i| = \frac{|2\cos\frac{\pi-\phi_i}{2}|}{\|\vec{\mathrm{vv}}_i\|}, \tag{9}$$

   where ϕ_i is the turning angle between $\vec{n}_{\mathrm{v}}$ and the projection $\vec{n}^p_{\mathrm{v}_i}$ of $\vec{n}_{\mathrm{v}_i}$ onto the arc plane (formed by v, $\vec{n}_{\mathrm{v}}$ and v_i). The following calculations lead to ϕ_i:

$$\vec{p}_i = \vec{n}_{\mathrm{v}} \times \vec{t}_i, \quad \vec{n}^p_{\mathrm{v}_i} = \vec{n}_{\mathrm{v}_i} - (\vec{p}_i^{\,t}\vec{n}_{\mathrm{v}_i})\vec{p}_i$$
$$\cos\phi_i = \frac{\vec{n}_{\mathrm{v}}^t\vec{n}^p_{\mathrm{v}_i}}{\|\vec{n}_i\|}. \tag{10}$$

For surface generation, we use the convention that normals point inwards in a convex surface. Then, the curvature is positive if the surface patch is curved towards the normal and negative otherwise. Therefore, the sign of κ_i is set by:

$$\kappa_i = -\vec{t}_i^{\,t}\vec{n}^p_{\mathrm{v}_i}|\kappa_i|. \tag{11}$$

For a vertex v and its calculated matrix B_{v}, we calculate the principal directions, maximum $\vec{t}_1$ and minimum $\vec{t}_2$, and the respective curvatures, κ_1 and κ_2, at this vertex. This is done using eigen-decomposition of B_{v}, resulting in three eigenvalues $b_1 \geq b_2 \geq b_3$ and their corresponding

eigenvectors $\vec{b}_1$, $\vec{b}_2$ and $\vec{b}_3$. The eigenvectors $\vec{b}_1$ and $\vec{b}_2$ are the principal directions. The principal curvatures are found with linear transformations of the first two eigenvalues [35]:

$$\begin{aligned} \kappa_1 &= 3b_1 - b_2 \\ \kappa_2 &= 3b_2 - b_1. \end{aligned} \tag{12}$$

The smallest eigenvalue b_3 has to be close to zero and the corresponding eigenvector $\vec{b}_3$ has to be similar to the normal $\vec{n}_v$ [33].

Algorithm variants. We implemented the following algorithm variants within PyCurv.

Vector Voting (VV): Estimation of surface normals algorithm, which is the same for all our algorithms listed below.

Regular Vector Voting (RVV): Estimation of principal directions and curvatures algorithm described above. Modifications of this algorithm were implemented to determine the best solution for cryo-ET:

Normal Vector Voting (NVV): In [33], curvature is computed as the turning angle ϕ_i divided by arc length between the vertices v and v_i, which is the geodesic distance between them, g_i:

$$\kappa_i = \frac{\phi_i}{g_i}. \tag{13}$$

However, this definition of κ_i with the sign according to our normals convention (Eq 11) lead to erroneous eigenvalue analysis of B_v. The eigenvalue analysis was only successful for $\kappa_i > 0$, leading to wrong curvature sign estimation for non-convex surfaces (see Section Estimation of the curvature sign).

Augmented Vector Voting (AVV): Here, the weights of curvature votes, prioritizing neighbors with a closer geodesic distance to the central triangle vertex v, are normalized by relative triangle area as for normal votes using Eq 4 instead of Eq 7.

Surface Sampling Vector Voting (SSVV): We implemented the algorithm `GenCurvVote` from [40] to estimate the principal directions and curvatures. While RVV, NVV and AVV use all points within the geodesic neighborhood of a given surface point v, in SSVV only eight points on the surface are sampled using `rh`. For this, an arbitrary tangent vector $\vec{t}_i$ at v with length equal to `rh` is first generated, creating a point v_t in the plane formed by this tangent and the normal $\vec{n}_v$ at v (Fig 3D). Then, a line l crossing v_t and parallel to the normal $\vec{n}_v$ is drawn and its intersection point c with the surface is found. The tangent is rotated seven times around the normal by $\frac{\pi}{4}$ radians, generating another seven intersection points. Each vote is weighted equally, thus Eq 6 simplifies to:

$$B_v = \frac{1}{8}\sum \kappa_i \vec{t}_i \vec{t}_i^{\,t}. \tag{14}$$

The output of these curvature estimation algorithms comprises the surface with corrected normals, estimated principal directions and curvatures as well as different combined curvature measures: mean curvature H (Eq 15), Gaussian curvature K (Eq 16), curvedness C (Eq 17) and shape index SI (Eq 18) [50]. All these measures are stored as triangle properties in the VTP surface output file that can be viewed using e.g. the free visualization tool ParaView [51] (Fig 1E).

$$H = \frac{\kappa_1 + \kappa_2}{2} \tag{15}$$

$$K = \kappa_1 \kappa_2 \tag{16}$$

$$C = \sqrt{\frac{\kappa_1^2 + \kappa_2^2}{2}} \tag{17}$$

$$SI = \frac{2}{\pi} atan \frac{\kappa_1 + \kappa_2}{\kappa_1 - \kappa_2} \tag{18}$$

The complete workflow of our method including the input, processing steps and output is shown as an UML (Unified Modeling Language) activity diagram in Fig 1A. See also the video in S1 Video.

Other algorithms. We used the following alternative curvature estimation algorithms available in other software packages for comparison to our algorithms.

VTK [30]: The Visualization Toolkit (VTK) calculates curvature per triangle vertex using only its adjacent triangles and applying discrete differential operators [25]. In order to be able to compare VTK to our tensor voting-based algorithms operating on triangles, we average the values of each curvature type at three triangle vertices to obtain one value per triangle. VTK does not estimate principal directions.

FreeSurfer [52]: FreeSurfer's function `mris_curvature_stats` [41] estimates mean, Gaussian and principal curvatures, curvedness as well as other local and global derived curvature measures per triangle vertex, based on osculating circle fitting. FreeSurfer fails on surface edges and holes, so it cannot be applied to a cylindrical surface.

Mindboggle [42]: Mindboggle's default algorithm (`m = 0`) estimates mean, Gaussian and principal curvatures per triangle vertex, based on the relative directions of the normal vectors in a small neighborhood. We choose the optimal radius of neighborhood parameter (`n`) for each benchmark surface in the same way as for our algorithms (see Section Setting the neighborhood parameter).

Results

Quantitative results on benchmark surfaces

Calculation of errors. We first evaluate the accuracy of our algorithms using benchmark surfaces with known orientation and curvature. For that purpose, we define two types of errors:

1. For vectors (normals or principal directions):

$$Vector\ \ error = 1 - |\vec{v}_t \cdot \vec{v}_e|, \tag{19}$$

where $\vec{v}_t$ is a true vector and $\vec{v}_e$ is an estimated vector for the same triangle, both having length 1. The minimum error is 0, when the true and estimated vectors are parallel, and the maximum error is 1, when the vectors are perpendicular.

2. For scalars (principal curvatures) we use:

$$Scalar\ \ relative\ \ error = |\frac{\kappa_t - \kappa_e}{\kappa_t}|, \tag{20}$$

where κ_t is a true curvature and κ_e is an estimated curvature for the same triangle. The minimum error is 0, when the estimate equals to the true value, and there is no upper bound to the error.

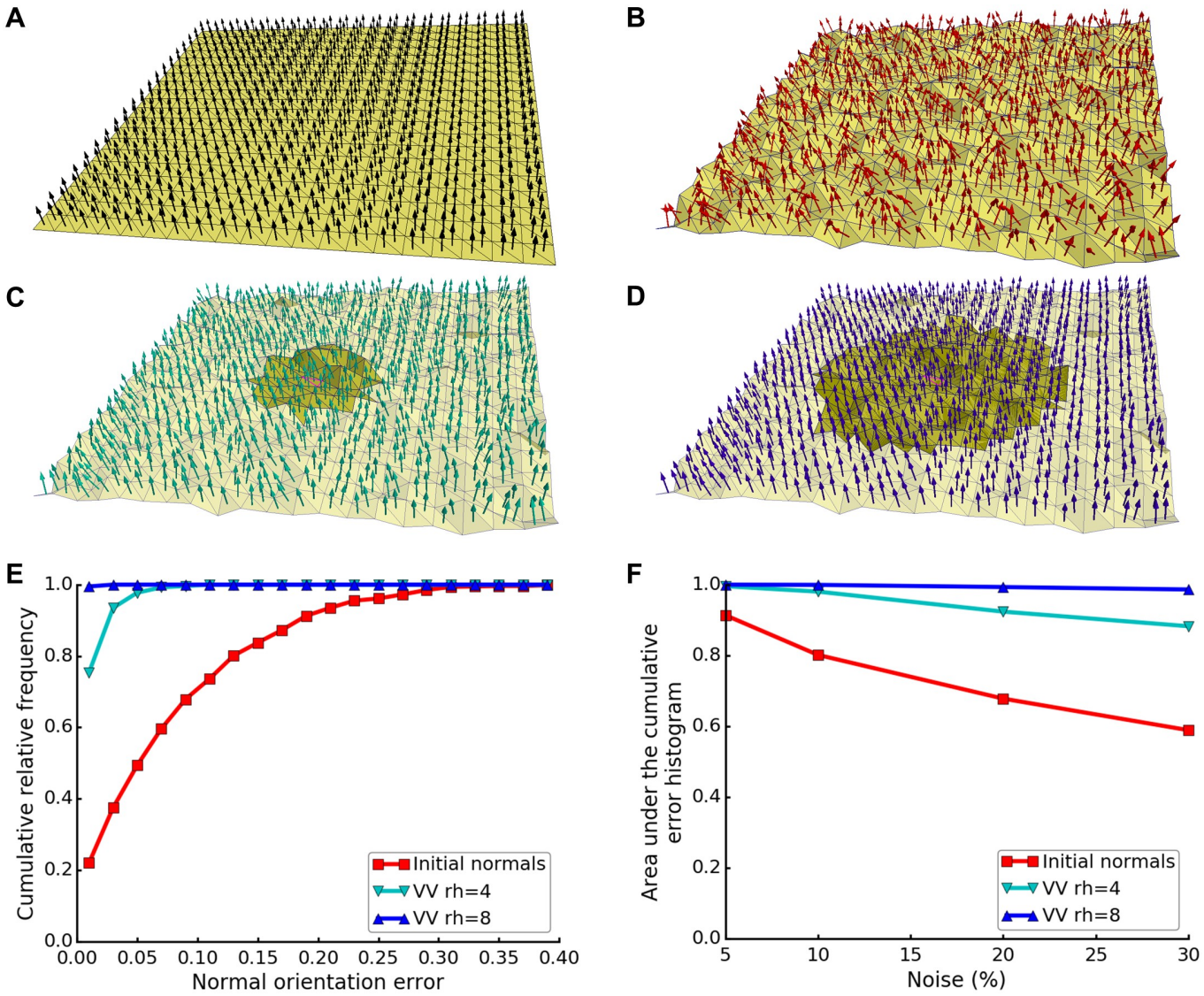

Fig 4. Estimation of normals on a noisy plane. (**A**) True normals (black arrows) on a smooth plane surface (yellow). (**B**) Normals on a noisy plane, where each triangle vertex in the original plane shown in (A) was moved in the direction of its normal vector with Gaussian variance equal to 10% of the average triangle edge. Panels (C-D) show normals on the noisy plane corrected by VV with `rh` of (**C**) 4 or (**D**) 8 voxels. The neighborhoods of a central triangle are shown in a darker yellow. (**E**) Cumulative relative frequency histogram of normal orientation error for the 10% noisy plane, for initial (uncorrected) normals and those corrected by VV with `rh` of 4 or 8 voxels. (**F**) Area under the curve of cumulative relative frequency histograms of normal orientation errors, as shown in (E), for planes with different noise levels. Initial normals and those corrected by VV with `rh` of 4 or 8 voxels are shown. Curve colors in (E-F) correspond to the colors of the normals in (B-D).

https://doi.org/10.1371/journal.pcbi.1007962.g004

Robust estimation of normals. Surface normals are required for a reliable estimation of the principal directions and principal curvatures. In this experiment, we wanted to ensure that VV restores the correct orientation of the normals. For this, we used a plane surface with artificially introduced noise to simulate the quantization noise present in surfaces generated from cryo-ET segmentations. The true normals are those from the plane without noise (i.e. parallel to Z-axis, Fig 4A). Noise was introduced to the original plane by moving each triangle vertex in the direction of its normal vector with Gaussian variance equal to e.g. 10% of the average triangle edge. As a result, the triangle normals of the 10% noisy plane were not parallel to each

other nor to Z-axis (Fig 4B), which was also reflected by the normal orientation errors up to ∼30% (Fig 4E). Using VV with rh of 4 voxels, the original orientation of the normals was almost restored (Fig 4C), and the errors reduced to below 10% (Fig 4E). Using rh of 8 voxels, the estimation further improved (Fig 4D and 4E), since more neighboring triangles helped to average out the noise. For planes with more noise, the normal orientation errors of the initial normals and the estimated ones with rh of 4 voxels increased, reducing the area under the histogram curve. However, the estimation stayed robust using rh of 8 voxels even for a 30% noisy plane (Fig 4F). Thus, using VV with a high enough rh substantially restores the original orientation of the normals.

Setting the neighborhood parameter. As shown above, the size of the neighborhood defined by the rh parameter influences the estimation of normals. Therefore, choosing an appropriate rh for the data is crucial for accurate curvature estimation.

To study the influence of rh in our different curvature estimation algorithms, we generated a synthetic segmentation (25^3 voxels) of a sphere with radius of 10 voxels, emulating the quantization noise present in cryo-ET data (the central slice of the sphere is shown in Fig 5A). Then, we generated an isosurface of this segmentation and estimated its curvature using the different algorithms and rh values. We define the optimal rh value for a sphere as the one leading to the least errors in both estimated principal curvatures taken together. As above, we measure the error rate by the normalized area under the cumulative error histograms. For this spherical surface, the lowest errors were reached for rh = 10 voxels for AVV and rh = 8 voxels for SSVV (Fig 5B and 5C, Table 1). These values are close to the sphere radius, suggesting that the most robust estimation can be achieved using a rh approximately similar to the feature radius. Performance of SSVV decreased drastically for rh = 10 voxels, because then less sampling points at exactly this radius lie on the surface, preventing a reliable estimation (Fig 5C, Table 1). Interestingly, the histogram area kept rising until rh = 16 voxels for RVV (Table 1), which exceeds the sphere radius. Actually, the histogram area kept rising even beyond rh = 16 voxels for κ_1 alone, whereas it started to decrease after rh = 12 voxels for κ_2 (Table 1). For practical reasons, we decided to always limit rh by the radius of the feature (Fig 5D).

The optimal rh, which can differ between surfaces and algorithms, defines a neighborhood sufficient for robust estimation of curvature. Features with a radius less than rh are averaged (RVV and AVV) or neglected (SSVV), so rh^{-1} can be set as a limit for the maximum curvature that can be reliably computed.

Estimation of the curvature sign. To determine the correct procedure for curvature sign determination, we used a torus as a benchmark, as this surface has regions with both positive, $\kappa_1\kappa_2 > 0$, and negative, $\kappa_1\kappa_2 < 0$, Gaussian curvature. Analytically calculated κ_2 is shown in Fig 6A. VTK, Mindboggle and FreeSurfer estimated the curvature sign correctly (Fig 6D, 6F and 6G). Whereas NVV did not distinguish negative from positive regions (Fig 6B), RVV and SSVV differentiated these regions correctly (Fig 6C and 6G). Since RVV and SSVV both calculate normal curvature using Eqs 9 and 11, while NVV uses Eq 13, the latter must be the source of the erroneous curvature sign estimation. Therefore, we exclude NVV from further consideration.

Accuracy of curvature estimation on smooth surfaces. To evaluate the performance of the different curvature estimation algorithms, we first calculated the errors in principal directions and curvatures using smooth surfaces.

First, we applied the algorithms to the smooth torus surface shown in Fig 6A using for each algorithm an rh optimal for κ_2 (10 voxels for RVV, 9 voxels for AVV and 6 voxels for SSVV). The $\vec{t}_2$ error histogram is shown in Fig 6E, and very similar results were observed for $\vec{t}_1$. SSVV estimated both principal directions and curvatures (Fig 6E–6G) more accurately than RVV.

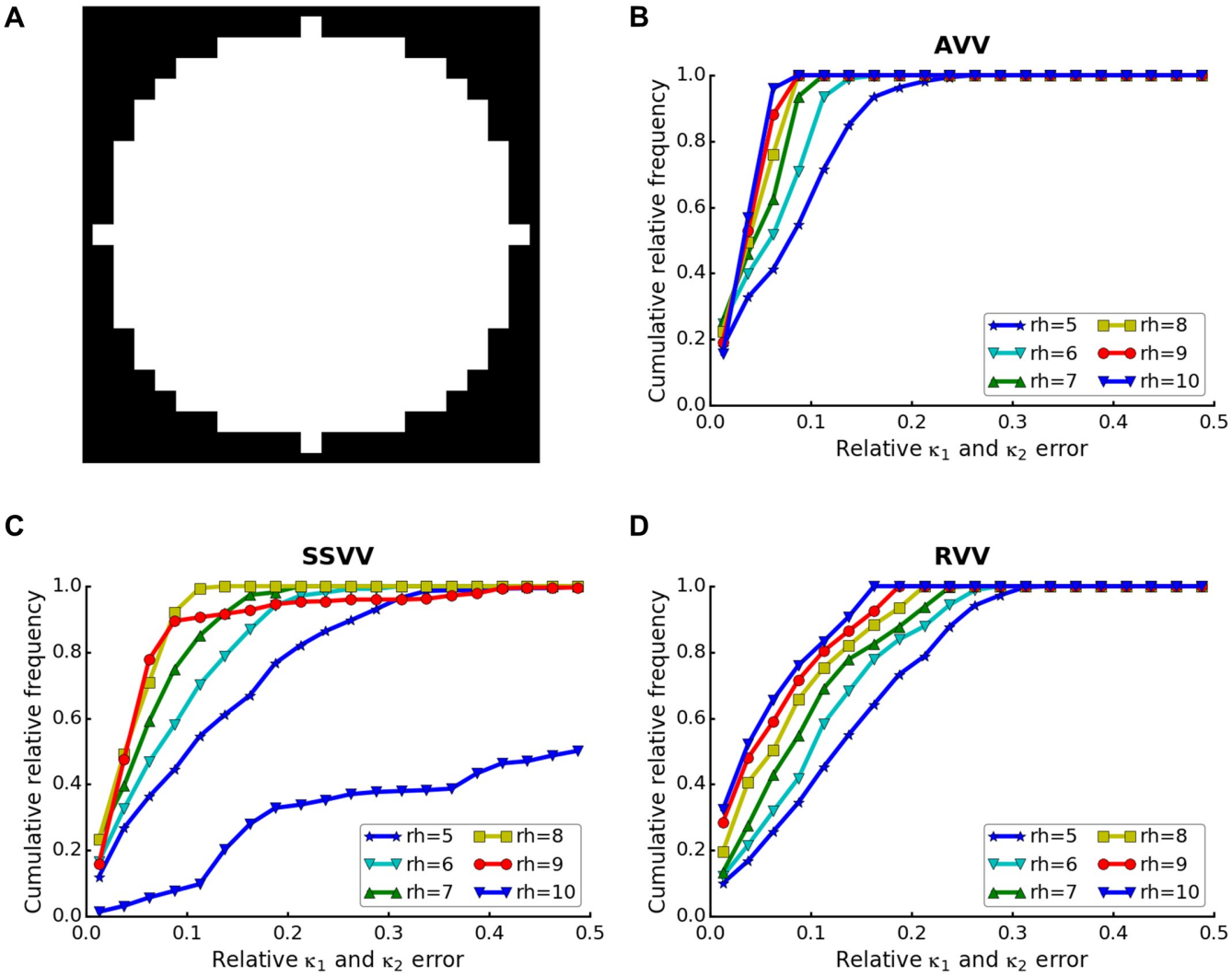

Fig 5. `rh` parameter choice. (**A**) A central slice of a synthetic segmentation of a sphere with radius = 10 voxels. Panels (B-D) show cumulative frequency histograms of the κ_1 and κ_2 errors on the surface extracted from the segmentation shown in (A), using different `rh` (5-10 voxels) and algorithms: (**B**) AVV, (**C**) SSVV and (**D**) RVV.

https://doi.org/10.1371/journal.pcbi.1007962.g005

AVV slightly outperformed RVV in the estimation of principal curvatures. However, VTK estimated principal curvatures slightly better than the tensor voting-based algorithms for this smooth surface with uniform triangles. Mindboggle with the optimal (for κ_2) `n` = 4 voxels was the best method for estimating κ_1 (Fig 6F), but the worst for κ_2 (Fig 6D and 6G), whereas FreeSurfer performed the best for κ_2 (Fig 6G). Note that the curvature errors for κ_1 (Fig 6F) were lower than for κ_2 (Fig 6G) for all algorithms. A possible explanation is that κ_1 is constant for a torus and thus easier to estimate, while κ_2 changes depending on the position.

We also compared the algorithms using a smooth spherical surface with a non-uniform triangle tessellation, generated from a spherical volume mask smoothed using a 3D Gaussian function (σ = 3.3) and applying an isosurface. Since both principal curvatures should be the same for a spherical surface, they were considered together. Also, no true principal directions exist for a spherical surface. For a sphere with radius = 10 voxels, the optimal values of `rh`

Table 1. `rh` parameter choice.

`rh`	RVV			AVV			SSVV		
	κ_1	κ_2	κ_1 and κ_2	κ_1	κ_2	κ_1 and κ_2	κ_1	κ_2	κ_1 and κ_2
5	64.62%	83.59%	74.10%	78.32%	90.68%	84.50%	70.05%	81.97%	76.01%
6	70.21%	87.44%	78.82%	83.80%	94.12%	88.96%	77.85%	89.90%	83.87%
7	74.47%	90.41%	82.44%	87.46%	95.30%	91.38%	83.16%	93.81%	88.48%
8	78.27%	93.24%	85.75%	89.13%	95.67%	92.40%	88.03%	95.46%	**91.75%**
9	80.89%	95.73%	88.31%	90.11%	95.90%	93.00%	87.25%	89.53%	88.39%
10	82.76%	97.24%	90.00%	90.75%	96.09%	**93.42%**	57.63%	2.61%	30.12%
11	84.31%	97.93%	91.12%	90.72%	95.95%	93.34%	0.00%	0.00%	0.00%
12	85.12%	98.23%	91.67%	90.71%	95.46%	93.09%			
13	85.55%	98.09%	91.82%	90.60%	95.14%	92.87%			
14	85.95%	98.01%	91.98%	90.76%	95.08%	92.92%			
15	86.15%	98.01%	92.08%	90.97%	95.02%	92.99%			
16	86.35%	97.92%	**92.13%**	91.14%	94.92%	93.03%			
17	86.53%	97.72%	92.13%	91.28%	94.86%	93.07%			

Performance of our proposed algorithms on noisy sphere with radius = 10 voxels depending on `rh` (in voxels) is measured by normalized area of the cumulative histograms of the principal curvature errors (separately and taken together). The "κ_1 and κ_2" maxima for each algorithm are shown in bold.

https://doi.org/10.1371/journal.pcbi.1007962.t001

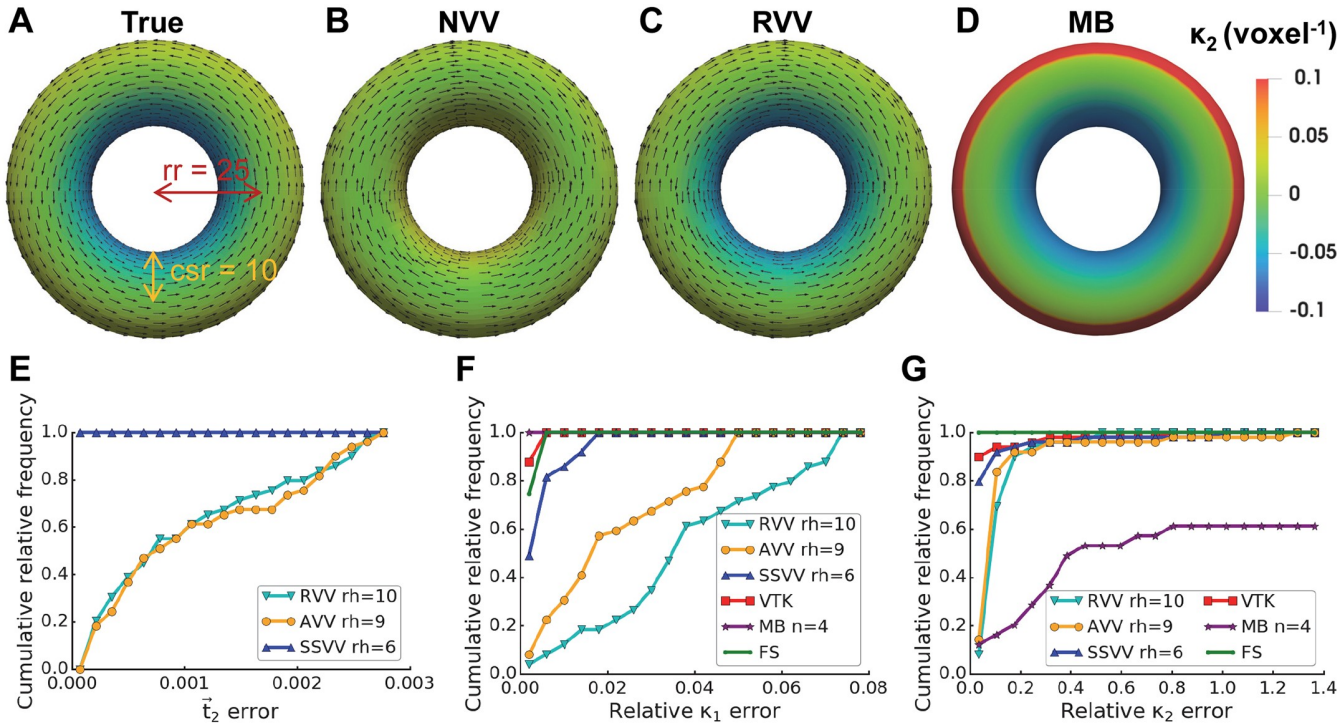

Fig 6. Curvature sign, principal direction and curvature estimation accuracy for a torus. Panels (A-D) show visualizations of κ_2 (voxel^{-1}, triangles are color-coded by curvature, see color bar on the right) and $\vec{t}_2$ (every fourth vector is shown as an arrow from a triangle center): (**A**) true values calculated analytically for a smooth torus surface with ring radius (rr) = 25 voxels and cross-section radius (csr) = 10 voxels, (**B**) estimated values using NVV, (**C**) RVV (both with `rh` = 8 voxels) and (**D**) Mindboggle (MB, with `n` = 4 voxels). Panels (E-G) show cumulative relative frequency histograms of the principal direction and curvature errors: (**E**) $\vec{t}_2$, (**F**) κ_1, (**G**) κ_2 on the torus surface using different algorithms: RVV, AVV, SSVV, VTK, MB and FreeSurfer (FS); the latter three algorithms only for curvatures in (F-G), since they do not estimate principle directions; the optimal `rh` or `n` (in voxels) were used for each algorithm and are indicated in the legends.

https://doi.org/10.1371/journal.pcbi.1007962.g006

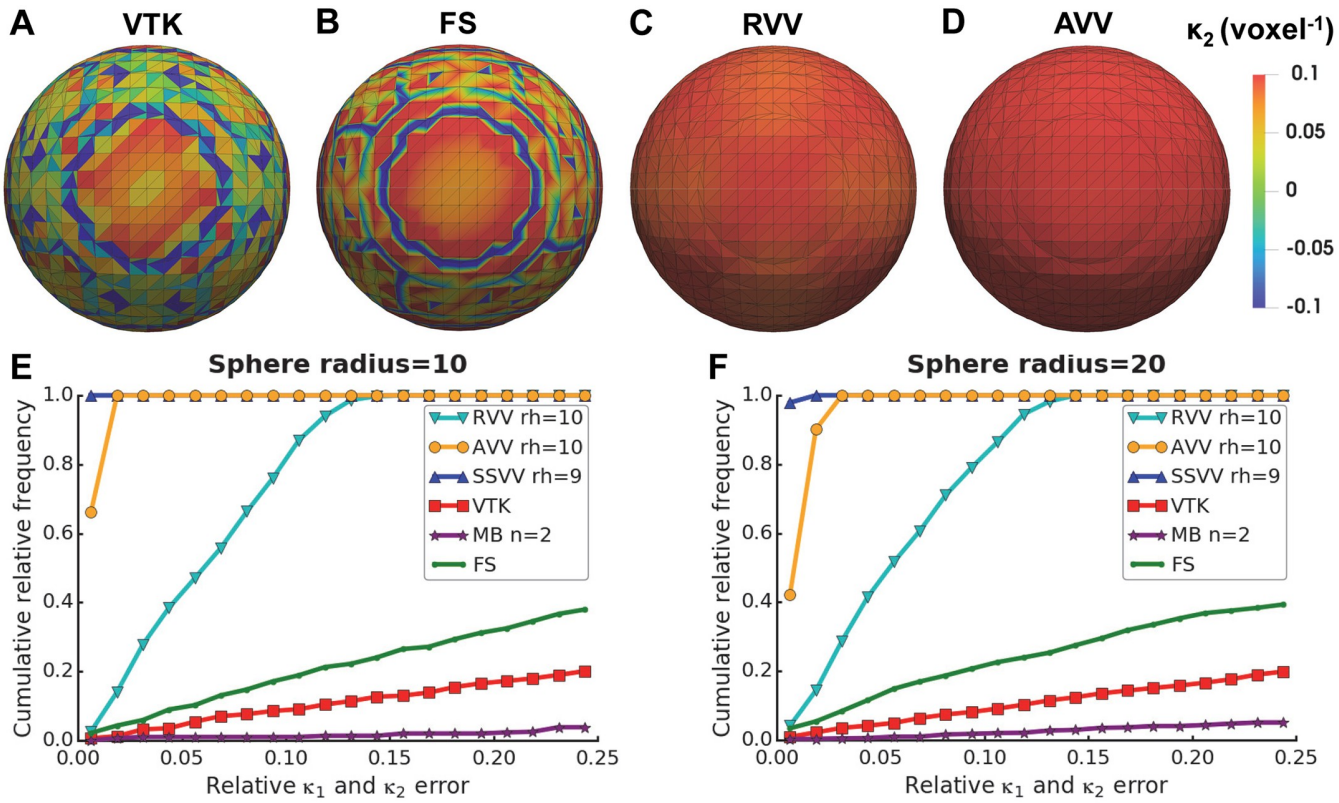

Fig 7. Accuracy of curvature estimation on a smooth spherical surface. Panels (A-D) show visualizations of κ_2 (voxel^{-1}) estimated by (**A**) VTK, (**B**) FreeSurfer (FS), (**C**) RVV or (**D**) AVV on a smooth sphere with radius = 10 voxels, using `rh` = 10 voxels for RVV and AVV. Panels (E-F) show cumulative relative frequency histograms of the principal curvature (κ_1 and κ_2) errors on a smooth sphere with radius = 10 (**E**) or 20 voxels (**F**) using different algorithms: RVV, AVV, SSVV, VTK, Mindboggle (MB) and FS; the values of `rh` or `n` (in voxels) used for each algorithm are indicated in the legends.

https://doi.org/10.1371/journal.pcbi.1007962.g007

were used: 10 voxels for RVV and AVV and 9 voxels for SSVV as well as the optimal `n` = 2 voxels for Mindboggle. VTK, Mindboggle and FreeSurfer had very high errors (Fig 7A, 7B and 7E). The maximum error was only ∼0.16 for RVV (Fig 7C and 7E), while AVV achieved a substantial improvement (maximum error ∼0.03) over RVV (Fig 7D and 7E), presumably because of the non-uniform tessellation of the sphere. SSVV performed slightly better than AVV (maximum error ∼0.01; Fig 7E).

To test how stable the algorithms are for different curvature scales, we increased the radius of the smooth sphere from 10 to 20 voxels, while leaving the `rh` and `n` values the same. All algorithms performed almost the same as for the sphere with radius 10 voxels (Fig 7F).

Altogether, the evaluation results on smooth benchmark surfaces show that the tensor voting-based algorithms are quite stable to feature sizes variations (beyond `rh`) and irregular triangles within one surface (Fig 7), whereas VTK, Mindboggle and FreeSurfer only perform well for a very smooth surface with a regular triangulation (Fig 6). AVV can deal with non-uniformly tessellated surfaces better than RVV, likely because curvature votes are also weighted by relative triangle area in AVV. In the original algorithm [33], weighting curvature votes by triangle area would not make sense because normals and curvatures are estimated at triangle vertices. Since we decided to estimate normals and curvatures at triangle centers instead, curvature votes are cast by complete triangles and weighting them by triangle area proved to be advantageous.

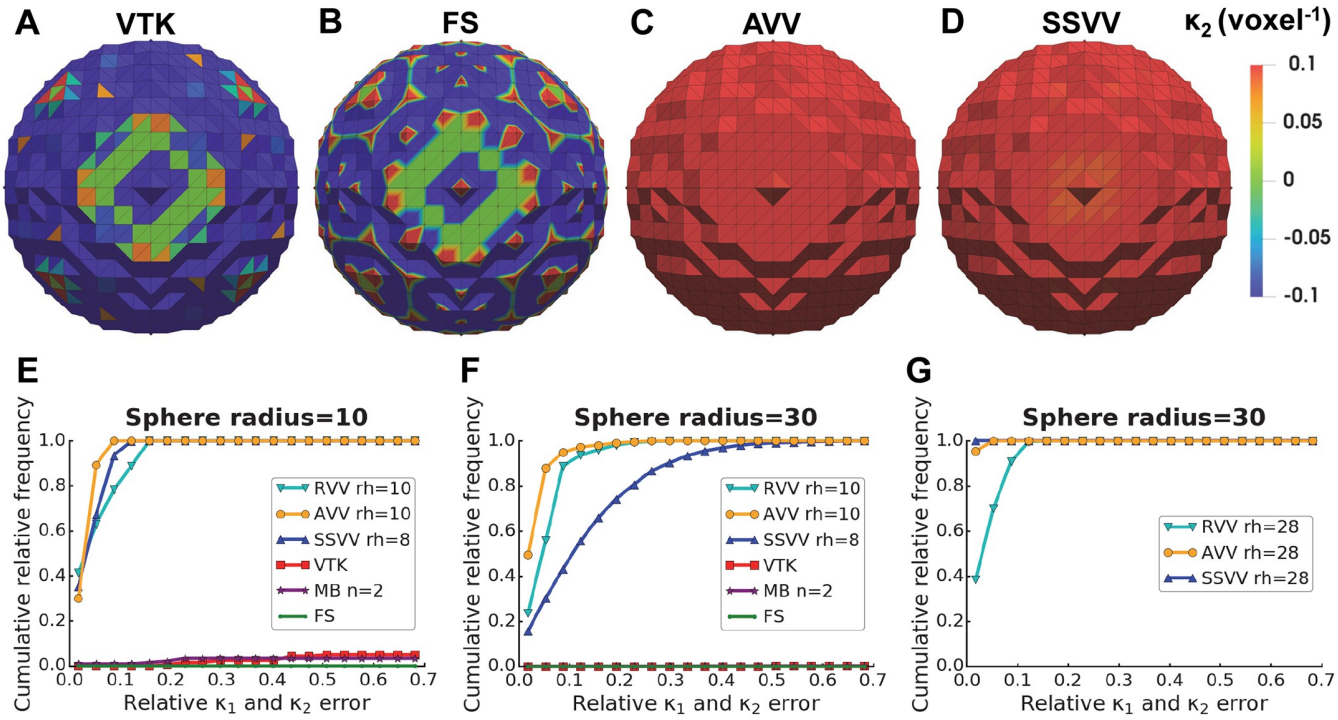

Fig 8. Accuracy of curvature estimation on a spherical surface with quantization noise. Panels (A-D) show visualizations of κ_2 (voxel^{-1}) estimated by (**A**) VTK, (**B**) FreeSurfer (FS), (**C**) AVV using the optimal `rh` = 10 voxels or (**D**) SSVV using the optimal `rh` = 8 voxels on a sphere with quantization noise and radius = 10 voxels. Panels (**E-G**) show cumulative relative frequency histograms of the principal curvature (κ_1 and κ_2) errors on a spherical surface with quantization noise and (E) radius = 10 or (F-G) 30 voxels using RVV, AVV, SSVV, VTK, Mindboggle (MB) and FS; latter three algorithms only in (E-F). The values of `rh` or `n` (in voxels) used for each algorithm are indicated in the legends.

https://doi.org/10.1371/journal.pcbi.1007962.g008

Robustness to surface noise. Surfaces generated from segmentations of biological membranes are not smooth, as the surface triangles tend to follow the voxel boundaries resulting in steps. As we are considering binary voxel values, the size of the steps depends on the voxel size of the segmented tomogram.

To test how the algorithms perform in presence of quantization noise, we generated a step-like surface of a sphere with a radius of 10 voxels, as in Fig 5. As expected, VTK only measured the curvature differences between directly neighboring triangles, resulting in high errors, similar to Mindboggle (using the optimal `n` = 2 voxels) and FreeSurfer (Fig 8A, 8B and 8E). To compare RVV, AVV and SSVV, we first used optimal `rh` values (10 voxels for RVV and AVV and 8 voxels for SSVV, Fig 5B–5D, Table 1). The principal curvature errors were higher for AVV and SSVV compared to the smooth sphere (5-10 fold, compare X-axis scales in Figs 7E and 8E), but were similar for RVV. However, AVV outperformed SSVV in this case (Fig 8C–8E), whereas the latter performed slightly better on the smooth spherical surface (Fig 7E).

We compared again the accuracy of the algorithms for increasing feature size and a constant `rh` value. When using a sphere with a radius of 30 voxels, VTK, Mindboggle and FreeSurfer still performed extremely poorly, and the estimation accuracy of SSVV decreased drastically, while the performance of AVV and RVV decreased only slightly (Fig 8F). The performance of SSVV improved using a `rh` value similar to the sphere radius, 28 voxels, which should be close to optimum (Fig 8G). Also the performance of AVV increased in this case, while the performance of RVV stayed similar (compare Fig 8F and 8G).

Therefore, when quantization noise is present, all our algorithms perform better than the currently available methods tested here. SSVV requires a higher `rh` in the range of the curvature radius, while AVV is quite stable with a lower `rh` value. Using a very high `rh` is generally not advisable, as it would lead to the underestimation of curvatures at smaller surface features. Since RVV performed consistently worse than AVV, we exclude RVV from further comparison.

Higher errors at surface borders. As explained previously, membranes in cryo-ET segmentations have holes and open ends. Thus, we aimed for a curvature estimation algorithm that is robust to such artifacts.

Tensor voting-based algorithms use a supporting neighborhood in order to improve the estimation, so holes much smaller than the neighborhood region do not affect them critically. However, a vertex close to surface border has considerably less neighbors. Therefore, we hypothesized that the estimation accuracy at vertices close to such borders would be worse. To prove this hypothesis, we generated a smooth cylindrical surface opened at both sides with radius = 10 and height = 25 voxels and evaluated the performance of our algorithms. Optimal `rh` values were used for AVV (5 voxels) and for SSVV (6 voxels), as well as optimal `n` for Mindboggle (2 voxels). FreeSurfer was not included in this test, since it failed on this open surface.

As expected, both tensor voting-based algorithms made a worse estimation near borders: AVV overestimated κ_1 gradually when moving towards the borders and κ_2 at the last triangles (Fig 9A), while SSVV underestimated κ_1 consistently and made a gradient of wrong estimations for κ_2 in the same region (Fig 9B). Since VTK does not use a bigger neighborhood, it showed high errors at changes in the triangle pattern all over the cylinder (Fig 9C). Mindboggle showed high errors for κ_1 in a striped pattern and for κ_2 at some patches near the borders (Fig 9D). SSVV and AVV showed $\vec{t}_2$ and κ_1 errors in the same range (Fig 9E and 9F), while VTK and Mindboggle made higher κ_1 errors than our algorithms (Fig 9F). When excluding values within the distance of 5 voxels to the graph border, the errors were virtually eliminated for AVV and SSVV, but did not change for VTK (Fig 9G and 9H). For Mindboggle, we could not exclude values at borders because our graph structure used for borders filtering is not available for that method. However, as one can see in Fig 9D, the high κ_1 errors of Mindboggle would not have been eliminated with this strategy.

Altogether, these benchmark results demonstrate the validity of our tensor voting-based algorithms and their robustness to quantization noise, especially of AVV. Additionally, curvature estimations at surface borders can be erroneous, so they should be excluded from an analysis.

Application to biological surfaces

Choice of algorithms and parameters for membranes from cryo-ET. AVV and SSVV proved most robust to quantization noise in synthetic surfaces. To evaluate their performance on real cryo-ET data, we used a cER compartment segmentation that contains several high curvature regions or peaks [16].

First, we studied the relationship between the `rh` parameter and the feature size. For this, we isolated a single cER peak with a maximum base radius of approximately 10 nm from a tomogram and estimated its curvature using several `rh` values. We observed that real membrane features have a diverse curvature distribution with several local maxima and minima (Fig 10A and 10B). For low values of `rh`, the distributions of curvature are broad, getting progressively sharper with increasing `rh`. For AVV (Fig 10A), the maximum amount of values around 0.1 nm^{-1} (corresponding to the 10 nm radius of the peak) is reached for `rh` = 10,

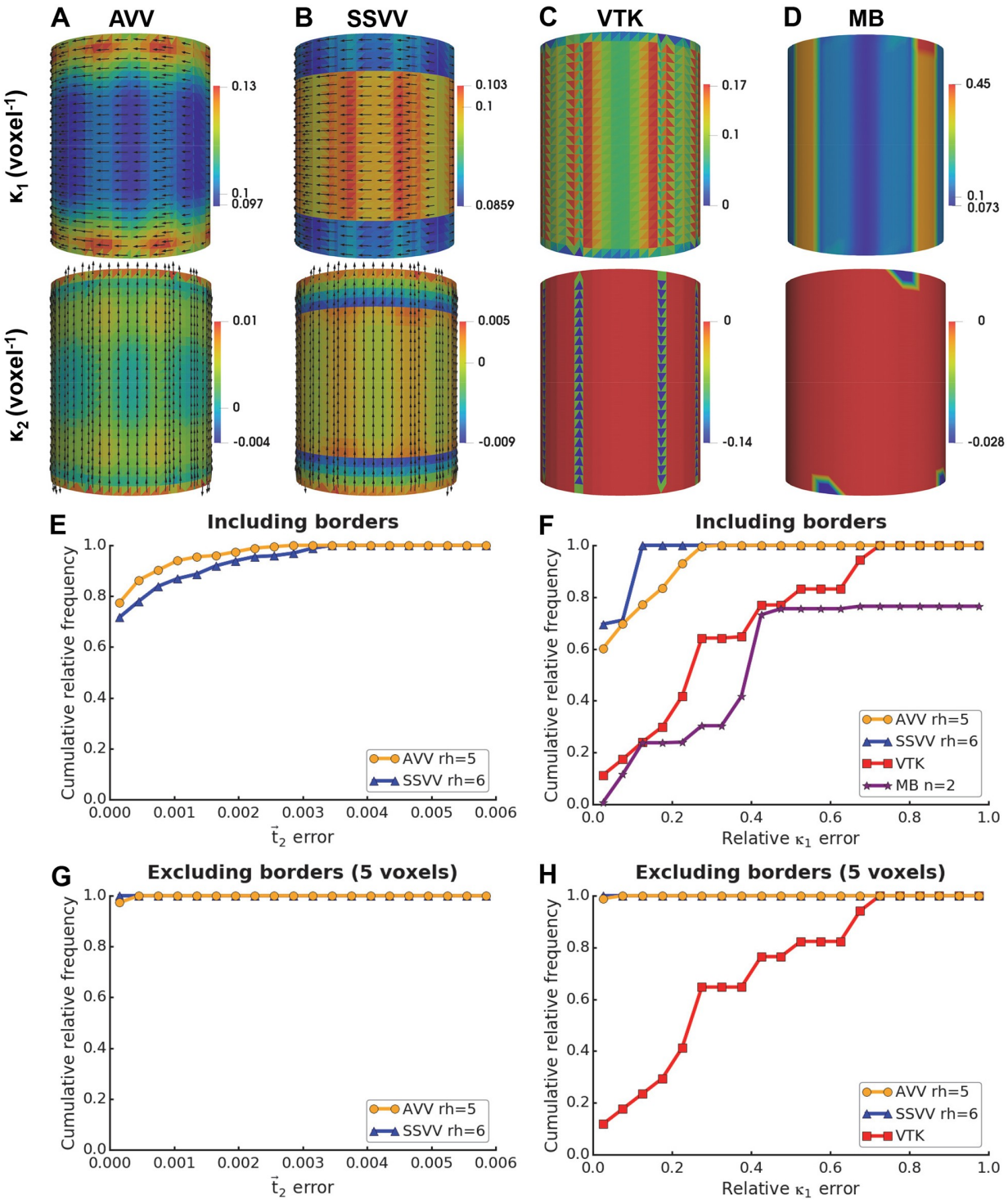

Fig 9. Estimation accuracy on a cylindrical surface. Panels (A-D) show principal curvatures on a smooth cylinder with radius = 10 and height = 25 voxels estimated by different algorithms: (**A**) AVV using the optimal `rh` = 5 voxels, (**B**) SSVV using the optimal `rh` = 6 voxels, (**C**) VTK and (**D**) Mindboggle (MB) using the optimal `n` = 2 voxels; the estimated κ_1 and κ_2 are shown in their original ranges; true $\kappa_1 = 0.1$, true $\kappa_2 = 0$ voxel^{-1}. Panels (E-H) show cumulative relative frequency histograms of the $\vec{t}_2$ errors (**E**, **G**) and κ_1 errors (**F**, **H**) on the cylinder using different algorithms: AVV, SSVV, VTK and MB; latter two algorithms only for κ_1 in (F, H); the optimal `rh` or `n` (in voxels) were used for each algorithm and are indicated in the legends. In panels (G-H), values within 5 voxels to the graph border were excluded.

https://doi.org/10.1371/journal.pcbi.1007962.g009

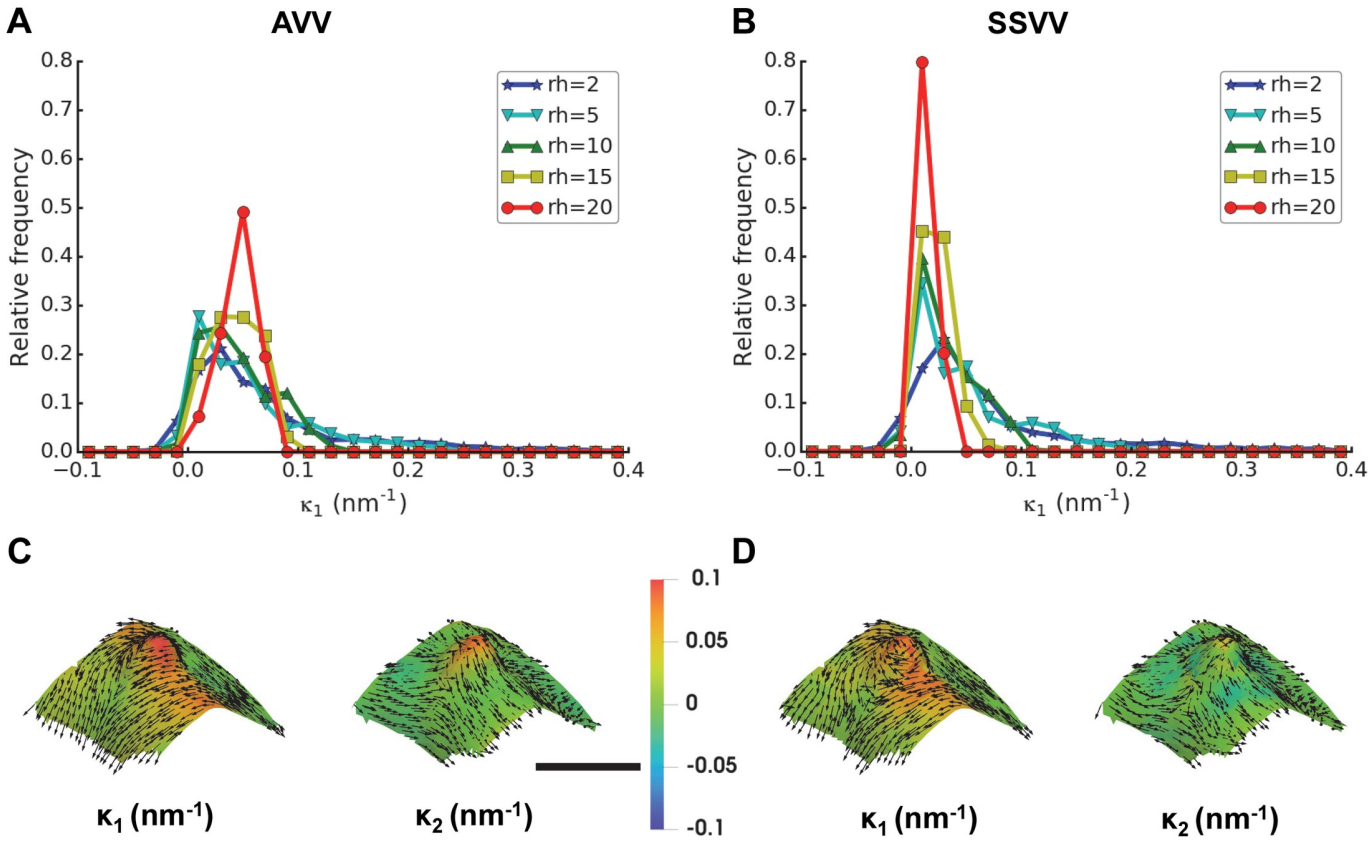

Fig 10. Algorithms and parameters comparison using a small cER membrane feature from cryo-ET. Surface of a cER membrane region with maximum base radius ~10 nm (from the same tomogram of a yeast cell as the cER in Fig 11) was generated using the compartment segmentation. Panels (A-B) show relative frequency histograms of κ_1 estimated by (**A**) AVV or (**B**) SSVV using `rh` = 2, 5, 10, 15 and 20 nm. Panels (C-D) show visualizations of the estimated κ_1 and κ_2 (color scale was set to the value range of [-0.1, 0.1] nm^{-1} in both panels) and the corresponding principal directions (black arrows, sampled for every forth triangle) by (**C**) AVV or (**D**) SSVV using `rh` = 10 nm (scale bar: 20 nm, applies for both panels).

https://doi.org/10.1371/journal.pcbi.1007962.g010

indicating that the feature is observed as a whole and its smaller components fade. Higher `rh` no longer produce curvature values around 0.1 nm^{-1}, indicating that the feature is averaged out. A similar trend is observed for SSVV (Fig 10B), although this method produces less curvature values around 0.1 nm^{-1}, thus underestimating the real curvature of the feature.

Second, we visualized the principal curvatures of the feature using `rh` = 10 nm to analyze the difference between the two curvature estimation algorithms. For this specific feature, its principal curvatures estimated by AVV (Fig 10C) increased in the direction from the base to the summit, while SSVV (Fig 10D) underestimated the curvatures, especially κ_2. Since SSVV sampled only surface points at distance equal to `rh` of 10 nm from each triangle center, it "oversaw" the high curvature at and near the summit. Contrary to SSVV, AVV considered all triangles within the geodesic neighborhood and thus estimated the curvature increase towards the summit correctly. This example confirms that AVV performs better than SSVV for complex surfaces like biological membranes.

Lastly, we applied AVV with `rh` = 10 nm to the full cER membrane surface, from which the peak shown in Fig 10 was extracted (Fig 11A and 11B). For comparison, we also applied VTK and Mindboggle to this surface (Fig 11C). Visually, `n` = 2 nm yielded the best results for Mindboggle. On this membrane surface, AVV clearly outperforms VTK and Mindboggle, which

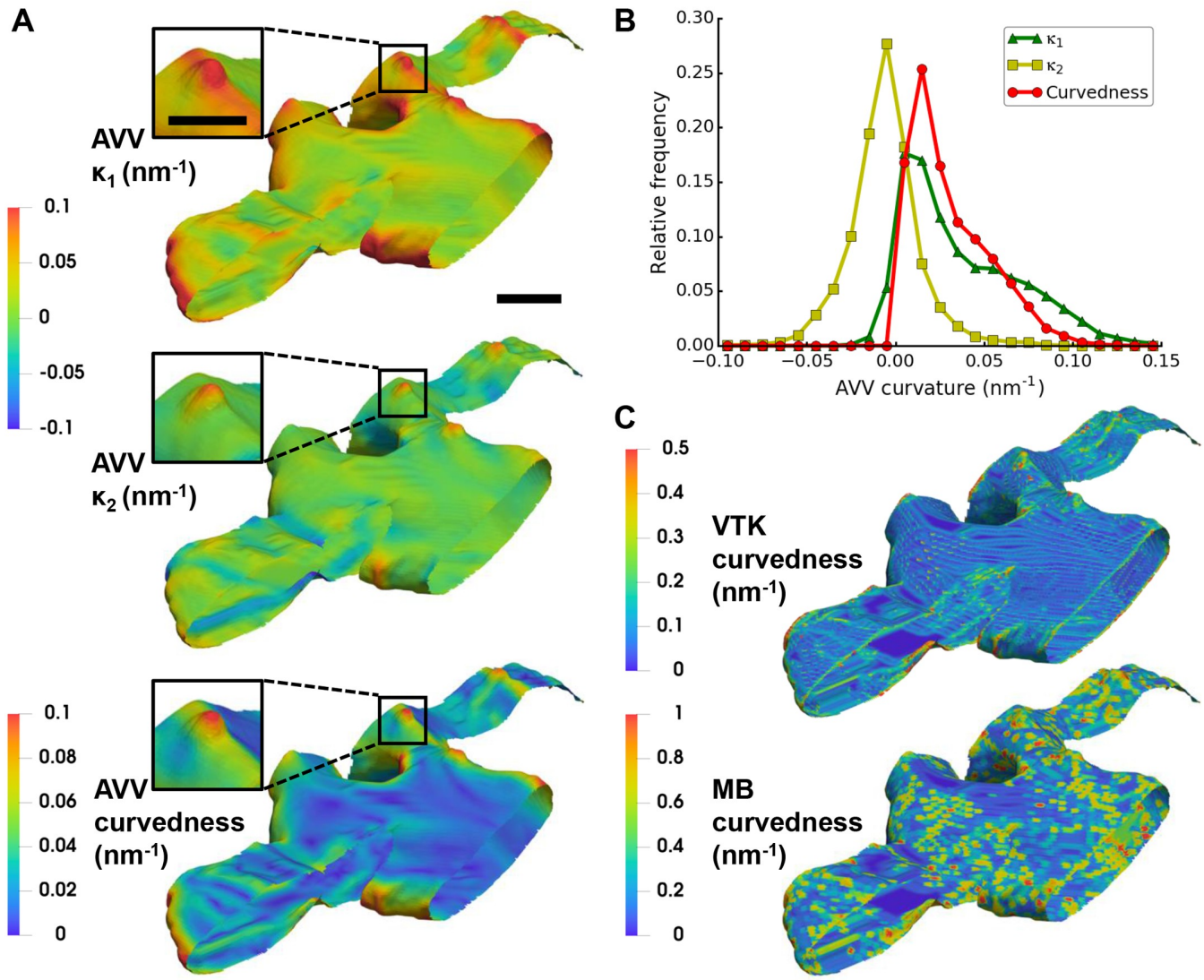

Fig 11. Application of curvature estimation algorithms to a cER membrane from cryo-ET. Analysis of yeast cER membrane curvature on a surface generated using the compartment segmentation. (**A**) Visualizations of the curvatures: κ_1, κ_2 and curvedness, estimated by AVV with `rh` of 10 nm (scale bar: 40 nm). The insets show the peak feature from Fig 10 (scale bar: 20 nm). Color scale was set to the value range of [-0.1, 0.1] nm^{-1} for κ_1 and κ_2 and of [0, 0.1] nm^{-1} for curvedness. (**B**) Relative frequency histograms of the curvatures estimated by AVV shown in (A). (**C**) Visualizations of curvedness on the same surface as in (A) calculated by VTK (top) and Mindboggle (MB; using `n` = 2 nm; bottom), scale bar as in the main panel (A). Since curvedness ranges were larger for these algorithms, color scales were set to the value range of [0, 0.5] nm^{-1} for VTK and [0, 1] nm^{-1} for Mindboggle. The tomogram and segmentation are deposited in EM Data Bank (EMD-10765).

https://doi.org/10.1371/journal.pcbi.1007962.g011

provide very noisy results with high values following the steps between neighboring triangles and the surface borders (compare the values of curvedness in Fig 11A and 11C).

Curvature comparison across cellular organelles. To test our method on membranes with different morphologies, we segmented the Golgi apparatus and Golgi-derived vesicles in a tomogram recorded on a mouse neuron. A Golgi apparatus is composed of flat cisternae stacked in a bent, semicircular shape. Again, we extracted the membrane surfaces using the compartment segmentation and estimated the curvatures using AVV with `rh` of 10 nm (Fig 12A). To minimize borders effects, values within 1 nm to surface border were excluded for

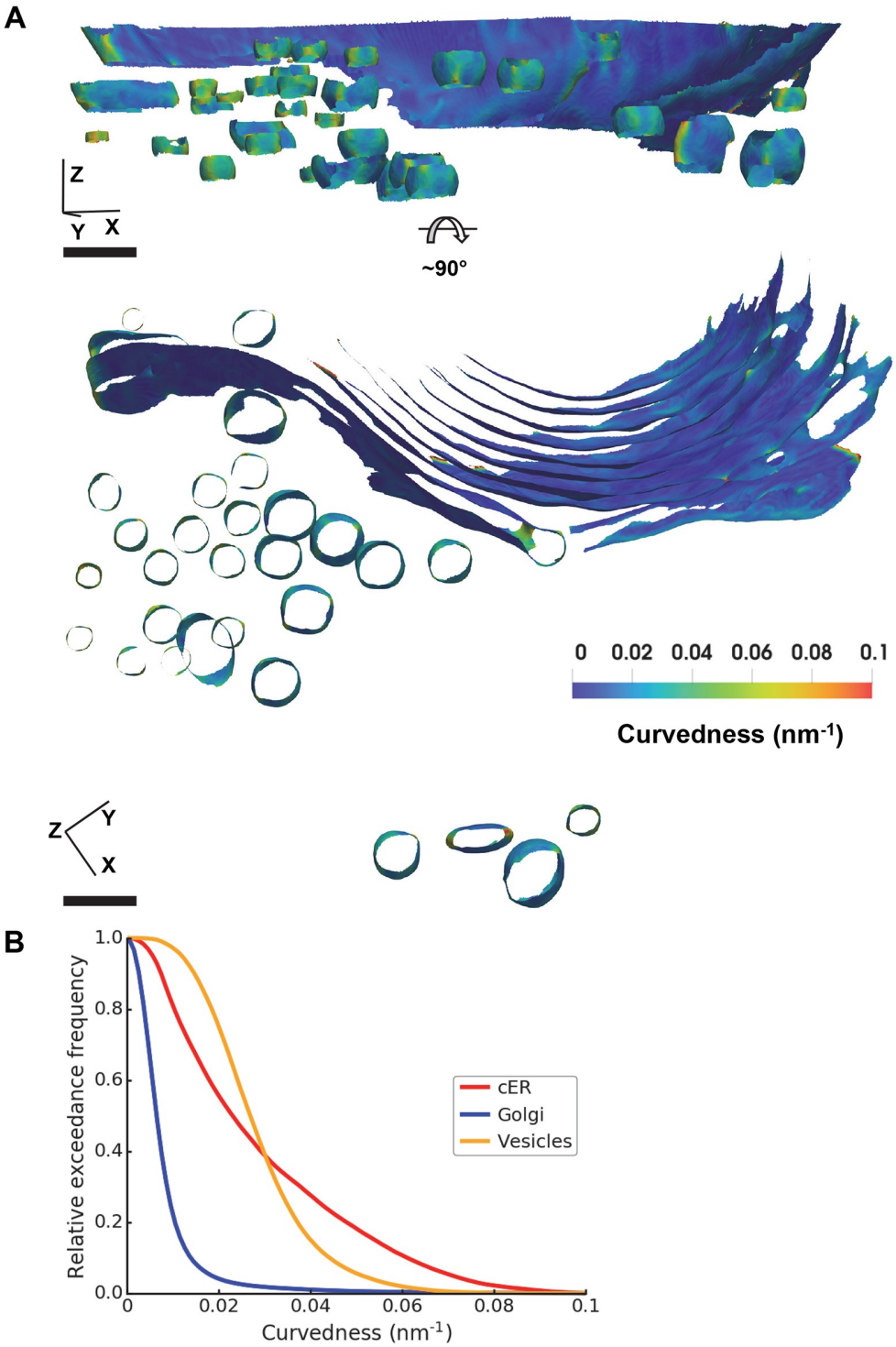

Fig 12. Application of AVV to Golgi and vesicles from cryo-ET. (**A**) Two different views of surfaces of Golgi and vesicles (from a primary mouse neuron) generated using the compartment segmentation showing curvedness estimated by AVV with `rh` of 10 nm. Color scale was set to the value range of [0, 0.1] nm^{-1} (scale bar: 100 nm). (**B**) Relative exceedance frequency histograms (reversed cululative histograms with frequency normalized to the total surface area of each compartment) of the curvedness of cER (shown in Fig 11A and 11B), Golgi and vesicles (shown in panel A of this figure), excluding values within 1 nm to surface border. The tomogram and segmentations are deposited in EM Data Bank (EMD-10766).

https://doi.org/10.1371/journal.pcbi.1007962.g012

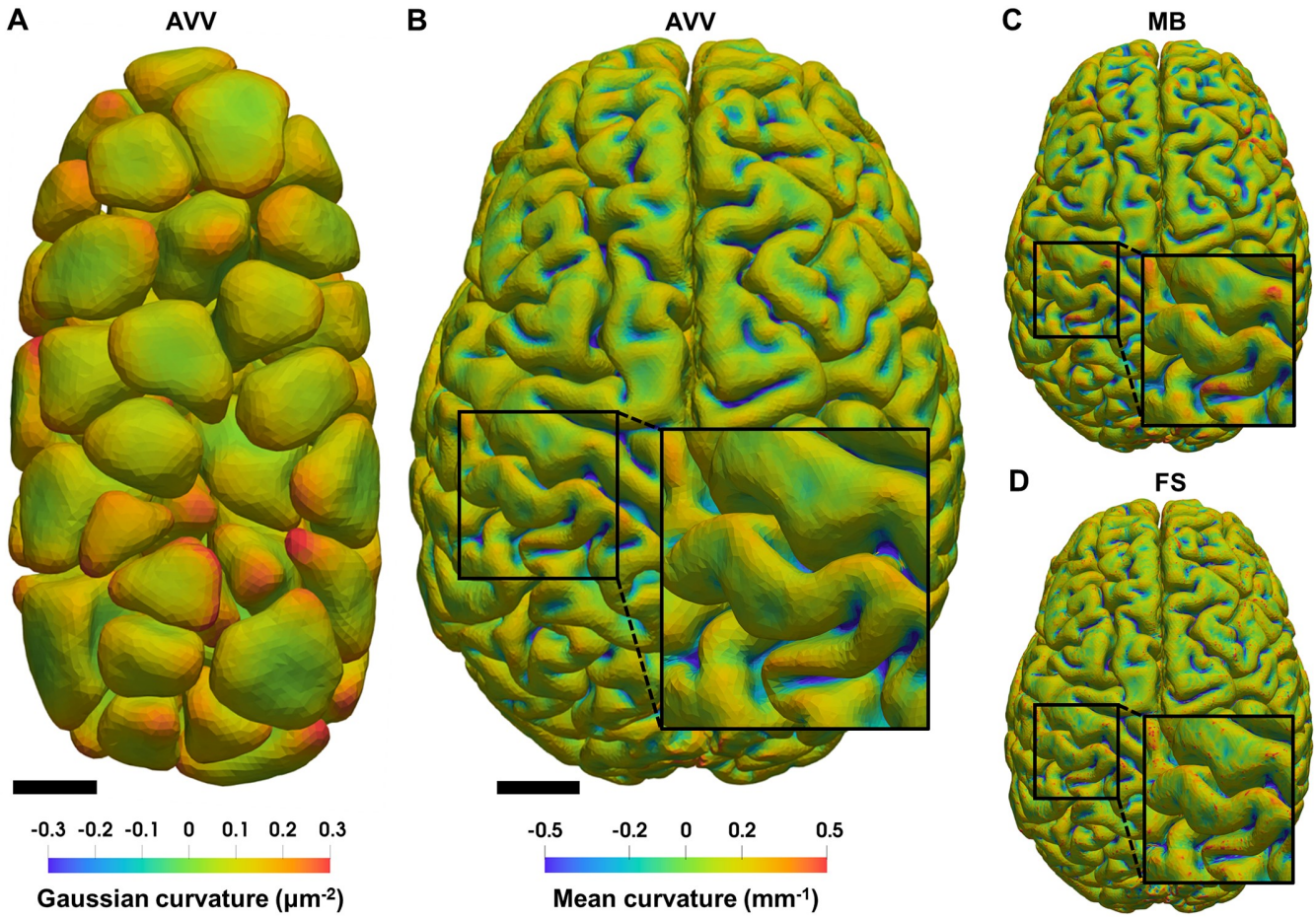

Fig 13. Application of curvature estimation algorithms to other data types. (**A**) Surfaces of *C. elegans* embryo cells imaged by confocal light microscopy and segmented by LimeSeg [22], colored by Gaussian curvature (μm^{-2}) estimated by AVV using `rh` = 3 μm (scale bar: 5 μm). (**B**) Cortical pial surfaces of both human brain hemispheres imaged by MRI and segmented by FreeSurfer [52], colored by mean curvature (mm^{-1}) estimated by AVV using `rh` = 2 mm (scale bar: 20 mm). Panels (C-D) show the same brain surface colored by mean curvature (mm^{-1}) with the same color scale as in (B) estimated by (**C**) Mindboggle (MB; using `n` = 2 mm) and (**D**) FreeSurfer (FS).

https://doi.org/10.1371/journal.pcbi.1007962.g013

plotting. Fig 12B compares the curvedness of the cER (Fig 11) with that of the Golgi and Golgi-derived vesicles. The histogram shows that the Golgi has much lower curvedness than the other two organelles, whereas the cER reaches higher curvedness values than the vesicles. The results can be visually confirmed: the thin and long Golgi cisternae are only slightly curved, while the vesicles are smaller and thus much more curved (Fig 12A). The cER is generally less curved than the vesicles, but has high curvature at the peaks and sides of its sheets (Fig 11A). These data show that curvedness estimated by AVV can be a useful descriptor of biological membranes.

Application to other data types. To demonstrate the applicability of AVV beyond cryo-ET, we applied it to two other data types. The first data set is comprised of *C. elegans* embryo cells imaged by confocal light microscopy and segmented by LimeSeg [22]. The cell surfaces colored by their Gaussian curvature estimated by AVV using `rh` = 3 μm are shown in Fig 13A. The second data set, taken from Mindboggle [42], are cortical pial surfaces of both human brain hemispheres imaged by MRI and segmented by FreeSurfer [52]. The cortical surfaces colored by their mean curvature estimated by AVV using `rh` = 2 mm are shown in Fig 13B.

The range of curvature values for the embryo and the brain is consistent with their sizes. Using Mindboggle [42] with $n = 2$ mm (Fig 13C) and FreeSurfer [41] (Fig 13D), we obtained comparable, but noisier, mean curvature distributions on the brain; FreeSurfer introduced finer-grained noise than Mindboggle. Despite the lack of ground truth, this comparison suggests that AVV provides a more accurate curvature estimation for different data types.

Implementation and availability

All the described algorithms and the tests on benchmark surfaces were implemented using Python and are available in PyCurv at https://github.com/kalemaria/pycurv, along with the experimental data sets and scripts allowing to obtain the results presented in the Section Application to biological surfaces. PyCurv depends only on open source packages, including: Pyto [53], Graph-tool [48] and VTK [30]. Note that FreeSurfer [52] and Mindboggle [42] had to be installed and called externally for the evaluation; FreeSurfer version "stable v6.0.0" for Linux and Mindboggle Docker container from 2019-09-24 were used.

Discussion

In this article, we described a method for the estimation of the local curvature of biological membranes and validated it on synthetic and real data. The curvature estimation workflow in PyCurv can be divided in two main steps. The first step is to represent the membrane as a triangle mesh surface that can be obtained from two different types of segmentation: segmentation of the membrane alone, or a filled segmentation of a membrane-bound cellular compartment. The second option usually demands more human intervention but the surface orientation could be recovered perfectly in our experiments. Smoothing of the filled segmentation prior to surface extraction leads to less quantization noise because the surface is extracted at subvoxel precision. Surface triangles are mapped to a graph to facilitate the computation of geodesic distances and to filter border artifacts. The second step is to determine the underlying surface orientation (represented by normal vectors), local curvatures and principal directions.

Here, we evaluated the performance of our curvature estimation algorithms, RVV, AVV and SSVV (adaptations of [33] and [40]) against the publicly available VTK [30], FreeSurfer [41] and Mindboggle [42]. Although we chose the optimal radius of the neighborhood (n) parameter for each benchmark surface, Mindboggle performed poorly on irregular and noisy surfaces. Also FreeSurfer, which performed the best on a smooth and regular surface, yielded high errors on irregular and noisy surfaces. Moreover, FreeSurfer cannot be applied to surfaces containing borders, so it is not applicable for cryo-ET data. Our tests using synthetic and biological surfaces showed that the proposed algorithms, RVV, AVV and SSVV, are more robust to quantization noise than the above-mentioned existing methods. AVV performs better than RVV for non-uniformly tessellated surfaces. For complex non-spherical surfaces like biological membranes, AVV yields better results than SSVV. Therefore, AVV is the default algorithm in PyCurv.

Curvature is a local property, so its value on discrete surfaces depends on the definition of a neighborhood. Robustness to noise increases with the neighborhood size by averaging the contributions of the neighboring triangles. However, features smaller than the neighborhood are averaged out. Therefore, the neighborhood size defines the scale of the features that can be analyzed. To achieve more reliable results for cryo-ET segmentations that contain holes, curvature values at surface borders and/or higher than rh^{-1} should be excluded from the analysis.

PyCurv was already applied in a cryo-ET study in yeast proposing that cER membrane curvature plays a key role in the regulation of ER-to-PM lipid homeostasis at membrane contact sites [16]. Moreover, the analysis of data generated by MRI and light microscopy shows that

our method can be applied to any segmented membrane compartments or other volumes from which a surface can be extracted, originating from any 3D imaging technique. We conclude that the open-source Python package PyCurv can be used to reliably process cryo-ET and other data to study membrane and surface curvature in a large variety of applications.

Supporting information

S1 Video. PyCurv workflow. The visualization of PyCurv processing workflow, as described in Fig 1A, for the tomogram from Fig 2, showing in the order of occurrence: *membrane* and *compartment segmentations* of the cortical ER, generated surface, normals estimated by Vector Voting (VV) and curvedness estimated by Augmented Vector Voting (AVV) algorithms. (MP4)

Acknowledgments

We thank Markus Hohle, Vladan Lučić and Martin Salfer for helpful discussions as well as Felix J.B. Bäuerlein and Tillman Schäfer for tomography data.

Author Contributions

Conceptualization: Maria Salfer, Wolfgang Baumeister, Rubén Fernández-Busnadiego, Antonio Martínez-Sánchez.

Data curation: Maria Salfer, Javier F. Collado.

Formal analysis: Antonio Martínez-Sánchez.

Funding acquisition: Maria Salfer, Javier F. Collado, Wolfgang Baumeister, Rubén Fernández-Busnadiego.

Investigation: Maria Salfer, Javier F. Collado.

Methodology: Rubén Fernández-Busnadiego, Antonio Martínez-Sánchez.

Project administration: Wolfgang Baumeister, Rubén Fernández-Busnadiego.

Resources: Wolfgang Baumeister.

Software: Maria Salfer.

Supervision: Rubén Fernández-Busnadiego, Antonio Martínez-Sánchez.

Validation: Maria Salfer, Rubén Fernández-Busnadiego, Antonio Martínez-Sánchez.

Visualization: Maria Salfer, Rubén Fernández-Busnadiego, Antonio Martínez-Sánchez.

Writing – original draft: Maria Salfer, Rubén Fernández-Busnadiego, Antonio Martínez-Sánchez.

Writing – review & editing: Maria Salfer, Rubén Fernández-Busnadiego, Antonio Martínez-Sánchez.

References

1. McMahon HT, Boucrot E. Membrane curvature at a glance. J Cell Sci. 2015; 128(6):1065–1070. https://doi.org/10.1242/jcs.114454 PMID: 25774051
2. Bassereau P, Jin R, Baumgart T, Deserno M, Dimova R, Frolov VA, et al. The 2018 biomembrane curvature and remodeling roadmap. J Phys D Appl Phys. 2018; 51(34). https://doi.org/10.1088/1361-6463/aacb98 PMID: 30655651

3. Kozlov MM, Campelo F, Liska N, Chernomordik LV, Marrink SJ, McMahon HT. Mechanisms shaping cell membranes. Curr Opin Cell Biol. 2014; 29:53–60. https://doi.org/10.1016/j.ceb.2014.03.006 PMID: 24747171
4. Lučić V, Förster F, Baumeister W. Structural Studies By Electron Tomography: From Cells to Molecules. Annu Rev Biochem. 2005; 74:833–865. https://doi.org/10.1146/annurev.biochem.73.011303.074112 PMID: 15952904
5. Beck M, Baumeister W. Cryo-Electron Tomography: Can it Reveal the Molecular Sociology of Cells in Atomic Detail? Trends Cell Biol. 2016; 26(11):825–837. https://doi.org/10.1016/j.tcb.2016.08.006 PMID: 27671779
6. Wagner J, Schaffer M, Fernández-Busnadiego R. Cryo-electron tomography—the cell biology that came in from the cold. FEBS Lett. 2017; 591:2520–2533. https://doi.org/10.1002/1873-3468.12757 PMID: 28726246
7. Collado J, Fernández-Busnadiego R. Deciphering the molecular architecture of membrane contact sites by cryo-electron tomography. Biochim Biophys Acta Mol Cell Res. 2017; 1864:1507–1512. https://doi.org/10.1016/j.bbamcr.2017.03.009 PMID: 28330771
8. O'Reilly FJ, Xue L, Graziadei A, Sinn L, Lenz S, Tegunov D, et al. In-cell architecture of an actively transcribing-translating expressome. Science 2020; 369(6503):554–557. https://doi.org/10.1126/science.abb3758 PMID: 32732422
9. Chen Y, Yong J, Martínez-Sánchez A, Yang Y, Wu Y, De Camilli P, et al. Dynamic instability of clathrin assembly provides proofreading control for endocytosis. J Cell Biol. 2019; 218(10):3200–3211. https://doi.org/10.1083/jcb.201804136 PMID: 31451612
10. Lee KK. Architecture of a nascent viral fusion pore. EMBO J. 2010; 29(7):1299–1311. https://doi.org/10.1038/emboj.2010.13 PMID: 20168302
11. Cardone G, Brecher M, Fontana J, Winkler DC, Butan C, White JM, et al. Visualization of the Two-Step Fusion Process of the Retrovirus Avian Sarcoma/Leukosis Virus by Cryo-Electron Tomography. J Virol. 2012; 86(22):12129–12137. https://doi.org/10.1128/JVI.01880-12 PMID: 22933285
12. Bharat TAM, Malsam J, Hagen WJH, Scheutzow A, Söllner TH, Briggs JAG. SNARE and regulatory proteins induce local membrane protrusions to prime docked vesicles for fast calcium-triggered fusion. EMBO Rep. 2014; 15(3):308–314. https://doi.org/10.1002/embr.201337807 PMID: 24493260
13. Chlanda P, Mekhedov E, Waters H, Schwartz CL, Fischer ER, Ryham RJ, et al. The hemifusion structure induced by influenza virus haemagglutinin is determined by physical properties of the target membranes. Nat Microbiol. 2016; 1(6):1–8. https://doi.org/10.1038/nmicrobiol.2016.50 PMID: 27572837
14. Yao Q, Jewett AI, Chang YW, Oikonomou CM, Beeby M, Iancu CV, et al. Short FtsZ filaments can drive asymmetric cell envelope constriction at the onset of bacterial cytokinesis. EMBO J. 2017; 36(11):1577–1589. https://doi.org/10.15252/embj.201696235 PMID: 28438890
15. Bharat TAM, Hoffmann PC, Kukulski W. Correlative Microscopy of Vitreous Sections Provides Insights into BAR-Domain Organization In Situ. Structure. 2018; 26(6):879–886. https://doi.org/10.1016/j.str.2018.03.015 PMID: 29681471
16. Collado J, Kalemanov M, Campelo F, Bourgoint C, Thomas F, Loewith R, et al. Tricalbin-Mediated Contact Sites Control ER Curvature to Maintain Plasma Membrane Integrity. Dev Cell. 2019; 51:476–487. https://doi.org/10.1016/j.devcel.2019.10.018 PMID: 31743662
17. Bäuerlein FJB, Saha I, Mishra A, Kalemanov M, Martínez-Sánchez A, Klein R, et al. In Situ Architecture and Cellular Interactions of PolyQ Inclusions. Cell. 2017; 171:179–187. https://doi.org/10.1016/j.cell.2017.08.009 PMID: 28890085
18. Martinez-Sanchez A, Garcia I, Asano S, Lucic V, Fernandez JJ. Robust membrane detection based on tensor voting for electron tomography. J Struct Biol. 2014; 186:49–61. https://doi.org/10.1016/j.jsb.2014.02.015 PMID: 24625523
19. Martinez-Sanchez A, Kochovski Z, Laugks U, Meyer zum Alten Borgloh J, Chakraborty S, Pfeffer S, et al. Template-free detection and classification of membrane-bound complexes in cryo-electron tomograms. Nat Methods. 2020; p. 1–15. https://doi.org/10.1038/s41592-019-0675-5 PMID: 31907446
20. Mosaliganti KR, Noche RR, Xiong F, Swinburne IA, Megason SG. ACME: Automated Cell Morphology Extractor for Comprehensive Reconstruction of Cell Membranes. PLoS Comput Biol. 2012; 8(12):e1002780. https://doi.org/10.1371/journal.pcbi.1002780 PMID: 23236265
21. Chen M, Dai W, Sun SY, Jonasch D, He CY, Schmid MF, et al. Convolutional neural networks for automated annotation of cellular cryo-electron tomograms. Nat Methods. 2017; 14(10):983–985. https://doi.org/10.1038/nmeth.4405 PMID: 28846087
22. Machado S, Mercier V, Chiaruttini N. LimeSeg: A coarse-grained lipid membrane simulation for 3D image segmentation. BMC Bioinformatics. 2019; 20(2):1–12. https://doi.org/10.1186/s12859-018-2471-0 PMID: 30606118

23. Martinez-Sanchez A, Garcia I, Fernandez JJ. A differential structure approach to membrane segmentation in electron tomography. J Struct Biol. 2011; 175:372–383. https://doi.org/10.1016/j.jsb.2011.05.010 PMID: 21616152

24. do Carmo MP. Differential geometry of curves and surfaces. New Jersey: Prentice-Hall, Inc., Englewood Cliffs; 1976.

25. Meyer M, Desbrun M, Schröder P, Barr AH. Discrete Differential-Geometry Operators for Triangulated 2-Manifolds. Springer, Berlin, Heidelberg; 2003.

26. Hoppe H, DeRose T, Duchamp T, McDonald J, Stuetzle W. Surface reconstruction from unorganized points. In: SIGGRAPH'92 Proceedings of the 19th annual conference on Computer graphics and interactive techniques. New York: ACM; 1992. p. 71–78. https://doi.org/10.1145/133994.134011

27. Magid E, Soldea O, Rivlin E. A comparison of Gaussian and mean curvature estimation methods on triangular meshes of range image data. Comput Vis Image Underst. 2007; 107:139–159. https://doi.org/10.1016/j.cviu.2006.09.007

28. Polthier K, Schmies M. Straightest Geodesics on Polyhedral Surfaces. In: Mathematical Visualization. Springer Verlag; 1998. p. 391–409.

29. Desbrun M, Meyer M, Schröder P, Barr AH. Implicit fairing of irregular meshes using diffusion and curvature flow. In: SIGGRAPH'99 Proceedings of the 26th annual conference on Computer graphics and interactive techniques. New York: ACM Press/Addison-Wesley Publishing; 1999. p. 317–324. https://doi.org/10.1145/311535.311576

30. Schroeder W, Martin K, Lorensen B. The Visualization Toolkit (4th ed.). Kitware; 2006.

31. Szilvási-Nagy M. Face-based estimations of curvatures on triangle meshes. Journal for Geometry and Graphics. 2008; 12(1):63–73.

32. Razdan A, Bae M. Curvature estimation scheme for triangle meshes using biquadratic Bézier patches. Comput Aided Des. 2005; 37:1481–1491. https://doi.org/10.1016/j.cad.2005.03.003

33. Page DL, Sun Y, Koschan AF, Paik J, Abidi MA. Normal Vector Voting: Crease Detection and Curvature Estimation on Large, Noisy Meshes. Graph Models. 2002; 64:199–229. https://doi.org/10.1006/gmod.2002.0574

34. Goldfeather J, Interrante V. A novel cubic-order algorithm for approximating principal direction vectors. ACM Trans Graph. 2004; 23(1):45–63. https://doi.org/10.1145/966131.966134

35. Taubin G. Estimating the tensor of curvature of a surface from a polyhedral approximation. In: Proceedings of IEEE International Conference on Computer Vision. Cambridge: IEEE; 1995. p. 902–907. https://doi.org/10.1109/ICCV.1995.466840

36. Theisel H, Rössl C, Zayer R, Seidel HP. Normal based estimation of the curvature tensor for triangular meshes. In: 12th Pacific Conference on Computer Graphics and Applications. Seoul, South Korea: IEEE; 2004. p. 288–297. https://doi.org/10.1109/PCCGA.2004.1348359

37. Rusinkiewicz S. Estimating curvatures and their derivatives on triangle meshes. In: Proceedings of the 2nd International Symposium on 3D Data Processing, Visualization, and Transmission. Thessaloniki, Greece: IEEE; 2004. p. 486–493. https://doi.org/10.1109/TDPVT.2004.1335277

38. Medioni G, Lee MS, Tang CK. A Computational Framework for Segmentation and Grouping. Amsterdam: Elsevier Science B.V.; 2000.

39. Tang CK, Medioni G. Robust Estimation of Curvature Information from Noisy 3D Data for Shape Description. In: Proceedings of the Seventh IEEE International Conference on Computer Vision. Kerkyra, Greece: IEEE; 1999. https://doi.org/10.1109/ICCV.1999.791252

40. Tong WS, Tang CK. Robust Estimation of Adaptive Tensors of Curvature by Tensor Voting. In: IEEE Trans. Pattern Anal. Mach. Intell. vol. 27; 2005. p. 434–449. https://doi.org/10.1109/tpami.2005.62 PMID: 15747797

41. Pienaar R, Fischl B, Caviness V, Makris N, Grant PE. A methodology for analyzing curvature in the developing brain from preterm to adult. Int J Imaging Syst Technol. 2008; 18:42–68. https://doi.org/10.1002/ima.v18:1 PMID: 19936261

42. Klein A, Ghosh SS, Bao FS, Giard J, Häme Y, Stavsky E, et al. Mindboggling morphometry of human brains. PLoS Comput Biol. 2017; 13(2):1–40. PMID: 28231282

43. Moses DA, Axel L. Quantification of the curvature and shape of the interventricular septum. Magnetic Resonance in Medicine. 2004; 52(1):154–163. https://doi.org/10.1002/mrm.20105 PMID: 15236379

44. Bechstedt S, Lu K, Brouhard GJ. Doublecortin recognizes the longitudinal curvature of the microtubule end and lattice. Curr Biol. 2014; 24:2366–2375. https://doi.org/10.1016/j.cub.2014.08.039 PMID: 25283777

45. Xu M, Wu Y, Shroff H, Wu M, Mani M. A scheme for 3-dimensional morphological reconstruction and force inference in the early C. elegans embryo. PLoS One. 2018; 13(7). https://doi.org/10.1371/journal.pone.0199151 PMID: 29990323

46. Hoffman DP, Shtengel G, Xu CS, Campbell KR, Freeman M, Wang L, et al. Correlative three-dimensional super-resolution and block face electron microscopy of whole vitreously frozen cells. Science. 2020; 367(265):14. https://doi.org/10.1126/science.aaz5357 PMID: 31949053

47. Lorensen WE, Cline HE. Marching Cubes: A High Resolution 3D Surface Construction Algorithm. ACM SIGGRAPH Comput Graph. 1987; 21(4):163–169. https://doi.org/10.1145/37401.37422

48. Peixoto TP. The graph-tool python library. Database: figshare [Internet]; 2014. Available from: http://figshare.com/articles/graph_tool/1164194.

49. Dijkstra EW. A Note on Two Problems in Connexion with Graphs. Numer Math. 1959; 1:269–271.

50. Koenderink JJ, van Doorn AJ. Surface shape and curvature scales. Image Vis Comput. 1992; 10 (8):557–564. https://doi.org/10.1016/0262-8856(92)90076-F

51. Ahrens J, Geveci B, Law C. ParaView: An end-user tool for large-data visualization. Visualization Handbook. 2005; 836:717–731. https://doi.org/10.1016/B978-012387582-2%2F50038-1

52. Dale AM, Fischl B, Sereno MI. Cortical Surface-Based Analysis. Neuroimage. 1999; 9:179–194. https://doi.org/10.1006/nimg.1998.0395 PMID: 9931268

53. Lučić V, Fernández-Busnadiego R, Laugks U, Baumeister W. Hierarchical detection and analysis of macromolecular complexes in cryo-electron tomograms using Pyto software. J Struct Biol. 2016; 196 (3):503–514. https://doi.org/10.1016/j.jsb.2016.10.004 PMID: 27742578

54. Rigort A, Bäuerlein FJB, Villa E, Eibauer M, Laugks T, Baumeister W, et al. Focused ion beam micromachining of eukaryotic cells for cryoelectron tomography. PNAS. 2012; 109(12):4449–4454. https://doi.org/10.1073/pnas.1201333109 PMID: 22392984

55. Mastronarde DN. Automated electron microscope tomography using robust prediction of specimen movements. J Struct Biol. 2005; 152:36–51. https://doi.org/10.1016/j.jsb.2005.07.007 PMID: 16182563

56. Li X, Mooney P, Zheng S, Booth CR, Braunfeld MB, Gubbens S, et al. Electron counting and beam-induced motion correction enable near-atomic-resolution single-particle cryo-EM. Nat Methods. 2013; 10(6):584–590. https://doi.org/10.1038/nmeth.2472 PMID: 23644547

57. Kremer JR, Mastronarde DN, McIntosh JR. Computer visualization of three-dimensional image data using IMOD. J Struct Biol. 1996; 116:71–76. https://doi.org/10.1006/jsbi.1996.0013 PMID: 8742726

58. Moreno JJ, Martínez-Sánchez A, Martínez JA, Garzón EM, Fernández JJ. TomoEED: fast edge-enhancing denoising of tomographic volumes. Bioinformatics. 2018; 34(21):3776–3778. https://doi.org/10.1093/bioinformatics/bty435 PMID: 29850773

59. Nickell S, Förster F, Linaroudis A, Net WD, Beck F, Hegerl R, et al. TOM software toolbox: acquisition and analysis for electron tomography. J Struct Biol. 2005; 149(3):227–234. https://doi.org/10.1016/j.jsb.2004.10.006 PMID: 15721576

Erratum

The covariance matrix used in Equation (3) on page 8 should be calculated as

$$V_i = \vec{n}_i \vec{n}_i^t$$

instead of

$$V_i = \vec{n}_i^t \vec{n}_i.$$

Equation (10) on page 10 should be

$$\cos\phi_i = \frac{\vec{n}_{\mathrm{v}}^t \vec{n}_{\mathrm{v}_i}^p}{||\vec{n}_{\mathrm{v}_i}^p||}$$

instead of

$$\cos\phi_i = \frac{\vec{n}_{\mathrm{v}}^t \vec{n}_{\mathrm{v}_i}^p}{||\vec{n}_i||}.$$

3 Summary of results and discussion

3.1 Developed algorithms

3.1.1 Surface generation

First, we optimized surface generation from membrane segmentations to eliminate border artifacts and have a notion of orientation, as described on page 6 and Figure 2 in (Salfer et al., 2020). Membrane segmentations (set of voxels) have to be represented by surfaces (triangle meshes) since curvature is a feature of a single-layered surface. However, one of the main limiting factors for membrane curvature estimation in cryo-ET is quantization noise in the membrane segmentations, resulting in step-like surfaces (Section 1.4.5). Therefore, our initial *membrane segmentation* surface extraction algorithm used in (Bäuerlein et al., 2017) that is based on the surface reconstruction algorithm from Hoppe et al. (1992) generates step-like surfaces among other artifacts caused by wrong surface orientation (Figure 2B,D-E in (Salfer et al., 2020)). To overcome these surface orientation artifacts, we proposed the *compartment segmentation* algorithm on page e4 in (Collado et al., 2019), which requires additionally a filled segmentation of the compartment but extracts the surface correctly using the Marching Cubes algorithm (Lorensen and Cline, 1987) (Figure 2C and G in (Salfer et al., 2020)).

As seen from the evaluation results of the curvature estimation algorithms in PyCurv software package (Salfer et al., 2020), smoother surfaces enable higher estimation accuracy of the surface normals (pages 13-14, Figure 4F in (Salfer et al., 2020)), principal directions and curvatures (pages 17-18, Figures 7E and 8E in (Salfer et al., 2020)). However, a direct surface smoothing is not advisable, because it would fade small membrane features such as Tcb-mediated cER peaks (Collado et al., 2019), which are just $\sim$10 nm or $\sim$3.5 voxels in radius (e.g. Figure S2B-C in (Collado et al., 2019) and Figure 11A in (Salfer et al., 2020)).

In our *compartment segmentation* surface extraction algorithm, sometimes triangles protruding perpendicularly to the surface were produced at manually-segmented regions by Marching Cubes (Figure 2H in (Salfer et al., 2020)). Smoothing the segmentation prior to surface extraction helped to achieve subvoxel precision and eliminate those triangles (Figure 2H in (Salfer et al., 2020)). To minimize the impact of quantization noise and achieve subvoxel precision, we decided to smooth the filled membrane segmentation only slightly prior to Marching Cubes application (Figure 2J-K in (Salfer et al., 2020)).

3.1.2 Graph classes and their applications

To precisely compute the density of membrane-bound ribosomes, estimate membrane curvature and detect surface borders, geodesic distances are required. In order to easily calculate geodesic distances along a membrane, we decided to represent it by a graph structure, which is a set of vertices and edges that connect pairs of vertices.

Then, it is possible to find a shortest path between two vertices along the graph edges using e.g. Dijkstra algorithm (Dijkstra, 1959) and to obtain the geodesic distance by summing up the lengths of the edges along the shortest path, as described on page 8 in (Salfer et al., 2020). PyCurv implements two different types (classes) of graphs: `VoxelGraph` and `TriangleGraph`.

The `VoxelGraph` class was used for the calculation of ribosome density on ER membrane (see Section 3.1.3) in (Bäuerlein et al., 2017), as described on page e5 in that paper. In brief, a `VoxelGraph` instance is generated directly from a membrane segmentation by adding all membrane voxels to the set of vertices and connecting all pairs of vertices representing neighboring voxels by edges.

The `TriangleGraph` class was used for the estimation of surface curvature descriptors (see Section 3.1.4) in (Bäuerlein et al., 2017; Collado et al., 2019; Salfer et al., 2020). A `TriangleGraph` instance is generated from a signed, single-layered triangle mesh surface (e.g. extracted from a membrane segmentation), so that every triangle center is added to the set of graph vertices. Then, neighboring triangle pairs sharing an edge are connected by *strong edges*, while those sharing only a vertex are connected by *weak edges*. Both edges types are involved in geodesic distances calculation, while only the *strong edges* are used for borders detection. Borders detection is another advantage of the graph representation that enables filtering out of wrong curvature estimations near surface borders. See Figure 1A, D and pages 6,8 in (Salfer et al., 2020) for more details.

Both graph classes are implemented using the graph-tool python library[1] (Peixoto, 2014). The shortest path Dijkstra algorithm is used for the three procedures: (1) to calculate the geodesic distances to all reachable ribosomes from a `VoxelGraph` vertex for the calculation of the ribosome density (page e5 in (Bäuerlein et al., 2017)), (2) to find neighboring triangles within a maximal geodesic distance from a `TriangleGraph` vertex for the estimation of surface curvature descriptors (pages 7-8 in (Salfer et al., 2020)), and (3) to detect `TriangleGraph` borders for surface borders filtering (page 8 in (Salfer et al., 2020)). See Section 4.1.1 for a runtime analysis of the graph generation algorithms.

3.1.3 Calculation of ribosome density on ER membrane

A computational approach for analyzing ribosome density on ER membrane was developed and applied in (Bäuerlein et al., 2017). As discussed above (Section 3.1.2), the membrane segmentation was represented by a graph that interconnects neighboring membrane voxels by edges (`VoxelGraph`), instead of first extracting a surface and then representing it by a graph that interconnects neighboring triangles by edges (`SurfaceGraph`), as done for the curvature estimation (Section 3.1.4). In general, it is not ideal to calculate surface-based properties on voxels. However, the voxel-based approach was legitimate here for the following reasons. (1) The coordinates of membrane-bound ribosomes obtained by template matching were projected on the nearest ER membrane voxels. The projected ribosome coordinates were automatically a subset of the `VoxelGraph` vertices, corresponding to the membrane voxels. Thus, geodesic distances between the membrane voxels and reachable ribosome coordinates could be directly calculated using the graph edges, as described above. (2) The obtained ribosome density values also corresponded to membrane voxels, enabling

[1] https://git.skewed.de/count0/graph-tool

color-mapping the ribosome density on the ER membrane segmentation, as visualized in Figure 3G in (Bäuerlein et al., 2017).

As briefly described on page e5 in (Bäuerlein et al., 2017), the ribosome density (D) for each membrane voxel was defined using the geodesic distances (d) to the projected ribosome voxels on the membrane as:

$$D = \sum_{(reachable\ ribosomes)} \frac{1}{d+1}$$

Reachable ribosomes are those that can be reached via the membrane from the source voxel by a path via the graph edges. In the denominator, 1 was added to d in order to eliminate division by zero in case a ribosome is located at the source membrane voxel (d=0). Thus, the contribution of each ribosome to D is maximum 1 and becomes smaller as d grows. In conclusion, the higher the number of reachable ribosomes and the shorter the distances to them, the higher the D value.

As clearly seen from the visualization in Figure 3G in (Bäuerlein et al., 2017), ribosome density is low (starting with 0) at ER membrane regions interacting with Htt fibrils and gradually raises (until 1.8) as ER distance from the fibrils increases. To numerically prove this positive correlation, it would be possible to compute nearest distances between ER segmentation voxels and fibril coordinates and correlate them to the ribosome density.

3.1.4 Estimation of surface curvature of membranes

The original aim of this thesis was to quantitatively compare curvature of the ER membranes interacting with a Htt inclusion to controls without an inclusion (Bäuerlein et al., 2017). For this, I implemented the *membrane segmentation* procedure for surface generation from a membrane segmentation (Figure 2B in Salfer et al. (2020)), as summarized in Section 3.1.1. To reduce the surface artifacts that mainly occurred at segmentation regions with holes, I first applied a morphological operator to close small holes in the segmentation. Dilation (growth) followed by erosion (shrinkage) with a cube of 3 or 5 voxels in size was sufficient for obtaining reasonable surfaces from those seven segmentations. Additionally, small disconnected surface components up to 100 triangles were filtered out.

To estimate ER curvature in (Bäuerlein et al., 2017), I implemented the Normal Vector Voting (NVV) algorithm from (Page et al., 2002) with adaptations. In brief, the original algorithm calculates curvature descriptors per triangle vertex and geodesic distances by linear interpolation upon the surface (Kimmel and Sethian, 1998; Sun and Abidi, 2001), whereas NVV calculates curvature descriptors per triangle face and geodesic distances using our `TriangleGraph` structure. However, as shown in the evaluation of our algorithms (page 14 and in Figure 6A-B in (Salfer et al., 2020)), NVV output only positive principle curvatures, even for saddle surfaces like the inside of a torus, where κ_2 must be negative. As the magnitude of the estimated κ_2 was comparable to the true κ_2, we decided to use curvedness in (Bäuerlein et al., 2017) (see page e6 in (Bäuerlein et al., 2017) or Equation 17 on page 12 in (Salfer et al., 2020)), which is always positive independent of the principal curvatures sign. To determine the neighborhood size set by the maximal geodesic distance parameter g_{max}, my initial NVV version used `k` parameter similar to the original algorithm (Page et al., 2002). While in the original

algorithm k was multiplied by the average surface triangle edge length to set g_{max}, in my initial version k was multiplied by the average weak triangle graph edge length. Weak graph edges were used as they are more similar in length to the surface triangle edges than the shorter strong graph edges. We set k to 3, resulting in g_{max} around 9 nm. Inspired by Tong and Tang (2005), the rh parameter was introduced in the later NVV version described on pages 8-11 in (Salfer et al., 2020). This parameter should be set to the radius of the smallest spherical feature of interest. Then, g_{max} is set to 1/4 circumference of a circle with radius equal to rh. This enables a more direct control over the scale of features to be estimated reliably. Moreover, rh can be set independently from the triangle size of the input surface, contrary to k that has to be adapted to it in order to achieve the desired g_{max}. See Section 4.2.1 and Figure 4.3 for comparison of ER curvedness from Figure S2D in (Bäuerlein et al., 2017) to the one estimated by the algorithm with corrected sign estimation and rh parameter, Augmented Vector Voting (AVV), which is described on pages 10-11 in (Salfer et al., 2020). Briefly, both algorithms showed higher ER curvedness values near Htt IBs (n=4 tomograms) than in the controls without Htt IBs (n=3 tomograms), the difference was even higher using AVV. To see whether there is a negative correlation between the distance to fibrils and ER membrane curvature, it would be possible to compute shortest distances between the ER triangle centers and the Htt fibrils coordinates and correlate them to the ER curvedness.

For comparison of curvature of cER in yeast cells expressing specific ER-PM tether proteins in Figure 3E in (Collado et al., 2019), the AVV algorithm was used with rh value of 10 nm to reliably estimate the curvature of cER peaks with radius of around 10 nm. To exclude unreliable estimations, values within 1 nm to the surface border as well as triangles with curvedness above 0.1 nm^{-1} were excluded from the analysis. Later, we used the same workflow to estimate the curvature of Golgi cisternae and Golgi-derived vesicles from a tomogram of a mouse neuron (pages 22-24 and Figure 12 in (Salfer et al., 2020)). See Section 4.2.2 and Figure 4.4 for a comparative analysis of the estimated curvature distributions of all those organelles and of their curvatures known from the literature.

Error analysis

A reliable curvature estimation method has to be robust to noise. In cryo-ET, there are many possible noise sources: measurement noise during the image acquisition caused by e.g. low SNR and missing wedge (Section 1.2.5), computational errors made by the projections alignment algorithms for tomogram reconstruction (Section 1.2.4) as well as by automatic and manual image analysis, e.g. membrane segmentation (Section 1.3.4). Moreover, extraction of a surface from a segmented volume might also introduce errors (Section 3.1.1). Since we could not account for all these sources of errors, we mainly considered the quantization noise (Section 1.4.5). For range imaging data, which is a 2D image showing the distance to points of an object from a specific point, it was found that accuracy of curvature is limited mainly by combination of quantization and smoothing error (Trucco and Fisher, 1995). On one hand, smoothing is necessary for a better estimation of curvature on discrete data. On the other hand, smoothing lowers the actual curvature values. The authors also found that smoothing a small sphere deforms it and decreases its curvature. These findings must also apply for microscopy data. In order not to loose small membrane features of interest, we decided

not to smooth the surfaces much (Section 3.1.1) and instead average the information contained in a bigger geodesic neighborhood (Section 2.3).

One could estimate small manual segmentation errors of one voxel at material boundaries, e.g. between a membrane and the cytosol (Pienaar et al., 2008). Tomograms usually have voxel sizes of ∼0.2-0.4 nm (equal in X, Y and Z) and are binned twice for segmentation to increase contrast, resulting in segmentations with voxel sizes of ∼0.8-1.6 nm. Assuming a standing out incorrectly segmented voxel of size 1^3 nm, the surface reconstruction would produce a cubic bump at that place, which would have the radius of curvature of one-half voxel, i.e., 0.5 nm. Thus, curvature values above $\frac{1}{0.5} = 2$ nm^{-1} are due to single voxel miss-classifications. Curvatures above this value are unreliable and should be excluded from analysis. However, we already suggested to use the `rh` parameter to approximate the highest curvature value PyCurv can estimate reliably, which is ½`rh` (Section 2.3). `rh` is usually set to a higher value than one-half voxel, thus bounding the curvature at already lower values than 2 nm^{-1}, e.g. 0.1 nm^{-1} for the default `rh` value of 10 nm. Therefore, PyCurv curvature estimation algorithms are tolerant to quantization noise and small segmentation errors.

We evaluated our proposed four curvature estimation algorithms against three currently existing ones using synthetic surfaces with known curvature, as summarized in Section 2.3. This enabled calculation of errors between the estimated and the true values for quantitative comparison between the algorithms. *Vector error* was calculated for normals and principle directions and *scalar relative error* for principle curvatures using, respectively, Equations 19 and 20 on page 12 in (Salfer et al., 2020).

To sum up, our surface curvature estimation algorithms were inspired by tensor voting-based algorithms, especially by those of Page et al. (2002) and Tong and Tang (2005) (Section 1.4.3). To correct the erroneous curvature sign in NVV, I combined and adapted both algorithms leading to Regular Vector Voting (RVV). Then, I further improved the accuracy on irregular surfaces resulting in AVV. Finally, Surface Sampling Vector Voting (SSVV) was implemented for higher speed, however it was shown to be less robust to variable feature size. The differences between the four algorithms are explained on page 11 and the evaluation results are shown on pages 13-19 in (Salfer et al., 2020). For an extensive runtime analysis of our two best-performing surface curvature estimation algorithms, AVV and SSVV, see Section 4.1.2.

3.1.5 Calculation of intermembrane distances

To measure intermembrane distances at MCS in yeast (Collado et al., 2019), e.g. between cER and PM, Prof. Dr. Antonio Martínez-Sanchez initially implemented a segmentation-based algorithm. In this algorithm, normals generated by TomoSegMemTV (Martinez-Sanchez et al., 2014) at each voxel of the first membrane label are extended until their intersection with the second membrane label. Then, the distances between the two membranes are calculated as lengths of these extended normals. For the distances to be closer to the shortest distances, the straighter membrane should be chosen as the first membrane, e.g. PM in case of ER-PM MCS.

However, this segmentation-based algorithm has two major problems. First, only the membrane voxels segmented automatically by TomoSegMemTV have a normal, but not the manually added ones during the refinement with Amira software (Thermo Fisher Scientific). Second, the distances calculated like this are between the central layers of the two membranes, as TomoSegMemTV segments the central membrane ridges. Thus,

the calculated distances are bigger than the actual distances between the cytosolic leaflets of the membranes. While the second problem can be approximately solved by subtracting the membrane bilayer thickness in nm from the calculated distances, the first problem leads to missing values.

To solve the major problems of the segmentation-based algorithm, we developed a surface-based one, which has the following five steps. (1) The membrane segmentations are grown by morphological operators to match the membrane thickness, and the intermembrane cytosolic space is filled. (2) Surfaces following the cytosolic side of the membranes are generated using the *compartment segmentation* algorithm. (3) NVV is applied to the source membrane surface to denoise the normals. (4) Each denoised normal is extended until the intersection with the target membrane surface. (5) The Euclidean distance between the source triangle center of the normal and its intersection point on the target surface is calculated. Additionally, the algorithm was extended to calculate the cER thickness using the cER lumen segmentation. For this, Euclidean distance is calculated between two intersection points of each PM normal and the surface following the luminal side of the cER membrane. As triangle-mesh surfaces go through the centers of the voxels on the edge of the segmentations, one voxel size in nm is added to the distances and thicknesses for correction. For more details like the used thresholds, see page e4 in (Collado et al., 2019). For full results, see Figure 2G-H and pages 477-478 in (Collado et al., 2019) or Section 2.2 for a summary.

3.2 Future work

Our curvature estimation algorithms included in PyCurv can be used to quantify the morphological descriptors of any segmented cellular membranous organelles in tomograms of cells in a native state or under different conditions, like mutations of certain proteins or heat stress. The long term plan is to characterize the curvature profiles of different cellular organelles, and maybe even use curvature as a useful descriptor to e.g. annotate membrane segmentations. See Section 4.2.2 as a first step in that direction. Given enough reliably segmented data with curvature profiles, it would be possible to train a model for classification of different organelles based on their curvature. Such a model can help to automatically separate generic membrane labels into different organelles and so shorten the manual labeling and refinement process.

Knowing the curvature landscape of cellular membranes raises the question which proteins are responsible for the local curvature generation or maintenance. After curvature estimation by PyCurv, it is possible to answer this question by filtering the output membrane surface to regions having a certain curvature range and then searching for candidate proteins near those regions by template matching or by a template-free method e.g. PySeg (Section 1.3.2). To generate the search mask, a distance threshold from the triangle vertices within the surface regions can be simply used. Since the membrane surface is oriented, it is possible to look only for densities on the cytosolic or lumenal side of the organelle. Ideally, PyCurv would connect directly to PySeg to find those membrane-bound densities and cluster them using the unsupervised clustering method AP.

One of the major limitations of applying PyCurv is that it requires nearly perfect membrane segmentations to correctly extract surfaces, ideally with filled lumen (Section 3.1.1). As explained in Section 1.3.4, due to the complexity and the low SNR in

tomograms, segmentations generated by an automatic segmentation tool like TomoSeg-MemTV (Martinez-Sanchez et al., 2014) still have to be refined manually, which is a very time consuming task. One way to solve this limitation is to improve the automatic membrane segmentation, e.g. by using deep learning-based methods like (Chen et al., 2017). However, these methods are supervised and require a big training set, i.e. many tomograms with manually refined membrane labels, which would be time consuming to generate. Maybe the aforementioned unsupervised clustering of membrane profiles by combination of PyCurv with PySeg can even help to improve membrane segmentations without any labeled training set. A different way would be to adapt the curvature estimation algorithms to work on an alternative data structure generated directly from unrefined membrane segmentations, instead of triangle meshes represented by graphs. As mentioned in Section 1.4.2, there are more flexible point-based surface representation techniques as point clouds and surface splats. Actually, the algorithm of Tong and Tang (2005) was designed for point clouds. Elliptical splats might be especially interesting for curvature estimation, as they can be aligned to the principal directions of the underlying surface.

Another drawback of PyCurv is that the normals and curvature estimation algorithms are calculation-intense. As described in Section 4.1.2, we have improved the performance of the relevant algorithms by symmetric multiprocessing using several parallel processes in a single processor. To go further with the parallelization, it is possible to explore implementations that use other high-performance computing architectures, such as computer clusters or graphics processing units.

Lastly, at the moment PyCurv is not an easy to use tool. Although all the code, including workflow scripts, is documented and the curvature estimation workflow is explained step-by-step, users should be familiar with basic Python programming. To make PyCurv a broadly used tool that ideally everybody could apply to analyze their favorite 3D data (not only from cryo-ET but also from e.g. confocal light microscopy or MRI, see Figure 13 in (Salfer et al., 2020)), further developments are needed. A minimum requirement is a command line interface with a detailed user manual. The ideal solution would be an intuitive graphical user interface, but it would be very time consuming to design and implement. Also making PyCurv available on other operating systems apart from Linux, at least Windows, would be beneficial. The big advantage of PyCurv is being an open source and publicly available project on GitHub[2], which makes it open for further developments and freely accessible to the broad scientific community.

[2] https://github.com/kalemaria/pycurv

4 Appendix

4.1 Runtime analysis of main PyCurv algorithms

For the runtime analysis described in this section, PyCurv version 2.1.0 was executed on a single processor with 500 GB of RAM, 36 processors Intel(R) Xeon(R) CPU E5-2699 v3 @ 2.30GHz and a SUSE Linux Enterprise Server 12 SLES 12 SP 1 operating system.

4.1.1 Runtime analysis of graph generation

In both graph classes discussed in Section 3.1.2, large graphs are generated that include all the voxels of the input segmentation (for `VoxelGraph`) or triangle centers of the input surface (for `TriangleGraph`) in the set of vertices. This enables us to get as many ribosome density or curvature values as possible for a reliable statistical analysis or for a smooth gradient when visualizing the values on the membrane. However, iterating over all neighboring vertices for each graph vertex and generating all unique pairs of edges is computationally demanding and is not trivial to be parallelized due to the serial nature. Graph generation is expected to grow linearly with the number of voxels (for VoxelGraph) or triangles (for TriangleGraph), which might become time consuming for a large segmentation or surface.

To analyze the runtime of the graph generation algorithms depending on the input size, instances of VoxelGraph were generated for hollow spherical masks and instances of TriangleGraph for noisy spherical surfaces with different radii (5, 10, ..., 50 voxels). As expected, the duration in seconds grows linearly with the number of voxels for VoxelGraph (Figure 4.1A) and with the number of triangles for TriangleGraph (Figure 4.1B), in both cases with a similar slope. Also the number of graph edges grows linearly with the number of graph vertices. The slope is slightly higher for TriangleGraph than for VoxelGraph, as the TriangleGraph has more edges per vertex.

4.1.2 Runtime analysis of curvature estimation

The surface curvature descriptors are estimated per triangle (represented by a TriangleGraph vertex) and using a supporting neighborhood of triangles (defined by `rh` parameter). Thus, normals and curvature estimation might become time consuming for large surfaces and a bigger neighborhood.

To analyze the runtime depending on surface size, I applied our two best performing algorithms, AVV and SSVV, to noisy sphere surfaces with different radii (5, 10, ..., 50 voxels) using a constant `rh` of 10 voxels. The duration of both algorithms, consisting of normals and curvature estimation steps, grows linearly with the number of triangles, however $\sim$2.4 times steeper for AVV (Figure 4.2A, processes=1, slope$\sim$0.7) than for SSVV (Figure 4.2B, processes=1, slope$\sim$0.29), as estimated by fitting a straight line. This is due to the difference between the two algorithms: While the normals estimation step of SSVV is the same as for AVV and incorporates all the neighboring triangles

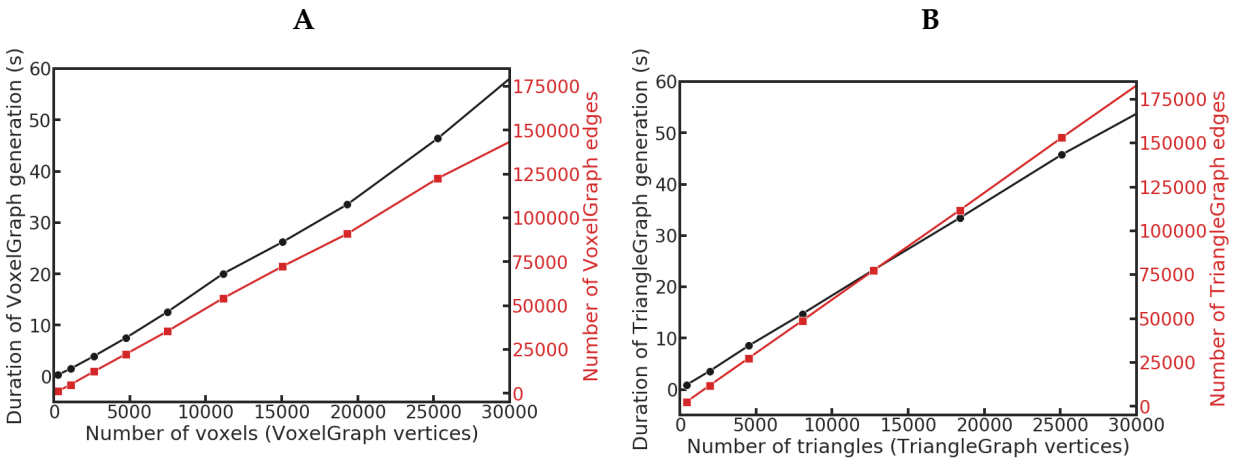

Figure 4.1: Runtime analysis of graph generation. (**A**) Duration of VoxelGraph generation and its number of edges depending on number of voxels in the mask (number of graph vertices). A hollow spherical mask with different radii (5, 10, ..., 50 voxels) was used. (**B**) Duration of TriangleGraph generation and its number of edges depending on number of triangles in the surface (number of graph vertices). A noisy spherical surface with different radii (5, 10, ..., 50 voxels) was used. Both plots in (A) and (B) were cropped to the same axes ranges.

defined by `rh`, in the curvature estimation step SSVV samples only 8 points around a central triangle center, leading to a shorter duration of this step independent of `rh`.

As normals and curvatures are estimated per triangle using a local neighborhood, these steps of our algorithms can benefit from parallel processing of subsets of graph vertices on multiple cores. I implemented a parallelized version of the normals estimation step (common for both algorithms) and of the curvature estimation step for AVV (as it is already faster for SSVV). This implementation exploits a multi-core single processor architecture by using a Python multiprocessing package Pathos[1]. In this shared-memory context, several processes are executed simultaneously and the operating system dynamically distributes them to the free available cores. Using 10 processes, the duration of both algorithms could be substantially shortened, still growing linearly with the number of triangles but with a much lower slope (Figure 4.2A-B, processes=10).

To analyze the runtime depending on the neighborhood size and the scalability of the parallel implementation with number of processes, the algorithms were applied to a noisy sphere surface with a radius of 10 voxels (having 1952 triangles) using different `rh` values (8-10 voxels) and numbers of parallel processes (1-20). As before, the duration of AVV (Figure 4.2C) is roughly twice higher than the duration of SSVV (Figure 4.2D). Using a larger neighborhood set by a higher `rh` value results in longer runtimes of both algorithms, especially for AVV, since both AVV steps incorporate all the neighboring triangles.

Additionally, speedup of both algorithms for different `rh` values was calculated as a ratio between the total duration of the sequential version (without multiprocessing) to the total duration of the parallel version on n processes, for n=1-20. The total duration here is comprised of the three steps:

[1] https://pypi.org/project/pathos/

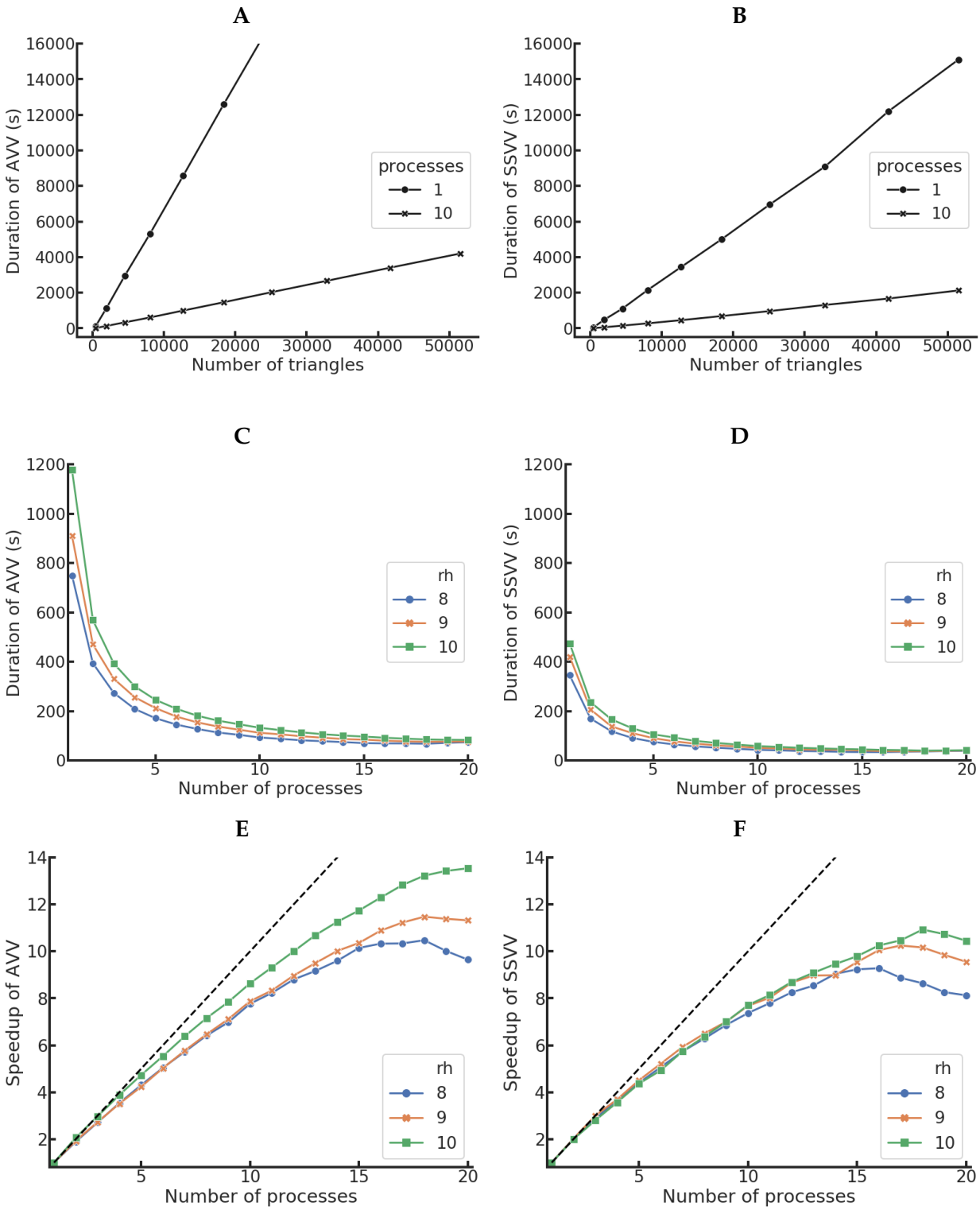

Figure 4.2: Runtime analysis of curvature estimation. (**A-B**) Total duration of AVV and SSVV dependent on number of triangles and processes (1 or 10). The runs were performed on noisy sphere surfaces with different radii (5, 10, ..., 50 voxels) using `rh` of 10 voxels. (**C-D**) Total duration of AVV and SSVV dependent on number of processes (1-20) for different `rh` values (8-10 voxels). (**E-F**) Speedup of AVV and SSVV dependent on number of processes (1-20) for different `rh` values (8-10 voxels); ideal speedup that is equal to the number of processes is shown as a dashed black line. For panels (C-F), the runs were performed on a noisy sphere surface with radius of 10 voxels having 1952 triangles.

1. graph generation (always sequential and the same for both algorithms),
2. normals estimation (sequential vs. parallel and the same for both algorithms),
3. curvature estimation (sequential vs. parallel for AVV and always sequential for SSVV).

As predicted by Amdahl's law (Amdahl, 1967; Hill and Marty, 2008), the speedup of our parallel implementations is lower than the ideal linear speedup with the number of processes (Figure 4.2E-F) and it is limited by the sequential part: Since the total sequential part of SSVV is bigger compared to AVV, the speedup of SSVV (Figure 4.2F) is slightly lower compared to AVV (Figure 4.2E) for a higher number of processes. The slowdown in speedup, saturation for a certain number of cores available and subsequent deterioration as seen here are normal due to other potential bottlenecks in parallel computation like memory and I/O bandwidth[2]. The optimal number of processes was around 16-18 for both algorithms (even 20 for AVV with `rh` of 10 voxels) for this sphere surface example measurement.

As PyCurv application to real data involves additional pre- and postprocessing steps like surface generation and cleaning (i.e. removing borders and small components), the sequential part is higher. Therefore, the speedup is expected to reach saturation with a lower number of processes. We set 10 processes as default for the parallel parts of PyCurv algorithms. Despite its longer duration, as AVV is more robust to quantization noise and feature size variation than SSVV (Salfer et al., 2020), we recommend to use AVV for membranes from cryo-ET. For a typical cER membrane surface from (Collado et al., 2019) leading to a graph with ∼400k vertices and ∼2480k edges, the whole workflow from surface generation until curvature estimation took ∼10.85 hours using 10 processes, `rh` of 10 nm, the current PyCurv version and Python 3.7.4. The sequential graph generation and surface cleaning took ∼15 minutes, the normals and curvature estimation steps running in parallel on 10 processes took ∼4.63 and ∼5.86 hours, respectively.

4.2 Unpublished membrane curvature estimation results

4.2.1 ER curvature increase near Htt fibrils estimated by AVV

The corrected algorithm, AVV using `rh` of 10 nm, was applied to the ER membrane segmentations from (Bäuerlein et al., 2017) to compare to the results obtained using the initial algorithm, NVV using `k` of 3 (discussed in 3.1.4). The curvedness distributions estimated by AVV are shifted towards lower values (Figure 4.3B) compared to NVV (Figure 4.3A). The curvedness ratio between ER membranes in the vicinity of Htt IBs (n=4 tomograms) and control conditions (n=3 tomograms) is even higher using AVV compared to the initial NVV algorithm. As estimated by NVV, sites with curvedness above 1/10 nm^{-1} were 20%–60% more abundant in the vicinity of inclusions, while AVV estimation shows a much higher increase of around 70%-100%. This strengthens the conclusion from the paper that Htt fibrils deform and disrupt endocellular membranes by increasing their curvature.

[2] Amdahl's law, Wikipedia, 2020-09-25, 13:42

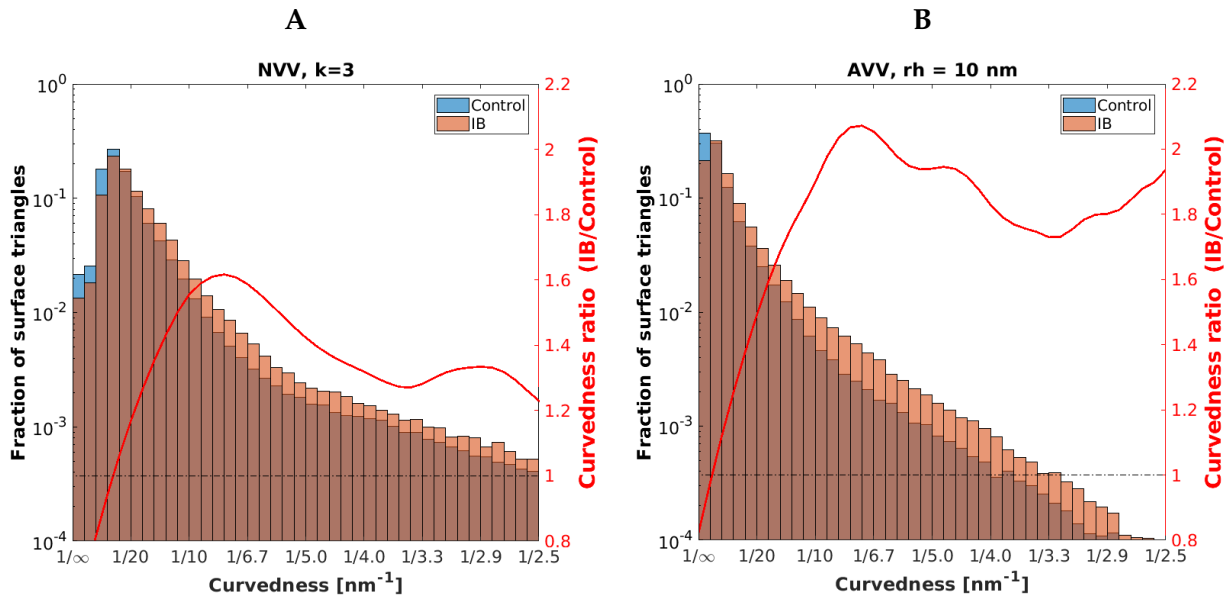

Figure 4.3: ER membrane curvedness estimated by NVV vs. AVV. (**A**) Histograms of ER membrane curvedness estimated by NVV using `k`=3, reproduced from (Bäuerlein et al., 2017). The distributions around inclusions and in control cells were significantly different ($p < 0.001$ by Kolmogorov–Smirnov test). (**B**) Histograms of ER membrane curvedness estimated by AVV using `rh`=10 nm. In both panels, curvedness was calculated for ER membranes in the vicinity of Htt IBs (n=4 tomograms, including two Htt97Q IBs in HeLa cells, one Htt97Q-GFP IB in a neuron and one Htt64Q-GFP IB in a HeLa cell) and in control conditions (n=3 tomograms, including one of a Htt97Q-GFP IB-containing HeLa cell in an area distal from the IB, one of a HeLa cell expressing diffuse Htt97Q-GFP without visible IB and one of a HeLa cell expressing non-pathogenic Htt25Q-GFP). The red line shows the ratio between ER membrane curvedness around IBs and in control cells.

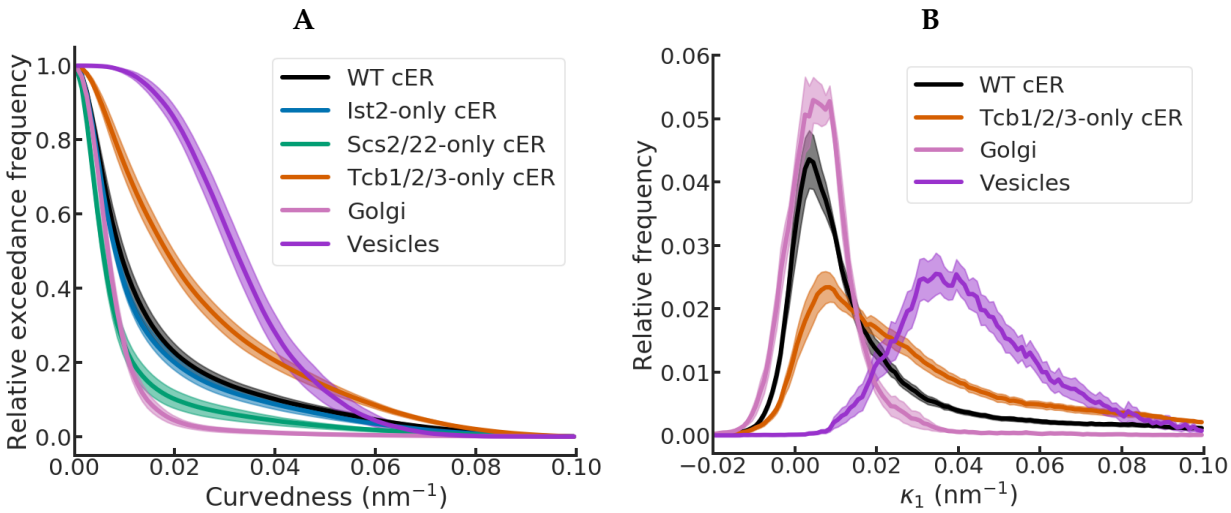

Figure 4.4: Comparison of membrane curvature estimated by AVV in tomograms of different cER tether mutants, Golgi cisternae and Golgi-derived vesicles. (**A**) A reverse-cumulative histogram (exceedance plot) of curvedness of cER in WT yeast and its four main tether mutants as well as of Golgi and vesicles in mouse neurons. (**B**) A histogram of κ_1 of the WT and Tcb1/2/3-only cER, the Golgi and the vesicles. In both panels, the solid line shows the mean value and the shaded region the standard error for each bin either among tomograms (in case of cER) or regions (in case of Golgi and vesicles).

4.2.2 Curvature comparison between different organelles

To more closely compare curvatures of different organelles, we combined the AVV results for cER membranes from (Collado et al., 2019) with those for Golgi cisternae and Golgi-derived vesicles from (Salfer et al., 2020). Please note that this comparison is not ideal, because the cell types are very different. Figure 4.4A shows the curvedness of cER in WT yeast and its four main tether mutants and the curvedness of Golgi and vesicles in mouse neurons in one reverse-cumulative histogram. The solid line shows the mean value and the shaded region the standard error for each bin either among tomograms (in case of cER) or regions (in case of Golgi and vesicles). The nearly spherical vesicles have the highest curvedness, even higher than the cER in the mostly tubular Tcb1/2/3-only mutant. The narrow Golgi cisternae show the lowest curvedness, even lower than the cER in the Scs2/22-only mutant that consists mostly of thin sheets.

To compare our curvature estimation results to the organelle shapes and sizes described by Kozlov et al. (2014), Figure 4.4B shows κ_1 histograms of the WT and Tcb1/2/3-only cER, the Golgi and the vesicles. According to Kozlov et al. (2014), ER tubules are 30–50 nm thick (radius of 15–25 nm). Thus, κ_1 of cER tubules should be around 0.04-0.07 nm^{-1}. The distribution of κ_1 of the cER in Tcb1/2/3-only mutant is quite broad but includes substantially more values in that range than the WT cER (Figure 4.4B). This is consistent with our observation that the cER in this mutant is more tubular than in the WT (Collado et al., 2019). Moreover, Kozlov et al. (2014) report that cisternae of the Golgi complex are 10–20 nm thick (radius of 5–10 nm). This corresponds to the maximum κ_1 at the cisternae sides between 0.1 and 0.2 nm^{-1}. Our data complied with this as the maximum κ_1 of the Golgi is 0.14 nm^{-1}.

Bibliography

Aimon, S., Callan-Jones, A., Berthaud, A., Pinot, M., Toombes, G. E., and Bassereau, P. (2014). Membrane Shape Modulates Transmembrane Protein Distribution. *Dev Cell*, 28(2):212–218.

Amdahl, G. M. (1967). Validity of the single processor approach to achieving large scale computing capabilities. In *AFIPS Conference Proceedings - 1967 Spring Joint Computer Conference, AFIPS 1967*, pages 483–485.

Amos, L. A., Henderson, R., and Unwin, P. N. (1982). Three-dimensional structure determination by electron microscopy of two-dimensional crystals. *Progress in Biophysics and Molecular Biology*, 39(C):183–231.

Asano, S., Engel, B. D., and Baumeister, W. (2016). In Situ Cryo-Electron Tomography: A Post-Reductionist Approach to Structural Biology. *J Mol Biol*, 428(2):332–343.

Bassereau, P., Jin, R., Baumgart, T., Deserno, M., Dimova, R., Frolov, V. A., Bashkirov, P. V., Grubmüller, H., Jahn, R., Risselada, H. J., Johannes, L., Kozlov, M. M., Lipowsky, R., Pucadyil, T. J., Zeno, W. F., Stachowiak, J. C., Stamou, D., Breuer, A., Lauritsen, L., Simon, C., Sykes, C., Voth, G. A., and Weikl, T. R. (2018). The 2018 biomembrane curvature and remodeling roadmap. *J Phys D Appl Phys*, 51(34).

Batson, J. and Royer, L. (2019). Noise2Self: Blind denoising by self-supervision. *ArXiv*, pages 1–16.

Bäuerlein, F. J. B. (2018). *In Situ Architecture and Cellular Interactions of PolyQ Inclusions*. PhD thesis, Technical University Munich, Max Planck Institute of Biochemistry.

Bäuerlein, F. J. B., Saha, I., Mishra, A., Kalemanov, M., Martínez-Sánchez, A., Klein, R., Dudanova, I., Hipp, M. S., Ulrich Hartl, F., Baumeister, W., and Fernández-Busnadiego, R. (2017). In Situ Architecture and Cellular Interactions of PolyQ Inclusions. *Cell*, 171:179–187.

Bechstedt, S., Lu, K., and Brouhard, G. J. (2014). Doublecortin recognizes the longitudinal curvature of the microtubule end and lattice. *Curr Biol*, 24:2366–2375.

Beck, M. and Baumeister, W. (2016). Cryo-Electron Tomography: Can it Reveal the Molecular Sociology of Cells in Atomic Detail? *Trends Cell Biol*, 26(11):825–837.

Bharat, T. A., Hoffmann, P. C., and Kukulski, W. (2018). Correlative Microscopy of Vitreous Sections Provides Insights into BAR-Domain Organization In Situ. *Structure*, 26(6):879–886.

Bharat, T. A., Malsam, J., Hagen, W. J., Scheutzow, A., Söllner, T. H., and Briggs, J. A. (2014). SNARE and regulatory proteins induce local membrane protrusions to prime docked vesicles for fast calcium-triggered fusion. *EMBO Rep*, 15(3):308–314.

Bharat, T. A. and Scheres, S. H. (2016). Resolving macromolecular structures from electron cryo-Tomography data using subtomogram averaging in RELION. *Nat Protocols*, 11(11):2054–2065.

Böhm, J., Frangakis, A. S., Hegerl, R., Nickell, S., Typke, D., and Baumeister, W. (2000). Toward detecting and identifying macromolecules in a cellular context: Template matching applied to electron tomograms. *PNAS*, 97(26):14245–14250.

Booth, C. R., Mooney, P. E., Lee, B. C., Lent, M., and Gubbens, A. J. (2012). K2: A Super-Resolution Electron Counting Direct Detection Camera for Cryo-EM. *Microsc Microanal*, 18(S2):78–79.

Bornschlogl, T., Romero, S., Vestergaard, C. L., Joanny, J. F., Nhieu, G. T. V., and Bassereau, P. (2013). Filopodial retraction force is generated by cortical actin dynamics and controlled by reversible tethering at the tip. *PNAS*, 110(47):18928–18933.

Boucrot, E., Pick, A., Çamdere, G., Liska, N., Evergren, E., McMahon, H. T., and Kozlov, M. M. (2012). Membrane fission is promoted by insertion of amphipathic helices and is restricted by crescent BAR domains. *Cell*, 149(1):124–136.

Boudin, H., Doan, A., Xia, J., Shigemoto, R., Huganir, R. L., Worley, P., and Craig, A. M. (2000). Presynaptic clustering of mGluR7a requires the PICK1 PDZ domain binding site. *Neuron*, 28(2):485–497.

Boutin, M. (2000). Numerically invariant signature curves. *Int J Comput Vis*, 40(3):235–248.

Braun, A. R., Sevcsik, E., Chin, P., Rhoades, E., Tristram-Nagle, S., and Sachs, J. N. (2012). α-Synuclein Induces Both Positive Mean Curvature and Negative Gaussian Curvature in Membranes. *J Am Chem Soc*, 134(5):2613–2620.

Buchholz, T. O., Jordan, M., Pigino, G., and Jug, F. (2019a). Cryo-CARE: Content-aware image restoration for cryo-transmission electron microscopy data. *Proceedings - International Symposium on Biomedical Imaging*, 2019-April(Isbi):502–506.

Buchholz, T. O., Krull, A., Shahidi, R., Pigino, G., Jékely, G., and Jug, F. (2019b). Content-aware image restoration for electron microscopy. *Methods in Cell Biology*, 152:277–289.

Campelo, F., McMahon, H. T., and Kozlov, M. M. (2008). The hydrophobic insertion mechanism of membrane curvature generation by proteins. *Biophys J*, 95(5):2325–2339.

Cardone, G., Brecher, M., Fontana, J., Winkler, D. C., Butan, C., White, J. M., and Steven, A. C. (2012). Visualization of the Two-Step Fusion Process of the Retrovirus Avian Sarcoma/Leukosis Virus by Cryo-Electron Tomography. *J Virol*, 86(22):12129–12137.

Castón, J. R. (2013). *Conventional Electron Microscopy, Cryo-Electron Microscopy and Cryo-Electron Tomography of Viruses*, pages 79–115. Springer Netherlands, Dordrecht.

Chakraborty, S., Jasnin, M., and Baumeister, W. (2020). Three-dimensional organization of the cytoskeleton: a cryo-electron tomography perspective. *Protein Sci*.

Che, C., Lin, R., Zeng, X., Elmaaroufi, K., Galeotti, J., and Xu, M. (2018). Improved deep learning-based macromolecules structure classification from electron cryo-tomograms. *Mach Vis Appl*, 29(8):1227–1236.

Chen, M., Dai, W., Sun, S. Y., Jonasch, D., He, C. Y., Schmid, M. F., Chiu, W., and Ludtke, S. J. (2017). Convolutional neural networks for automated annotation of cellular cryo-electron tomograms. *Nat Methods*, 14(10):983–985.

Chen, Y. and Förster, F. (2014). Iterative reconstruction of cryo-electron tomograms using nonuniform fast Fourier transforms. *J Struct Biol*, 185(3):309–316.

Chen, Y., Pfeffer, S., Fernández, J. J., Sorzano, C. O. S., and Förster, F. (2014). Autofocused 3D classification of cryoelectron subtomograms. *Structure*, 22(10):1528–1537.

Chen, Y., Yong, J., Martínez-Sánchez, A., Yang, Y., Wu, Y., De Camilli, P., Fernández-Busnadiego, R., and Wu, M. (2019). Dynamic instability of clathrin assembly provides proofreading control for endocytosis. *J Cell Biol*, 218(10):3200–3211.

Chernomordik, L. V. and Kozlov, M. M. (2003). Protein-Lipid Interplay in Fusion and Fission of Biological Membranes. *Annu Rev Biochem*, 72(1):175–207.

Chlanda, P., Mekhedov, E., Waters, H., Schwartz, C. L., Fischer, E. R., Ryham, R. J., Cohen, F. S., Blank, P. S., and Zimmerberg, J. (2016). The hemifusion structure induced by influenza virus haemagglutinin is determined by physical properties of the target membranes. *Nat Microbiol*, 1(6):1–8.

Collado, J. and Fernández-Busnadiego, R. (2017). Deciphering the molecular architecture of membrane contact sites by cryo-electron tomography. *Biochim Biophys Acta Mol Cell Res*, 1864:1507–1512.

Collado, J., Kalemanov, M., Campelo, F., Bourgoint, C., Thomas, F., Loewith, R., Martínez-Sínchez, A., Baumeister, W., Stefan, C. J., and Fernéndez-Busnadiego, R. (2019). Tricalbin-Mediated Contact Sites Control ER Curvature to Maintain Plasma Membrane Integrity. *Dev Cell*, 51:476–487.

Crowther, R. A., DeRosier, D., and Klug, A. (1970). The reconstruction of a three-dimensional structure from projections and its application to electron microscopy. *Proc. Roy. Soc. Lond. A.*, 317:319–340.

Cui, H., Mim, C., Vázquez, F. X., Lyman, E., Unger, V. M., and Voth, G. A. (2013). Understanding the role of amphipathic helices in N-bar domain driven membrane remodeling. *Biophys J*, 104(2):404–411.

Dale, A. M., Fischl, B., and Sereno, M. I. (1999). Cortical Surface-Based Analysis. *Neuroimage*, 9:179–194.

Danev, R., Buijsse, B., Khoshouei, M., Plitzko, J. M., and Baumeister, W. (2014). Volta potential phase plate for in-focus phase contrast transmission electron microscopy. *PNAS*, 111(44):15635–15640.

De Rosier, D. J. and Klug, A. (1968). Reconstruction of three dimensional fiber structures from orthogonal projections. *Nature*, 217:130–134.

Desbrun, M., Meyer, M., Schröder, P., and Barr, A. H. (1999). Implicit fairing of irregular meshes using diffusion and curvature flow. In *SIGGRAPH '99 Proceedings of the 26th annual conference on Computer graphics and interactive techniques*, pages 317–324, New York. ACM Press/Addison-Wesley Publishing.

Devaux, P. F. (2000). Is lipid translocation involved during endo- and exocytosis? *Biochimie*, 82(5):497–509.

Di Paolo, G. and De Camilli, P. (2006). Phosphoinositides in cell regulation and membrane dynamics. *Nature*, 443(7112):651–657.

Dierksen, K., Typke, D., Hegerl, R., and Baumeister, W. (1993). Towards automatic electron tomography II . Implementation of autofocus and low-dose procedures. *Ultramicroscopy*, 49:109–120.

Dierksen, K., Typke, D., Hegerl, R., Koster, A., and Baumeister, W. (1992). Towards automatic electron tomography. *Ultramicroscopy*, 40:71–87.

Dierksen, K., Typke, D., Hegerl, R., Walz, J., Sackmann, E., and Baumeister, W. (1995). Three-Dimensional Structure of Lipid Vesicles Embedded in Vitreous Ice and Investigated by Automated Electron Tomography. *Biophysical Journal*, 68(4):1416–1422.

Dijkstra, E. W. (1959). A Note on Two Problems in Connexion with Graphs. *Numer Math*, 1:269–271.

do Carmo, M. P. (1976). *Differential geometry of curves and surfaces*. Prentice-Hall, Inc., Englewood Cliffs, New Jersey.

Dubochet, J. and Sartori Blanc, N. (2001). The cell in absence of aggregation artifacts. *Micron*, 32(1):91–99.

Eckler, S. A., Kuehn, R., and Gautam, M. (2005). Deletion of N-terminal rapsyn domains disrupts clustering and has dominant negative effects on clustering of full-length rapsyn. *Neuroscience*, 131(3):661–670.

Ehrlich, M., Boll, W., Van Oijen, A., Hariharan, R., Chandran, K., Nibert, M. L., and Kirchhausen, T. (2004). Endocytosis by random initiation and stabilization of clathrin-coated pits. *Cell*, 118(5):591–605.

Faini, M., Beck, R., Wieland, F. T., and Briggs, J. A. (2013). Vesicle coats: Structure, function, and general principles of assembly. *Trends Cell Biol*, 23(6):279–288.

Fan, G. Y. and Ellisman, M. H. (2000). Digital imaging in transmission electron microscopy. *Journal of Microscopy*, 200(June):1–13.

Faruqi, A. R. and Henderson, R. (2007). Electronic detectors for electron microscopy. *Curr Opin Struct Biol*, 17(5):549–555.

Fenney, S. (2018). Rendering a computer generated image using a stencil buffer with primitive concatenation. U.S. Patent 10163259B2, Dec. 25, 2018.

Ferguson, S. M. and De Camilli, P. (2012). Dynamin, a membrane-remodelling GTPase. *Nat Rev Mol Cell Biol*, 13(2):75–88.

Fernández, J. J. and Li, S. (2003). An improved algorithm for anisotropic nonlinear diffusion for denoising cryo-tomograms. *J Struct Biol*, 144(1-2):152–161.

Fernández-Busnadiego, R., Asano, S., Oprisoreanu, A. M., Sakata, E., Doengi, M., Kochovski, Z., Zürner, M., Stein, V., Schoch, S., Baumeister, W., and Lučić, V. (2013). Cryo-electron tomography reveals a critical role of RIM1 α in synaptic vesicle tethering. *J Cell Biol*, 201(5):725–740.

Fernández-Busnadiego, R., Saheki, Y., and De Camilli, P. (2015). Three-dimensional architecture of extended synaptotagmin-mediated endoplasmic reticulum-plasma membrane contact sites. *Proceedings of the National Academy of Sciences*, 112(16):E2004–E2013.

Fertuck, H. C. and Salpeter, M. M. (1974). Localization of acetylcholine receptor by 125I labeled α bungarotoxin binding at mouse motor endplates. *PNAS*, 71(4):1376–1378.

Ford, M. G., Mills, I. G., Peter, B. J., Vallis, Y., Praefcke, G. J., Evans, P. R., and McMahon, H. T. (2002). Curvature of clathrin-coated pits driven by epsin. *Nature*, 419(6905):361–366.

Forman, R. (2002). A user's guide to discrete morse theory. *Seminaire Lotharingin de Combinatoire*, 48:1–35.

Förster, F. (2005). *Quantitative Analyse von Makromolekülen in Kryoelektronentomogrammen mittels Korrelationsmethoden*. PhD thesis, Technical University Munich, Max Planck Institute of Biochemistry.

Förster, F., Han, B. G., and Beck, M. (2010). *Visual proteomics*, volume 483. Elsevier Inc., 1 edition.

Förster, F., Medalia, O., Zauberman, N., Baumeister, W., and Fass, D. (2005). Retrovirus envelope protein complex structure in situ studied by cryo-electron tomography. *PNAS*, 102(13):4729–4734.

Förster, F., Pruggnaller, S., Seybert, A., and Frangakis, A. S. (2008). Classification of cryo-electron sub-tomograms using constrained correlation. *J Struct Biol*, 161(3):276–86.

Frangakis, A. S., Böhm, J., Förster, F., Nickell, S., Nicastro, D., Typke, D., Hegerl, R., and Baumeister, W. (2002). Identification of macromolecular complexes in cryoelectron tomograms of phantom cells. *PNAS*, 99(22):14153–14158.

Frangakis, A. S. and Förster, F. (2004). Computational exploration of structural information from cryo-electron tomograms. *Curr Opin Struct Biol*, 14(3):325–331.

Frangakis, A. S. and Hegerl, R. (2001). Noise reduction in electron tomographic reconstructions using nonlinear anisotropic diffusion. *J Struct Biol*, 135(3):239–250.

Frey, B. J. and Dueck, D. (2007). Clustering by passing messages between data points. *Science*, 315(5814):972–976.

Fribourg, P. F., Chami, M., Sorzano, C. O. S., Gubellini, F., Marabini, R., Marco, S., Jault, J. M., and Lévy, D. (2014). 3D cryo-electron reconstruction of BmrA, a bacterial multidrug ABC transporter in an inward-facing conformation and in a lipidic environment. *J Mol Biol*, 426(10):2059–2069.

Frost, A., De Camilli, P., and Unger, V. M. (2007). F-BAR Proteins Join the BAR Family Fold. *Structure*, 15(7):751–753.

Fuhrmans, M. and Marrink, S. J. (2012). Molecular view of the role of fusion peptides in promoting positive membrane curvature. *J Am Chem Soc*, 134(3):1543–1552.

Fukuda, Y., Laugks, U., Lučić, V., Baumeister, W., and Danev, R. (2015). Electron cryotomography of vitrified cells with a Volta phase plate. *J Struct Biol*, 190(2):143–154.

Gilbert, P. (1972). Iterative methods for the three-dimensional reconstruction of an object from projections. *J Theor Biol*, 36(1):105–117.

Goldfeather, J. and Interrante, V. (2004). A novel cubic-order algorithm for approximating principal direction vectors. *ACM Trans Graph*, 23(1):45–63.

Gordon, R., Bender, R., and Herman, G. T. (1970). Algebraic Reconstruction Techniques (ART) for Three-dimensional Electron Microscopy and X-ray Photography. *J Theor Biol*, 29:471–481.

Graham, T. R. and Kozlov, M. M. (2010). Interplay of proteins and lipids in generating membrane curvature. *Curr Opin Cell Biol*, 22(4):430–436.

Grimm, R., Bärmann, M., Häckl, W., Typke, D., Sackmann, E., and Baumeister, W. (1997). Energy Filtered Electron Tomography of Ice-Embedded Actin and Vesicles. *Biophysical Journal*, 72(January):482–489.

Grimm, R., Koster, A. J., Ziese, U., Typke, D., and Baumeister, W. (1996). Zero-loss energy filtering under low-dose conditions using a post-column energy filter. *J Microsc*, 183(1):60–68.

Groffen, A. J., Martens, S., Arazola, R. D., Cornelisse, L. N., Lozovaya, M., Jong, D., H., A. P., Goriunova, N. A., Habets, R. L. P., Takai, Y., Borst, G. J., Brose, N., McMahon, H. T., and Verhage, M. (2010). Doc2b Is a High-Affinity Ca2+ Sensor for Spontaneous Neurotransmitter Release. *Science*, 327:1614–1618.

Guckenberger, R. (1982). Determination of a common origin in the micrographs of tilt series in three-dimensional electron microscopy. *Ultramicroscopy*, 9:167–174.

Guo, Q., Huang, B., Cheng, J., Seefelder, M., Engler, T., Pfeifer, G., Oeckl, P., Otto, M., Moser, F., Maurer, M., Pautsch, A., Baumeister, W., Fernández-Busnadiego, R., and Kochanek, S. (2018a). The cryo-electron microscopy structure of huntingtin. *Nature*, 555(7694):117–120.

Guo, Q., Lehmer, C., Martínez-Sánchez, A., Rudack, T., Beck, F., Hartmann, H., Pérez-Berlanga, M., Frottin, F., Hipp, M. S., Hartl, F. U., Edbauer, D., Baumeister, W., and Fernández-Busnadiego, R. (2018b). In Situ Structure of Neuronal C9orf72 Poly-GA Aggregates Reveals Proteasome Recruitment. *Cell*, 172(4):696–705.e12.

Hagen, W. J., Wan, W., and Briggs, J. A. (2017). Implementation of a cryo-electron tomography tilt-scheme optimized for high resolution subtomogram averaging. *J Struct Biol*, 197(2):191–198.

Han, R., Wang, L., Liu, Z., Sun, F., and Zhang, F. (2015). A novel fully automatic scheme for fiducial marker-based alignment in electron tomography. *J Struct Biol*, 192(3):403–417.

Hayles, M. F., Stokes, D. J., Phifer, D., and Findlay, K. C. (2007). A technique for improved focused ion beam milling of cryo-prepared life science specimens. *J Microsc*, 226(3):263–269.

Helfrich, W. (1986). Size Distributions of Vesicles: the Role of the Effective Rigidity of Membranes. *Journal de physique Paris*, 47(2):321–329.

Hill, M. D. and Marty, M. R. (2008). *Amdahl's law in the multicore era*. IEEE Computer Society.

Himes, B. A. and Zhang, P. (2018). emClarity: Software for High Resolution Cryo-electron Tomography and Sub-tomogram Averaging. *Nat Methods*, 15(11):955–961.

Hoffman, D. P., Shtengel, G., Xu, C. S., Campbell, K. R., Freeman, M., Wang, L., Milkie, D. E., Pasolli, H. A., Iyer, N., Bogovic, J. A., Stabley, D. R., Shirinifard, A., Pang, S., Peale, D., Schaefer, K., Pomp, W., Chang, C.-L., Lippincott-Schwartz, J., Kirchhausen, T., Solecki, D. J., Betzig, E., and Hess, H. (2020). Correlative three-dimensional super-resolution and block face electron microscopy of whole vitreously frozen cells. *Science*, 367(265):14.

Hoppe, H. (1999). Optimization of mesh locality for transparent vertex caching. In *Proc. of ACM SIGGRAPH 99*, pages 269–276.

Hoppe, H., DeRose, T., Duchamp, T., McDonald, J., and Stuetzle, W. (1992). Surface reconstruction from unorganized points. In *SIGGRAPH '92 Proceedings of the 19th annual conference on Computer graphics and interactive techniques*, pages 71–78, New York. ACM.

Hrabe, T., Chen, Y., Pfeffer, S., Kuhn Cuellar, L., Mangold, A.-V., and Förster, F. (2012). PyTom: A python-based toolbox for localization of macromolecules in cryo-electron tomograms and subtomogram analysis. *J Struct Biol*, 178(2):177–188.

Hu, H.-H., Chen, H.-Y., Hung, C.-I., Guo, W.-Y., and Wu, Y.-T. (2012). Shape and curvedness analysis of brain morphology using human fetal magnetic resonance images in utero. *Brain Struct Funct*, 218(6):1451–1462.

Hui, E., Johnson, C. P., Yao, J., Dunning, F. M., and Chapman, E. R. (2009). Synaptotagmin-Mediated Bending of the Target Membrane Is a Critical Step in Ca2+-Regulated Fusion. *Cell*, 138(4):709–721.

Hurley, J. H. and Hanson, P. I. (2010). Membrane budding and scission by the ESCRT machinery: It's all in the neck. *Nat Rev Mol Cell Biol*, 11(8):556–566.

Itoh, T. and De Camilli, P. (2006). BAR, F-BAR (EFC) and ENTH/ANTH domains in the regulation of membrane-cytosol interfaces and membrane curvature. *Biochim Biophys Acta Mol Cell Biol Lipids*, 1761(8):897–912.

Jaiswal, R., Breitsprecher, D., Collins, A., Corrêa, I. R., Xu, M. Q., and Goode, B. L. (2013). The formin daam1 and fascin directly collaborate to promote filopodia formation. *Curr Biol*, 23(14):1373–1379.

Jensen, D. and Schekman, R. (2011). COPII-mediated vesicle formation at a glance. *J Cell Sci*, 124(1):1–4.

Jiang, W., Baker, M. L., Wu, Q., Bajaj, C., and Chiu, W. (2003). Applications of a bilateral denoising filter in biological electron microscopy. *J Struct Biol*, 144(1-2):114–122.

Kimmel, R. and Sethian, J. A. (1998). Computing geodesic paths on manifolds. *PNAS*, 95(15):8431–8435.

Kirchhaussen, T. (2000). Three ways to make a vesicle. *Nat Rev Mol Cell Biol*, 1(December):187–198.

Klein, A. (2016). Mindboggle-101 manually labeled individual brains.

Klein, A., Ghosh, S. S., Bao, F. S., Giard, J., Häme, Y., Stavsky, E., Lee, N., Rossa, B., Reuter, M., Chaibub Neto, E., and Keshavan, A. (2017). Mindboggling morphometry of human brains. *PLoS Comput Biol*, 13(2):1–40.

Klein, A. and Tourville, J. (2012). 101 Labeled Brain Images and a Consistent Human Cortical Labeling Protocol. *Front Neurosci*, 6:1–12.

Kobbelt, L. and Botsch, M. (2004). A survey of point-based techniques in computer graphics. *Computers and Graphics (Pergamon)*, 28(6):801–814.

Kochovski, Z. (2014). *Image analysis of molecular complexes present in cryo-tomograms of neuronal synapses*. PhD thesis, Technical University Munich, Max Planck Institute of Biochemistry.

Koenderink, J. J. and van Doorn, A. J. (1992). Surface shape and curvature scales. *Image Vis Comput*, 10(8):557–564.

Kozlov, M. M., Campelo, F., Liska, N., Chernomordik, L. V., Marrink, S. J., and McMahon, H. T. (2014). Mechanisms shaping cell membranes. *Curr Opin Cell Biol*, 29:53–60.

Kremer, J. R., Mastronarde, D. N., and McIntosh, J. R. (1996). Computer visualization of three-dimensional image data using IMOD. *J Struct Biol*, 116:71–76.

Krivanek, O. L. and Mooney, P. E. (1993). Applications of slow-scan CCD cameras in transmission electron microscopy. *Ultramicroscopy*, 49(1-4):95–108.

Krull, A., Buchholz, T. O., and Jug, F. (2019). Noise2void-Learning denoising from single noisy images. *ArXiv*, pages 1–9.

Lai, C. L., Jao, C. C., Lyman, E., Gallop, J. L., Peter, B. J., McMahon, H. T., Langen, R., and Voth, G. A. (2012). Membrane Binding and Self-Association of the Epsin N-Terminal Homology Domain. *J Mol Biol*, 423(5):800–817.

Laine, S., Karras, T., Lehtinen, J., and Aila, T. (2019). High-Quality Self-Supervised Deep Image Denoising. *ArXiv*.

Leduc, C., Campàs, O., Joanny, J. F., Prost, J., and Bassereau, P. (2010). Mechanism of membrane nanotube formation by molecular motors. *Biochim Biophys Acta Biomembr*, 1798(7):1418–1426.

Lee, K. K. (2010). Architecture of a nascent viral fusion pore. *EMBO J*, 29(7):1299–1311.

Lehtinen, J., Munkberg, J., Hasselgren, J., Laine, S., Karras, T., Aittala, M., and Aila, T. (2018). Noise2Noise: Learning image restoration without clean data. *ArXiv*, pages 1–12.

Li, X., Mooney, P., Zheng, S., Booth, C. R., Braunfeld, M. B., Gubbens, S., Agard, D. A., and Cheng, Y. (2013). Electron counting and beam-induced motion correction enable near-atomic-resolution single-particle cryo-EM. *Nat Methods*, 10(6):584–590.

Liu, Y., Penczek, P. A., McEwen, B. F., and Frank, J. (1995). A marker-free alignment method for electron tomography. *Ultramicroscopy*, 58:393–402.

Lorensen, W. E. and Cline, H. E. (1987). Marching Cubes: A High Resolution 3D Surface Construction Algorithm. *ACM SIGGRAPH Comput Graph*, 21(4):163–169.

Lučić, V., Fernández-Busnadiego, R., Laugks, U., and Baumeister, W. (2016). Hierarchical detection and analysis of macromolecular complexes in cryo-electron tomograms using Pyto software. *J Struct Biol*, 196(3):503–514.

Lučić, V., Förster, F., and Baumeister, W. (2005). Structural Studies By Electron Tomography: From Cells to Molecules. *Annu Rev Biochem*, 74:833–865.

Lucic, V., Rigort, A., and Baumeister, W. (2013). Cryo-electron tomography : The challenge of doing structural biology in situ. *J Cell Biol*, 202(3):407–419.

Machado, S., Mercier, V., and Chiaruttini, N. (2019). LimeSeg: A coarse-grained lipid membrane simulation for 3D image segmentation. *BMC Bioinformatics*, 20(2):1–12.

MacKinnon, R. (2003). Potassium channels. *FEBS Lett*, 555(1):62–65.

Magid, E., Soldea, O., and Rivlin, E. (2007). A comparison of Gaussian and mean curvature estimation methods on triangular meshes of range image data. *Comput Vis Image Underst*, 107:139–159.

Marko, M., Hsieh, C., Moberlychan, W., Mannella, C. A., and Frank, J. (2006). Focused ion beam milling of vitreous water: Prospects for an alternative to cryo-ultramicrotomy of frozen-hydrated biological samples. *J Microsc*, 222(1):42–47.

Martens, S., Kozlov, M. M., and McMahon, H. T. (2007). How Synaptotagmin Promotes Membrane Fusion. *Science*, 316(May):1205–1208.

Martens, S. and McMahon, H. T. (2008). Mechanisms of membrane fusion: Disparate players and common principles. *Nat Rev Mol Cell Biol*, 9(7):543–556.

Martinez-Sanchez, A., Garcia, I., Asano, S., Lucic, V., and Fernandez, J.-J. (2014). Robust membrane detection based on tensor voting for electron tomography. *J Struct Biol*, 186:49–61.

Martinez-Sanchez, A., Garcia, I., and Fernandez, J. J. (2011). A differential structure approach to membrane segmentation in electron tomography. *J Struct Biol*, 175:372–383.

Martinez-Sanchez, A., Garcia, I., and Fernandez, J. J. (2012). A ridge-based framework for segmentation of 3D electron microscopy datasets. *J Struct Biol*, 181(1):61–70.

Martinez-Sanchez, A., Kochovski, Z., Laugks, U., Meyer zum Alten Borgloh, J., Chakraborty, S., Pfeffer, S., Baumeister, W., and Lučić, V. (2020). Template-free detection and classification of membrane-bound complexes in cryo-electron tomograms. *Nat Methods*, pages 1–15.

Mastronarde, D. N. (1997). Dual-axis tomography: an approach with alignment methods that preserve resolution. *J Struct Biol*, 120(3):343–352.

Mastronarde, D. N. (2005). Automated electron microscope tomography using robust prediction of specimen movements. *J Struct Biol*, 152:36–51.

McMahon, H. T. and Boucrot, E. (2011). Molecular mechanism and physiological functions of clathrin-mediated endocytosis. *Nat Rev Mol Cell Biol*, 12(8):517–533.

McMahon, H. T. and Boucrot, E. (2015). Membrane curvature at a glance. *J Cell Sci*, 128(6):1065–1070.

McMahon, H. T. and Gallop, J. L. (2005). Membrane curvature and mechanisms of dynamic cell membrane remodellin. *Nature*, 438:590–596.

McMahon, H. T., Kozlov, M. M., and Martens, S. (2010). Membrane Curvature in Synaptic Vesicle Fusion and Beyond. *Cell*, 140(5):601–605.

Medioni, G., Lee, M.-S., and Tang, C.-K. (2000). *A Computational Framework for Segmentation and Grouping*. Elsevier Science B.V., Amsterdam.

Meyer, M., Desbrun, M., Schröder, P., and Barr, A. (2003). *Discrete Differential-Geometry Operators for Triangulated 2-Manifolds*. Springer, Berlin, Heidelberg.

Milnor, J. (1963). *Morse theory*. Princeton University Press, Princeton, New Jersey.

Moebel, E., Martinez-sanchez, A., Larivi, D., Fourmentin, E., Ortiz, J., Baumeister, W., and Kervrann, C. (2020). Deep Learning Improves Macromolecules Localization and Identification in 3D Cellular Cryo-Electron Tomograms. *bioRxiv*.

Mooney, P. (2017). Improving Detectors for Cryo-Electron Microscopy. *Microsc Microanal*, 23(S1):832–833.

Moreno, J. J., Martínez-Sánchez, A., Martínez, J. A., Garzón, E. M., and Fernández, J. J. (2018). TomoEED : fast edge-enhancing denoising of tomographic volumes. *Bioinformatics*, 34(21):3776–3778.

Mosaliganti, K. R., Noche, R. R., Xiong, F., Swinburne, I. A., and Megason, S. G. (2012). ACME: Automated Cell Morphology Extractor for Comprehensive Reconstruction of Cell Membranes. *PLoS Comput Biol*, 8(12):e1002780.

Moses, D. A. and Axel, L. (2004). Quantification of the curvature and shape of the interventricular septum. *Magnetic Resonance in Medicine*, 52(1):154–163.

Mühleip, A. W., Joos, F., Wigge, C., Frangakis, A. S., Kühlbrandt, W., and Davies, K. M. (2016). Helical arrays of U-shaped ATP synthase dimers form tubular cristae in ciliate mitochondria. *PNAS*, 113(30):8442–8447.

Murk, J. L., Posthuma, G., Koster, A. J., Geuze, H. J., Verkleij, A. J., Kleijmeer, M. J., and Humbel, B. M. (2003). Influence of aldehyde fixation on the morphology of endosomes and lysosomes: Quantitative analysis and electron tomography. *J Microsc*, 212(1):81–90.

Nakane, T., Kotecha, A., Sente, A., McMullan, G., Masiulis, S., Brown, P., Grigoras, I., Malinauskaite, L., Malinauskas, T., Miehling, J., Uchański, T., Yu, L., Karia, D., Pechnikova, E., de Jong, E., Keizer, J., Bischoff, M., McCormack, J., Tiemeijer, P., Hardwick, S., Chirgadze, D., Murshudov, G., Aricescu, A., and Scheres, S. (2020). Single-particle cryo-EM at atomic resolution. *Nature*, 587(May).

Nickell, S., Förster, F., Linaroudis, A., Net, W. D., Beck, F., Hegerl, R., Baumeister, W., and Plitzko, J. M. (2005). TOM software toolbox: acquisition and analysis for electron tomography. *J Struct Biol*, 149(3):227–234.

Nickell, S., Kofler, C., Leis, A. P., and Baumeister, W. (2006). Innovation: A visual approach to proteomics. *Nat Rev Mol Cell Biol*, 7(3):225–230.

O'Reilly, F. J., Xue, L., Graziadei, A., Sinn, L., Lenz, S., Tegunov, D., Blötz, C., Hagen, W. J., Cramer, P., Stülke, J., Mahamid, J., and Rappsilber, J. (2020). In-cell architecture of an actively transcribing-translating expressome. *BioRxiv [Preprint]*, pages 1–15.

Page, D. L., Sun, Y., Koschan, A. F., Paik, J., and Abidi, M. A. (2002). Normal Vector Voting: Crease Detection and Curvature Estimation on Large, Noisy Meshes. *Graph Models*, 64:199–229.

Peixoto, T. P. (2014). The graph-tool python library. Database: figshare [Internet].

Peter, B. J., Kent, H. M., Mills, I. G., Vallis, Y., Butler, P. J. G., Evans, P. R., and McMahon, H. T. (2004). BAR Domains as Sensors of Membrane Curvature: The Amphiphysin BAR Structure. *Science*, 303(5657):495–499.

Pienaar, R., Fischl, B., Caviness, V., Makris, N., and Grant, P. E. (2008). A methodology for analyzing curvature in the developing brain from preterm to adult. *Int J Imaging Syst Technol*, 18:42–68.

Polthier, K. and Schmies, M. (1998). Straightest Geodesics on Polyhedral Surfaces. In *Mathematical Visualization*, pages 391–409. Springer Verlag.

Rafelski, S. M. and Marshall, W. F. (2008). Building the cell: Design principles of cellular architecture. *Nat Rev Mol Cell Biol*, 9(8):593–602.

Razdan, A. and Bae, M. (2005). Curvature estimation scheme for triangle meshes using biquadratic Bézier patches. *Comput Aided Des*, 37:1481–1491.

Rigort, A., Bäuerlein, F. J. B., Villa, E., Eibauer, M., Laugks, T., Baumeister, W., and Plitzko, J. M. (2012a). Focused ion beam micromachining of eukaryotic cells for cryoelectron tomography. *PNAS*, 109(12):4449–4454.

Rigort, A., Günther, D., Hegerl, R., Baum, D., Weber, B., Prohaska, S., Medalia, O., Baumeister, W., and Hege, H. C. (2012b). Automated segmentation of electron tomograms for a quantitative description of actin filament networks. *J Struct Biol*, 177(1):135–144.

Rossman, J. S. and Lamb, R. A. (2013). Viral Membrane Scission. *Annu Rev Cell Dev Biol*, 29(1):551–569.

Rusinkiewicz, S. (2004). Estimating curvatures and their derivatives on triangle meshes. In *Proceedings of the 2nd International Symposium on 3D Data Processing, Visualization, and Transmission*, pages 486–493, Thessaloniki, Greece. IEEE.

Salfer, M., Collado, J., Baumeister, W., Fernández-Busnadiego, R., and Martínez-Sánchez, A. (2020). Reliable Estimation of Membrane Curvature for Cryo-Electron Tomography. *PLoS Comput Biol*, pages 1–29.

Sander, P. V., Nehab, D., and Barczak, J. (2007). Fast triangle reordering for vertex locality and reduced overdraw. *ACM Transactions on Graphics*, 26(3):89.

Shibata, Y., Voeltz, G. K., and Rapoport, T. A. (2006). Rough Sheets and Smooth Tubules. *Cell*, 126(3):435–439.

Sousbie, T. (2011). The persistent cosmic web and its filamentary structure–I. Theory and implementation. *Monthly Notices of the Royal Astronomical Society*, 414(1):350–383.

Stachowiak, J. C., Schmid, E. M., Ryan, C. J., Ann, H. S., Sasaki, D. Y., Sherman, M. B., Geissler, P. L., Fletcher, D. A., and Hayden, C. C. (2012). Membrane bending by protein-protein crowding. *Nat Cell Biol*, 14(9):944–949.

Stoschek, A. and Hegerl, R. (1997). Denoising of electron tomographic reconstructions using multiscale transformations. *J Struct Biol*, 120(3):257–265.

Sun, Y. and Abidi, M. (2001). Surface matching by 3D point's fingerprint. In *Proceedings Eighth IEEE International Conference on Computer Vision. ICCV 2001*, pages 263–269.

Szilvási-Nagy, M. (2008). Face-based estimations of curvatures on triangle meshes. *Journal for Geometry and Graphics*, 12(1):63–73.

Tang, C. K. and Medioni, G. (1999). Robust Estimation of Curvature Information from Noisy 3D Data for Shape Description. In *Proceedings of the Seventh IEEE International Conference on Computer Vision*, Kerkyra, Greece. IEEE.

Tang, G., Peng, L., Baldwin, P. R., Mann, D. S., Jiang, W., Rees, I., and Ludtke, S. J. (2007). EMAN2: An extensible image processing suite for electron microscopy. *Jo Struct Biol*, 157(1):38–46.

Taubin, G. (1995). Estimating the tensor of curvature of a surface from a polyhedral approximation. In *Proceedings of IEEE International Conference on Computer Vision*, pages 902–907, Cambridge. IEEE.

Taylor, K. A., Tang, J., Cheng, Y., and Winkler, H. (1997). The Use of Electron Tomography for Structural Analysis of Disordered Protein Arrays. *J Struct Biol*, 386(120):372–386.

Theisel, H., Rössl, C., Zayer, R., and Seidel, H. P. (2004). Normal based estimation of the curvature tensor for triangular meshes. In *12th Pacific Conference on Computer Graphics and Applications*, pages 288–297, Seoul, South Korea. IEEE.

Thirion, J.-P. and Gourdon, A. (1993). The marching lines algorithm: new results and proofs. Technical report, Institut National de Recherche en Informa- tique et en Automatique.

Tobler, R. F. and Maierhofer, S. (2006). A mesh data structure for rendering and subdivision. In *14th International Conference in Central Europe on Computer Graphics, Visualization and Computer Vision 2006, WSCG'2006 - In Co-operation with EUROGRAPHICS, Full Papers Proceedings*, pages 157–162.

Tong, W. S. and Tang, C. K. (2005). Robust Estimation of Adaptive Tensors of Curvature by Tensor Voting. In *IEEE Transactions on Pattern Analysis and Machine Intelligence*, volume 27, pages 434–449.

Toyoshima, C. and Unwin, N. (1988). Contrast transfer for frozen-hydrated specimens: Determination from pairs of defocused images. *Ultramicroscopy*, 25(4):279–291.

Trucco, E. and Fisher, R. B. (1995). Experiments in Curvature-Based Segmentation of Range Data. *IEEE Transactions on Pattern Analysis and Machine Intelligence*, 17(2):177–182.

Turoňová, B., Schur, F. K., Wan, W., and Briggs, J. A. (2017). Efficient 3D-CTF correction for cryo-electron tomography using NovaCTF improves subtomogram averaging resolution to 3.4 Å. *J Struct Biol*, 199(3):187–195.

Unwin, N. (2005). Refined structure of the nicotinic acetylcholine receptor at 4 Å resolution. *J Mol Biol*, 346(4):967–989.

Voeltz, G. K., Rolls, M. M., and Rapoport, T. A. (2002). Structural organization of the endoplasmic reticulum. *EMBO Rep*, 3(10):944–950.

Voss, N. R., Yoshioka, C. K., Radermacher, M., Potter, C. S., and Carragher, B. (2009). DoG Picker and TiltPicker: Software tools to facilitate particle selection in single particle electron microscopy. *J Struct Biol*, 166(2):205–213.

Wagner, J., Schaffer, M., and Fernández-Busnadiego, R. (2017). Cryo-electron tomography - the cell biology that came in from the cold. *FEBS Lett*, 591:2520–2533.

Walz, J., Tamura, T., Tamura, N., Grimm, R., Baumeister, W., and Koster, A. J. (1997). Tricorn protease exists as an icosahedral supermolecule in vivo. *Molecular Cell*, 1(1):59–65.

Wan, W. and Briggs, J. A. (2016). *Cryo-Electron Tomography and Subtomogram Averaging*, volume 579. Elsevier Inc., 1 edition.

Wiener, N. (1964). *Extrapolation, Interpolation, and Smoothing of Stationary Time Series*. The MIT Press.

Xu, M., Chai, X., Muthakana, H., Liang, X., Yang, G., Zeev-Ben-Mordehai, T., and Xing, E. P. (2017). Deep learning-based subdivision approach for large scale macromolecules structure recovery from electron cryo tomograms. *Bioinformatics*, 33(14):i13–i22.

Xu, M., Singla, J., Tocheva, E. I., Chang, Y. W., Stevens, R. C., Jensen, G. J., and Alber, F. (2019). De Novo Structural Pattern Mining in Cellular Electron Cryotomograms. *Structure*, 27(4):679–691.e14.

Xu, M., Wu, Y., Shroff, H., Wu, M., and Mani, M. (2018). A scheme for 3-dimensional morphological reconstruction and force inference in the early C. elegans embryo. *PLoS One*, 13(7).

Yao, Q., Jewett, A. I., Chang, Y.-W., Oikonomou, C. M., Beeby, M., Iancu, C. V., Briegel, A., Ghosal, D., and Jensen, G. J. (2017). Short FtsZ filaments can drive asymmetric cell envelope constriction at the onset of bacterial cytokinesis. *EMBO J*, 36(11):1577–1589.

Yip, K. M., Fischer, N., Paknia, E., Chari, A., and Stark, H. (2020). Atomic-resolution protein structure determination by cryo-EM. *Nature*, 587(May):1–5.

Yu, Z. and Frangakis, A. S. (2011). Classification of electron sub-tomograms with neural networks and its application to template-matching. *J Struct Biol*, 174(3):494–504.

Zanetti, G., Pahuja, K. B., Studer, S., Shim, S., and Schekman, R. (2012). COPII and the regulation of protein sorting in mammals. *Nat Cell Biol*, 14(1):20–28.

Zimmerberg, J. and Kozlov, M. M. (2006). How proteins produce cellular membrane curvature. *Nat Rev Mol Cell Biol*, 7(1):9–19.